

**Alma Mater Studiorum – Università di Bologna**

**DOTTORATO DI RICERCA IN  
GEOFISICA**

**Ciclo XXVIII**

**Settore Concorsuale di afferenza: 04/A4**

**Settore Scientifico disciplinare: GEO/10**

**TITOLO TESI**

**Stress Field and Seismicity at Campi Flegrei Caldera**

**Presentata da:** Elena Cristiano

**Coordinatore Dottorato**

**Pinardi Nadia**

**Relatore**

**Luca D'Auria**

---

**Esame finale anno 2016**



# Index

## Abstract

## Chapter I – Framework of the Area

### 1.1 Campanian Plane

### 1.2 Caldera generation

#### 1.2.1 Super Eruptions

### 1.3 Campi flegrei Caldera

#### 1.3.1 Structure of Campi Flegrei Caldera

#### 1.3.2 Other caldera

#### 1.3.3 Campi Flegrei caldera characteristics and precursors

## Chapter II – Analysis of seismic data

### 2.1 Seismic data related to volcanic area

### 2.2 Campi Flegrei caldera seismicity

#### 2.2.1 Details about the 2005–2006 uplift

#### 2.2.2 Comparison between bradyseismic crisis of 1982–84 and Other uplifts

## 2.3 Data Analysis

2.3.1 Picking of the earthquakes

2.3.2 Velocity model

## 2.4 Absolute and Relative locations of the earthquakes

2.4.1 Relative location & Double difference Alghoritm.

## 2.5 Focal mechanisms Solution

2.5.1 Results

## 2.6 1970-1973 Analysis

# Chapter III – Stress and Focal mechanism inversion

## 3.1 General overview of the stress

3.1.1 Pressure types

3.1.2 Mohr

3.1.3 Mohr-Coulomb Criterion

3.1.4 Coulomb – Navier criterion

3.1.5 Optimal principal stress orientation

3.1.6 Anderson's criterion

## 3.2 Stress in the magmatic chamber

- 3.3 Determination of stress
- 3.4 Stress Inversion
- 3.5 Inversion of Focal Mechanisms
  - 3.5.1 Analytical method
  - 3.5.2 Graphical Approach – RDM
    - 3.5.2.1 RDM modified (D'Auria et al., 2014)
  - 3.5.3 Graphical Approach – MIM
    - 3.5.3.1 MIM software & Results

## Chapter IV– Analysis of ground deformation data & Joint Inversion

- 4.1 Bradysism
  - 4.1.1 Similarity between 1970–1972 and 1982–1984
- 4.2 “1982–84” Bradyseismic crisis
  - 4.2.1 Other episodes of unrest
- 4.3 Leveling dataset & Analysis
- 4.4 Inverse method
  - 4.4.1 Linear and non-linear problems

4.4.2 Model estimation

4.4.3 Deformation Model

## 4.5 Joint inversion

4.5.1 Campi Flegrei caldera joint inversion

# Chapter V – Seismogenesis & Discussions

5.1 Hydrothermal system of Campi flegrei Caldera

5.2 Pore pressure Analysis

5.3 Thermo – fluid simulations (MUFITS)

5.4 The Campi Flegrei caldera Model

5.5 Simulations of the Hydrothermal system

5.5.1 Results

5.6 Bradyseismic crisis simulations

5.6.1 Results

5.7 Discussions & Conclusions

Bibliography



# Abstract

Aim of this work is the study of the stress field in the Campi Flegrei caldera during the bradyseismic crisis of 1982–1984.

Campi Flegrei caldera activity consist of secular ground movements, generally of subsidence, with rates of the order of 1 m per century (De Natale et al. 2001), and rapid unrest episodes, that in the recent time, just in one occasion culminate with eruptions, in 1538.

During period of uplift, the caldera is interested by phenomena of seismicity characterized by a determined spatial distribution.

In the first part of the work has been analysed old cretaceous and digital seismic datasets relative to 70<sup>th</sup> years, and the bradyseismic crisis of 1982–1984 where has been recorded the earthquakes linked to uplifts that interested Campi flegrei caldera during 1969–72 and 1982–84.

The seismicity dataset has been used to made some analysis as location and focal mechanisms generation. The focal mechanisms are than analysed using two software to determine the principal state of stress that was predominant in that period.

Then, starting from ground deformation data, relative to 1100 optical levelling measure done during the bradyseismic crisis, has been use the inversion method to modelling the source of the deformation. Has been used many model as the Mogi model, the penny shaped-crack, and the rectangular crack of Okada.

Consequently, a joint inversion was applicate on ground deformation data and seismicity together to better understand the dynamic of the stress in the area. Using this type of inversion, the aim was to know if existed a regional stress field in the area during bradyseismic crisis and if was dominant

on the local stress. It was possible estimate also if was present a “memory” in the system Campi Flegrei of precedent episode of unrest.

In the last part of the work, has been determined the excess of pore pressure in the Flegrean area, using focal mechanisms to study the influence of fluid pore pressure on change in the Coulomb stress of the area.

Has been used the Coulomb–Navier criterion and Terakawa method (2010) to estimate the excess of pore pressure.

Finally, in order to evaluate the reliability of the calculated pore pressures, was done thermo-fluid dynamic simulation and analysed the hydrothermal system of Campi Flegrei caldera. So, has been performed a series of simulation thermo-fluid dynamic injecting a flow in the system varying temperature, pressure and injection rate to model the Campi Flegrei caldera during the unrest.

# Chapter I – Framework of the Area

## 1.1 Campanian Plane

Italian Volcanism is linked to geodynamics of Tyrrhenian area, where a marked lithospheric thinning is observed (Wang et al., 1989 and references therein). This area is characterized by active tectonic linked to convergence of Euroasiatic and African plates, on what limits are located Italian volcanoes. Magma comes from the Earth mantel and interacts with the Earth crust. For Mt.Etna, Vesuvius and Campi Flegrei, the magma source is the mantel and the magma is generated for sucking of asthenospheric material from African Plate (Gvritzaman & Nur, 1999), or enriched of fluids or melt released by underlying oceanic slab(De Natale et al., E. Sc.Rev,2006). Junction of three faults system explains the magma rising through the Earth crust. Magma generation may be linked with slab withdrawal(Fig.1).

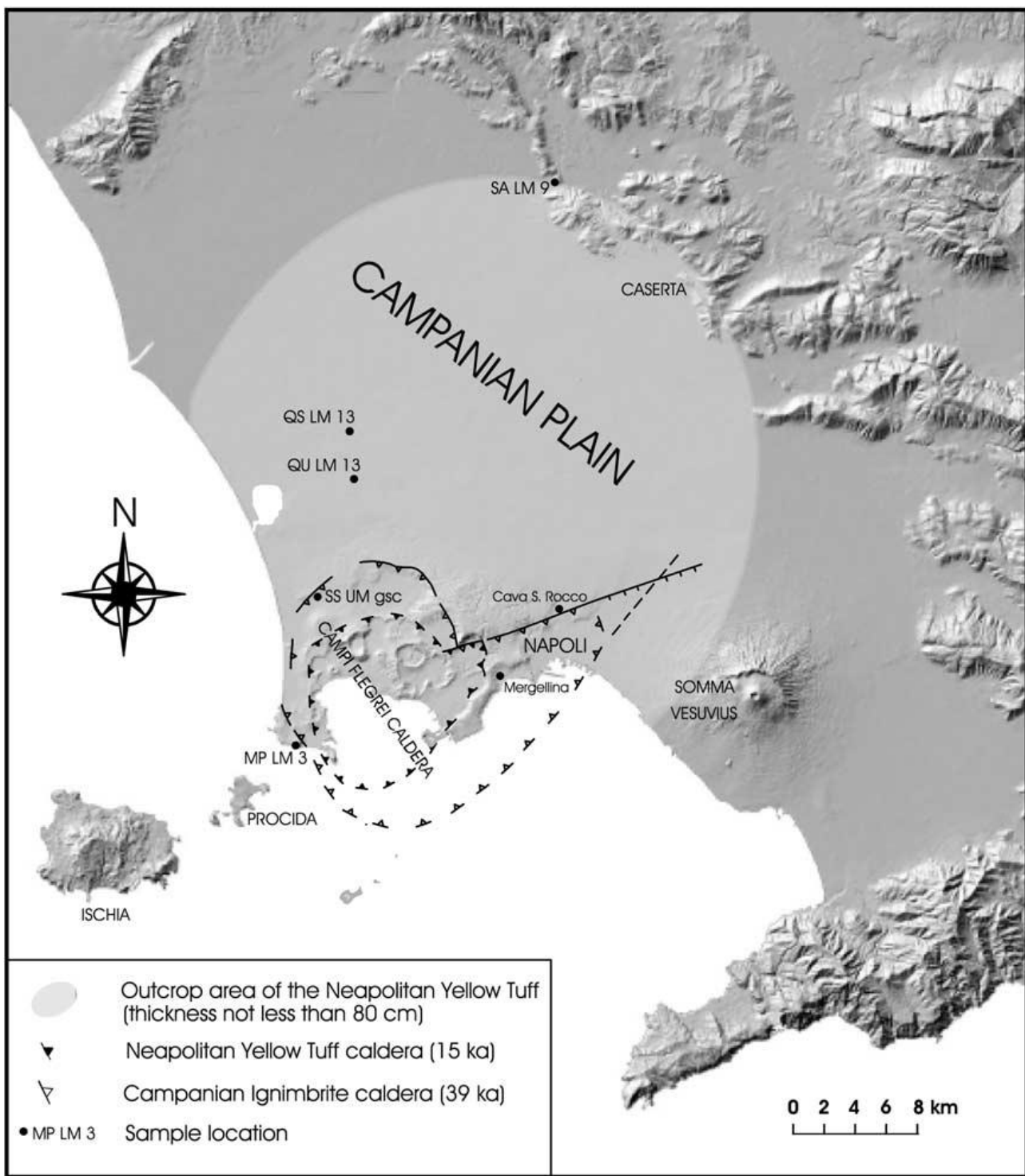


Figure 1 – (Deino et al., 2004) Campanian Plain

Tirrenian sea is an extensional neogenic basin generate during the formation of Appenninc chain and accompanies the anticlockwise rotation of Italian peninsula.

It's possible identify three periods where different tectonic situation interested the area:

- From Tortonian to Pliocene period: N-S and NNW-SSE Normal faults characterized initial extensional phases.
- Plio-quaternary period: NW-SE, NE-SW interested Tirrenic edge.
- Quaternary: NW-SE and NE-SW direct fault determined subsidence sectors that is the case of Campanian plate delimited at the North- Northwest by the morpho-structural high of Massico Monte and to south-east by Monti Lattari that constitute the Penisola Sorrentina. Along the coastline into the Campanian plane, there are the volcanic morpho-structures of Somma-Vesuvius complex and Campi Flegrei polocrateric district.

According with Scandone (1991), Campanian volcanoes are in a depressive zone: a graben bordered by Mesozoic carbonate platform, subject to sinking in the quaternary period. Under this depression, the platform deep is between 1 to 4-5 Km. Its origin is linked to continental crust thinning due to anticlockwise rotation of the Italian peninsula and in the same time due to the opening of Tirrenian sea. This movement involved carbonatic platform subsidence along the tirrenian coast (Scandone, 1979).

Then 1 Ma years ago, started a potassic volcanic intense phase in the zones of Campania and Rome. The stretching of the crust induced mantle uplift in the central zone of the tyrrhenian sea, which thickness seems to be from 5 to 10Km. Moho depth increases under Apennine chain while in certain zones is very shallow, as under Campi Flegrei where is 15 km due to upwelling ( Ferrucci et al, 1989).

The southern Apennine chain is a Neogene thrust belt built up for the continental collision between the Corsica-Sardinia microplate and the African plate (Zuppetta, 1991). Since the Upper Pliocene, regional extension has broken the Southern Apennine chain in several blocks, which led horst and graben development and formation of the Campanian plane. Its structure is controlled by two major normal faults system that have had a major influence on the location, within the plain of volcanic

fields as Roccamonfina, Campi Flegrei and Vesuvius. The recent seismic activity and the evolution of Tyrrhenian area (Scandone, 1979) shows an extensional tectonic regime.

In accord with Troise et al., (1998) the actual stress state of Apennine chain, deduced from focal mechanisms of bigger earthquakes, is extensional in the central and south part, instead is compressional in the north part of the chain. These two states seem to be due to anticlockwise rotation of the Adriatic plate around a pole located in the chain part bordering the Padanian plate where were observed moderate earthquakes thrust type.

On the basis of historical seismicity, it's possible divide the chain in various seismotectonics domains each one characterized by a certain style of seismicity and tectonic characteristics. Many of this domains, in the most part for the central segments and to the south of the chain, produced destructive earthquakes with magnitude up to 7. Every seismically active domain is characterized by normal fault, generally with strike in the direction of the chain. Other areas have low magnitude earthquake with occurrence of swarms. These areas are characterized by complex faulting mechanisms not easily linked to normal extension of the chain.

The Napolitan – Phleorean volcanic area is the consequence of alternating constructive and destructive volcanic and volcano-tectonic events. This area includes either a submerged and subaerial part in which lying Campi Flegrei and the city of Naples. The central part of Campi Flegrei is characterized by many tuff-rings and tuff-cones. To the north of Naples there are some plains that are bordered by steep cliffs. To the East there is a NE-SW elongated hill, bordered by steep scarp to the west and a dipping coast to the east and extends north-eastward into a chain of morphological heights (Fig. 2) (Orsi, 1996).

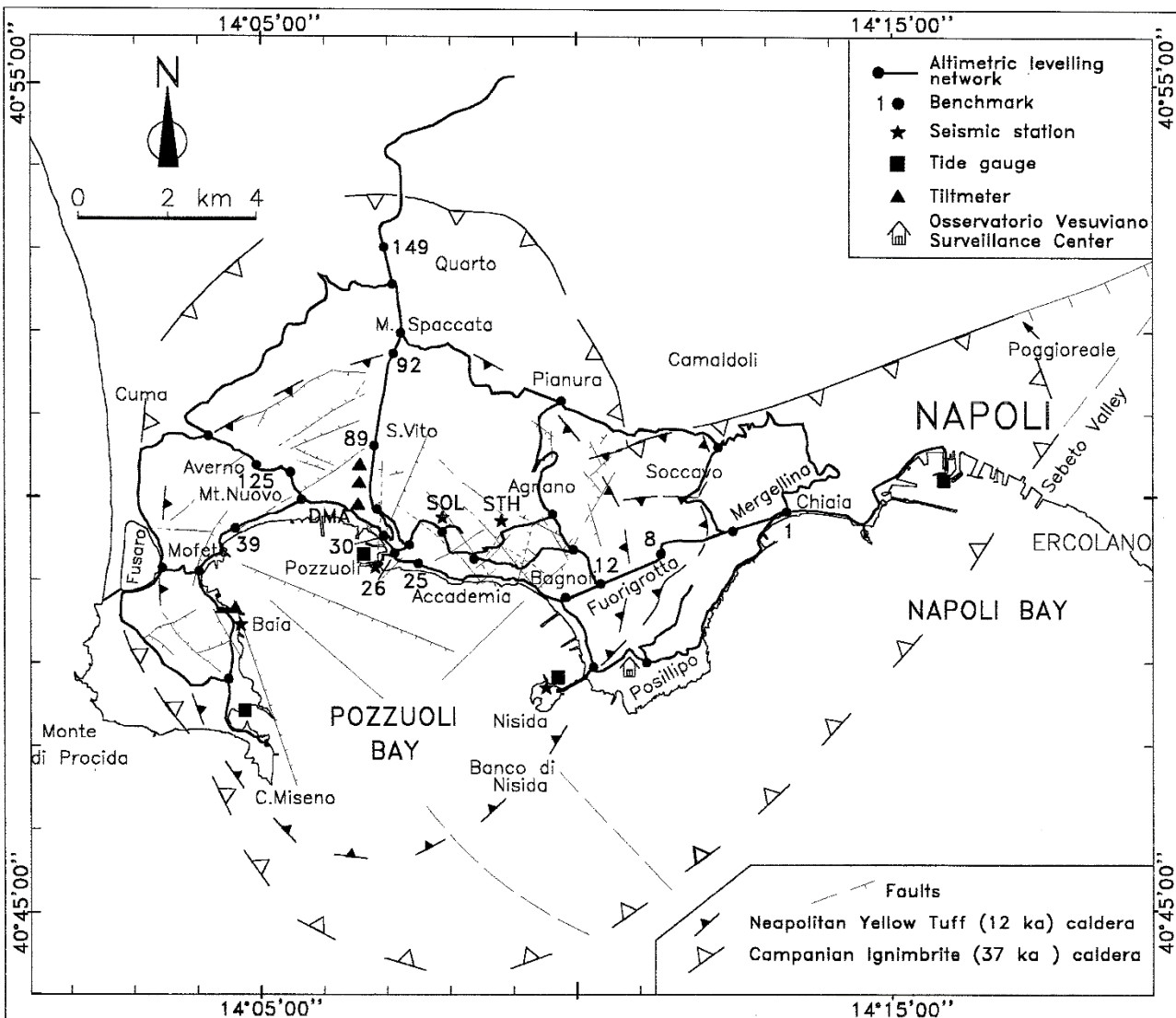


Figure 2 – Campi Flegrei caldera (Orsi et al., 1999).

## 1.2 Caldera generation

The simplest way to define a caldera is: a large depression due to sinking of a building volcanic part into the magma chamber after it was emptied. Macdonald (1972) define them as circular or elliptical volcanic depression with diameter major or equal to 1.6 Km. structures with smaller diameter are called *pit craters*.

Like other volcanic phenomena, caldera formation derives from a long process that involve generation of magma at depth, its ascent at shallower depth, differentiation and eruption from the earth surface. It's associated to most magma type from basalts to more evolved magma. Respect to the other volcanic process, caldera-forming eruption are rare because they require very specific stress and thermodynamic conditions for collapse to occur (Druitt and Sparks, 1984; Gudmundsson, 1998, Martí et al., 2000).

Calderization for many volcano fields with elliptical shape is due to pressure from the basis that normally is relative to magma accumulation that push forming a dome in the area bigger than the magmatic chamber. This situation generates calderization of the shallow crust.

Caldera and relative collapse are very common on the earth. Caldera structures are generally similar but with variable dimensions. The caldera with the biggest dimension has a diameter of 80 Km, the medium diameter for associated caldera is 6 Km. Some calderas are associated to regional fault, the most part of collapses however, happen along ring-faults associated to crustal magmatic chamber. The start of faulting and movement depend on local stresses which are controlled by load condition and mechanical proprieties of rocks and structures that constitute the volcano (Gudmudsson, 2008 ).

In particular, a ring fault is a shear fracture that is different respect the fault that generated earthquake. First of all, ring faults are closed fault with an elliptical shape, while faults that generate earthquakes are generally lines. More, the movement along the faults for generate collapse is bigger than for earthquake; in fact, large earthquakes may reach 10/20 meters of movement. Calderic collapse may reach even Km. For both of them, the movement is driven by shear stresses concentrated on fault plane. Another difference regards the fault inclination: ring faults are dip-slip faults. Dip-slip of earthquake normally are inclined of 45–75°, while many ring faults are near vertical. Because is improbable that the principal angle between direction of maximum principal

stress and fault plane differs for two fault types, this observation indicated that there is a fundamental difference between local stress field that control these different faults and different orientations of principal stress at the moment of fault formation and movement ( Gudmudsson, 2008 ).

Many ring faults are formed from local stresses around the crustal magmatic chamber. The general mechanism of formation is unclear but there are many clear aspects. It's known that these faults are shear fracture and their starting and development depends on the state of stress of the host rock. The state of stress in a volcano is partially controlled by mechanical propriety of their rock units and structures as existent contacts, faults and joints. Partially, volcanic stresses are controlled by load conditions at which the volcano is subject. In particular, the geometry and magma pressure into the associated chamber and the tectonic regime into which is located the chamber.

Ring faults are generally concentric and their inclination is outward from the caldera centre. Many of them are occupied by dikes many of which are inward and vertical.

All the models made to explain the formation of ring faults and calderic collapse are concordant on the fact that the movement along the ring fault is relative to the existence of a crustal magmatic chamber in which the calderic block subsides.

Many calderas are filled by lava fluxes from their edges. These fluxes indicated that under the caldera exists an active magmatic chamber and that the caldera is able to sustain an overload on the edges without slipping (Gudmudsson, 2008).

An outward fault that goes into a shallow magma chamber tends to slip while increasing the thickness of lava inside the caldera causes to the lava load, the extension and the friction loss, between the calderic block subsiding and the wall of the ring fault (Fig. 3). For an inward fault the load is concentrated along the fault because of concentration of tensile stress of domes. When the eruption is due to dikes, compressive stresses are generated from the dikes that encourage inverse slip on a

normal fault trying to close it. Thanks to friction along the fault plane, slip of ring-fault is stopped easily on an inward fault (after a certain slip).

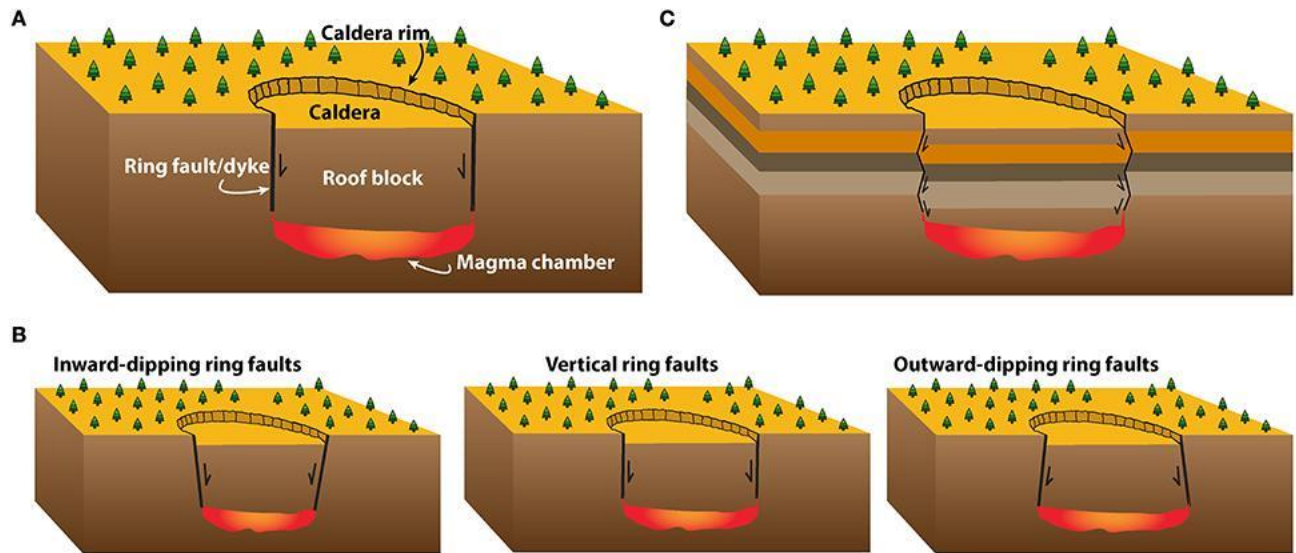


Figure 3. sketch of the different dip direction options for the outer normal ring faults (Geyer and Marti).

Caldera may be classified on the basis of the type of volcanism at which belong, because their dimension change. In fact, caldera associated with basaltic volcanoes are smaller (6–7 Km) than that associated of compounds volcanoes (18–19 Km). The quaternary calderas have dimension from 1.6 to 50 Km but generally, 94% are of 20 Km (Gudmudsson, 2008).

Deep calderas are normally located in crustal segment that during the unrest, have an elastic behaviour (Gudmudsson, 2008). This type of camera should be modelled in a bi-dimensional model as a cavity with finite dimensions:

- as a whole in an elastic host rock when it is fluid, where the fluid may have a zero young module;
- as an inclusion and elastic when it is solid, where the solid has a young module different than zero.

In the last case the magma stiffness in the magmatic chamber increase until the rock in the camera and the host rock not reach similar temperature (Gudmudsson, 2008) and, if has the same

composition, the stiffness of solidified magma in the camera could be similar to that of host rock so the camera is an elastic inclusion.

All the cavities and inclusions with different stiffness than the host rock and subject to stress load, concentrate stresses and generate local stresses, which control formation and slip of ring faults.

Magmatic chamber associated with caldera collapses are usually modelled as sill or spherical geometry.

One of the possible explanation for the formation of a magmatic chamber is that, stress barriers bring to formation of sill that subsequently absorbs the magma of dike who enters and evolves into a proto-camera that is smaller than “mature” camera, as if would generate a space for themselves.

It's clear that the space for plutons of big dimension is partially generated from elasto-plastic expansion of the crust, partially from partial fusion of the crust and partially from stoping<sup>1</sup>.

During the grown, the magmatic chamber could change its shape, transferring the effects on the local stresses around the camera increasing the probability of generate calderic collapses. For example, shapes as sill favour the collapse.

Due to external load, the maximum of stress concentration is along borders of the associated magmatic chamber. For these geometries, the resulting caldera collapse dimension is approximately equal to the area of the cross section of the associated magmatic chamber. If another caldera collapse occurs near the old caldera, it means that the magmatic chamber associated migrated within another position in the crust.

It's convenient to consider only the magmatic pressure in excess that is defined as total magmatic pressure minus lithostatic pressure in the crust near the magmatic body. In this way it's possible

---

<sup>1</sup> Process of magma accomodation ascent at the surface from a mantel source or lower crust

consider gravitational effects. This is because lithostatic pressure is an isotropic stress state that increase with depth proportional to crustal rock densities.

Considering elliptic crustal plate subjected to uniform vertical excess due to magmatic pressure at its basis, plate uplift,  $w$  is

$$\nabla^2 \nabla^2 w = p_e D$$

Where  $\nabla^2$  is laplacian operator,  $D$  flexural rigidity of crustal plate

$$D = \frac{Eh^3}{\{12(1 - \nu^2)\}}$$

With  $E$  the young's modulus, the thin  $h$ , Poisson ratio  $\nu$  of the crustal plate.

During the caldera collapse the thin of that crustal plate part occupied by the caldera is gradually reduced of a mass equal to the subsidence of the caldera at each particular moment.

Magmatic pressure in the deepest reservoir that induces crustal doming of hosting plate the caldera may be analysed by elliptical slab subject to uniform load at the base. Since the slab may be thin one-tenth of its diameter, the appropriated model is the deflection one relative to a thin slab. For a crustal elliptical plate of half-width  $a$  and half-length  $b$ , where  $b>>a$ , vertical movement will be

$$w = \frac{p_e}{24D} (a^2 - x^2)$$

Maximum movement  $w_m$  occurs in the slab center where  $x=0$  so

$$w_m 24D = P_e a^4$$

Longitudinal strain  $\epsilon$  is linked to vertical movement  $w$  through

$$\epsilon = z \frac{d^2 w}{(dx^2)}$$

Differentiating twice and substituting for  $P_e$

$$\epsilon = \left(\frac{4w_m z}{a^4}\right) (3x^2 - a^2)$$

Where  $z$  is the vertical axis, measured from the neutral surface and considered positive upwards.

For the uplift, many parts of crustal plate are subject of tensile strain, instead the others are subject to compressive strain. Either the roof of the regional magma reservoir and the central part are subject to compressive strain, creating difficult for dyke injection in that part. The marginal part is subject to tensile strain, favouring dyke injection. Dyke injection from regional reservoir tend to became sill that, if there is frequent injection, may develop in a new shallow magmatic chamber.

One of calderic collapses mechanism may be the underpressure model. in this model the mechanism is the underpressure of magmatic chamber in which the calderic floor goes down eventually. This mechanism is defined as withdrawal of magmatic support, and is the first trial to explain the caldera formation (Anderson, 1936).

In that model, the underpressure is modelled as the centre of compression nucleus of strain. In the extreme version, is assumed that after the eruption, remain a vacant cavity that forms part of the magmatic chamber, or all of it, into which the roof of the caldera goes down. The volume of the vacation and consequently of the caldera, is supposed correspond to the material ejected and intruded during the eruption. This model is very simple but there aren't evidences of the vacation presence after the calderization because the vacations generally are shallow while calderic collapses generally are linked to chamber located in depth and are too big in order that the absolute tension acts except near the camera. More, there is a volume loss that there isn't explain in the model corresponding to the moment in which the magma leaves the chamber and the collapse. And there is no explanation of how the magma may be bring outside the chamber when the pressure excess is supposed be zero or negative.

Ring dyke, instead, are associated with many ring faults. One possibility is that the dyke starts in the superficial part of magmatic chamber and then meets a ring fault that propagates downward or that the ring fault propagates downward, either from free surface or from some layers of the camera

roof, to the top of the chamber and so is flooded of magma when meet the magmatic chamber becoming a ring dyke.

### 1.2.1 Super-Eruptions

The USA host three calderics system responsible of super eruptions of 2 million of years ago, two of which Long Valley and Yellowstone show frequently sign of unrest like earthquakes, ground deformations and gas emissions with high temperature. The third system, Valles caldera in New Mexico, seems to be quiescent but erupted more recently than Yellowstone (40.000 vs 70.000 years ago).

The term Super eruption is an informal term referred to huge pyroclastic eruptions, volcanic events in which almost  $300 \text{ Km}^3$  of magma are erupted explosively from chamber surface and deposit in the surrounding zone as pyroclastic fragments pumice and ash. The fast ejection of big volume of magma is cause of collapse of ground overlying the magmatic chamber and incorporate of surrounding zone generating a volcanic depression that may have diameter major than 30 Km.

To categorize explosivity of volcanic eruptions is used the volcanic explosivity index (VEI) by Newall & Self(1982) that organize eruption on the basis of ejected volume and highness of eruptive plume.

To product rapid eruption with big magma volume that:

- has to be stored near the earth surface in the way that may be expulse quickly;
- has to contain enough dissolved gas so that every initial eruption and consequent uncorking of magma result in a continuous forced expulsion of magma.
- has to be viscous and has high superficial tension so that bubbles cannot form easily.

Is the case of rhyolitic fluid that has from 10 to 1000 times major viscosity than basaltic fluids. So there will be a quickly degassing that brings magma fragmentation and incandescent ash clouds generation that expand above of the stratosphere and partially collapse laterally in ash clusters that flow radially from the eruptive centre. Many magmatic chambers in the crust are formed from repeated and sustained intrusions of hot basaltic melt poor in silica created from below mantel.

The evolution of a potential super eruption may be summed up as mix of melt crust with basaltic fluid that cools and crystallizes generating more advanced and reach in silica melt. If the magma fails to reach the surface and to make little eruption, the system may develop in one which is able to generate a super eruption. Many calderic system produced and may produce more of one big eruption, so that the conditions that bring to super-eruption may be in the same spot many times.

But also the area in which stay the magmatic chamber is important to allow the super-eruption where the silica magma may quickly generate.

- subduction zone of pacific chain
- area with high input of mantel magma and tend to create magma with silica composition.

Generally, the area that not create these big eruptions are which with low rate of volcanism or oceanic areas with basaltic melt.

### 1.3 Campi Flegrei caldera

The Campi Flegrei caldera (CFC) is an active volcanic complex of about 12 km of diameters, inhabited by about 2 million people (Fig. 4). For the intense urbanization of the area, it's associated to high volcanic risk (Ricci et al, 2013). Its activity is constantly monitored and studied to better understand the dynamic of the area. It's an holocene caldera located at the west of Naples in an area of regional expansion (Bruno,2003).

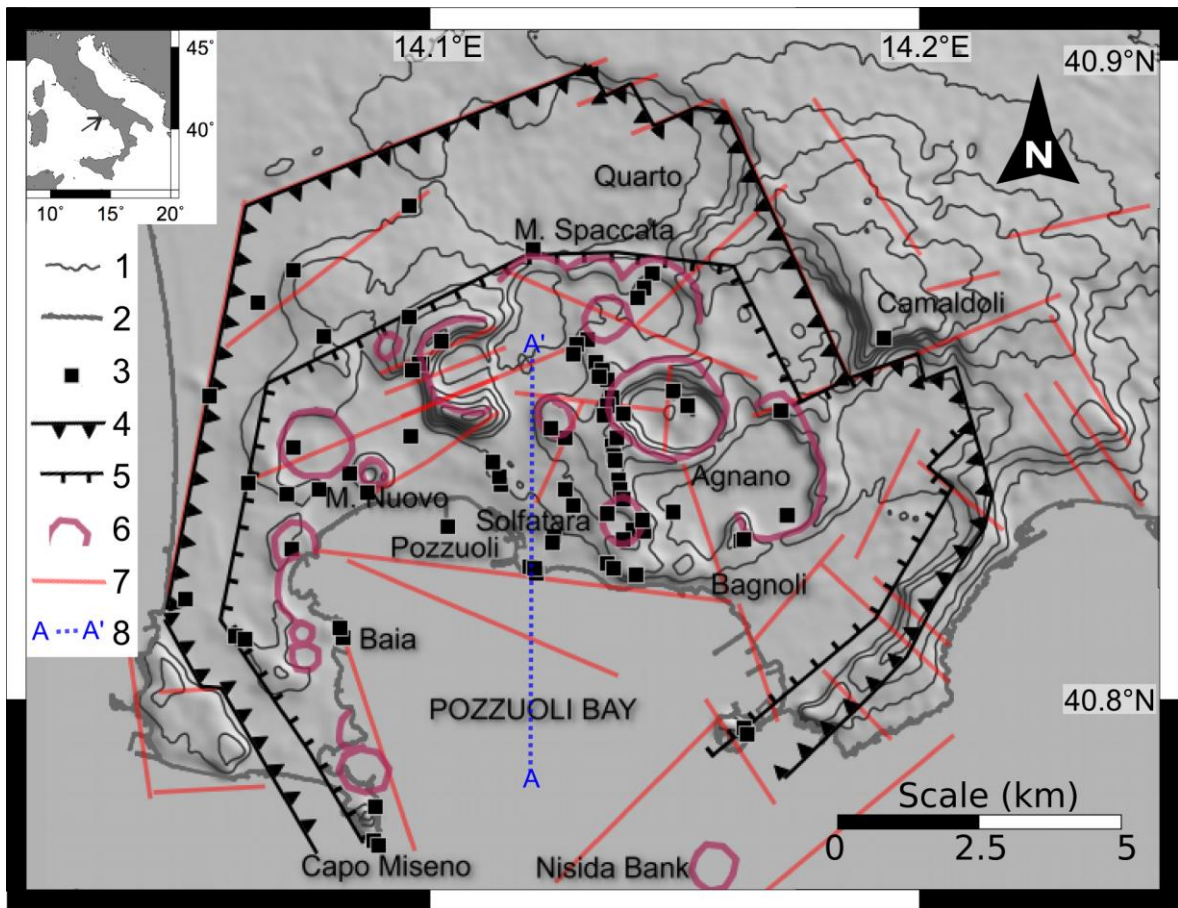


Figure 4 – Campi Flegrei caldera

This depression, belongs to the Phleorean Volcanic District, which includes the islands of Procida-Vivara and Ischia. The District is also characterized to numerous Quaternary vents inside the caldera and submarine vents in the Gulf of Naples.

The continental volcanism and insular of Campi Flegrei is imposed on a structural high (Di Girolamo et al 1984; Bruno et al,2002), which low zone are represented by Naples Gulf and Volturno plane. This horst continues inside the land with an anti-appenninic trend until the area most norther (Finetti & Morelli,1974; DI Girolamo et al.,1984).

Napoletan gulf is crossing by a Campi Flegrei - Ischia fault (De Alteriis & Toscano,2003) and by the Dhorn fault (Milia & Torrente,1999). At south confined with Capri-Penisola Sorrentina fault (Sacchi et al.1994). during the inferior Pleistocene one tectonic event is responsible of generation

of Napoletan gulf, through NO-SE normal faults system; the second event happened among inferior and medium Pleistocene, produced asymmetric structures as half-graben with anti-appenninic axis with NW-SE, NE-SW and E-W faults of new generation or along precedent lineament responsible of actual Napolitan Gulf disposition and interesting also the flegrean vulcanites (Beneduce & Schiattarella, 1989-1990).

Bianco et al. (2004), found that the hydrothermal area of the Solfatara crater is characterised by a system of NE-SW striking, mineral-filled fractures and cracks superimposing the general NW-SE orientation of the fault system in the area. This explained the coexistence of these two orthogonal fracture fields in terms of increased fluid pressure in the main faults that induce a compressive stress on the surrounding rocks. This stress may generate new cracks or reactivate pre-existing cracks, parallel to the direction of the maximum compressive stress and perpendicular to the pre-existing fault, allowing fluids flow along this direction on the basis of the properties of the surrounding rocks.

Two major eruptive events have occurred in this area: the Campanian Ignimbrite eruption (39ka) and the Neapolitan Yellow tuff eruption (15ka). De Lorenzo (1904) divided the Campi Flegrei activity in three periods. The first includes the CI, the second the NYT and in the third are located the recent activity products inside the caldera. Zaniboni (1919) was the first that interpreted the CI eruption products as deposits linked to a deposition of ash flow mechanism. Rittman et al. (1950) postulated the existence of a central volcano (Archi-flegreo) destroyed by the CI eruption with successive calderic collapse (Lirer, 1987).

The NYT eruption happened 12000 years ago. Deposits are founded most of all outside the Campi Flegrei Caldera and under the recent activity. Rittman et al. (1950) and Rosi et al. (1983) suggest that these products are results of eruptions from many different centres. However other studies (Nardi and Incoronato, 1986) using magnetization and maps of products suggest the principal

source in the oriental sectors. The actual caldera was formed after this eruption due to a collapse of hundreds of meters in the central part. The collapse had to happened along some of the fractures relative to the precedent collapses due to emplacement of CI. Minimum volume estimate is of 10  $Km^3$  DRE, while a rough estimation of the filling of the caldera bring to 16  $Km^3$ .

According to Di Vito et al. (1999), volcanic activity occurred between 12ka and 3.8ka. The oldest products are the Punta Marmolite dome (47.000 yr bp) and Cuma (37000 yr bp) situated at the edges of CFc and put in place in a sub-aerial environment. The biggest eruption happened 34000 years ago and product ash floe deposits that covered the entire Campanian plane. Ash flow volume and fall deposits is 80  $Km^3$  of DRE (dense rock equivalent). Mlekstsev et al. (1984) discovered an ash layer linked to CI in Russian; that suggest an under estimation of the volume. Volcanic islands of Vivara and Procida are generate from many eruptions that originated a polycrateric field. De Astis et al. (2004) suggests 70ka as starting of volcanic activity of Procida, while at Fiumicello volcano is attributed 60-75 ka (Fedele et al.,2010). The last eruptive event (Solchiaro volcano) is dated 19ka (Alessio et al. 1976) or 17ka (Lirer et al.1991). All of these buildings are tuff cone type.

Di Girolamo (???) studied the deposits continuity and observed lateral chemical variations linked to differentiation of processes happened in the magmatic chamber.

Rosi et al. (1983) suggest a ring shape fracture surrounding CFc as source of feeding of CI eruption. Di Girolamo (1984) instead suggest arched fracture at north of CFc. Whatever is the alimentation system, this eruption brings the collapse of an area that included the CF. Borehole and stratigraphic data indicate that after this eruption and before the NYT there was a period of submarine and subaerial activity.

Basing on products, the character of this eruption is transitional between surge and pyroclastic flow.

Successive activity was located at the edge of the area more collapsed bring to numerous monogenetic volcano.

Between 12,000 an 8000 yr bp was identify a phase of activity starting with the Pomici Principali (PP) eruption characterized by a thin layer of air fall deposits founded east the caldera. At this phase are linked the Archiaveno, Gauro e Montagna spaccata volcanoes. Between NYT and PP was found a thin paleo-soil indicating a low activity period or volcanic quiescence.

Part of NYT caldera is characterized by the NNW-SSE volcanic alignment of Miseno Bank located along the Pozzuoli gulf that is younger of NYT and older of Nisida volcano. The youngest of this bank, Fondi di Baia, overhangs a bronze age settlement.

A significant uplift in the central part of caldera happen before 4500 yr bp resulting in an echelon pattern of normal faults located in the north sector of Pozzuoli gulf.

The caldera centre is signed by marine terrace raised that actually is 40 m above the sea level. The starting point of the uplift is happened after the formation of the caldera of NYT eruption at the same time the Pozzuoli bay subsided at south . Another palaeosoil dated 6750 yr bp is located under a new phase of activity culminating between 4500 and 3700 yr bp during which in the centre of caldera formed other volcanoes structures that in chronological order are:

- Cigliano;
- Monte Spina;
- Solfatara;
- Monte Olibano;
- Astroni (3800 yr);
- Averno (3700 yr);
- Senga.

Then, after a long period of quiescence, there was a possible phreatic event in 1198. The activity generally consists in strombolian, phreatomagmatic and dome eruptions, with magma composition that ranges from shoshonitic to trachytic to trachifonolitic (D'antonio et al.1999). The last eruptive activity reported occurred in 1538 A.D with the Monte Nuovo eruption.

### 1.3.1 Structure of Campi Flegrei Caldera

The structure of the caldera has been investigating via several 1-to-3 km deep boreholes using local earthquake seismic tomography, gravity and magnetic surveys and some teleseismic and wide-angle seismic observation (Rosi and Sbrana, 1987; Aster and Meyer, 1988; Ferrucci et al.,1992). The boreholes shown that the caldera is characterized by high temperatures at shallow depths (390° measured at 3 km depth) (De Lorenzo et al., 2001). The caldera is filled by a layer of volcanic deposits, a few kilometres thick, which forms an inner basin that is characterized by a low P-velocity ( $V_p$ ), high  $V_p$ - $V_s$  ratio, and high P-wave attenuation and low density.

Vanorio (2005) modelling of rock physical properties interpret a low  $V_p/V_s$  anomaly at 4 km depth as the top of formations enriched in gas under supercritical conditions. This interpretation excludes the presence of melted rocks at 4Km depth that require high  $V_p/V_s$  ratio. This is also in accord with the results of Zollo et al. (2003). He analysed the dataset of 82–84 bradyseismic crisis where the earthquake locations are mostly distributed on the top of velocity reversals and within the low  $V_p/V_s$  anomaly hypnotizing that seismicity might be induced by overpressured fluids.

In September 2001, a marine active seismic survey (SERAPIS) was performed in the bay of Naples to investigate the shallow structure and detecting the deeper magmatic system using seismic tomography and migration techniques (Zollo et al., 2003; Judenherc and Zollo, 2004). The high resolution 3D tomographic images of the Campi Flegrei caldera revealed the presence of a ring like,

high P-velocity and high density body at 800–2.000 m in depth, with diameter of about 8.000 – 12.000 m and a thickness of 1.000–2.000 m, which has been interpreted as the buried rim of the caldera (Zollo et al., 2003). Tomographic images revealed also the position of dikes, volcanic structures and the off-shore fumaroles detected in the Gulf of Pozzuoli (De Bonatibus et al., 1970; Pescatore et al., 1984; Milia, 1998; Milia and Torrente, 2003). The presence of these structures suggests the existence of a highly fractured area, through which the magma and gases may rise to the surface (Dello Iacono, 2009).

The eastern side of the caldera is bordered by a regional SW-NE normal fault that affects the carbonate basement at 4000 – 5000 m at depth suggesting that the eruptive activity of CFc is fed by regional fractures that are directly linked to a deep magma reservoir.

Magnetotelluric surveys of Zollo et al. (2006) shown a low resistivity zone, 4000m under the town of Pozzuoli, while low VP/Vs anomalies recorded in the same area was interpreted as a constraint to evidence an horizontal interface around this depth. The high attenuation beneath La starza and Pozzuoli-Solfatara at -3000 m is interpreted as due to the presence of a vapour-filled conduit. Similar low-velocity ratio conduits was reported for Redoubt volcano in Alaska (Benz et al., 1996), Mt.Etna, Italy (Villaseñor et al., 1998) Aso volcano, Japan (Sudo and Kong, 2001) and Mt. Vesuvius (Scarpa et al., 2002) all interpreted as highly fractured zones and/ or active magma conduct system. Low Vp/Vs ratio is also detected in geo-and hydro-thermally active areas, such as the Yellowstone caldera (Chatterjee et al., 1985), the Coso Region (Walk, 1988) and the Geysers geothermal area, California (Julian et al., 1996). In CFc the strong attenuation can be explained by the presence of the vapour phase in the rock matrix, on the basis of the theory of Takei (2002). De Siena (2010) also detect a small melt patches present at 2000 m that may contribute to the magmatic gases flow and interact with the hydrothermal basins and gas reservoirs recognized at shallower depths. Another attenuation anomaly was found around -3200 m that may constitutes the upper part of a

vapour-filled conduit that may be connected with the -7500m sill and /or associated with the melt zone located at -3200 m contributing to the transport of magmatic gases towards the surface (De Siena, 2010) as suggest Nakajima and Hasegawa (2003) for Naruko volcano.

Zollo (2008) modelling magma properties based on measured seismic velocities, indicating the occurrence of a partial melting zone, with a relatively high melt percentage (65–90%). He showed that the horizontal extension of the melt layer beneath Campi Flegrei can be estimated not less than  $30 \text{ km}^2$  with an approximate thickness of 1 km. In CFC exists a shallow, extended fracturated rock layer saturated with supercritical fluids, above a mid–crustal melt zone. This is a similar observation at other unrest calderas, such as Yellowstone and Long Valley (Husent et al., 2004; Chang et al., 2007; Sorey et al., 1998). At 7000 m deep, Zollo (2008) also revealed 2000 m thick low velocity layer interpreted as being associated with a mid–crust, partial melting zone, suggesting a large magmatic sill present in the basement formation.

The attenuation tomography by De Siena (2010) suggest three geothermal basins, located beneath Pozzuoli, between 0 and -3000 m, Mofete and Mt.Nuovo, between -500m and -2500m, and beneath Agnano, between -1000 m and -3000 m. Geothermal drilling also has shown high-temperature gradients in all of these area ( $150^\circ\text{C km}^{-1}$ ), and the presence of two distinct aquifers in the Agnano area at 150–300 m and 1250–1600 m of depth. These aquifer may interact with the conduit, favouring the upward circulation of hot non-magmatic vapor that constitute the main part of the fumarole gases at the surface (Caliro et al., 2007). Todesco et al. (2003), Hansen et al.(2004) and Caliro et al.(2007) suggest and interpreted also a gas reservoir between 0 and -2500 m at north–westward of the solfatara crater, also on the basis of diffuse degassing (Fig 2). Chiarabba et al. (2006) suggest that the model of unrest is the fluctuation of gas over-pressure within the reservoir located at 2–4 km beneath the caldera (identified by low Vp and low Vp/Vs). In their

opinion, if exists a magma chamber responsible of the heat, it's located beneath 4 km identifiable with direct body wave arrivals of local earthquakes and shots.

### 1.3.2 Other calderas

Many caldera in the world present the same characteristic of Campi flegrei caldera

#### **Yellowstone**

Yellowstone is a volcanic field with 3 younger caldera with less of 2.1 mln years. Yellowstone belong to the more recent manifestation of hotspot that produced big caldera spread on 700Km along the Snake River plain starting from Nevada. Magmatism started about 16.5 Mln years ago and moved progressively to north-east as the principal North-American plate that moves constantly to south-west relatively to an apparently fixed hotspot of mantel. Movement rate of the plate seems to stay constant while volcanism rate decrease may be due to the cooler and more thin nature of the continental crust on which affect the hotspot.

Presence of mantle hotspot at low density create an anomaly of geode, that to Yellowstone is 10 meters above which of geometric ellipsoid. The size of the anomaly is similar to that of oceanic hotspot so how the Hawaii island, Azores and Galapagos. The anomaly is accompanied by topographic anomaly for which Yellowstone is located 600 m above surrounding area. Yellowstone also is located in a tectonically active zone, in a point of intersection really complex of the hotspot with Basin and Range district which diffuse actively and old fault and trust of rock mountains that tent to release part of regional stress.

Fault trend and earthquake epicentres change when are located in the Yellowstone area, passing from a north-south azimuth to north-east. Resulting a tectonic parable that rotate around

Yellowstone and shows clearly the high influence of Yellowstone and the influence of the hotspot on the regional stress field.

More, 640.000 years ago was generated the caldera that then was buried by lava.

Map of epicentres distribution in the caldera shows a linear trend that means that regional fault controls the most part of earthquakes under the caldera. More the post-calderic vents formed with lava flow follow linear trend through central caldera and along west edges, parallel to structural grains of mountains at south the caldera.

As many volcanoes, Yellowstone has hydrothermal system activity as steam and hot water, that stay between earth surface and magmatic chamber.

In 70's geodetic survey demonstrate that the central part of the caldera is rise of 80 cm from 20's identifying resurgent dome in central part. Other studies document formation of post glacial crater of hydrothermal explosions, young faults and plentiful seismicity.

Even if the Yellowstone fumaroles have lower temperatures than other volcanoes, millions of thermal zone cover the  $70Km^2$  area. Convective thermal flow estimate is 5–6 GW with a mean of  $2 W/m^2$  into the caldera that is 30 times the mean continental value. More, studying the value of  $CO_2$  reveals an anomaly that is that Yellowstone releasing over 45.000 tonnes per day.

It's unknown if Yellowstone is in cooling or warming because the heat and gas are consistent either with cooling of a big rhyolitic-static magmatic chamber either with accumulation of hot basalt with mantel source.

A P-waves anomaly is founded at 8 Km depth through seismic tomography based on local earthquake, that may interpreted as a partially melt zone with an inverted banana shape which final part are resurgent domes. From hypocentre maximum depth is understood that ductile rock with 350°C of temperature exists at 5 Km of depth. Out from the caldera these temperatures aren't

obtained more superficially of 15 Km. Gravity field of Yellowstone is dominated by 60 residual mGal centred on caldera and extended to north-east. Models relative to this data suggest that the caldera is at the basis of volcanic deposits at low density located on a top of a crystallized body of rhyolitic magma. Given the dimension of the caldera and the implicated depth, is reasonable that almost 15.000  $km^3$  of melt and crystal is linked above the caldera at 8-18 Km depth. If the melt fraction are 0.1-0.15, exist enough melt to form mass for super-eruption if it's removed and will accumulate in a manageable volume. Among signals type measured, earthquake swarms are a common way to release seismic energy to Yellowstone as in the other calderic system. At Yellowstone, from 1000 to 3000 / year earthquake are recorded by the monitoring system. 2/3 of them are recorded in the area with trending east-west linear that link Hebgen Lake with north edge of the caldera. The earthquakes seem to be concentrated along a trend of a buried ring-fractures system formed during calderic collapse during the eruption of 2.1 million of years and may be the result of stress transferred in the area from the earthquake of Hebgen Lake of 7.5 magnitude recorded in 1959.

Other earthquakes happen along a linear trend inside the caldera along faults located at south of the caldera in the hydrothermal zone and in geyser reservoirs. 1/3 of these earthquakes are linked to discrete swarms of little earthquake happen on an area concentrated for a limited time. Many of these happened in the first seismogenetic zone, others inside the caldera or south or east. A big swarm happened in the autumn of 1985 with 3000 events recordable until 4.9 magnitude in a period of three months in the area that go to north-east of the caldera until Hebgen lake.

### **Long Valley Caldera**

The Long Valley caldera is a complex volcanic system along the eastern Sierra Nevada, California of 600  $km^3$  large.

The Caldera was generated from a super eruption of 760000 years ago. The most recent eruptions were on the order of 50.000 years ago (Bayley, 1989) In the last few thousand years has taken place smaller-scale activity along the Mono/Inyo chain of craters, west and northwest of the caldera (Bailey, 1989). Geodetic data reveal a deformation since 1980 associated with uplift of resurgent dome and in the last years seems to be correlated with injection beneath the Mono/Inyo craters . Presence of magma body beneath the surface of the caldera has inferred by indirect evidence as velocity anomalies and S-wave shadowing. A deformation model used geodetic data suggest intrusion for the last unrest (1997) with inflating Mogi source from 5 to 12 km depth (Langbein et al., 1998). The seismic activity in the region has generally regarded as tectonic, either an accommodation of strain due to inflation of a resurgent dome or a reflection of the ongoing extensional tectonic process.

Scientist also recorded Lp and VLP volcanic earthquakes that reflect movement of magmatic fluid slug or hydrothermal from 3 to 30 Km of depth (Hill et al 2002 a,b). The seismic activity recently occurred beneath Mammoth Mountain with most notably swarm of six months' duration in 1989 (Hill et al. 1990)

Deep Lp earthquakes are documented in a certain volcano environment, usually during magma recharge periods at mid and lower crustal levels. These events aren't recorded in Yellowstone but is unknown if don't happen or aren't identify because too small.

Earthquake produce effects that may be recorded in other signals as deformation, gas temperatures and other signals. After a 7.5 magnitude earthquake, are recorded many changes of hydrothermal system. After some days was erupted geyser from 289 sources, 160 never erupted before. Change in the system cause increase in temperature and turbidity. 590 sources become muddy in the first days after the vent, many return clear after some days, others after years. Temperature data for Firehole river sources shown increase of temperature of 3° respect value of temperature before the

earthquake. Change in permeability in the surface caused conversion from cold ground to thermal ground for months, after the earthquake.

80 cm of uplift was measured before 1983 but until mid-1990 was present subsidence inside the caldera. At the end of 1990 deformation data shown that two resurgent domes may operate independently with one that arise and the other one still or in subduction. Today we know that uplift may happen either inside and outside of the caldera and thanks to GPS and INSAR data revealed that between 1997 and 2003, centre-north caldera suffered 20 cm of uplift, while resurgent domes subsided, then deformation shifted to resurgent domes that began to rise with more of 8 cm of movement recorded from gps stations continuously from 2004 until present. The reason for deformation may be magmatic intrusion, hydrothermal fluids migration or brine or gas.

The hydrothermal system exerts an own eruptive activity, including not only steam geyser and hot water, but also explosive hydrothermal eruption that ejected rock fragments. In the last 30 years, many of this events were small and formed small craters, even if geologist identify 10-20 crater of recent hydrothermal explosion with diameters that goes from 100 to 300 meters. The trigger of this events may include earthquake, rise of gas emission or decrease of hydrostatic pressure resulting from deglaciation or drought.

Uplifts located in the north-central caldera recently seem to be linked to temporary hydrothermal phenomena. During the period 1997–2003, uplift in this area produced dilatation more than 6 microstrain. This dilatation may be responsible for some unusual thermal phenomena notated near the Norris geyser basins during 2003, in which normally sleeping gayster steamboat erupted 3 times, opening a rift of 75 meters north Norris, created a new fumarole field and a disorder in the geyser generate new mud pools, fumarole and all the vegetation died by heat. In the autumn of 1985, bigger earthquake swarm coincide with a change from a long terms uplift to subsidence period. Earthquake happen for accumulated stress release in the caldera wall and permit at pressure

in the form of hydrothermal fluid, to be release in higher regions. Waite & smith (2002) interpreted swarms as migration fluids along an almost vertical crack from the caldera, while Husen et al. 2004 founded an area of anomalous seismicity speed that interpreted as evidence of gas accumulation in the same region of the 1985 swarm. These correlations are made also in the Campi Flegrei, where a long term record of fumarole output, show that cycles of uplift/subsidence are followed by change in the ratio  $CO_2$ /steam of discharge gas. Phenomenon interpreted as period of increase of release of magmatic gas (Todesco et al 2004)

In 1980 there was an unrest in the long valley caldera that started with 4 earthquake of 6 magnitude degrees, three of which happened in the same day. Recording quickly the deformation area found evidence for 20 cm of uplift respect the precedent summer. From 2006, caldera had 80cm of intermittent uplift with 1100 earthquake over 3 of magnitude.

### **Iwo jima**

Iwo jima is a volcanic island to 1200 Km from Tokyo that is a resurgent dome of a caldera apparently formed 3000 years ago during a big volcanic eruption. Many shoreline terraces preserve record of island rising of 120 Km in the last 420 years. Also in the last 25 years of volcanic monitoring, part of the island is rise of 3.5 meters. Geodetic unrest is follow by occasional hydrothermal explosion, swarms and hot fluids and gas.

### **Taupo**

The last super-eruptions happened in the volcanic area of Taupo in New Zeland 26000 years ago.

### **Pinatubo**

The most recent eruption with VEI 7 happened in 1815 in Tambora, Indonesia. Only one VEI 6 happened in the monitored volcano of Pinatubo in Philippine.

### **Nisyros**

It's a caldera that it's think is formed during an on large scale eruption about 25ka years ago and subsequently re-feeding by dacitic domes.

This island suffers 14 cm of uplift during the '90<sup>th</sup> volcanic crisis. Historical eruptions are limited to phreatic explosion how evidenced by numerous craters in the south-east of the caldera. Along the roof of the caldera and the south part of the wall, there are superficial expressions of the hydrothermal system included hydrothermal deposits, fumarole, mud pool and boiled water pool (Caliro et al., 2005).

Actual models of the source structure are

- Magmatic body at unknown depth that inject heat and fluids to the hydrothermal system
- Deep boiled aquifer situated more than 900 m under the sea level.
- Superficial reservoir with variable temperature alimented by steam mix separated from deep aquifer and meteoric water.

Gottsmann et al. (2005), shown and demonstrate existence of brief term dynamic in the order of 10 min, through analysis of residual gravity change visible only from the inside caldera, which change are of the order of that recorded in CFC during standard survey. GPS record shown a ground subsidence relative to gravity decrease. Similar brief term deformations are observed also in Yellowstone caldera.

In continuous record are founded spikes episodes near 30, 300, 450 e 520 minutes indicating a relative movement of the ground of 0.15 meters. Gravity records of these events shown a local minimum, the seismic record indicates a clear intensity spikes when there are these changes. Wave shape of some spike to 450, 480 and 490 minutes suggest episodes of tremor that for Caliro et al. 2005, may be interpreted as instability in degassing progress at superficial depth. It's not possible constrain their depth but it's possible exclude that hydrothermal aquifer that is at 1300-1800 meters' depth under the caldera roof, may be the source of seismic signal. Caliro et al. (2005) found

evidences of interaction between magmatic/hydrothermal fluids and host rock in depth through LP events. In Nisyros are founded discrete LP events but low frequency energy is present in continuous seismic record. Wave shapes similar to tremor are individuated during degassing with open conduct activity in volcano as Stromboli, Erta Ale, Ambrym interpreted as sovraposition of discrete series of burst that was proposed as interpretation also for nisyros. Are associated with that burst with instability during magmatic degassing but is not possible found source position (Gottsmann, 2007 and reference there in)

Tikku et al 2006 using a multiday gravimetric record interpreted variation in microseismicity record in an active basin of geyser in Yellowstone as induct tremor from fluids flow.

To Gottsman (2007) tremor result to be due to a sudden disorder of the hydrothermal system that may be caused by pressure variation for non statistical degassing of a deep magma reservoir that feed a deep aquifer with boiling temperature around 340°C (Caliro et al., 2005 and reference there in).

Supercritical fluids are source very efficient for volume variation that bring to a rude change of pressure. In that model, a sudden increase of pressure due for example to anomalous degassing in depth became shallow elastic deformation. Associated increase of gravity is caused by Bouger effects of deformation and resulting propagation of density boundaries in a planar reservoir.

The disorder that cause the tremor may be explained from coalescence and bubbles rise.

Dissipated pressurization from release upward of fluids and steam along new formation fractures and faults results in ground subsidence and decrease of residual gravity

Change in electrical properties that is also recorded is due to fluids and steams separation by high deep temperature of aquifer that recharge shallower and with low temperature reservoir.

So many studies concluded that the caldera unrest are due to put in place of magma in depth, which cause geophysical signals quantify in surface for weeks, months and years. But less periods of unrest in caldera are culminated in volcanic eruption so the attention is focused on hydrothermal system because fluids migration produces seismic signals.

### 1.3.3 Campi Flegrei caldera characteristics and precursors

Actually, the CFC is characterized by gas emissions, seismic activity, ground deformation (crustal uplift) and subsidence. For this reason, relative sea level variations are very intense in the Pozzuoli area, that is in the center of the caldera. The values of sea level variations contrast with the average 50 cm sea - level rise recorded in the north west Mediterranean Sea since Roman time. Local chronicles report repeated episodes of ground uplift preceding the 1538 A.D eruption and, two days before the eruption, a ground uplift of 7m and 200m seaward shift of the coastline was reported (Delli Falconi's report). Sea level measurement was estimate using the ruins of a Roman market built in the town of Pozzuoli that indicate that a subsidence was interrupted by a 7 meters uplift that took place west of Pozzuoli between 1530 and 1538 AD, culminating with the Monte Nuovo eruption.

The recent volcanic activity is confined in the NyT caldera (Orsi et al., 1996). After a period of subsidence that endures from 1538 A.D. Monte Nuovo eruption, three other major events affected this area dating to 1950–1952, with 73 cm of measured uplift; 1969 – 1972 with 177cm of measured uplift and 1982 – 84 (Del Gaudio et al., 2010). For the last one a maximum net uplift of 179cm was measured at Pozzuoli in the central part of the caldera (Orsi, 1999) and it was accompanied by almost 16000 shallow earthquakes.

During the past 12 ka, the CFC has been deformed by subsidence and resurgence events located inside the NYT caldera. Resurgence began between 10.5 and 8 ka (Giudicepietro, 1993). It's possible

that resurgence occurs when new magma entered the shallow reservoir and rose to the surface along a deep regional fault system. From investigations on the surface separating marine and continental deposits, the results show that the resurgence of the central part of the NYT caldera is not homogeneous (Orsi, 1996). Short-term deformations are studied in the recent times from Monte Nuovo eruptions where a slow uplift and seismic activity related to this uplift occur. Two days before the eruption occurred twenty violent earthquakes and was generating a vertical displacement of 7 m (Orsi, 1996). After the eruption and until 1969 the area was interested by a subsidence. Between 1969 and 1972 was recorder the first monitored uplift with a displacement of 1.7m and was detected in the area of Pozzuoli (Corrado et al. 1977). Also this uplift was accompanied by seismicity with epicentres concentrated in the north of Pozzuoli and in the area between Agnano and Averno. Until 1974 the ground continues to go up of 0.22 m, after that there was no seismicity and displacement. At the beginning of 1982 and until 1984 the Campi Flegrei caldera was interesting by a new and intense brady seismic crisis. The vertical displacement measured was of 1.8 m and almost 16000 was recorded, located in the area of Solfatara, Monte Nuovo and north of Pozzuoli, with depth up to 4–5 Km. After that, the general pattern was of subsidence with minor uplift accompanied by seismicity.

Self-sealing processes inducing transient fluid pressure effects may represent significant mechanisms in inflating calderas (Vanorio, 2005). Hydrothermal system are good environment for permeability destruction process due to mineral precipitation, crack healing and sealing competes together with permeability creation due to fracturing process. In CFC the Presence Of Self-sealing process (Chelini, 1984) might account for fluid pressure generation (Vanorio, 2005).

This dynamic may be done to pore pressure variation inside the hydrothermal reservoir of Campi Flegrei is due to gas rising from magmatic deeper source (Chiodini et al., 2010). Analyse of Vp/Vs ratio suggest anomaly values at 3Km depth that suggest the presence of a gas rich zone (Chiarabba

e Moretti, 2006). Uplift seems to be related to hydrothermal fluids migration through NW-SE faults and fracture in Solfatara-Agnano-Astroni area (Chiodini et al, 2010), instead subsidence seems to be due to pore pressure decrease and compaction.

Possible evidences of a magma reservoir at about 4 km of depth are in the identification of a P-SV converted phase in a seismic profile (Ferrucci et al., 1992), in the location of maximum depth of earthquakes and by petrological and geochemical data. The first model for a source for ground deformation was a pressure increase model at the top of a shallow magma chamber embedded in an elastic medium (Berrino et al., 1984; Bonasia et al., 1984; Bianchi et al., 1984, 1987; Dvorak and Berrino, 1991; De Natale and Pingue, 1993). Avallone et al., 1999 used DInSAR images collected between 1993-1996 for estimate a Mogi-type pressure source location located at 800 m offshore SW of the town of Pozzuoli at 2700 m deep. Bonafede et al.(1986) considered the pressure source in a viscoelastic medium. Como and Lembo (1992) developed a numerical model to simulate the effects of fracturation and conductive thermal propagation on the ground deformation. Gaeta et al. (1998) proposed a model based to the interaction between a thermal source and the circulation of groundwater in a permeable system, showing that hydrothermal system have effect of amplifying the ground deformation.

So ground deformation can be due to an inflation of magma chamber in depth or to the injection of gravitational fluids and it represents an important precursor. However, an important rule is played by heating and pressurization of pore fluids, which may result from an increased magmatic degassing (Morhange et.al, 2006). The subsidence that started in 1985 continues today and it is interrupted by short uplift episodes recorded at 1989, 1994, 2000, 2004, 2010 accompanied by microseismicity. Recent seismicity consists in volcano-tectonic and long Period events (D'Auria et al.2011).

Ground deformation is one of most important precursor phenomena and one of principal instrument for short-term forecast of eruptive activity. So it's widely studied with various techniques and equipment.

Actually, Solfatara crater is the area with strongest geothermal emission and consists in about 5000  $t\ d^{-1}$  of  $CO_2 - H_2O$  mixture with power of 100 M that is 10 times higher than the heat flux in the whole caldera surface (Chiodini et al. 2010).

Chiodini et al. (2003) proposed that an enhanced flooding of fluids caused by degassing from a deeper magmatic reservoir may be the source of gas. Vanorio(2005) suggest instead that also the CO<sub>2</sub> production promoted by decarbonation reactions (D'Amico et al., 1987; Rosi and Sbrana, 1987) which occur in carbonate rocks under high temperatures ( $T \geq 300^\circ C$ ) may be as well. This hypothesis is supported by the evidence of a carbonatic basement reported by Zollo et al. (2003) and the finding of tuffits with carbonatic matrix in the thermo metamorphic basement at 3000 m (Chelini, 1984).

Only the Solfatara crater releases about 1500 t/day of volcanic-hydrothermal CO<sub>2</sub> as a result of diffuse degassing through ground. During this process, about 3350 t/day of steam condenses, generating hydrothermal fluid circulation (Chiodini et al., 2001); The heat ( $7.5 \times 10^{12} J/day$ ) released by condensation represents the largest part of the total heat dissipated by hydrothermal degassing at Solfatara. Hypothesis suggest that hydrothermal fluids at Solfatara induce enhance rock deformation (Oliveri del Castillo and Montagna, 1984; Bonafede, 1991; De Natale et al., 1991; Gaeta et al., 1998) increasing pore pressure, so modifying effective stress, and rock temperature.

## Chapter II – Analysis of seismic data

## 2.1 Seismic data

Volcanic areas are complex structures characterized by solidified intrusion, partially molten regions, geothermally altered rocks and indicates deposits of different shapes, thickness and compositions.

The seismicity associate to volcanic areas is often characterized by swarm-type earthquake with features different respect those occurring in other tectonically active zone (Klein et al., 1977).

Models for the occurring of these seismic events that occur grouped in space and time, explain this behaviour with highly heterogeneous distribution of material fracture strength and/or stress concentration (Mogi, 1963; Sholz, 1968).

Usually the seismicity associated with active volcanism is characterized by Long- Period (LP) signals accompanied by VT events in the same period. There are examples of this correlation not only in Campi Flegrei caldera but also in Long Valley (Hough et al., 2000), Nisyros (Caliro et al., 2005). In all the cases it was interpreted as the effects of fluid migration.

The presence of LP signals in volcanic/hydrothermal areas is indicative of a source mechanism associated with fluid-rock interaction and could represent an indicator of renewing activity (Chouet, 1996a,2003).

While VT events are due to brittle failure in response to stress changes associate with magmatic activity, LP events are attributed to resonance of fluid-filled crack or conduits induced by pressure transients in the fluid (Aki et al., 1977; Chouet, 1985, 1988,1992). LP events are discrete signals having an amplitude envelope similar to normal earthquakes but spectral characteristic similar to tremor. These events often show high frequencies superimposed on their waveforms near the onset of the signal (Fehler and Chouet 1982; Bame and Fehler 1986). Tipically the duration of the long

period events is of the order of 150ms and the dominant frequency is in the range 100–300 Hz (Bame and Fehler 1986).

In 1979, Lawrence and Qamar noted for the first time similarity between long-period events occurring on volcanoes and low-frequency glacial icequakes postulating that the two types of events may be linked to fluid transients in fluid-filled conduits under volcanoes and glaciers. Bume and Fehler (1986) also found evidence that the first seismic events to occur during hydraulic fracturing of virgin rock are long-period events with duration and amplitude very small in comparison with volcanic long period. Long period events have similarity also with tremor, noted by various investigators (Dibble, 1974; Capaldi et al., 1978; Latter, 1979; Fehler, 1983; Malone, 1983; Qamar et al., 1983; Koyanagi et al., 1987) bring to the hypothesis that harmonic tremor is a swarm of long-period events (Fehler, 1983; Koyanagi et al., 1987). Chouet (1985) showed the relationship between the long-period events and tremor suggesting that the two signals represent different excitations of a common fluid-filled cavity where the long period represent the impulse response of the tremor-generating system and the tremor is the response of the cavity to a more sustained driving mechanism.

In nature, exists events that have similar waveform at all observation stations. These events are called microseismic doublets or multiplets. Member of this category of events, generally occur close together so as to define a cluster and have similar focal mechanisms (Poupinet et al., 1984; Moriya et al., 1994; Philips et al., 1997). Because of the waveform similarity, it's possible performed a relative-location analysis using a cross-correlation technique.

In seismology are interesting into research of correlation between effusive activity, volcano structures, chemic-physic magma properties and seismic manifestation in volcanic area. In the last time, micro-earthquakes agitation is considered separately with earthquake, because they are distinct events and in certain limit also independent each other.

Microseismic events represent shear or mixed-mode failure of rocks along pre-existing planes of weakness that is accompanied by significant seismic energy release at relatively high frequencies (Tezuka 2000).

These type of events are usually recorded during the bradyseismic crisis of Campi Flegrei Caldera. Parameters that better characterize the micro-earthquakes are period and amplitude and in second time also propagation velocity. In the opinion of Minakami in the study of microseismic period, cannot rescind from magma chemistry; In particular, greater period correspond mostly to basic magmatism and so to relatively fluids lavas. From other authors period variation of microseism are related with depth of lavas source position and with the phase of volcano activity. It was observed that during quiescence phases, when magma is at greater depth in the volcano conduct, the period is bigger than which corresponding to effusive eruptive phases.

Regards the amplitudes, micro-earthquakes with volcanic origin are not so distant with which due to other causes like wind, wave motion and human activities, but the different with the others is that the micro-earthquake shown the characteristic of rapid attenuation with source distance. K is the attenuation coefficient that is present in this relation:

$$A_n(T, \Delta) = A_0(T) * e^{(-K(T)\Delta)} * \Delta_n^{-\alpha}$$

With  $A_n$  the amplitude at the n-th station.  $A_0$  amplitude at the source point.  $\Delta_n$  distance between source and station n,  $\alpha$  is the numeric constant.

Minakami calculated k for Sakura-jima e mihara volcanoes:

$$0.8 - 0.9 * 10^{-5} / cm$$

$$0.2 - 0.3 * 10^{-5} / cm$$

In relation with hypocentre depth, Minakami distinguish four types of seismic manifestation

- a) Volcanic pulsation constitutes from train of harmonic oscillations which origins are in the area of terminal crater.
- b) Earthquake B-type that have origin in the up part of volcano. Seems to be associated to eruptive activity.

- c) Earthquake associated to explosive eruption.
- d) Earthquake A-type with hypocentre at some kilometres depth and relatively less frequent.  
(Bottari-ruscetti, 1967).

Attenuation of elastic waves depends on many factors through which temperature and presence of fractures that may be permeated by fluids (Eberhart-Phillips et al., 2005)

It's possible quantify alteration using the quality factor  $Q$ , that is the ratio between the energy lost by a wave cycle and the energy of the cycle itself (De Siena, 2010) or through the attenuation coefficient  $\alpha = \pi f r / v Q$  that is a function of distance  $r$  and of frequency  $f$ . The coefficient may vary for the same amount of rock on the basis of chemical composition, temperature and degree of fracturing. In particular, for volcanic areas is essential to know either the  $Q_p$  P-wave quality factor and the  $Q_s$  S-wave quality factor for a complete characterization of the rocks inside the volcano cause the different response of the rocks to longitudinal and shear waves.

Another important parameter to take in account is the scattering. When a wavefield interacts with small scale heterogeneities in the elastic parameters happened that the High-frequency energy of direct P and S-waves is transferred in the coda of the seismograms, that is the scattering process (Sato and Fehler, 1998)

## 2.2 Campi Flegrei caldera seismicity

Campi Flegrei caldera is a site of intense seismicity related to magmatic activity. As report from historical record from Selli Falconi(1538), Simone Porzio (1551) and Mercalli(1891), the caldera was interested by an intense seismic activity 2 years preceding the Monte Nuovo eruption increasing in the last 2 days. Since 1969, the level of activity is variable in dependence from

variation of dynamics of the caldera. Also nowadays, the seismicity occurs in the caldera accompanying uplift events, instead is absent during subsidence periods.

From 1970 the seismicity was monitored initially by three permanent station, while in time was implemented. In 1982 the network included 22, two of which three component station located at the Accademia in Pozzuoli and Nisida, the others, vertical component stations installed by Osservatorio Vesuviano and few by Agip.

The configuration was chosen according to the areal distribution of the events but because the strange horse-shoe shape, the network had a gap in the bay of Pozzuoli (between Nisida and Miseno) (Orsi,1999). The reciprocal distance between the stations was determined using the oscillations produced by the earthquakes which were characterize by wavelength on the average of 300 meters, that is a distance that permits also to distinguish between seismic events and cultural noise. From September to November 1983, the Institute of Physique du Globe de Paris, installed a temporal network of 18 digital three-component seismic stations (D'Auria et al., 2015). From December 1983 to June 1984 the university of Wisconsin implemented the OV network with 10 digital three component stations (Aster and Meyer, 1988).

Studies about microearthquakes source parameters using inversion (Del pezzo et al., 1987b) and standard polarity method (Gaudiosi and Iannaccone, 1984; Adter et al., 1992) shown a variability of fault plane orientations, which seems to be controlled by local stress rather than by the regional or induced stress by the ground deformation. On the other hand, the earthquake mechanisms for the swarm sequence that occurred on April 1 define a rather coherent pattern of inferred P axes pointing out radially from the maximum uplift centre thus suggesting a strong link between swarm activity and stress regime induced by the ground inflation (De Natale et al., 1995). De Lorenzo (2001) estimate microearthquake source parameters through the space variation of the P wave attenuation parameter founding a low stress drop values (0.01 – 1 MPa ) that with the swarm-like

activity (De Natale and Zollo, 1986) of the CFc earthquakes suggest the low strength and the highly brittle behaviour of the rock materials filling the caldera. The high variability of the stress drop values may represent evidence for heterogeneity in the elastic properties of the material.

In particular, during the bradiseismic crisis when is in action an uplift movement, CFc is interested by swarms of LP events and Vt events as well.

D'Auria et al. (2011) estimated eight episodes of Lp events consisting in

- A case of LP event was found in old recordings at 27 January 1982 at 0316 UT, recorded by few station
- 15 LP events were recorded at 30 and 31 March 1989 followed by a swarm of VT events 3 days later, consisted in 82 events ( $M \leq 2.2$ ).
- At 23 August 1994 a seismic transient called “explosion-like event” of 30 sec was recorded followed by a dense LP swarm of about 30 events (D'Auria et al. 2011). This transient was associated with acoustic phenomena heard in the surrounding areas of Solfatara crater (Orsi et. Al, 1999) and was followed by a VT swarm of 50 events ( $M \leq 1.0$ ) and 22 LP events.
- a swarm of 20 Lp events in July 2000 (Saccorotti et al, 2001).
- an Lp swarm in October 2006 where more of 870 Lp events were recorded in 7 days. Saccorotti et al.(2007) analysed three clusters of LP waveform founding a very high degree of similarity. These events were accompanied by 150 VT events ( $M < 1.0$ )
- four Lp events and a VT swarm of 44 events ( $M \leq 0.7$ ) on January 2008
- 2 events on 24 March 2005, followed by few VT events.
- 12 events on 8 June 2010.

The Sompi analysis of the LP waveforms (Kumazawa et al., 1990; Nakano et al., 1998) and comparison between waveforms shows that the waveforms of 1989, 2006 and 2008 have very similar spectral contents. The events of 1982, 1994 and 2000 have different spectral contents (D'Auria et al., 2011).

The anomalous ground deformation of 1982–1984 was accompanied by high seismicity activity with more than 15.000 small magnitude earthquakes ( $0 < M_L < 4$ ) (Aster et al., 1992).

The April 1, 1984, were recorded a dense swarm with more than 500 recorded earthquakes in 12 hours, recorded by a 13 station, digital three-component network operated by the University of Wisconsin–Madison.

In many research, seismic events that accompanied the uplift of 1982–84 were analysed. All the studies showed that the epicentres were scattered in the area between the town of Pozzuoli and Agnano with a maximum distribution between 2 or 3 km and few events located down to 7 km in Depth (D'Auria, 2011). The events recorded during 1989–2010, is instead concentrated in a smaller area under the Solfatara crater and Agnano plain with the depth distribution similar to the previous period. In both cases the seismicity distribution is asymmetric respect to the ground deformation pattern (Orsi et al., 1999; Manconi et al., 2010).

A possible interpretation of the behaviour 1982–1984, plastic yield and /or viscoelastic mechanisms were used (Bonafede et al., 1986; Fournier, 1999) it's the hydrothermal fluids, that may drive the occurrence of VT events increasing pore pressure causing a reduction on the effective normal stresses (Shapiro et al., 2003) favouring shear failure or slip on pre-existing fractures (Baisch and Harjes, 2003).

### 2.2.1 Details about the 2005–2006 uplift

Saccorotti et al., (2007) shown that in coincidence with the uplift phase, VT seismicity starts which time occurrence doesn't exhibit a clear evolution pattern. The VT events were located in the Solfatara- Accademia area at depth between 1 and 4 km b.s.l.. Lp events instead were located beneath the southern border of the Solfatara Crater at depths of 500 m b.s.l. Using comparison with spectra from background noise, comparison with spectra from VT events with common locations

and particle motion, was shown that the wave-field was dominated by P-waves. That suggested that the marked spectral peaks exhibited by LP signals reflected a source effect. Saccarotti (2007) then showed that the relation between VT and LP signals suggest that a cause-effect link exist between the two phenomena. The 6 day-long LP activity occurred right after the most significant step in the VT energy release. D'Auria et al. (2011) identified a large, persistent, fluid filled structure as source of the LP swarm of October 2006 located below Solfatara, and source of other LP events (1989–2006–2008) suggesting an increased fluid flow connected to ground uplift. D'Auria et al. (2012) showed a possible correlation between VT events occurred after 2000 and the ground deformation, evocating a pore pressure gradient that controls VT seismogenesis.

In the LP recorded during this uplift are not observed clear shear-wave arrival in the LP waveforms thus indicating a non-destructive source mechanism (Cusano, 2008). Both waveform signature and spectral characteristics suggest that our LP events are associated with the resonant oscillations of a fluid-filled cavity triggered by a pressure transient (Chouet, 1996a; Nakano et al., 2003). In this situation, the most likely LP source mechanism is more likely be the opening/closure of a tensile crack (Hudson et al., 1989; Julian et al., 1998; Chouet 1996b; Kumagai et al., 2002; Nakano et al., 2003).

Using the spectral properties and waveform and so the decay rate of the signal is possible know something about nature of the fluids involved in the Lp generation (Kumagai and Chouet, 1999,2000). Eliminating the site effect and local heterogeneities, Cusano (2008) for example restrict the possible fluids to water-gas mixture. Others informations about hydrothermal or volcanic origin of LP events come from examination of temporally-correlated time series between gas emission and seismicity. The composition and physical properties of the fluid contained in the cavity may be provide by a quality factor of the resonator

$$Q = \frac{f}{\Delta f}$$

With  $f$  is the frequency corresponding to a dominant spectral peak and  $\Delta f$  is the width of that peak at half the peak's magnitude. The quality factor is composed by

$$Q^{-1} = Q_i^{-1} + Q_r^{-1}$$

Where  $Q_i^{-1}$  is the intrinsic attenuation in the fluid and depends on the physical properties of the fluid only, while  $Q_r^{-1}$  is the energy losses at the fluid–rock interface and is a function of both the impedance contrast at the interface and the geometry resonating cavity.

The source models for LP events concern cylindrical (Chouet, 1985), spherical (Crosson and Bame, 1985; Fujiita et al., 1995; Fujita and Ida, 1999) or crack-like (Chouet, 1988) geometries. In his studies, Chouet also demonstrate the presence of a slow wave developing at the fluid–rock interface of the fluid-filled crack, called crack wave, that may give more realistic estimates of the size and the volume of the resonator.

Applicate this factor to CFc the value was around 4 that is significantly smaller than the range value of other volcanoes that is 10–500 range observed in Kilauea volcano (Kumagai et al., 2005) and Galeras volcano, Colombia (Kumagai and Chouet, 1999). The wide range of value may be explained in terms of different physical properties of the multiphase fluid mixtures and the surrounding rock matrix (Saccorotti, 2007). The absence of surface visible phenomena indicate that the generator process of LP is the vibration of a fracture filled by water vapour mixture at low gas–volume fractions.

LP activity in the case of CFc may reflects the response of a shallow hydrothermal system to the heating and pressurization caused by upward migration of magmatic fluids (Saccorotti et al., 2007). Considering the pressurization hypothesis, the recent unrest may be interpreted as due to overpressure in a cavity located at 3–4 km containing fluids of magmatic origin such as volatiles and brines accumulating at the top of a degassing magma chamber maybe due to arrival of new gas-rich magma from a deep source. The pressurization may explain also the occurrence of VT seismicity probably to due brittle failure in the overlying rigid layer (Saccorotti et al., 2007). During

the unrest of October 2006, there must have been high level of fracturing that permitted significant fluid passages from a deeper reservoir toward the shallow hydrothermal system triggering in resonant the Solfatara hydrothermal system producing LP vibration.

Other example of correlation between earthquake swarms, low Vp/Vs anomalies and Co2 emissions is known from other caldera, such as Long Valley Caldera (Farrar et al., 1995; Sanders et al., 1995; Hill et al., 1990) and Yellowstone (Husen et al., 2004).

## 2.3 Comparison between bradyseismic crisis of 1982–84 and Other uplifts

Considering the statistical distribution of the earthquake magnitudes, the Gutenberg-Richter distributions (Gutenberg and Richter, 1954) of the two periods are compared. Based on the maximum likelihood technique of Aki (1965) were computed the b values and their uncertainties that show homogeneous distribution except for the Pozzuoli Bay area (D'Auria, 2011).

The Benioff strain (Benioff, 1951) released during the 1982–1984 crisis was 2 orders of magnitude higher than the cumulative strain release over the following years (Fig. 5)

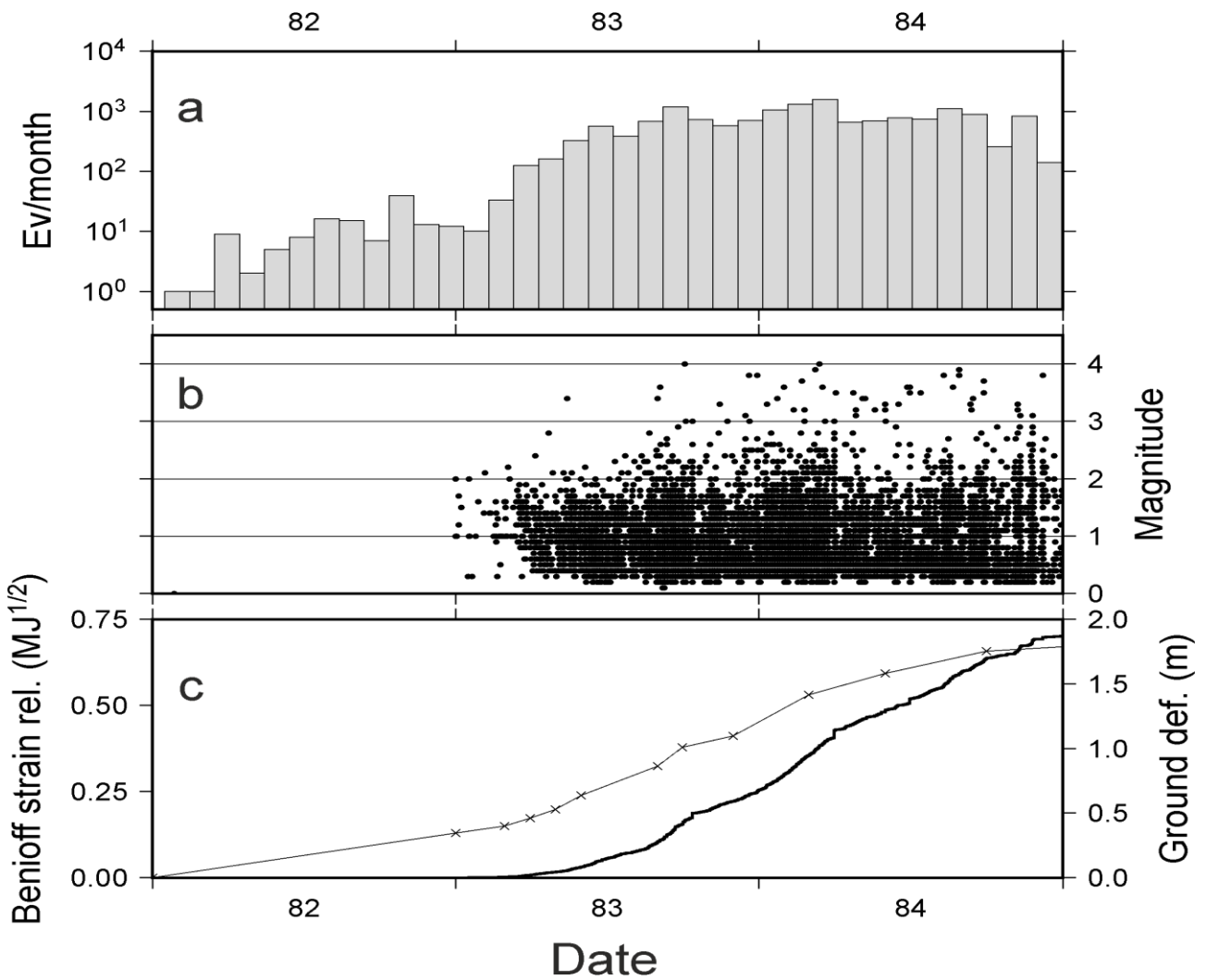


Figure 5. Time series of seismicity and ground deformation (D'Auria et al. 2015) a) monthly number of earthquakes since 1/1/1982. b) earthquakes magnitudes since 1/1/1983, c) comparison between the cumulative Benioff strain release and the vertical deformation at benchmark 25 A.

In the 1982–1984 bradiseismic crisis, most of the strain released was concentrated in the area between Solfatara and Agnano ( $2 \text{ km}^2$ ), although the seismicity occurred in a wider area ( $12 \text{ km}^2$ ). There are other two areas of significant strain release in the same interval, one located in the bay of Pozzuoli, the other one was located along the coast from Pozzuoli where occurred just two strong earthquakes during 29 August. The depth of the strain release occurred between 2 and 3 km (D'Auria, 2011). The same pattern, occurred in the 1989–2010 period, although it had a smaller extension of seismicity occurrence (about  $0.15 \text{ km}^2$ ) (D'Auria et al., 2011).

The seismicity associated to volcanic areas is often characterized by swarm-type earthquake with features different respect those occurring in other tectonically active zone (Klein et al., 1977).

Models for the occurring of these seismic events that occur grouped in space and time, explain this behaviour with highly heterogeneous distribution of material fracture strength and/or stress concentration (Mogi, 1963; Sholz, 1968).

## 2.3 Data Analysis

The bradyseismic crisis of 1982-84 was characterized by intense seismicity. About 16000 earthquakes were recorded with a magnitude ranges between 0.5 to 4.2 (D'Auria et al., 2011).

For this research I mainly made a recovery of events either from digital either cartaceous supports, recorded by Vesuvian Observatory network. The events choose are included between 1982 and 2012 with Magnitude  $\geq 2.0$ . From the cartaceous dataset are evidenced 25 earthquakes never analysed, recorded from a temporary network installed by a French research group. The total number of events in the dataset analysed is of 222 events. 192 have been relocated and their focal mechanism have been calculated using the P-polarities. Additional 30 mechanisms have been retrieved from Orsi et al. (1999).

The data analysis is consisted in

- Picking
- Absolute Location using a nonlinear probabilistic approach (NonLinLoc software) in a 3-D velocity model (D'Auria et al., 2008).
- Relative Location using HypoDD software based on the double difference algorithm.
- Focal Mechanism using FPFIT software (Reasenberg and Oppenheimer, 1985).

### 2.3.1 Picking of the earthquakes

Visualization and data analysis of the events for which was available wave shapes, is made with KUDS program, running in Linux environment and developed by Osservatorio Vesuviano to data analysis. This program visualizes three seismic components (north-south, east-west, vertical) of all records available in a selected period, allowing the use of functions for identification and marking(picking) of the P-wave first arrivals on the vertical component, on which are better show, and of the S-waves on the horizontal components.

For some events was possible also recognizes the tail. Than the picked events were saved in daily catalogue.

The events were not visible always on all the station for the low ratio signal-noise due to strong noise relative to badly atmospheric condition or anthropic noise.

Analysed data were then used for re-location of events and focal mechanism calculations.

### 2.3.2 Velocity model

The first velocity models of Campi Flegrei were obtained using the data recorded in 1982–1984 (Aster and Meyer, 1988,1989; Pujol and Aster, 1990). In recent times, these data are combined with data obtained by a high resolution offshore reflection survey – Serapis project (Zollo et al., 2006). Battaglia et al. (2008) obtained a velocity model of Campi Flegrei for P-waves and S-waves by merging passive and active data sets of travel-times that were obtained during the 1984 seismic crisis and the 2001 Serapis experiment. Their method used the difference travel-time computation joint with inverting the velocity model and the event locations using a weighted damped least square.

In this research was used a three-dimensional (3-D) velocity model that was derived from the merging of different tomographic models (D'Auria et al., 2008). For Campi Flegrei area is used Serapis model (Zollo et al., 2003; Judenherc and Zollo, 2004), and the tomographic model of Vanorio et al. (2005) resulted from local earthquake travel time inversion. The first model is characterized by high spatial resolution using P wave velocity only. The second model provides S wave velocity(Fig.6, Fig 7).

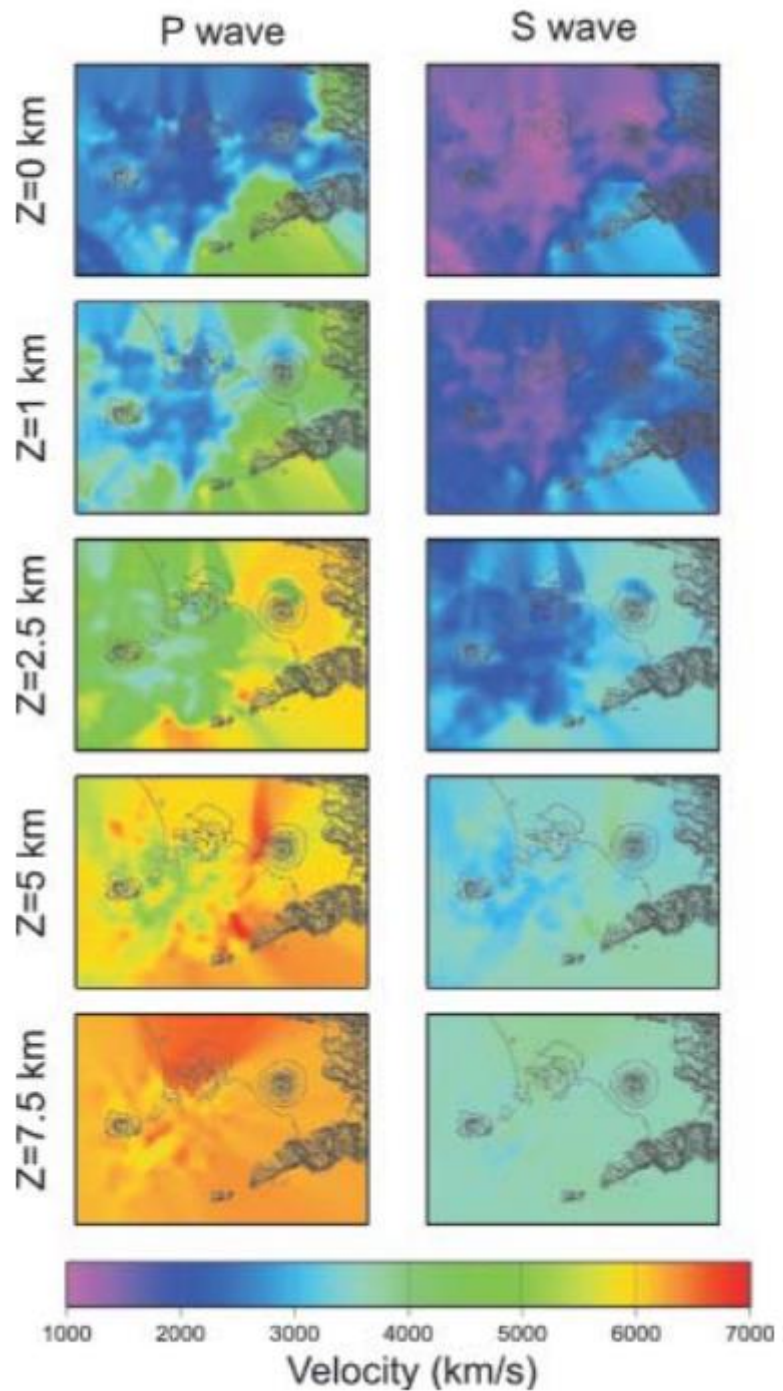


Figure 6. P and S wave velocities at different depth

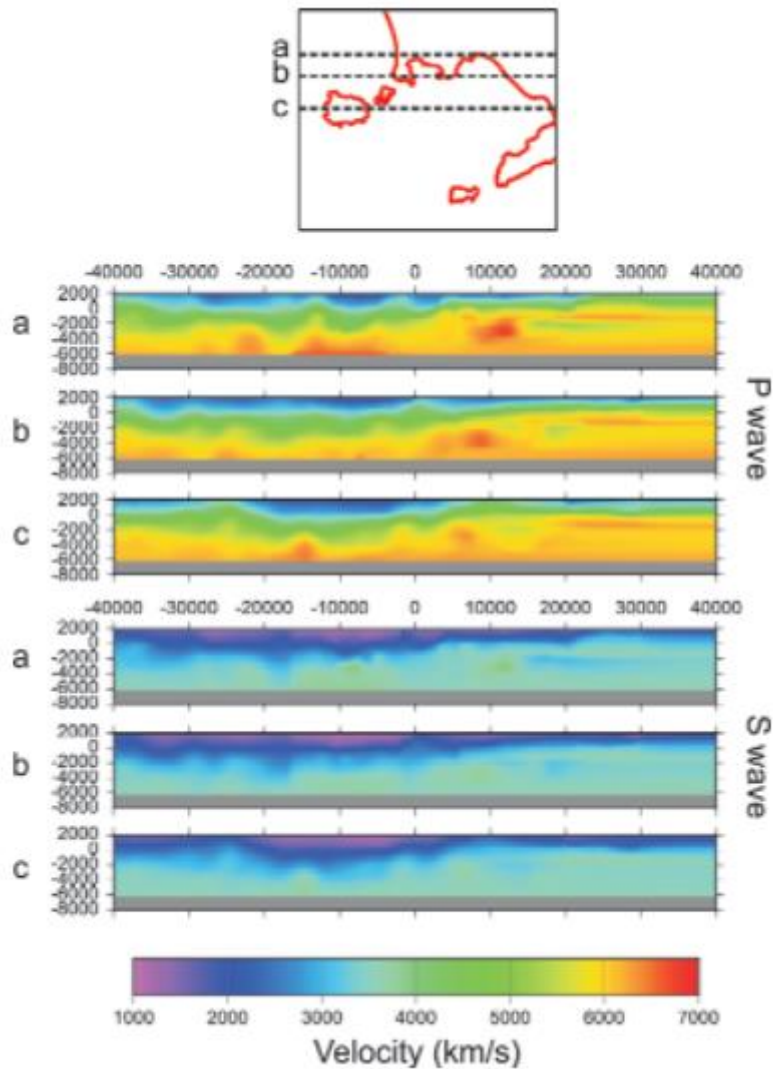


Figure 7. EW cross-sections of the velocity model. Section traces are depicted in the top panel.

## 2. 4 Absolute and Relative locations of the earthquakes

Absolute location is based on the principle that to locate an event are used information received from fixed point as seismic station to determine hypocentre location.

Picking of each events studied were used to determine hypocentre parameters (position and time origin). The hypocentres were represented on a digital topography of Campi Flegrei Caldera.

For Absolute location, a probabilistic technique was used. This technique minimizes simultaneously all residuals between observed and calculated phases. NonLinLoc is the software for location used for this aim, that allows to obtain an estimate of probability density function, PDF, to find hypocentre spatial coordinates x,y,z. This function makes a complete description of location and its uncertainties.

Errors in the observations, such as selection of phase times and errors on the calculation of travel time are assumed to be Gaussian. This assumption allows direct and analytic calculation of origin time probability, given by observed arrival time and calculated travel times by means of the observed station and one point in the space x,y,z. So the 4D problem about hypocenter location is reduced of 3 dimensions (latitude, longitude and depth). Travel time between each station and every points on the spatial grid x,y,z are calculate using a 3D version of the finite difference scheme of Podovin and Lecomte(1991) iconal equation, stored on disk as a file of travel times.

During location, time calculation is reduced at access of travel time files, to calculate misfit function. The hypocentre location technique used in the program follow the probabilistic inversion formulated by Tarantola and Valette (1982) and Tatarntola (1987). This formulation consists in the use of normalized and not normalized PDF to express our knowledge about parameter values.

Given the normalized density function, for parameter value,  $p$ , the probability that  $p$  has value between  $x$  and  $x + dx$  is:

$$P(x < p < x + dx) = \int_x^{x+dx} f(p)dp$$

In geophysics inversions we want to put constraints on the unknown parameters vectors  $\mathbf{p}$ , given a vector of observed data  $\mathbf{d}$  and a theoric relation  $q(\mathbf{d},\mathbf{p})$  between  $\mathbf{d}$  and  $\mathbf{p}$ . To locate earthquake, unknown parameters are hypocentral coordinates (x,y,z) and origin time T. observed data are arrival time of P and S waves.

The PDF expression is

$$\sigma(x) \propto e^{-\frac{1}{2}g(x)}$$

$$g(x) = \sum_i \frac{(t_i^{obs} - t_i^{calc})}{s_i^2}$$

Where  $s_i$  are uncertainties associated with picking.

$\sigma(x)$  is the complete, probabilistic, solution of the location problem, including uncertainties and resolution information. NNloc determine systematically  $\sigma(x)$  on 3D spatial grid through various calculation technique. Max probability point, or minimum misfit, is selected as hypocentre. Hypocenter Uncertainty is not ellipsoidal (not Gaussian) because the calculation involves not linear relation between hypocentre position and travel time. Ellipsoid of Confidence can be obtained from analysis of  $\sigma(x)$  function. It's a good indicator of location uncertainties only in the case if  $\sigma(x)$  PDF has one maximum and an approximately ellipsoidal shape.

Relative location use as information arrival times of a seismic phase respect to another phase and calculate the event position in function of the other events. In absolute location hypocentre may be calculate individually, instead in relative location is a linear problem of difficult situation. We want to know how much is distant the event's relative position, starting from absolute position, calculated, for example, through a non-linear method as NonLinLoc.

$p$  is the solution that we are searching for

$$p = \Delta M + m_0$$

$m_0$  is the absolute location,  $\Delta M$  is the relative locations.

#### 2.4.1 Relative location & Double difference Alghoritm.

For relocating earthquakes, is possible uses also the method of relative location that is refers to the position of an event with respect to other events, instead to respect of a stationary point. For this

purpose was developed in Fortran environment the HypoDD program based on Double-difference (DD) algorithm of Waldhauser e Ellsworth(2000).

For relative location it's possible use the double-difference algorithm created by Waldhauser e Ellsworth(2000). The DD technique takes advantage of the fact that if the hypocentral separation between two earthquakes is small compared to the event-station distance, then the ray paths between the source region and a common station are similar along almost the entire ray path (Frechet, 1985; Got et al., 1994)

Practically this method allows to make a simultaneous re-location of events distributed into a large range "hypocentre – station distance", using an inversion method that consider either the time difference deduced from travel time took from the seismic database either the time difference deduced from cross-correlation methods. This method allow to obtain an accurate estimation of hypocentre parameters of events grouped into family with location errors average lower to Km.

Data of arrival time for events dataset considered simultaneously may better constrain the relative location between events.

Because phases crossing similar trajectories if two earthquakes are relative to another one, difference into travel time may use to obtain precise estimations relative the location reducing velocity model errors. The fundamental point of double-difference algorithm is given by the linear relation

$$dr_k^{ij} = \frac{\delta t_k^i}{\delta m} \Delta m^i - \frac{\delta t_k^j}{\delta m} \Delta m^j$$

Where

- $t_k^i$  is arrival time of seismic phase  $i$  to the station  $k$  given by  $t_k^i = t^i + \int_i^k u ds$  .
- $\Delta m^i$  is the perturbation for the  $i$ -th model parameter. Travel times and event position have a non linear ration and it's possible linearized it through the Taylor expansion  $\Delta m^{ij} = dr_k^{ij}$  where  $\Delta m^{ij} = (\Delta dx^{ij}, \Delta dy^{ij}, \Delta dz^{ij}, \Delta dt^{ij})$ , which partial derivate  $t$  relative to  $m^{ij}$  are the slowness vector components that is the ray that links source

and receiver with  $t$  absolute arrival time or arrival times differences calculating with cross-correlation.

- $dr_k^{ij}$  is the double difference, fixed a constant slowness vector, defined as

$$dr_k^{ij} = (t_k^i - t_k^j)^{obs} - (t_k^i - t_k^j)^{calc}$$

The cross correlation of digital waves shape may be used to reduce errors on travel times differences making a comparison between earthquakes.

Double differences are the data of inverse problem, instead model parameters are the initial hypocentre perturbation ( $\Delta x_i, \Delta y_i, \Delta z_i$ ). In the Wildshauser and Ellsworth algorithm (2000), used in the software HypoDD, this is done converting arrival times in times differences between common phases of different earthquakes recorded at the same stations. HypoDD is used often for hypocentre location.

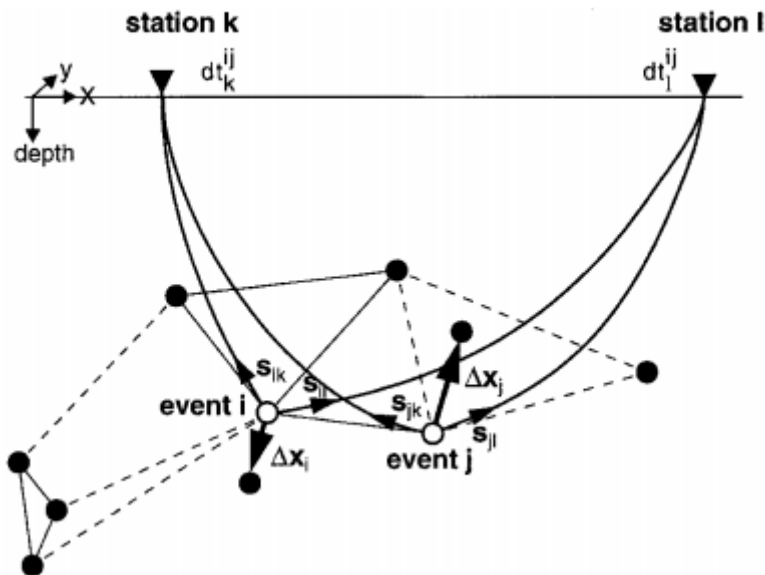


Figure 8. Illustration of the double-difference earthquake relocation algorithm(Waldhauser and William L. Ellsworth 2000).

In this figure, white circle represent poof of the hypocentre linked to the near events from cross-correlation, represented in this figure as inter lines, or from catalogue data, represented as dashed lines. For two events  $i$  and  $j$ , are shown initial position as white dots and their correspondent vectors,  $s$ , respect to two stations  $k$  and  $l$ . It's also indicate the ray trajectory from source to stations. Black arrows  $(\Delta x_i, \Delta x_j)$  indicate re-positions of event vectors  $i$  and  $j$ .  $dt$  is the travel time difference between events  $i$  and  $j$ , respectively observed from  $k$  and  $l$  stations (Fig. 8).

Then the chosen events were plotted in Matlab software on a 3D grid having x as latitude, y as longitude, z as altitude. At the top of the grid was put a Campi Flegrei topography to better show the events distribution from various prospective.

## 2.5 Focal mechanisms Solution

The radiation pattern of energy emitted by an earthquake can be modelled using the double force couple that is mathematically described by the moment tensor. This is a 9 component symmetrical tensor that can be described in terms of three orthogonal axes: P, pressure; T, tension; N, null. The fault surface along which the earthquake was generated is  $45^\circ$  from P and T axes, and contain N. For each moment tensor, there are two possible planes, one nodal plane is the fault surface, the other is the auxiliary plane and is perpendicular to the line describing the direction of slip in the earthquake. The focal mechanism solution is based on the derivation of a moment tensor from analysis of sets of waveform data. The beach-ball diagram is a product of the moment tensor inversion or we can obtain it by graphic techniques from a study of P-wave first motions. From the preliminary determination of the epicentre, we know the location and origin time of the earthquake. Given a certain numbers of station, we compute the distance between each station and the epicentre.

Then with a seismic velocity model we define the exact time that the P-wave should have arrived at each station. Consulting the vertical component of the seismogram recording at each station, we evaluate if the first motion is an up motion or a down motion, or no apparent signal.

Then all the first motions are plotted on a circle, and define the nodal plane and the quadrants.

Focal mechanisms describe faulting motions that produced an earthquake, using great circles with nodal planes, in the centre of which there is the earthquake's hypocentre. The beach balls depict the stress orientation of the stress field that generated the rupture and governed the direction of slip on the fault plane.

This symbols are the projection on a horizontal plane of the lower half on an imaginary, focal sphere surrounding the earthquake source. They are characterized by two lines, that identifies nodal planes, so one line describes the fault plane and the other one describes an auxiliary plane. These two lines divide the sphere in four sectors or quadrants. In the fig (9) the dark one contains the tension axis (T) which reflects the minimum compressive stress direction, and the white quadrant contains the pressure axis (P).

With the focal mechanism Solution it's possible deduce the orientation of the fault plane, the direction of hanging-wall slip, and the type of fault involved in the earthquake, so strike-slip, reverse, normal, oblique. The analysis of FMS related to a sequence of shock-aftershock allows us to map the faults that slipped and evaluate the number of faults that are slipped during the sequence(Fig.9).

## Schematic diagram of a focal mechanism

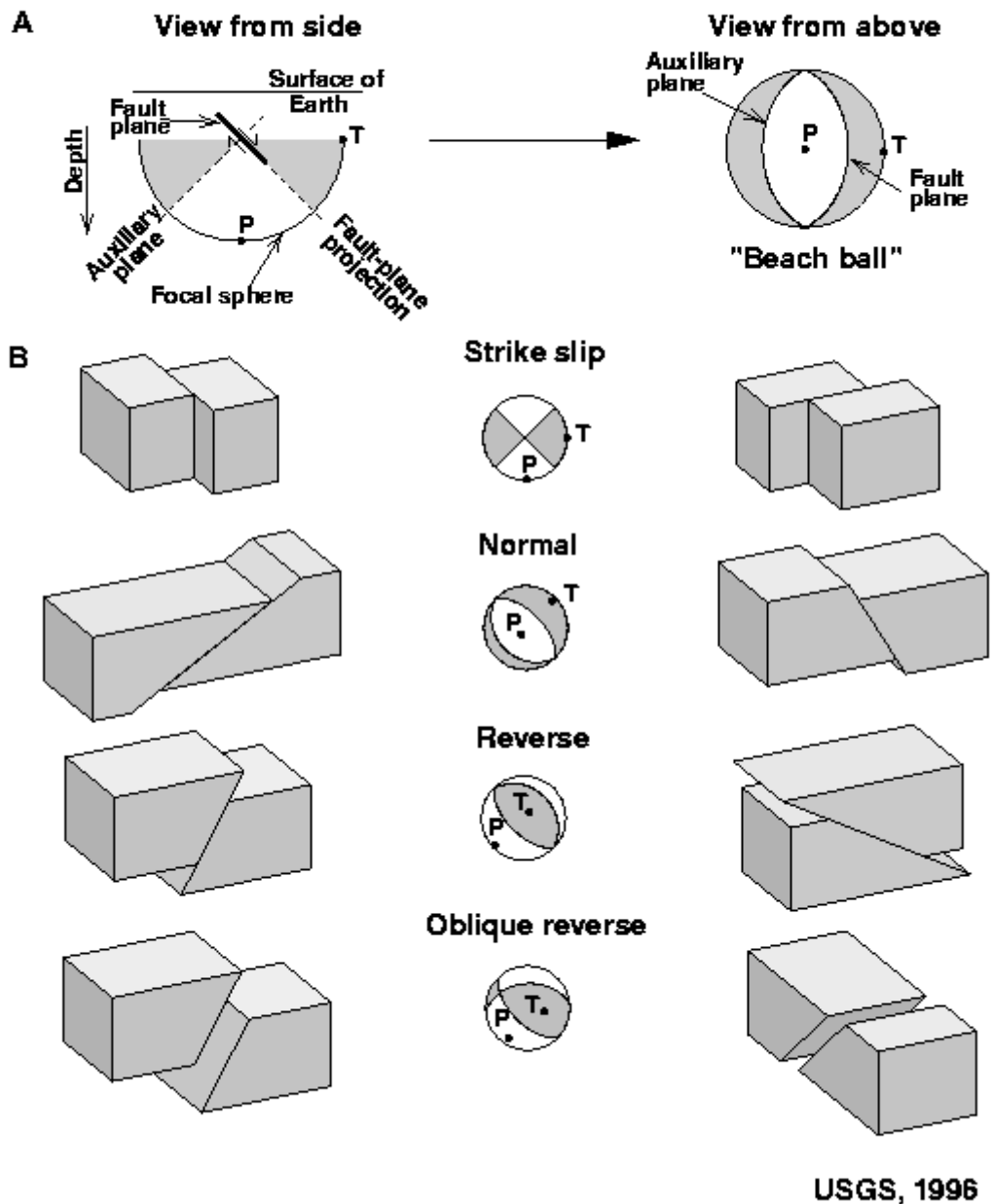


Figure 9. Focal mechanisms schematic diagram.

The study of the focal mechanisms for these earthquakes is important to provide an estimate of the tectonic stress directions.

To computing focal mechanisms of small-magnitude earthquakes occurring in volcanic areas, Zollo and Bernard (1991) and De Natale et al. (1991) developed similar methods to compute focal mechanism of earthquakes which are based on the Bayesian estimate of the probability density function of the fault mechanism parameters (strike, slip and dip fault angles).

The limited extent of the deformed area, requires a source depth of 2–3 Km inferring minimum depth of the magma chamber of 3.5–4 Km (Ferrucci et al., 1992). De Natale et al. (1991) hypothesize that the source of pressure was the heating of shallow aquifers by an increasing heat flow from the magma chamber.

Method of focal mechanism determination described by De Natale et al. (1991) and Zollo and Bernard(1991) based on Bayes' rule which provides a quantitative way to incorporate the prior information on the model space and to compute the posterior probability (De Natale, 1995)

$$P(d) = \text{const} \cdot P(m)P_0(m)\mu(m)$$

With  $m$  the model parameter vector,  $d$  the data vector  $P_0(m)$  is the prior probability density function(pdf) related to other independent data set.  $P(m)$  is the conditional pdf of the measured S-wave vector directions  $d_2 = (p_1, \dots, p_N)$ ,  $N_2$  is the number of observations.

$\mu(m) = \mu_0(m)dm$  is denoted, according to Tarantola and Valette(1982) as the “null information” ( $\mu_0(m)$  is the noninformative pdf). Given the strike  $\phi$ , dip  $\delta$ , and slip  $\lambda$  fault angles; Zollo and Bernard (1991) showed that  $\mu_0(m) = \text{const} \sin \delta$

In this research has been used the software named FPFIT that is a Fortran program that computes double-couple fault plane solutions starting from P-wave first motion. This software uses a grid search method.

## 2.5.1 Results

The seismicity during the 1982–1984 uplift have a gradual increase since the second half of 1982 until the beginning of 1983 when there was a marked increase of the rate and magnitude. During 1984 the pattern was principal stationary with episodes of intense seismic swarms. The epicentres were located in two clusters. One bigger cluster of events was located in the area between Pozzuoli and Agnano. The smaller was located in the Pozzuoli bay. For both clusters the depth of the events is from 0 to 3 km (D'Auria et al., 2011), (Fig.10)

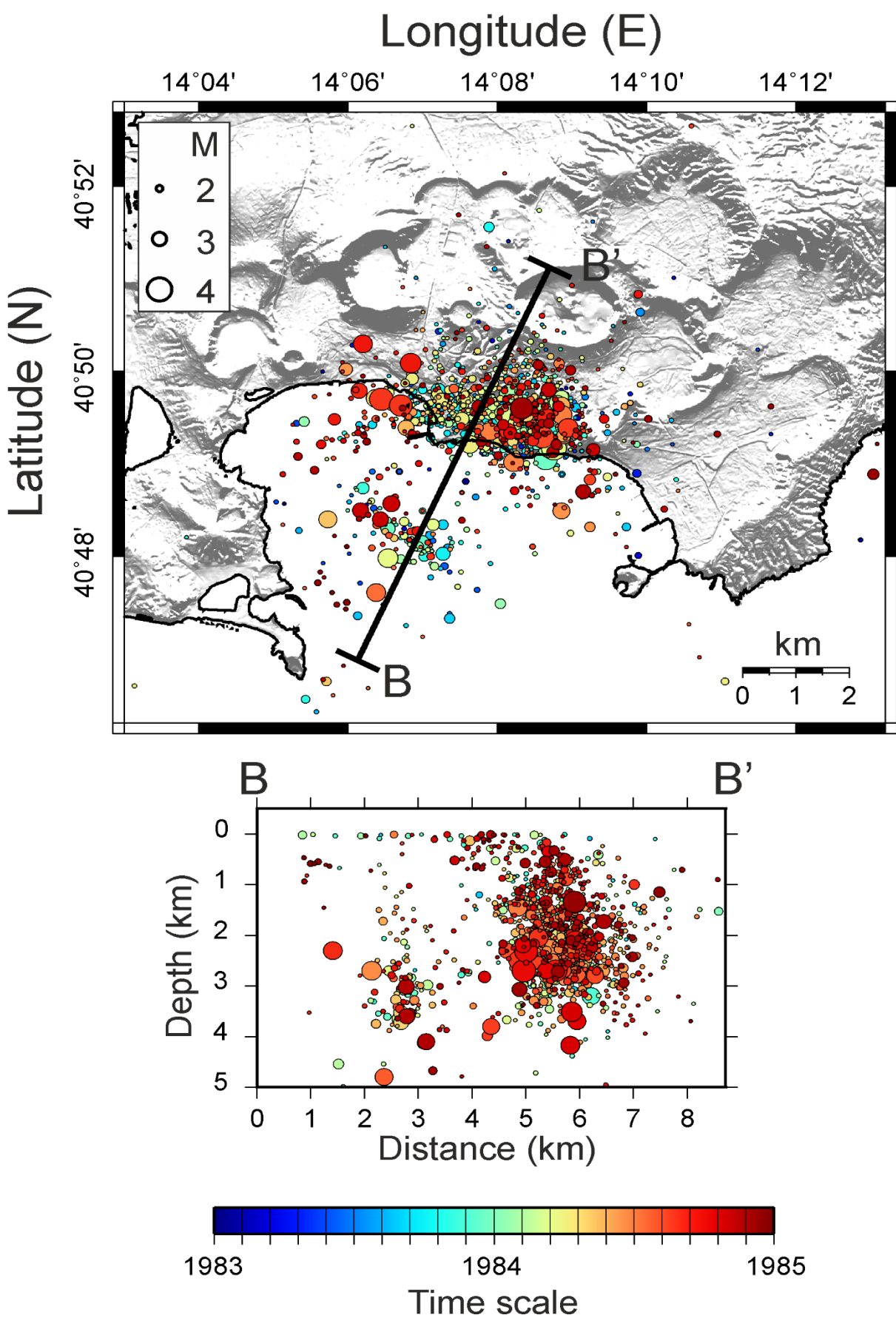


Figure 10 - Earthquake hypocenters during 1983–1985. The size of symbols is proportional to the magnitude while the colour scale indicates the time of occurrence.

The 192 reanalysed events have a number of P-wave polarities that vary from 6 and 19 (average value of 8.5).

The Frolich triangular plot was used to displaying focal mechanism plotting them on a triangular diagram where the vertices represent normal, thrust and strike-slip focal mechanism. In this way, it's possible determining the proportions of the different type of motion for any earthquake focal mechanism (Frolich 1992). In our case, the Frolich plot shows a prevalence of normal mechanisms (47%), followed by strike slip mechanisms (30%) and inverse mechanisms (23%), showing a very heterogeneous distribution (Fig. 11)

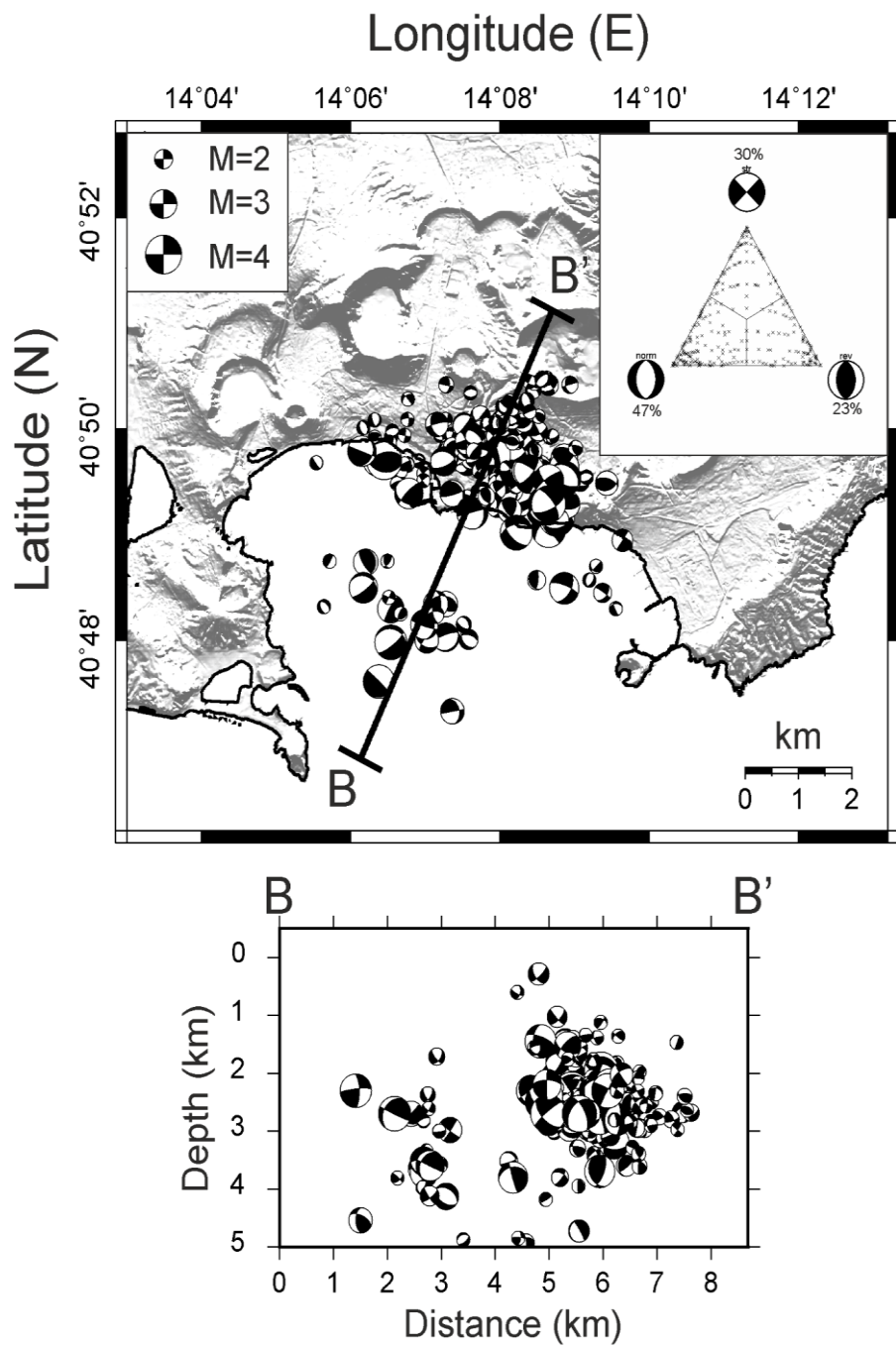


Figure 11 – focal mechanisms dataset. The distribution of types of mechanisms is shown in the top-right figure following Frohlich criterion (1992), (D’auria et al., 2015).

## 2.6 1970–1973 Analysis

Has been analysed an old cartaceous dataset of events recorded between 1970–1973 relative to a minor uplift that interested Campi Flegrei area. The analysis is consisted in digitalization of events from the cartaceous dataset and where possible, localization of the events. The record start in 28 February 1970 at 15.02 and finished at 28 February 1973 at 06.12. In total was recorded 7653 events from 9 stations installed in that period, part of the Osservatorio Vesuviano seismic network. Most of the events were record just from one station and the representation of the record is yy/mm/dd/hhmm/ms (Fig.12).

Q5Q\$0\$*TPF\$(0).DATI		
1	PVE 70022815024950	01002BX
2	PVE 70022815032000	01003BX
3	PVE 70022815040200	01000BX
4	PVE 70022815042580	01003BX
5	PVE 7002281504450	02003BX
6	PVE 70022815061300	01003BX
7	PVE 70022815073650	02003BX
8	PVE 70022815075600	02003BX
9	PVE 70022815210100	01002BX
10	PVE 70022815211600	01002BX
11	PVE 70022815213450	01003BX
12	PVE 70022815215050	01003BX
13	PVE 70022815221250	01003BX
14	PVE 70022815223350	01003BX
15	PVE 70022815232550	03003BX
16	PVE 70022815534150425002004AX	
17	PVE 70022815593350343001003AX	
18	PVE 70030102205900598043017AX	
19	PVE 7003011023450356006006AX	
20	PVE 7003011024370450002005AX	
21	PVE 70030111124520462005006AX	
22	PVE 70030111192650278001004AX	
23	PVE 70030111234750	02003AX
24	PVE 70030111235000	02002AX
25	PVE 70030112233660380004005AX	
26	PVE 70030115520900100003004AX	
27	PVE ILLEGIBILE	02003AX
28	PVE ILLEGIBILE	S-P102003AX

Figure 12. Extract of the cartaceous dataset.

The data are then collected in an histogram (Fig. 13), where have been represented all the events at about 2 months steps. As we seen, during 1972 were recorded almost 180 events in few months that may be interpreted as intense activity in that period may be linked to bradyseismic crisis or a minor uplift episode that interrupt the subsidence that interested the area after Monte Nuovo

eruption, before the huge crisis of 1982–84.

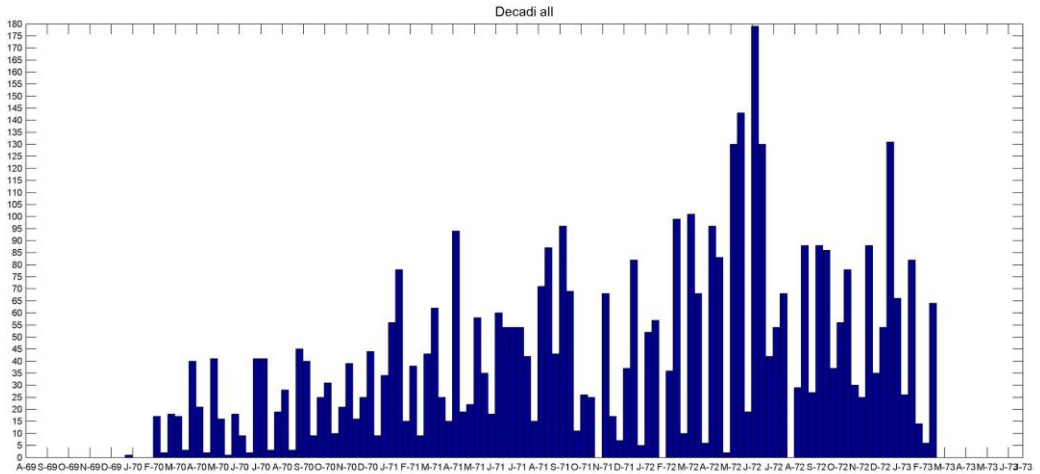
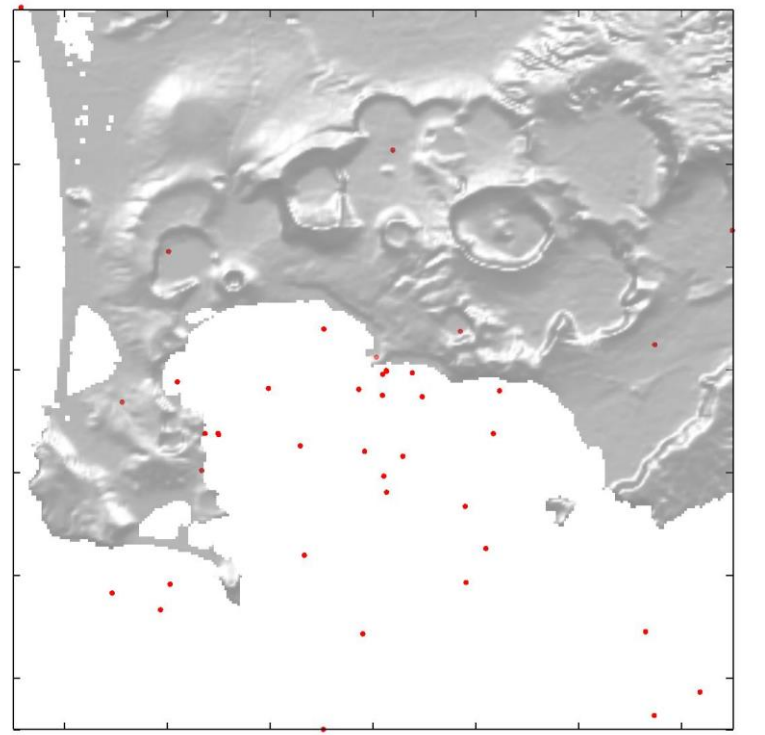


Figure 13 – Histogram of all the event in decades. It's possible notice that there is an evident strike during 1972 where most of 170 events are recorded.

Because the events were record just from one station, it's impossible made focal mechanism analysis or other more detailed analysis. So has been tried to made a relative locations using double difference algorithm using HypoDD software. The results of the relative location show that the events are mostly located in the centre of the caldera under the city of Pozzuoli and Solfatara crater, congruently with the other unrest episodes. The events are located between surface and 4000 m in depth (Fig. 14, Fig. 15). There are no presence of clusters.



•	Erh<2
•	Erh>6
•	Erh<10

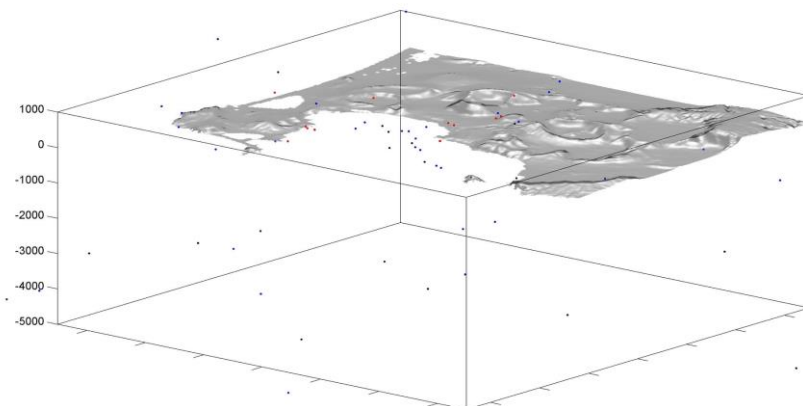


Figure 14,15 – Relative location of 1969–72 events founded in cartaceous record. These events are located mostly under the city of Pozzuoli and Solfatara crater.

# Chapter III – Stress and Focal mechanism inversion

## 3.1 General overview of the stress

In a rock, identified as a deformable object assuming as a continuum, we define Internal forces as products between particles that react to the external forces. These forces are distributed on the body uniformly. Two type of external forces exist: body forces and superficial forces. The measure of the intensity of that forces is defined as *stress*. This measure is convenient to assess the resistance of a material to permanent deformation as well as rupture. An object is in equilibrium if the resultant of forces acting on the object is zero.

The body force acts on the entire volume of the object and depends of the body mass.

Cut the body by a plane that passes through a point Q. We want to find the state of stress at the arbitrary point Q. The cut plane is oriented by unit normal direction vector  $\vec{n}$ .

With respect to  $\{x, y, z\}$  coordinate system the normal vector has components:

$$\vec{n} = [n_x \ n_y \ n_z]$$

In which  $\{n_x, n_y, n_z\}$  are the direction cosines of  $\vec{n}$ . Since  $\vec{n}$  is a unit vector, those components must verify the unit length condition

$$n_x^2 + n_y^2 + n_z^2 = 1.$$

Considering the cut plane with the exterior normal parallel to +x.

Consequently

$$\vec{n} = [1 \ 0 \ 0]$$

If  $\Delta A$  is an elemental area around Q that lies on the cut plane and  $\Delta \vec{F}$  the resultant of the internal

forces that act on  $\Delta A$ ,  $T$  is the stress vector:

$$\vec{T}(n) = \lim_{\Delta A \rightarrow 0} \frac{\Delta \vec{F}_0}{\Delta A}$$

$T$  is called *traction* vector and depends on the orientation of  $n$ .

If we project the internal force resultant  $\Delta \vec{F}$  on the reference axes  $\{x, y, z\}$ . This produce three component:  $\Delta F_x$ , aligned with the cut-plane normal, called *normal internal force component*,  $\Delta F_y, \Delta F_z$ , lie on the cut plane, called *tangential internal force components*.

$$\sigma_{xx} = \lim_{\Delta A \rightarrow 0} \frac{\Delta \vec{F}_x}{\Delta A} , \quad \tau_{xy} = \lim_{\Delta A \rightarrow 0} \frac{\Delta \vec{F}_y}{\Delta A} , \quad \tau_{xz} = \lim_{\Delta A \rightarrow 0} \frac{\Delta \vec{F}_z}{\Delta A}$$

$\sigma_{xx}$  is the normal stress or the stress component normal to the surface;

$\tau_{xy}$  and  $\tau_{xz}$  are the shear stresses or the components tangent to the surface. Shear stress components have two different subscript indices. The first one identifies the cut plane on which it acts as defined by the unit normal to that plane. The second index identifies component directions.

To fully characterize the stress state of the point we need nine stress components. Taking two more cut planes normal to the other two axes  $y$  and  $z$ , we found  $y$ - and  $z$ - stress components.

All the stresses acting on an infinitesimal volume  $\Delta A \rightarrow 0$  describe the stress state in this volume.

Stress distribution calculation imply the determination of the stress in each point of the body.

The stress tensor with positive components is refer to compression.

The nine components of Stress (Fig.16) referred to  $x, y, z$  axes may be arranged as a  $3 \times 3$  matrix, in which the first index is the normal surface parallel to one of the coordinate axis, so defined a surface on which a stress component acts and the second index defined the direction along which the stress component acts.

$$\sigma_{ij} = (\sigma_{xx} \ \tau_{xy} \ \tau_{xz} \ \tau_{yx} \ \sigma_{yy} \ \tau_{yz} \ \tau_{zx} \ \tau_{yz} \ \sigma_{zz})$$

Mathematically speaking, according with Cauchy, the stress in each point is completely defined by nine components of the second order tensor of type (2,0),  $\sigma$ , called *Cauchy stress tensor*.

In two dimension, the stress tensor in a given point is completely defined by three components: normal stresses ( $\sigma_x, \sigma_y$ ) and tangential component of shear ( $\tau$ ).

$$\sigma = [\sigma_{xx} \ \tau_{xy} \ 0 \ \tau_{yx} \ \sigma_{yy} \ 0 \ 0 \ 0 \ 0] = [\sigma_{xx} \ \tau_{xy} \ \tau_{yx} \ \sigma_{yy}]$$

This two-dimensional simplification is called a *plane stress state*. Since  $\tau_{xy} = \tau_{yx}$ , plane stress is fully characterized by just three independent stress component: the two normal stresses  $\sigma_{xx}$  and  $\sigma_{yy}$  and the shear stress  $\tau_{xy}$ .

The tensor may vary point to point. This means that they are expressed as functions of the position coordinates. In mathematical physics such functions are called fields.

So, to calculate normal stress and shear stress is necessary calculate the traction vector.

The traction vector  $T(\hat{n}) = (T_x, T_y, T_z)$  represent the force per unit area exerted by the side in the direction of  $\hat{n}$  across the plane. In general, the magnitude and direction of the traction vector will vary as a function of the orientation of the plan. Thus, to fully describe the internal forces in the medium we need a general method to determining the traction vector in function of  $\hat{n}$

In the general form the stress vector acting on a surface element is

$$T(\hat{n}) = \sigma^T \cdot n$$

Normal and shear stresses are the components of  $T(\hat{n})$  parallel and normal to  $n$ , respectively so

Normal stress will be (Fig.16)

$$\sigma_n = T(n) \cdot n$$

Shear stress will be

$$\tau = \sqrt{|T(n)|^2 - \sigma_n^2}$$

So the traction acting across any arbitrary plane of orientation defined by  $n$  may be obtained by multiplying the stress tensor by  $n$  that is

$$[T_x^{(n)} \ T_y^{(n)} \ T_z^{(n)}] = [\sigma_{xx} \ \sigma_{xy} \ \sigma_{xz} \ \sigma_{yx} \ \sigma_{yy} \ \sigma_{yz} \ \sigma_{zx} \ \sigma_{yz} \ \sigma_{zz}] [n_x \ n_y \ n_z]$$

$$T_x^{(n)} = \sigma_{xx} n_x + \sigma_{yx} n_y$$

The normal stress will be

$$\sigma_{nn} = T^{(n)} \cdot n$$

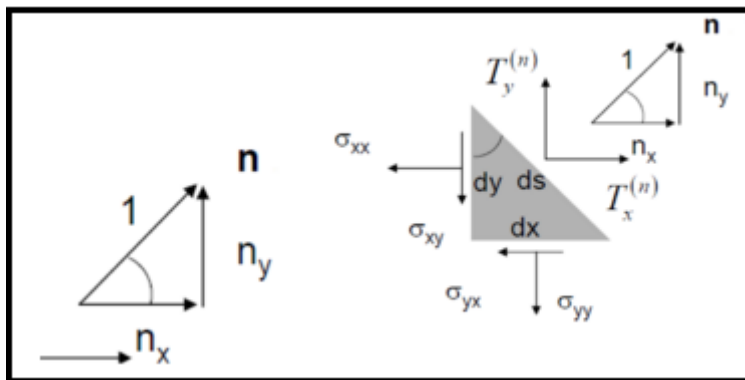


Figure 16 – On the right there are the representation of the shear stresses, the traction vector and of the normal vector  $n$ . On the left there is a zoom of the normal vector  $n$ .

Because of symmetry the stress tensor  $\sigma$  has real eigenvalues and mutually perpendicular eigenvectors. The eigenvalues are called the *principal stresses* of the stress. These principal stresses are numbered conventionally in descending order of magnitude  $\sigma_1 \geq \sigma_2 \geq \sigma_3$ ; they are respectively the maximum, intermediate and minimum principal stresses and indicate the magnitudes of compressional stress. The orientations are defined by the eigenvectors and are called *principal axes of stress* and the orientation corresponding to the principal stress. So principal planes of stress are the planes parallel to two of the stress axes, or perpendicular to one of the stress axes.

Physically, eigenvalues and eigenvectors properties could be interpreted in this way: in a continuum exist three directions, called principal axis of the stress, mutually orthogonal that define three planes, called principal planes on which are just normal stresses and shear stresses are null. If we use the principal axis as coordinate axis, the stress tensor takes a diagonal shape and its components match with eigenvalues. For this reason, sorting in a crescent order the eigenvalues, we have  $n^{(1)}$  as maximum compression axis,  $n^{(3)}$  as maximum tension axis, and  $n^{(2)}$  intermediate axis.

### 3.1.1 Pressure types

Earth surface is generally consider as stresses free, because atmospheric pressure and wind stresses are normally negligible. If  $x$  and  $y$  are horizontal coordinates and  $z$  is vertical, downward directed,  $\tau_{xz} = \tau_{yz} = \tau_{zz} = 0$  in  $z=0$ . Consequently the free surface  $z=0$  is a principal plane with null eigenvalue and the relative principal axis is vertical, while the other two axes are horizontals and, in first approximation, this configuration is valid also for  $z>0$ , near the surface.

The third Cauchy-Navier equation's component requires:

$$\rho g + \frac{\partial \tau_{j3}}{\partial x_j} = 0$$

Suppose that the principal axis is vertical also in depth,  $\tau_{13} = \tau_{23} = 0$ , so

$$\rho g + \frac{\partial \sigma_z}{\partial z} = 0 \implies \sigma_z = - \int pg dz + h(x, y) = - \int_0^z pg dz$$

Where  $h(x, y)$  is a generic function, that must be null for free surface ( $\sigma_z = 0$  in  $z = 0$ ).

Equations for horizontal component require:

$$\frac{\partial \sigma_x}{\partial x} = 0 \implies \sigma_x = h_1(y, z) \quad (\sigma_x \text{ not depend from } x)$$

$$\frac{\partial \sigma_y}{\partial y} = 0 \implies \sigma_y = h_2(x, z) \quad (\sigma_y \text{ not depend from } y)$$

The approximation of the vertical principal axis is true just near the surface, it's not true in general

that the principal axis in depth is vertical.

Anisotropic stress causes tectonic deformations. The differential stress is

$$\Delta\sigma = \sigma_1 - \sigma_3$$

Cauchy's stress formula will be

$$T(n) = (T_1(n) \ T_2(n) \ T_3(n)) = (\sigma_1 \ 0 \ 0 \ 0 \ \sigma_2 \ 0 \ 0 \ 0 \ \sigma_3)(n_1 \ n_2 \ n_3)$$

So

$$T_1(n) = \sigma_1 n_1, \quad T_2(n) = \sigma_2 n_2, \quad T_3(n) = \sigma_3 n_3 \quad (x)$$

We can write normal and shear stresses as

$$\sigma_n = T(n) \cdot n = \sigma_1^2 n_1^2 + \sigma_2^2 n_2^2 + \sigma_3^2 n_3^2$$

$$\tau = [|T(n)|^2 - |\sigma_n|^2]^{1/2} = [\sigma_1^2 n_1^2 + \sigma_2^2 n_2^2 + \sigma_3^2 n_3^2 - (\sigma_1 n_1^2 + \sigma_2 n_2^2 + \sigma_3 n_3^2)^2]^{1/2}$$

If there is a plane on which traction vanishes, the state of stress is said to be *plane stress* and the stress tensor corresponding to this state has a null principal stress.

Combining (x) and  $n_1^2 + n_2^2 + n_3^2 = 1$  we have the *Lame's stress ellipsoid* equation that describe the state of stress whose principal axes coincide with the stress axes:

$$[\frac{T_1(n)}{\sigma_1}]^2 + [\frac{T_2(n)}{\sigma_2}]^2 + [\frac{T_3(n)}{\sigma_3}]^2 = 1$$

An important parameter is the *Stress ratio*, that describes the ratio between principal stresses and designates the shape of the stress ellipsoid

$$\Phi = \frac{\sigma_2 - \sigma_3}{\sigma_1 - \sigma_3}$$

The ratio is in the range of  $0 \leq \Phi \leq 1$ .

If  $\Phi = 0$ ,  $\sigma_3 = \sigma_2 < \sigma_1$  and the ellipsoid is prolate. If  $\Phi = 1$ ,  $\sigma_3 < \sigma_2 = \sigma_1$  and the ellipsoid is

oblate. In these cases, the stress ellipsoide has axial symmetry, instead for intermediate  $\Phi$  indicates  $\sigma_3 \neq \sigma_2 \neq \sigma_1$  and the stress ellipsoid and stress tensor have orthorhombic symmetry.

We can classify the state of stress as

- *Lithostatic or hydrostatic pressure*

$$\sigma_3 = \sigma_2 = \sigma_1 = p$$

Where the normal stress is equal to pressure  $p$  and there aren't shear stresses.

The simplest stress configuration is that lithostatic, in which we assume that at a certain depth  $z$ , principal stresses are equals between themselves  $\sigma^{(1)} = \sigma^{(2)} = \sigma^{(3)} = -p_{lit}$

The stress tensor will be  $\tau_{ij} = -p_{lit}\delta_{ij}$ .

Equilibrium equation

$$\rho g \delta_{i3} + \frac{\partial \tau_{ij}}{\partial x_j} = 0$$

Imposes

$$\frac{\partial p_{lit}}{\partial x} = \frac{\partial p_{lit}}{\partial y} = 0 \quad \frac{\partial p_{lit}}{\partial z} = \rho g$$

$p_{lit}$  doesn't depend on  $x$  and  $y$  so

$$p_{lit}(z) = \int_0^z \rho g dz.$$

If we assume that  $\rho$  and  $g$  are constants,  $p_{lit} = \rho g z$ , so the lithostatic pressure is major than the atmospheric at few meters of depth.

$p_{lit}$  is the lithostatic pressure and increases linearly with depth.

- *Uniaxial compression*

$$0 = \sigma_3 = \sigma_2 < \sigma_1$$

There is only compressive stress in one direction.

- *Uniaxial tension*

$$\sigma_3 < \sigma_2 = \sigma_1 = 0$$

There is only tension in one direction.

- *Pure shear stress*

$$\sigma_3 = -\sigma_1, \sigma_2 = 0$$

The normal stress on planes of maximum shear stress is zero.

- *Triaxial stress*

$$\sigma_3 < \sigma_2 < \sigma_1$$

all the principal stresses are different.

We call Free surfaces or free boundaries the planes on which traction vanishes.

Other parameters are: the *mean stress*  $\sigma_0 \equiv \frac{\sigma_1 + \sigma_2 + \sigma_3}{3} = \frac{\text{trace } \sigma}{3} = \frac{\sigma_I}{3}$  that for lithostatic stresses,

coincides with pressure;

- *Deviatoric stress*

$$\mathbf{T} = \boldsymbol{\sigma} - \sigma_0 \mathbf{I}$$

that identify the deviation from the lithostatic state of stress. The deviatoric tensor is symmetric so its principal orientations are parallel to the stress axes.

Traction on a surface element depends on the directions of its normal  $n$ , and the normal and shear components also change with  $n$ .

The constitutive relations consider that increasing deformations are coupled with increasing stresses. But every crystal has limited capability to stay under stresses and molecular links break under stress values comparable with rigidity  $\mu$ . However, rocks have different crystalline licks and the rupture come at low values of stress respect to the rigidity

Displacement on the fracture surface could be normal and outward the surface only if  $\sigma_3$  is positive and near the surface because lithostatic pressure get the stresses always compressive in depth. Only

if a fluid like magma, pushes from inside to outside, overcoming lithostatic pressure, could be generate tensile fractures in depth. In deep Movement on the fracture surface is tangent to the surface so tractions are shear tractions. Because on principal plane exist just normal traction, fracture surfaces must be oriented in intermediate directions between principal planes.

Tectonic movements produce stress growing in time located in particular along plates margins. Fractures, on a fault surface with relative movements between two blocks, are generated when material résistance is reaching.

### 3.1.2 Mohr

To illustrate the state of stress generally is used the Mohr diagram. The diagram shows the combination of normal and shear stresses on a shear fracture plane arbitrary oriented into a rock sample, on which act principal stresses  $\sigma_1$  and  $\sigma_3$ . The possible combinations of normal and shear stress on fracture planes oriented between  $0^\circ \leq \theta \leq 90^\circ$  are shown with circles(or semicircles) into a  $\tau - \sigma_n$  diagram(Fig. 17), through which it's possible determinate the maximum shear stress

$$\frac{\sigma_1 - \sigma_3}{2}$$

That is  $\tau_{max}$ , where  $\sigma_1 - \sigma_3$  is a differential stress  $\sigma_d$ . Instead  $\sigma_1 + \sigma_3/2$  is the circle's centre.

Shear stress maximum is for  $2\theta = 90^\circ$

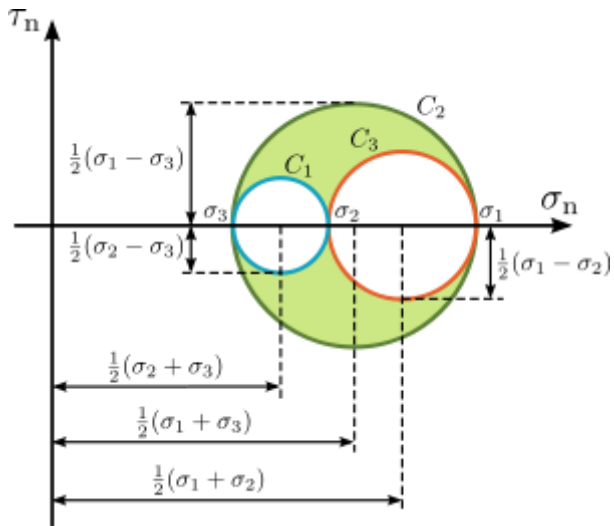


Figure 17 – schematic representation of Mohr circle

### 3.1.3 Mohr-Coulomb Criterion

Using a rupture criterion in combination with mohr circle, it's possible to know the state of stress on the plane. The most common criterion in Mohr-Coulomb. It describes the relation between  $\tau$  and  $\sigma_n$  generated by the principal stress  $\sigma_1$  and  $\sigma_3$ , acting on a potential fracture plane tilts of  $\theta$  angle.

In 1776, Coulomb deduced the shear stress equation required to cause break on the potential plane

$$\tau_{crit} = C + \mu^* \sigma_n$$

$C$  is cohesion,  $\mu^*$  is the friction coefficient and can be expresses

$$\mu^* = \tan\theta$$

$\theta$  is the internal friction angle.

But  $\mu^*$  cannot be directly measured so it must be considered as gradient of this equation

$$\mu^* = \tau - C/\sigma_n$$

The line given by the equation is called rupture limit. All the state of stress that are under this limit are in a stable state and there isn't rupture.

Considering a two-dimensional problem, whit only two principal stresses  $\sigma_1$  and  $\sigma_2$  accompanied

by two principal axes, one of which is parallel to the axis of symmetry for the state of stress. The stress tensor will be

$$\sigma = (\sigma_1 \ 0 \ 0 \ \sigma_2)$$

After the determination of stress distribution in a coordinate system  $\{x,y\}$ , is useful determine the same distribution in a rotate coordinate system  $\{x',y'\}$ . the stress acting on the same plane with different orientation, passing through the same interest point, make an angle with the coordinate system  $\{x,y\}$  ,  $\theta$ .

So the stress components are transformed in

$$\begin{aligned}(\sigma'_{11} \ \sigma'_{12} \ \sigma'_{21} \ \sigma'_{22}) &= (\cos\theta \sin\theta \ - \sin\theta \cos\theta) (\sigma_1 \ 0 \ 0 \ \sigma_2) (\cos\theta \ - \sin\theta \sin\theta \cos\theta) \\&= (\sigma_1 \cos^2\theta + \sigma_2 \sin^2\theta \ - (\sigma_1 - \sigma_2) \sin\theta \cos\theta \ - (\sigma_1 - \sigma_2) \sin\theta \cos\theta \ \sigma_1 \cos^2\theta \\&\quad + \sigma_2 \sin^2\theta)\end{aligned}$$

Since  $\sigma_n$  and  $\tau$  are equivalent to  $\sigma'_{11}$  and  $\sigma'_{12}$ , respectively:

$$\begin{aligned}\sigma_n &= \sigma'_{11} = \sigma_1 \cos^2\theta + \sigma_2 \sin^2\theta \\ \tau &= \sigma'_{12} = -(\sigma_1 - \sigma_2) \sin\theta \cos\theta\end{aligned}$$

Using the formulas  $\sin^2\theta = (1 - \cos 2\theta)/2$ ,  $\cos^2\theta = (1 + \cos 2\theta)/2$  and  $\sin\theta \cos\theta = \frac{1}{2} \sin 2\theta$

We obtain

$$\begin{aligned}\sigma_n &= \frac{1}{2}(\sigma_1 + \sigma_2) + \frac{1}{2}(\sigma_1 - \sigma_2) \cos 2\theta \\ \tau &= -\frac{1}{2}(\sigma_1 - \sigma_2) \sin 2\theta\end{aligned}$$

Physically speaking,  $\theta$  is the fracture plane angle, that is the angle between  $\sigma_1$  and the fracture plane. This angle is equal to the orientation perpendicular to the fracture plane, so the normal and shear stresses are indicated by the point that makes an angle of  $2\theta$  from  $(\sigma_2, 0)$  along the mohr circle. The point on it represents the critical condition for shear fracturing. Other point on the diagram (Fig. 18) are critical points due to experiments conducted for specific type of rocks with various confining pressure. Connecting the points, we obtain the failure envelope. This envelope creates a region that represent the combinations of normal and shear stresses that could be support

from the rock not failing. The envelope represents the *fracture strength* of the rocks.

$\sigma_T$  is the tensile strength that is the normal stress designated by the intercept. When  $\sigma_n < \sigma_T$ , tension fracture occurs.

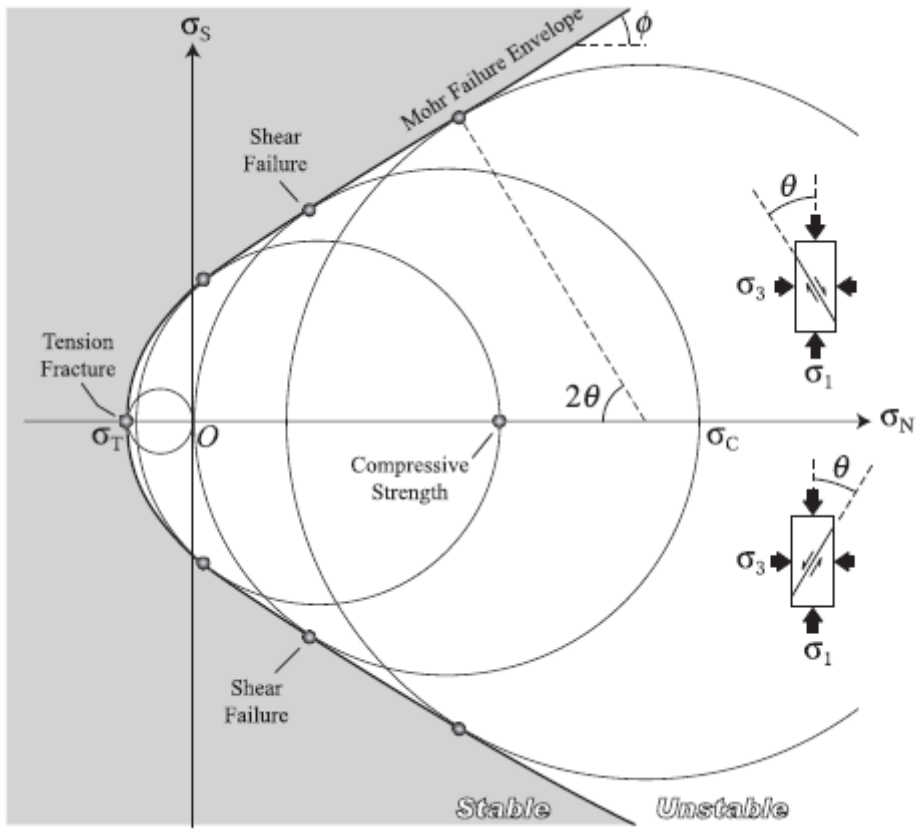


Figure 18- Schematic diagram showing the normal and shear stresses at which the cylindrical specimens of the same rock are fractured by axial stresses (Yamaji, 2007) .

For  $\sigma_1 > 0, \sigma_2 = \sigma_3 = 0$  longitudinal splitting occurs. The splitting causes expansion perpendicular to the compressive axis. Hence, positive confining pressures suppress the splitting, resulting in the formation of shear fractures.

Rocks have numberless micro cracks with various orientations which growth and coalescence control macroscopic failure. Stress concentration occurs at the tips of those cracks which are grown by the concentrated stresses. The crack propagation increases the concentration. This happened when the cracks are perpendicular to the applied tensile stress, resulting in tension fracture.

For the case of shear fracture, propagation starts at the tips of the crack to the  $\sigma_1$  orientation due to the frictional sliding oblique to the  $\sigma_1$ -axis.

The frictional resistance or *Frictional strength*,  $\tau_f$ , is represented by the shear stress on the surface

$$\tau_f = \mu_f \sigma_n$$

$\sigma_n$  is the normal stress acting on the surface,

$\mu_f$  the coefficient of friction.

For  $\sigma_n < \tau_f$  the surface is locked, otherwise sliding occurs on the surface. The study of frictional strength is important to investigate earthquake and landslides, so the coefficient of friction of various rock types was experimentally estimated in the range of 0.6–1.0

The strength obeys to this linear relationship:

$$\begin{aligned} \mu_f &= \{0.85\sigma_n & (\sigma_n < 200MPa) \\ \tau_f &= \sigma_n^{0.94} & (\sigma_n < 1700MPa) \end{aligned}$$

$$0.6\sigma_n + 50MPa \quad (0.2 < \sigma_n < 1700MPa) \}$$

One of the stress axes in the shallow part of the solid Earth is perpendicular to the surface, the other stress axes lie on the surface. If one of the stress axes is vertical, stress in the shallow part of the Earth is expressed as

$$\sigma = (\sigma_H \ 0 \ 0 \ 0 \ \sigma_h \ 0 \ 0 \ 0 \ \sigma_v)$$

Where  $\sigma_H$  and  $\sigma_h$  are the maximum and minimum horizontal stresses, and  $\sigma_v$  the vertical stress.

Dikes, are tabular intrusion of magma pushed from the magma through the country rock via its pressure for intrusion. We can use the mohr diagram to shows the admissible orientations of dike intrusion relative to the principal axes of stress in the country rock.

$p_m$  is the magma pressure intruding in a rock mass, that has to overcome the normal stress for intrusion. Magma can intrude cracks with determined orientations that are shown in the mohr diagrams. As the magma pressure increases, if  $p_m$  is smaller than  $\sigma_3$ , no magma intrusion occurs.

When  $p_m \lesssim \sigma_3$ , magmas can only intrude cracks nearly perpendicular to the  $\sigma_3$ -axis.

When the pressure increases, the admissible orientations of dike intrusion expand. If  $p_m > \sigma_1$  it means that magma could intrudes any crack, like in a network of intrusions.

### 3.1.4 Coulomb – Navier criterion

Coulomb – Navier criterion puts in relation brittle strength linearly related with normal stress.

$$|\tau| = \tau_0 + \mu\sigma_n$$

$\tau_0$  is the cohesion that is a material constant depending on lithology and other factors like temperature and strain rate.

$\mu$  is the coefficient of the internal friction.

$$\mu = \tan \varphi$$

$\varphi$  is the angle of internal friction.

So this criterion predicts that the formation of a fault in an intact rock needs a differential stress as great as the cohesion  $\tau_0$ . Instead, shear stress needed for frictional sliding is smaller than that for forming a shear fracture in an intact rock. In general, pre-existing fractures are activated as faults if they have not been cemented.

Generally speaking, about Mohr circles, when the circle that defines the stress, touches the failure envelope, a shear fracture is formed and a fault generated.

The line A-F links  $\sigma_1$  and  $\sigma_3$  and represent the surface that contain the  $\sigma_2$ -axis, the attitude of the fault plane predicted is parallel to the  $\sigma_2$ -axis. Looking the Fig(19) we can notice two failure envelope, and two points C and D that touch the mohr circle, so two possibilities of shear traction.

Just one in the pair is chosen to form a fault. The two surface are called *conjugate shear planes*. The point E indicates the normal stress  $\sigma_3$ , the half line BC or BD makes an angle  $2\theta$  with E so the point C or D indicates the angle of the shear,  $\theta$ , between the  $\sigma_3$ -axis and the line perpendicular to the fault surface. B is the centre of the Mohr circle so  $\angle BCA = 90^\circ$  so we have

$$2\theta + \varphi = 90^\circ$$

Rearranging the equation we have  $\mu = \tan \varphi = \tan (90^\circ - 2\theta) = \cot 2\theta$

The relation between the coefficient of internal friction and the shear angle is

$$\tan 2\theta = 1/\mu.$$

So  $\mu$  is inversely correlated with the angle of shear that has a minimum  $\theta=0$  for  $\mu = \infty$  and a maximum  $\theta = 45^\circ$  for  $\mu = 0$ .

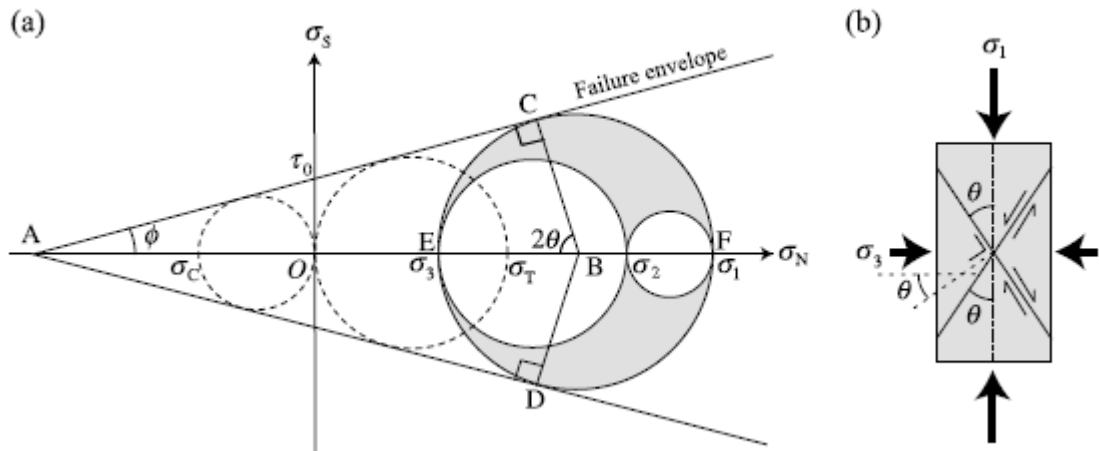


Figure 19 – Mohr diagram showing the Coulomb-Navier criterion (Yamaji,2007)

### 3.1.5 Optimal principal stress orientation

Considering the stereogram of Bucher(1920)we could make a paleostress directions determination. The stereogram is called optimal stress orientation because for constant stress magnitudes, it maximizes the difference between the shear stress and the frictional resistance due to the normal stress applied on the fault plane.

On the stereogram, the slip direction is perpendicular to the conjugate planes' intersection,  $\vec{s}_1, \vec{s}_2, \vec{s}_3$  are the principal stress orientations deduced rotating the slip directions  $\vec{a}, \vec{b}, \vec{c}$  by an angle around  $-b$ ,  $\phi_2$  equal to  $\phi_2 = 45^\circ - \frac{\phi_0}{2}$ , where  $\phi_0$  is the angle of internal friction. The plane of moment is that plane that contains  $\vec{a}$  and  $\vec{c}$  and thus the optimal directions  $\vec{s}_1$  and  $\vec{s}_3$ .

### 3.1.6 Anderson's criterion

If the surface is largely horizontal, one of the stress axis, is vertical. Combining this and the Coulomb-Navier criterion, Anderson obtains an important relationship between the type of faulting and stress. This relationship is known as Anderson's theory of faulting.

The criterion suggests that fault planes are parallel to  $\sigma_2$ -axis and that the planes make angles  $\frac{1}{2} \tan^{-1} - (1/\mu)$  which is less tan  $45^\circ$  with the  $\sigma_1$ -axis.

If  $\sigma_3$ -axis is vertical the stress gives rise to reverse faulting with dip angle less than  $45^\circ$ .

If  $\sigma_1$ - or  $\sigma_2$ - axis is vertical, normal or strike-slip faults are formed. This theory is used to identify stress regimes in the lithosphere:

$\sigma_v > \sigma_H$  normal fault regime

$\sigma_H > \sigma_h > \sigma_v$  reverse fault regime

$\sigma_H > \sigma_v > \sigma_h$  strike-slip regime.

The state of stress controls the mobility of pre-existing fractures. Fractures that can be re-activated have orientation controlled by the same differential stress expand with decreasing  $\sigma_3$ , because the brittle and frictional strengths increase with  $\sigma_n$ . But in general the situations of reactivation are more limited: the orientations are limited with increasing of depth and pore pressure; the normal fault regime of stress are more favourable to reactivation than reverse fault regime at same differential stress and burial stress.

Vertical stress obeys the relationship,  $\sigma_v \approx \int_0^z \rho(z)gdz \approx \rho g z$ . Generally  $\rho$  is assumed as constant because common rock have densities about  $\rho \approx 3 \times 10^3 \text{ kg m}^{-3}$ . So we could assume that  $\sigma_v$  is determined by depth.

If a rock mass is in the normal faulting regime

$$\sigma_v = \sigma_1$$

$$\sigma_h = \sigma_3 = \sigma_v - \Delta\sigma < \sigma_v$$

In the reverse faulting regime is

$$\sigma_v = \sigma_3 = \sigma_1 - \Delta\sigma < \sigma_H \quad \sigma_H = \sigma_1$$

This theory is convenient for inferring the state of stress from faults but is not always correct because doesn't take in account oblique-slip faults.

### 3.2 Stress in the magmatic chamber

In order that the magma is brought outside of the room, needs that a sheet or dike go to camera edges and propagate in the host rock. For the eruption, this sheet or dike have to propagate itself through all the rock layers and contracts between rupture point at the edge of the chamber and free surface of associated volcano. Based on crack theory of Griffith and supported from analogy with result of numerous experiment of hydraulic fracture, the rupture of full magmatic chamber starting from a sheet or dike when are satisfy this condition

$$p_l + p_e = \sigma_3 + T_0$$

That are respectively lithostatic pressure to depth of chamber, excess of magmatic pressure that is the difference between total magmatic pressure in the chamber at the rupture moment and the lithostatic pressure, minimum principal stress and the tensile strength in situ at the rupture point.

In this case the compressive stress is considerate positive. When there is an absolute tension,  $\sigma_3$  is negative, while the maximum principal compressive stress is always positive.

It follows that the injection happen when the conditions of equation are reach in every at the caldera edge, independently from the chamber shape and depth. Condition of that equation is reach when  $p_e$  increase or when  $\sigma_3$  decrease or both of them. This equation is referred to stress concentration of  $\sigma_3$  local stress, due to magmatic chamber shape, included edge irregularity.

In the equation the normal condition everywhere along the chamber edge is

$$p_l = \sigma_3 = \sigma_1$$

During brief period as unrest, the situation may be  $p_e > 0$ , either because of adds of magma volume, so increment of excess pressure of camera, or reduction of  $\sigma_3$ . Is during this period that the condition of eq 1 may be satisfy, resulting from rupture or dike or sheet initiation. They can propagate for a brief distance from the chamber or upward the surface and feed a magma for an eruption.

The equation however doesn't represent the rupture condition for a cavity full of fluid in terms of maximum and minimum compressive regional stress ( $\sigma_H, \sigma_h$ ).

A magmatic chamber is a structure full of fluid with long life that presumably is in lithostatic equilibrium with the surrounding area for many time of its life.

Considering a chamber located in an elastic host rock and a sheet that form an angle  $\alpha$  with the surface, with z vertical coordinate positive upward. From the Navier-stokes equation follow that the volumetric rate  $Q_L^e$  through a fracture full of ideal magma is

$$Q_L^e = \frac{(\Delta u^3 W)}{12\mu} [(p_r - p_m)g \sin \alpha - (\frac{\delta p_e}{\delta L})]$$

With

E=used to indicate that the fracture is in an elastic rock,

L=is the dip-dimension or distance of magma transportation

$\Delta u$  is the fracture opening

$\mu$  is the dynamic viscosity of magma.

$p_r$  is the host rock density.

$p_m$  is the magma density assumed constant.

G is the acceleration because the gravity.

$(\frac{\delta p_e}{\delta L})$  is the pressure gradient in the flux direction.

$\alpha$  is the dip respect the surface and vary from  $0 > \alpha > 90^\circ$ .  $\alpha = 90^\circ$  when the flux is vertical, along a vertical dike and derive from it  $\sin\alpha=1$  and  $\alpha = 0$  when the flux is horizontal.

W is the width in the perpendicular direction to the flow (assuming  $W \gg \Delta u$  while the transversal section of perpendicular fracture of flux direction is  $A=\Delta u W$ ). For a sill in the xy horizontal plane W is the measure along y. For a lateral propagation in the vertical plane xz W is the measure along z. In both of the cases, if the flux is assumed along a mechanical layer with equal density to which of magma and the length L is measured along x axis, we may substitute x with L to obtain the volumetric magmatic flux:

$$Q_x^e = \frac{(\Delta u^3 W)}{12\mu} \left[ \left( \frac{\delta p_e}{\delta x} \right) \right]$$

In absence of stress gradient, the excess pressure is the only pressure gradient for a magmatic flux through a dike located laterally along a layer to neutral buoyancy is of magmatic chamber. In terms of mechanic of formation of calderic collapse, the equation indicates that in order that a flow may be drive out the chamber needs to be a pressure excess  $p_e > 0$  in the chamber. If this fall to zero, there isn't pressure gradient available to drive the magma out the chamber and so the flux should stop.

It follows that this hypothesis may be used to explain the model under pressurized or to magmatic support withdrawal, and to explain the fault ring formation that commonly used that the under pressurized is generated from the magma flux out of the chamber along a dike laterally propagated. But has to be explain why the equation is not valid during the calderic collapses.

A reason may be that the conduit was open at the surface during the eruption, the static pressure in a magma column has to be minor than which in a similar column near the host rock.

The magmastic pressure is  $p_m = \rho_m gh$  with h the depth. The lithostatic pressure in a rock column may be is  $p_l = \rho_r gh$ . When  $\rho_r > \rho_m$  that is the host rock density greater than magma density  $p_m < p_l$  that is the magmastic pressure is minor of lithostatic stress and there is the possibility that

may exist

$$p_m + p_e < p_l = \sigma_3 \text{ even if } p_e > 0$$

If this is correct, may be an excess of positive pressure so  $p_e > 0$  should drive out the magma even if the magmastic pressure plus the excess of pressure is minor than the minimum compressional stress  $\sigma_3$ . Field observation show that many fault ring and dike is originated in the neighborhood of lateral limit of associate magmatic chambers.

A necessary condition for the ring fault formation is that the shear stress and the tensile stress near the surface favoured dip-slip fault, has to be maximum on lateral limit of the chamber. Stress has to be maximum on the “equator” of spherical chamber and the vertex of and oblate ellipsoidal chamber, this because the fault ring are primarily shear fracture and cannot form or slip unless the local shear stress satisfy the condition for faulting that normally is represented by the Navier-Coulomb criterion, Von Mises criterion and other.

This equation ignores the possible stress gradient in the host rock due to variation of mechanical propriety and so variation of local stress, topography of volcano or both.

The local stress field around a magmatic chamber may trigger many injection of sheet of magma during their life, resulting in many eruption, instead calderic collapses are rare. Stress local field depends primary on the magmatic chamber shape, load condition and host rock mechanical proprieties.

Magmatic chamber could have many shapes: prolate or oblate ellipsoid and spherical. A prolate ellipsoidal magmatic chamber has a long vertical axis and normally is improbable generate local stress usefull for the ring fault formation.

In numerical model are used four type of load condicions:

-excess of magmatic intern pressure in the chamber

-horizontal extern stress tensile applicate at the crustal segment hosting the chamber

-magma accumulation and pressure excess applied at the basis of crustal segment resulting in a

dome very small of crustal segment

-excess of negative pressure of the chamber.

Is unlikely that the stress field around a circular magmatic chamber in a homogeneous crust, isotropic and subject to many types of load, trigger the starting of fault ring.

When the load is intern magmatic load in excess, the maximum surface on which act shear and tensile stresses are in the point directly under the centre of the magmatic chamber. When the chamber is subject to underpressure, shear stress surface has the maximum at the centre of the camera and when the crustal layer hold the chamber is subject to external horizontal tension or doming pressure at the lower edge due to magma accumulation and the maximum shear and tensile stress at the edge of caldera is in the point near the free surface so in a position not good for the generation of ring fault or ring dyke.

Horizontal doming and generation of dome bring similar results. For horizontal tension, maximum tensil stress  $\sigma_3$  at the edge of magmatic chamber is 5 MPa, while reach picks of 15 MPa at the free surface of the chamber. At the same way the Von Mises shear stress  $\tau$  at the edge reach 4 MPa, at the free surface 13 MPa. Doming stress at the base of crustal segment generate tensile and shear stress at the surface with 25 MPa of  $\sigma_3$  and 22 MPa of  $\tau$  and at the edge 14 and 12 MPa respectively.

### 3.3 Determination of stress

Fault-slip data are used to define the state of stress of observed fault on various scale. It's more easy and useful use mesoscale faults than large-scale faults to investigate the stresses responsible for the movement of the faults. Mesoscale faults are minor faults interesting by displacement, that we could

found in one outcrop. They could have a displacement from few millimetres to several meters. So there is much greater number density of those faults. Than in comparison with large scale faults, they can be reactivated as well, but have a simple history and their deformation of a rock mass can be treated as an infinitesimal deformation if the rock mass is very large. We call fault-slip data: orientation of a fault surface, sense of shear and slip direction.

To determine the slip orientation of a fault, generally are used the fault striations or simply *striae* that are scratches or grooves on a fault surface produced by fault movements. In the same way we could identify the sense of shear looking for the offset of pre-faulting fractures.

There are several methods to estimate the state of stress from faults. Anderson's theory of faulting is one of it and is still used. However, Bott [...] showed the abundance of oblique slip faults which were incompatible with Anderson's theory. Wallace-Bott(..) showed that shear traction applied on a given fault plane causes a slip in the direction and orientation of that shear traction.

McKenzie utilized Wallace-Bott's hypothesis[...] to infer the state of stress at an earthquake source[...] and the most part of modern inverse method formulated to know the state of stress, are based on this principle. Carey and Brunier[...] and Angelier[...] used it to infer paleostress from geological faults.

Wallace-Bott's hypothesis predicted the slip direction for a given fault and stress.

Given a fault plane with unit normal  $\mathbf{n}$  the traction vector is given by

$$t(n) = \sigma \cdot n$$

So the normal and tangential components of this vector are the normal and shear traction vectors

$$\sigma_n = N \cdot \sigma \cdot n = n[n \cdot (\sigma \cdot n)]$$

$$\tau = (I - N) \cdot \sigma \cdot n = \sigma \cdot n - n[n \cdot (\sigma \cdot n)]$$

Faulting occurs to release the shear stress so the slip direction will be indicated by  $-\tau/|\tau|$ .

As we can see, not all the stress components are determined. The Wallace-bott hypothesis didn't take in account the pore fluid pressure, although it controls the strength of faults.

The pore fluid pressure doesn't interest the shear traction and doesn't affect the slip direction of a fault so it's difficult to know the pore fluid pressure on a fault surface when the fault moved.

It's also difficult estimate the depth of burial of a fault when it was activated. In general, crustal stress is limited by the brittle strength and faulting occurs when stress is brought the limit. Let  $\sigma_0$  be an arbitrary stress tensor and  $\sigma = q\sigma_0$ . Since the slip directions due to these stresses are the same, are independent from the depth of burial. The stress directions predicted by the Wallace-bott hypothesis for the stresses  $\sigma$  and  $\sigma = q\sigma_0 - pI$  are the same for a given fault, and we can interpreted  $p$  and  $q$  as pore pressure and depth. The tensor that represents those stresses is termed *reduced stress tensor* that we could express using

$$\sigma_0 = R^T(1 \ 0 \ 0 \ 0 \ \phi \ 0 \ 0 \ 0 \ 0) \cdot R$$

$R$  indicates the principal stress orientations and  $\phi = (\sigma_2 - \sigma_3)/(\sigma_1 - \sigma_3)$  is the stress ratio.

The tensor between  $R^T$  and  $R$  is the reduced stress tensor.  $\sigma_0$  is enough to calculate the slip directions of faults because represents the principal orientations and stress ratio.

### 3.4 Stress Inversion

Inverse methods are mainly used to define the spatial and/or temporal variation of stress fields.

The stress inversion is a non-linear inverse method, that is used to determine the state of stress from given fault-slip data. All the methods look for a common stress tensor that returns a shear stress parallel to the slip direction. Typical criteria use minimization of a misfit function searching for the right reduce stress tensor, define by principal stress orientation and the aspect ratio. The function generally uses is the unsigned angle between the observed slip and the shear stress.

Because the non-linearity that comes from the division of the unit vector  $-\sigma_s/\sigma_S$  the resolution of

the problem requires the use of other algorithms to linearize it, such as Montecarlo techniques (Etchecopar, 1984; Etchecopar et al. 1981; Vasseur et al. 1983) or grid search (Yamaji, 2000, 2003).

From this method we can obtain the optimal principal orientations and the optimal stress ratio.

From given fault-slip data it's possible determined the state of stress following that inverse method.

Assuming the principal stress orientations and a stress ratio we can compose a stress tensor  $\sigma_0$ . Then we could use the equations for each fault and decide that  $\Delta^{(i)}$  is the angular misfit between the theoretical and observed slip directions of the  $i$ -th fault. The measure of misfit of the assumed stress state to the data set is due to

$$S = \sum_{i=1}^N f(\Delta^{(i)})$$

Where N is the number of faults and  $f(\Delta^{(i)})$  is a monotonously decreasing function.

The optimal state of stress is determining minimizing  $S(\sigma_0)$ .

If the optimal stress cannot explain the observed slip directions of those faults, the fault-slip data are called heterogeneous and resulted from plural stress states responsible for the faults.

In this case there are several methods for distinguishing the different fault sets like consideration of stratigraphy or of the age of the rocks, characterization of the syn-sedimentary faults, cross-cutting relationship, superimposed striae on the same fault plane. These sorts of field observation allow us to classify faults by the stresses that activated the faults. Given that sorts, inverse methods (Angelier and Huchon, 1987) can readily identify the stresses. Unfortunately, these criteria are not always available in the field, especially in young geologic units. However, many faults with the same orientations and the same slip directions can be activated by different stresses. So prior to using the stress inversion, we need a fault classification that implicitly restricts solution. Many methods presented the way to separate the stresses from heterogeneous fault-slip data. With a priori knowledge that faults compose a conjugate set, is appropriate uses Huang's (1988) simple method.

However not all deformation result in simple conjugate sets and moreover, conjugate faults result

only in plane strains, but strains are generally three-dimensional. Angelier's (1979) inverse techniques can determine triaxial stresses.

Stress inversion assumes parallelism between striae and maximum shear stress on the fault plane. This is matter of debate (Reaches, 1987; Marrett and Allmendinger, 1990; Pollard et al., 1993). Twiss and Unruh (1998) show that they are parallel if fault block rotations are negligible and if stress and strain are linearly related.

## 3.5 Inversion of Focal Mechanisms

The application of stress inversion techniques is used to reconstruct the actual stress field that acting on an intensely fractured rock it's responsible of slip that occur on fault planes oriented along mechanically favourable directions. Several methods of stress inversion exist (Angelier and Mechler, 1977; Michael, 1984, 1987; Gephart and Forsyth, 1984; Rivera and Cisternas, 1990; Yamaji, 2000; Otsubo et al., 2008). It's possible divided the stress inversion methods into two big categories: Graphical and Analytical method. In this thesis, has been used both of the method, making a comparison from the results to better understand and reconstruct the stress field acting in the bradyseismic crisis of 1982–1984.

### 3.5.1 Analytical method

We set out with a view that it's unlikely that slip occurs for low values of shear stress. It occurs depending on a combination between normal and tangential stress components through a friction coefficient. Earthquake data tell us that a fault slip event occurs.

Tectonic analysis of faults populations includes the determination of principal characteristic of stress tensors. From a regional prospective, the most interesting quantities are three orthogonal

principal stress directions (azimuth and tilt) that are the axis of stress ellipsoid.

Angelier (1979) proposed a method to determine the position of principal stress axis of paleo-stress and to assign a numerical accurate value to bishop ratio, using some algoritm.

The basic hypothesis of Angelier method follow the Bott(1959) hypothesis that is : during a tectonical event the movement along a fault happens in parallel direction to the maximum shear stress direction generated from a common stress field. However, this hypothesis was denied by (Nastro et al,2001) which demonstrate that the movement on the fault change the stress distribution in the volume around and influence the fault surrounding.

In 1978 Angelier and Goguel proposed a technique of direct inversion based on Least square minimization of difference vector ( $p$ ) between shear stress tangential component and the measured lineation. To differentiate  $\sigma_1$  and  $\sigma_3$  must be determined the sense of the reduced stress tensor vector for every fault. Using this method, it's possible identificate paleo-stress principal axis and  $\Phi_B$  ratio relative value.

In 1984 Angelier proposed another method to determine the reduce stress tensor expressing the stress tensor as  $mT + nI$ . Varying the value of m and n the problem of distinction from neo formed fault and reactivated fault is resolved because prescinds from the ratio between fault disposition and principal stress axis. Then in 1990 Angelier (1990a) eliminate the iterative method for a simple calculation sequence. In Angelier(2002) he explains how applicate the direct inversion method without a priori choice of nodal plans, introducing the slip component due to shear stress (SSSC-slip shear stress component) that is the stress component actin on a fault in the slip direction(Fig. 20).

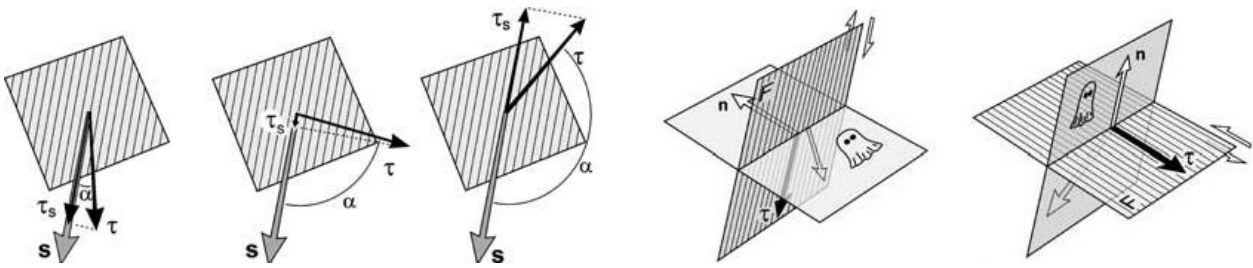


Figure 20.21 – Variation of SSSC value as function of the slip-shear angle & the ambiguity of the double couple focal mechanism..

Angelier's method allows to determine stress state that better accounts for a dataset of double couple focal mechanism of that earthquake.

The purpose of the method is to determine principal axis assuming that every faults population observed is due to a single tectonic event. This method doesn't need of a choice between nodal planes. This means that exist only one regional stress tensor.

In general, to know the state of stress we need of some parameters to deduce the mean stress tensor that induces on any planes the same direction and shear stress sense. Is not possible earn information as fracture parameters and friction, pressure state and depth of overburden because they cannot be consider uniform within the dataset because depend from other factors that are not the same for all the earthquake as shape of fault surface, fluid condition and mechanical and permeability proprieties.

So we can consider a reduce stress tensor (Angelier et al.1982) finding four independent variables  $(\sigma_1, \sigma_2, \sigma_3, \Phi_B)$ .

In a conjugate system of fault, faults plane orientations are determined by principal axis because the tectonic event induces not only the faults formation but also the movement along them. Slinkesides are the only way to reconstruct principal axis of the stress. In this method is assumed also that the faults planes distribution and stresses are independent. Following Carey and Brunier(1974) and Bott(1959) the last assumption is that movement along every fault is

independent and is in the shear direction governed by a single common mean deviatoric stress.

In tectonics and seismology, the spherical space around a fault can be divided into four dihedrals separated by the F fault plane and an A auxiliary plane perpendicular to S striae.

We can consider a fault, with a moment along the slip vector  $\mathbf{s}$  due to an applied stress  $\sigma$ . If the rock would be free to move in any direction of the rock mass, it would move in the direction of the shear stress  $\tau$ , but in the case of two blocks of rock, slip occurs in the direction of the slip vector. So we may consider the shear stress slip component, that is the component of the stress acting in the slip direction  $\tau_s$  that is the scalar product of  $\tau$  by the unit slip vector  $s$ , and also the scalar product of  $\sigma$  by  $\mathbf{s}$ . It's orthogonal to the shear stress projection  $\tau$  of the slip vector  $s$  and it's the orthogonal projection on  $s$  of the applied stress vector  $\sigma$ .

Now we consider the case of double couple focal mechanism of earthquake.

So given two perpendicular nodal planes, for each plane the potential slip plan is parallel to the normal of the other plane. Considering two perpendicular normal vectors  $n_1$  and  $n_2$  describing two nodal plane  $F_1$  and  $F_2$ , relative of a double couple mechanisms. They are the direction cosines of the normal to one of the nodal planes in the system of the principal axes. Angelier (1984) demonstrated that

$$n_1 n_2 n_3 \Phi(1 - \Phi) = 0 \quad \text{xx}$$

where  $\Phi$  is the ratio between the principal stress

$$\Phi = \frac{\sigma_2 - \sigma_3}{\sigma_1 - \sigma_3}$$

The equation xx shows that except in particular cases a stress tensor doesn't simultaneously explain two possible fault movements of an earthquake.

If  $T$  is the stress tensor,  $Tn_i$  is the stress vector exerted on the  $i$ -th nodal plan and  $\tau_{s_i}$  is the projection of  $\sigma$  on the potential parallel slip vector  $s_i$ , and its tangential component.

So we can deduce that  $\tau_{s_1} = T \cdot n_1 \cdot s_1$  and  $\tau_{s_2} = T \cdot n_2 \cdot s_2$

If the slip occurs on F1 nodal plane, the slip vector  $s_1$  is perpendicular to F2 so  $s_2$  and  $n_1$  are equal. Consequently  $\tau_{s_1} = T \cdot n_1 \cdot n_2$  and  $\tau_{s_2} = T \cdot n_2 \cdot n_1$ , and, for the product distributive propriety these two equations are equal. This shows that given one stress state and a double couple focal mechanism, exists one unique value  $\tau_s$  independently to the nodal plane acting as fault.

This value can be determined from simple consideration of the stress tensor T and from  $n_1$  and  $n_2$  unitary vectors that describe focal mechanism. So, the determination of slip component of the shear stress ( $\tau_s$ ) not requires the choice between two nodal planes. Note also that only one of the two nodal planes is the actual fault.

Let T be the average stress tensor solution, since direction and sense of shear stress not depend on pressure and a scale factor,  $kT + lI$  is also solution of the problem because it induces the same direction and sense of shear stress on any plane.  $k$  is a positive scale factor which modifies the magnitude of all stress components in the same proportion;  $I$  is an isotropic stress formed by  $I$  that is the unit matrix and  $l$  that is a pressure which not influence the shear stress. But also these two parameters cannot be determine without additional information as rupture, friction parameters and others, we may consider a reduced stress tensor with four unknown instead of six. Three control the orientation of the principal stress axes, the last one is a function of the ratio between principal stresses. These parameters are important to know type and orientation of the state of stress. In this case we use the stress tensor with separation between the components related to the orientations of the three principal axes and those related to the principal stress magnitude:  $\sigma_1 \geq \sigma_2 \geq \sigma_3$

$$(T_{11} \ T_{21} \ T_{31} \ T_{12} \ T_{22} \ T_{32} \ T_{13} \ T_{23} \ T_{33}) \\ = (x_1 \ x_2 \ x_3 \ y_1 \ y_2 \ y_3 \ z_1 \ z_2 \ z_3) \cdot (\sigma_1 \ 0 \ 0 \ 0 \ \sigma_2 \ 0 \ 0 \ 0 \ \sigma_3) \cdot (x_1 \ y_1 \ z_1 \ x_2 \ y_2 \ z_2 \ x_3 \ y_3 \ z_3)$$

On the right-hand side the first component is the rotation matrix and the last is the corresponding inverse matrix. They contain nine direction cosines that describe the orientation of principal stress axis in the reference frame that is constituted by x-axis in the east direction, the y-axis in the north and z-axis upward. The central term contains the principal stress values. This cannot be determined

with the sole directions and senses of shear stresses. So the central term can be simplified as a function of a single variable. One possibility consists of adopting an expression that contains a single unknown  $\psi$  (Angelier 1990)

$$(\sigma_1 \ 0 \ 0 \ 0 \ \sigma_2 \ 0 \ 0 \ 0 \ \sigma_3) = (\cos\psi \ 0 \ 0 \ 0 \ \cos(\psi + \frac{2}{3}\pi) \ 0 \ 0 \ 0 \ (\psi + \frac{4}{3}\pi))$$

In the reference frame we have also  $n_x, n_y, n_z$  that define the unit vector  $\mathbf{n}$ , normal to the nodal plane. These direction cosines are calculated as functions of two angles,  $d$ , the dip direction of the plane, and the fault dip  $p$

$$\begin{aligned}n_x &= \sin d \sin p \\n_x &= \cos d \sin p \\n_x &= \cos p\end{aligned}$$

Given the stress tensor  $\mathbf{T}$ , the stress vector acting on the plane  $\sigma$  is obtained as the product  $\mathbf{T}\mathbf{n}$  and the coordinates of  $\sigma$  are given by

$$(\sigma_x \ \sigma_y \ \sigma_z) = (T_{11} \ T_{21} \ T_{31} \ T_{12} \ T_{22} \ T_{32} \ T_{13} \ T_{23} \ T_{33}) \cdot (n_x \ n_y \ n_z) \quad xxx$$

The slip vector  $s$  from the direction cosines  $s_x, s_y, s_z$ . They depend on dip direction, fault dip and pitch of the slip vector

$$\begin{aligned}s_x &= \cos d \cos i - \sin d \cos p \sin i \\s_y &= -\sin d \cos i - \cos d \cos p \sin i \\s_z &= \sin p \sin i\end{aligned}$$

Because the SSSC vector is the orthogonal projection of  $\tau$  and  $\sigma$  on the unit vector  $\mathbf{s}$ , we may obtain it also as the scalar product  $\sigma \cdot s$

$$\tau_s = s_x \sigma_x + s_y \sigma_y + s_z \sigma_z \quad (xx)$$

Combining the equation xxx and xx, one obtains  $\tau_s$  as a function of the stress tensor components

$$\tau_s = n_x s_x T_{11} + n_y s_y T_{22} + n_z s_z T_{33} + (n_x s_y + n_y s_x) T_{12} + (n_y s_z + n_z s_y) T_{23} + (n_z s_x + n_x s_z) T_{31}$$

Another important parameter is the angle between the observed slip direction and the calculated shear stress. We call its shear-slip angle,  $\alpha$ . Minor is the angle, major will be the closeness between the magnitude of  $\tau_s$  and the slip direction. We could consider

$$\tau_s = \tau_i \cos \alpha_i$$

$\cos \alpha_i$  decreases from 1 to -1 as the angle varies from 0 to 180°. The value 1 corresponds to an ideal case in which the fault moves in the same shear stress direction and sense, instead 0 corresponds to perpendicular slip to the shear stress and -1 corresponds to movement in the opposite direction.

as  $\alpha$  increase, it is more difficult to account for the observed slip with the calculated shear stress. For angle greater than 90°, the SSSC acts in the opposite sense respect to the slip vector, so the calculated stress cannot explain the observed slip. Adopting this value as a criterion in stress-slip relationships, thus implies that the shear stress should be large enough to induce fault motion along the direction of the slip. This is a different assumption compared with Wallace-Bott hypothesis. Simply consider the shear stress magnitude would be inappropriate, we may consider also that the lower limit of  $\tau_s$  for slip to occur depends on the normal stress and the coefficient of friction through Mohr-coulomb relationships.

Give a set of K mechanisms, the aim is to find the largest value of  $\tau_s$  within the set. The extreme possible value is  $-\tau_{max}$  that correspond to the best fit and  $\tau_{max}$  that correspond to the largest misfit. These are the largest possible shear stress within the stress tensor. The maximum value of  $\tau_s$  must be done for all the mechanisms simultaneously through an analytical determination of the extrema of the sum of the SSSC value, S

$$S = \sum_{k=1}^{k=K} \tau_{sk}$$

With K is the number of data points. S ranges from  $-K\tau_{max}$  to  $K\tau_{max}$ .

To find the largest sum, this determination is followed by the selection of the algebraically largest extremum among few solutions. To perform the inversion in a least-square sense is possible use  $S'$

$$S' = \sum_{k=1}^{K=K} (\tau_{max} - \tau_s)^2$$

$(\tau_{max} - \tau_s)^2$  range from 0 (best possible fit) to  $4\tau_{max}^2$  (largest possible misfit) so

$S'$  range from 0 to  $4K\tau_{max}^2$ .

### 3.5.2 Graphical Approach – RDM

To reconstruct paleo-stress are generally applicate methods either using fault analysis, either focal mechanism analysis. The last one in the case of superficial earthquakes are connected with stress field that acts in that area. So they may be used with the same criterion as fault (Angelier and Mechler, 1977). The difference between focal mechanisms and faults is that the first one give two plans with slip vector related, but non the information on which of two plans represent the fault and which is the auxiliary plane. Determined which plan is the auxiliary plane is important because the slip vector related to the auxiliary plane is inconsistent if the stress state that generated the earthquake is triaxial type ( $\sigma_1 > \sigma_2 > \sigma_3 \neq 0$ ) (Carey-Gailhardis, Mercier, 1987).

For this reason, in the past, focal mechanisms were used only in graphical methods as the Right Diedra Method (Pegoraro, 1972; Angelier and Mechler, 1977) or Right Trihedra Method (Ramsay and Lisle, 2000).

The Dihedra method is based on the idea that  $\vec{s}_1$  and  $\vec{s}_3$  must belong to the dihedra limited by the fault plane and the auxiliary plane that contain respectively the P and T axis. The method proposes of superimpose these dihedral for all fault and slip data so we could find the location of the eventual common principal stress axis. This concept can be applied to earthquake focal mechanism with the advantage that it does not require to distinguish fault from auxiliary planes only assume that the slip direction is parallel to the resolved shear stress direction (Angelier and Mecheler, 1977; McKenzie, 1969). It's assumed that two dihedrals correspond to the domain with uniformly

probability to find P axis of compression and the other two dihedrals correspond to the domain with uniformly probability to find T axis of distension. So Angelier & Mechler 1977 proposed a graphic method to find the common areas in extension and the common areas in compression.

Practically: let N1 be the principal axis of mean stress  $\sigma_1$ , and N3 be the principal axis of mean stress  $\sigma_3$ . If every faults moving independently subdue at the same principal stress, N1 should be in the common part of all compressional dihedra, and N3 should be in the common part of the distensional dihedral.

The Right Dihedra Method is based on the principle that given a focal mechanism with an auxiliary plane perpendicular to a slip plane, the intersection of planes identifies two straight dihedral in compression and other two straight dihedral in extension, based on the movement on the fault (Angelier and Mechler, 1977). Two conditions are necessary to apply this method: all the fault should be created in the same tectonic event during which the medium stress state is constant and that the slip vector should be parallel to the maximum shear stress that acted on the fault plane. In these cases, in one of dihedral in compression there will be the  $\sigma_1$  axis and in the other one the  $\sigma_3$  axis (Bott, 1959).

Following this idea, overlaying beach balls it will identify common area to all compressional dihedral, in one of which there will be  $\sigma_1$  and in the common area to all extensional dihedral  $\sigma_3$ . This method is very useful with focal mechanism because it does not require the identification of the real fault plane but the determination of principal stresses position is probabilistic. RDM permits the identification of an interval in which the probability to find the principal stresses is higher so, more are the data, bigger is the probability to find restricted probability. This method doesn't give precisely the value of  $\Phi_B$  but just an approximation from the probability area.

$\Phi_B$  ratio may vary in the interval  $0 > \Phi_B > 1$ . It will be near 0 when, for example the probability area of  $\sigma_1$  is restricted and which of  $\sigma_3$  is large. In this case  $\sigma_1$  is well determined, while  $\sigma_3$  is poorly determined.  $\Phi_B$  ratio is near 1 in the opposite case. However the best solution is  $\Phi_B = 0.5$

that means very restricted area either for  $\sigma_1$  and  $\sigma_3$  (Angelier and Mecler, 1977).

In 1984 Gaudiosi and Iannaccone performed a preliminary analysis of 15 focal mechanisms of events recorded at CFc during April–December 1983 without using a stress inversion procedure. They sustained that no regional component of the stress dominate the stress field in the Campi Flegrei area linking the observed seismicity to the stress field due to a magmatic processes acting in the Pozzuoli area.

Zuppetta and Sava (1991) applying an analytical stress inversion procedure to 49 focal mechanism retrieved a stress field dominated by a sub-vertical  $\sigma_1$  and a NNE-SSW trending sub-horizontal  $\sigma_3$ .

### 3.5.2.1 RDM modified (D'Auria et al., 2014)

In this work has been used a new formulation of the classical RDM method proposed by D'Auria et al., (2014). This method is based on the analysis of normalized moment tensors of the events in the data set.

The RDM function is defined as:

$$RDM(\theta, \phi) = \frac{1}{N} \sum_k sgn[\hat{x}_k(\theta, \phi) M_k \hat{x}_k^T(\theta, \phi)]$$

Where  $(\theta, \phi)$  are the polar coordinates on the focal sphere,  $M_k$  is the normalized moment tensor for the event k,  $\hat{x}_k(\theta, \phi)$  is the position vector of the point on the focal sphere, and N is the number of events.

The function varies between -1 and 1. -1 is the high probabilities of representing the actual  $\sigma_3$  And 1 is the high probabilities to representing  $\sigma_1$  (D'Auria et al., 2014);

In the plot that shown results of RDM modified function, the blue shades indicate the probabilities of finding  $\sigma_3$ , the red shades instead, indicate the probabilities for  $\sigma_1$ .

To investigate the temporal evolution of the stress pattern in CFc, the focal mechanisms has been

divided into 10 interval (A-J, see table 1). In particular:

- the interval C\* is a subset of the interval B and contains the event with the high magnitude recorded during the bradyseismic crisis of 1982–1984 ( $M = 4.2$ ).
- The interval G contain an important swarm recorded in 1984-04-01 at 01:04 to 04:43 and is constituted by 39 events
- J is the entire dataset, contain all of the 222 events analysed and is performed to underline the stress field acting in the study area.

Time Intervals	Start	End	Normal	Thrust	Trascurrent	Total
A	1983-01-17 15:24	1983-08-22 07:31	4 (57%)	2 (28%)	1 (15%)	7
B	1983-09-01 23:04	1983-10-29 23:30	10 (42%)	8 (33%)	6 (25%)	24
C*	1983-10-04 08:09	1983-10-29 23:30	9 (52%)*	4 (24%)*	4 (24%)*	17*
D	1983-11-03 23:43	1983-12-30 23:19	9 (64%)	4 (29%)	1 (7%)	14
E	1984-01-11 05:13	1984-03-19 23:52	10 (38%)	5 (19%)	11 (43%)	26
F	1984-03-20 09:11	1984-03-26 20:53	12 (37%)	9 (28%)	11 (35%)	32
G	1984-04-01 01:04	1984-04-01 04:43	23 (59%)	3 (8%)	13 (33%)	39
H	1984-04-03 16:34	1984-04-27 15:10	25 (50%)	11 (22%)	14 (28%)	50
I	1984-05-05 14:43	1984-12-08 22:33	11 (37%)	10 (33%)	9 (30%)	30
J	1983-01-17 15:24	1984-12-08 22:33	104 (47%)	52 (23%)	66 (30%)	222

Table 1 – The dataset has been divided in temporal interval.

The result of RDM method on the focal mechanism dataset, using the time interval of Table 1 are shown in the Figure (22). In particular, results of interval J, that is the entire dataset are represented

in the window 7J and shows a well-defined  $\sigma_1$  attitude that appears sub-vertical, and a less defined  $\sigma_3$  roughly sub-horizontal and trending NNE–SSW. The other intervals show a general agreement with the global pattern indicating a substantial stability in the stress pattern during the whole period.

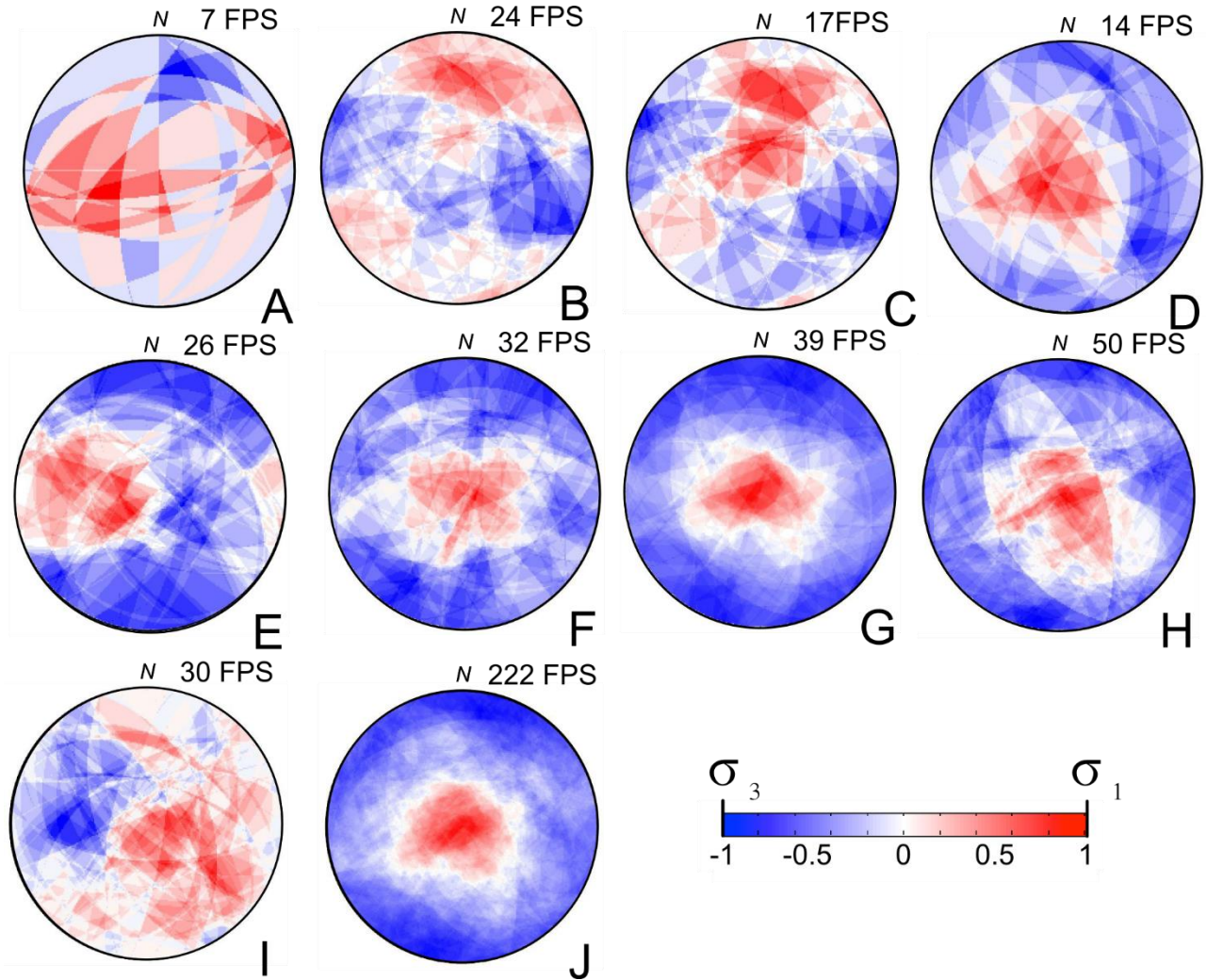


Figure 22- Results of the RDM. Blue shades indicate high probability of containing  $\sigma_3$ . Red Shades indicate high probability of containing  $\sigma_1$ .

### 3.5.3 Graphical Approach – MIM

One of the numerical technique using for separating stresses from heterogeneous fault slip data is the multiple inverse method (Yamji, 2000b). The basic idea of the method is applying a technique of artificial intelligence, named Hough transform, to detect object with arbitrary shapes and orientations. In our case, are stress ellipsoids with different shapes and different orientations.

The method refers to Fry(1999) that shows how is possible represent heterogeneity by a sort of cluster in six-dimensional parameter space. Possible stresses are identified by clusters on stereonets and the density of each cluster represents the reliability of each stress. The multiple inversion method is based on the classic inverse technique by Angelier(1984).

The inversion method is based on the hypothesis that the fault slips in the direction of shear stress acting on a fault plane (Angelier 1979, 1984). Suppose that  $\sigma$  is the stress under which all the faults slipped.  $n^\alpha$  is the unit vector normal to the  $\alpha$ -th fault. The vector points into the hanging wall block, so the stress vector acting on the block is  $t^\alpha = \sigma^T n^\alpha$  and subtracting normal stress, the shear traction  $s^\alpha$  is obtained by  $s^\alpha = \sigma n^\alpha - [(n^\alpha)^T \sigma n^\alpha] n^\alpha$ .

Generally, the slip relaxes the traction acting on the fault plane, therefore the slip direction of the  $\alpha$ -th fault is expected to be  $-s^\alpha$ . Because  $\sigma$  is unknown, the theoretical slip direction  $-s^\alpha$  could not coincide with the observed one, so we can use the angle between them  $\Delta^\alpha$  and determine the stress tensor minimizing the sum of the angular misfit

$$S = \sum_{\alpha=1}^N \Delta^\alpha \quad \alpha = 1, 2, \dots, N$$

The method determines also  $\mu_L$ , named the Lode number and it's the shape of the stress ellipsoid.

$$\mu_L = \frac{2\sigma_2 - \sigma_1 - \sigma_3}{\sigma_1 - \sigma_3}$$

$\sigma_1, \sigma_2, \sigma_3$  are the principal stresses and for  $\sigma_1 \geq \sigma_2 \geq \sigma_3, -1 \leq \mu_L \leq 1$  where -1 indicates compression, instead 1 indicates tension. Note that  $\mu_L$  is related to the bishop parameter  $\phi$  as  $\mu_L = 2\phi - 1$ .

The method is based on the cluster analysis with the aim of divide a set of faults into subsets corresponding to stresses that activate the subsets without a priori knowledge of the number of stress fields are into the dataset. There are two steps that the method follows. The method firstly constructs  $k$ -element subsets from the entire fault-slip data. So given  $N$  faults, we have  ${}_N C_k$  susubsets

$${}_N C_k = \frac{N!}{k! (N-k)!}$$

The choice of  $k$  is arbitrary. Need to keep in mind that  $k$  values too small may be provide uncertain solution and that using too high values, increase the computational time.  $K$  vary from 2 to 7. If  $k=2$  there are no identifiable cluster, so the best solution is for  $k=4$  or  $k=5$  because starting from this value the general attitude of data seems to converge on the same solution.

Secondly, using a classic inverse method for each subset, it's possible determined the optimal stress. So, the great circles are fitted to the subsets and significant stresses make clusters, visualized by stereograms. The poles of the great circles that represent the optimal stresses for the subsets are plotted on the unit sphere. The density of the clusters designates the statistical significance of the stresses represented by the clusters. Then, to detect the clusters, the optimal stresses are mapped onto a stereogram with the stress ratio of the optimal stresses depicted by colours.

### 1.5.3.1 MIM software & Results

Mim60 and Mi Viewer, are the main- and post-processors to application of Multi-invers method

(Otsubo et al., 2008). Given a geological and seismological data set, the main-processor calculate the coherent stress with data reading data files in a certain format giving in output .txt file; this processor may read two data type: geological data of fault slip and seismological data of focal mechanisms. To read this data, both of them have to stay in a .txt file with .fdt extension. For fault data, date should be in a certain sequence as azimuth of fault plane dip, fault plane dip angle, slip dip direction, slip dip angle and sense of movement. The sense of movement is indicated as N=normal, R=Reverse, D=Right, S=left.

In the case of focal mechanism data should be write in the form: fault plane dip direction, fault plane dip angle, slip dip direction, slip dip angle, sense of movement. MiM software contains also a program to convert data in FDT format needed to use the main program.

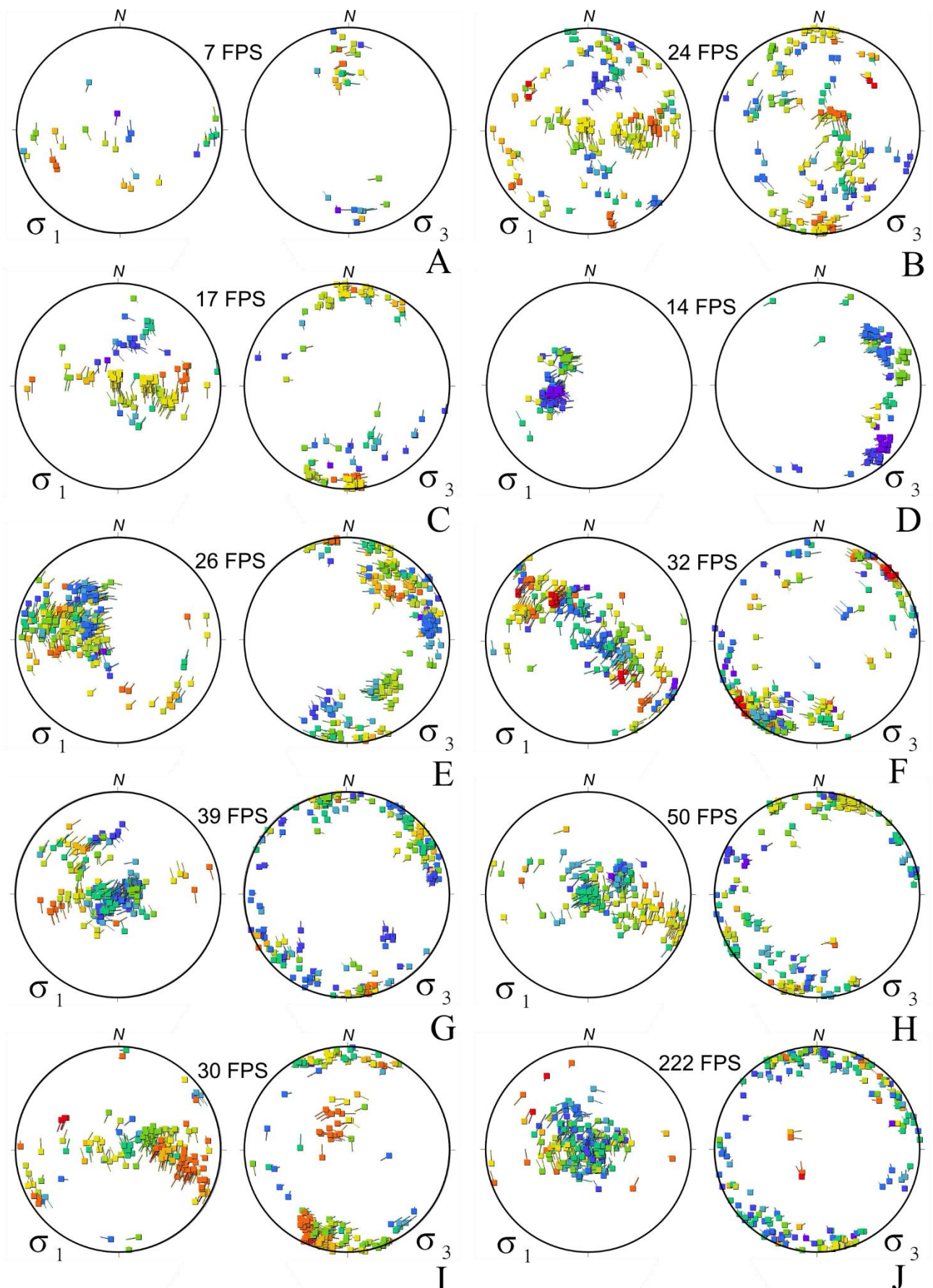
It's possible choice to input data relative to faults or focal mechanism and indicate the number of k-element subsets that for focal mechanism is just 4 or 5. Yamaji et al. (2004) suggest to use 5 just in case of dataset with more than 100 data.

the post-processor permits the visualization of stresses, using the .txt file from the output of the main processor. It contains also various function that permit data and stress analysis. The stress tensor inversion method uses data relative to fault plane and slip direction of the roof block (of the fault) to determine and reconstruct the stress field. Data are visualized on stereogram on which are shown stresses took from multi-inverse method. Stereograms uses equal-area projection on inferior hemisphere. Each symbol has a head that indicate the analysed stress position and a tale, that indicate the plunge of the second principal stress. Orientation of stress more probably for the analysed dataset are represented as cluster with the same colour of symbols. The colour represents the value of Bishop ratio  $\Phi$ . Generally,  $\Phi$  vary in the interval  $0 > \Phi > 1$ . For  $\Phi = 0$   $\sigma_1 > \sigma_2 = \sigma_3$ ;  $\Phi = 1$  represent  $\sigma_1 = \sigma_2 > \sigma_3$ . The program gives 11 colours with interval of 0.1 of the value assumed from the Bishop ratio.  $\Phi = 0.0$  is indicated with purple,  $\Phi = 1$  the symbols are in red.

On the left there is the stereogram that contain the symbols that represent the orientation of  $\sigma_1$ , instead on the right stereogram there are the point that represent the  $\sigma_3$  orientation. The software permits also the visualization of certain value of  $\Phi$ .

In fig. (23) has been shown the results of the MIM applied on the intervals of table 1.

On the same way followed for the RDM, in Fig. 23J are show the J interval that comprise the whole dataset. In this case, is present a big cluster of tadpoles representing sub-vertical  $\sigma_1$  attitudes(23J-left-plot), and there isn't presence of a finite cluster that represent  $\sigma_3$ (23J-Right plot) that instead of a big cluster, it show tadpoles located all around the primitive circle. It means a sub-horizontal  $\sigma_3$  with a slight prevalence of NNE-SSW clusters. The colours of tadpoles are representative of the  $\Phi$  value. The prevalence of green-to-blue clusters permit to estimate the Bishop's ratio values between 0 and 0.5. Comparing these results with RDM results, it's possible to find an accordance about the strong heterogeneity of the analysed dataset.



0 plunge 90

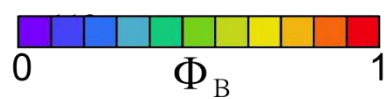


*Figure 23 – Results of the MIM processing of the focal mechanisms of each interval. The left plot indicate the  $\sigma_1$  results, the right plot the  $\sigma_3$  results. Results are represent as clusters of tadpoles and their colours are representative of Bishop' values. The tail of each  $\sigma_1$  tadpole on the left side, pointing towards the corresponding  $\sigma_3$  on the right side, and the length of the tail is inversely proportional to the  $\sigma_3$  plunge.*

Comparing the results between RDM and MIM for every interval, it's possible to notice that

2. The A subset(Fig23 A), that consist in only 7 mechanisms, through the RDM results shows a well-defined sub-horizontal  $\sigma_3$ , plunging toward NNE and a poorly defined  $\sigma_1$  (low plunge toward ENE, medium plunge toward WSW. In the MIM results appear heterogeneous wit a low clustering either for  $\sigma_1$  and  $\sigma_3$ .
3. The B subset (Fig 23 B).For RDM results  $\sigma_1$  plunging towards NNE, subvertical  $\sigma_3$  with trend WNW-ESE. MIM results give high heterogeneity and allow to suppose that exist a possible superposition of different stress fields. The prevailing one have  $\sigma_1$  medium to high plunging toward E and sub-horizontal N-S trending  $\sigma_3$ .  $\Phi = 0.5$
4. The C subset (Fig 23 C). substantially, the results are very similar to the B subset, so have  $\sigma_1$  medium to high plunging toward E and sub-horizontal N-S trending  $\sigma_3$ . Just the  $\Phi$  value results higher than 0.5.
5. The D subset (Fig 23 D). RDM solution shows a well defined high-plunge  $\sigma_1$ , poorly constrained  $\sigma_3$  axis associated to areas extended along a great circle dipping toward ENE. MIM solution is very similar.
6. The E subset (Fig 23 E). RDM result shows good definition of  $\sigma_1$  axis plunging toward WNW.  $\sigma_3$  less defined with blue areas extending along an E dipping great circle, poor prevalence of sub-horizontal N-S trending values. MIM have very similar results, as well.
7. F,G,H subsets (Fig 23 F,G,H). RDM inversion for these subsets give similar results compatible

with a well defined sub-vertical  $\sigma_1$ , a less defined low plunge  $\sigma_3$  trending NNE–SSW. In this case, the MIM results show higher variability of  $\sigma_1$  with a big prevailing cluster compatible to RDM results.

8. The I subset (Fig 23 I). RDM results show well defined  $\sigma_3$  plunging toward west and a less defined  $\sigma_1$  located along a wide E-dipping great circle. MIM results instead show a clear distribution of cluster, prevalence of medium to high E plunging  $\sigma_1$ , sub-horizontal NNE–SSW  $\sigma_3$  and high values of Bishop' ratio for the prevailing cluster.

## Chapter IV- Analysis of ground deformation data & Joint Inversion

### 4.1 Bradysism

Issel(1883) coined the word bradyseism from Greek (bradi=slow; seism=movement), indicating slow subsidence or uplift of the ground.

Orsi et al. (1996), called the same movement as short-term deformation to distinguish them to long-term deformation occurred at the caldera in the past 12 ka.

The Campi Flegrei was always interested by these vertical movements. After the Monte Nuovo eruption in 1538 there was a long subsidence with a rate of 11–14 mm/yr.

Del Gaudio et al. (2010) reconstructed the ground deformation history at Campi flegrei, showed that three major uplift events and several minor uplifts that interrupt the subsidence trend that began after the Monte Nuovo eruption, have occurred in the last century (Fig. 24)

In recent times, three period of unrest in rapid succession occur in the caldera., the first between 1950 and 1952 (73cm), the second between 1969 and the end of 1972(177 cm) and the second from the half of 1982 and December 1984 (179 cm) (Gaeta, 2003; Del Gaudio et al., 2010). Campi Flegrei shows a general quiescence / subsidence and after this major events, were recorded minor episodes of ground uplift and seismicity (Orsi et al., 1999; Troise et al., 2007; Del Gaudio et al., 2010) Ground deformation data show that the second event was follow by a brief subsidence events that permit to recover just a little fraction of inflation, after which the ground level remain constant for 8 years.

The third event instead, was follow by a long phase of subsidence still in progress, at the moment that, the ground deformation produced during 1982–84 it's already recovered.

The behaviour of uplift episodes in the CFC area was interpreted with alternative models referred to mechanical and fluids dynamics.

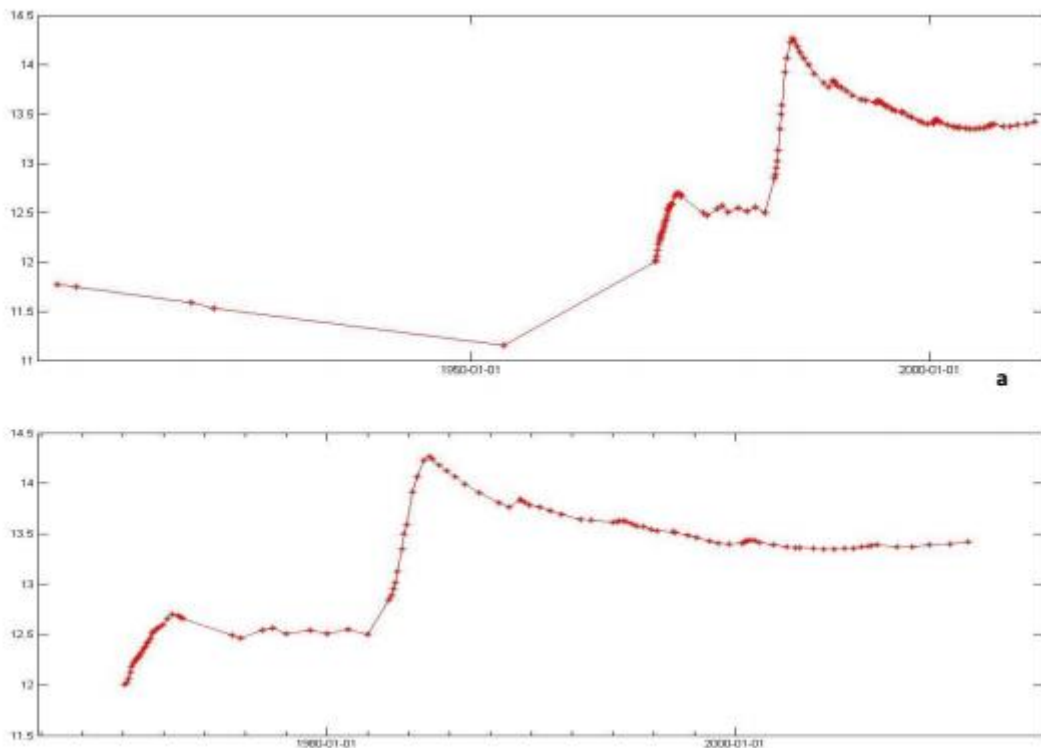


Figure 24 – Vertical deformation data at benchmark "26". On the x - axis in a) there

is time interval 1905 - 2011, in b) exclusion of the the first five points to highlight the ground deformation. So the time interval is 1970 - 2011. On the y - axis there is the value reported in the dataset correspondent of the monthly average for every year.

Mechanisms indicated for these phenomena generally involve pressure generation exerted either from a magma chamber (Bianchi et al., 1987; Dzurisin and Yamashita, 1987; Bonafede et al., 1986) or from hydrothermal reservoirs ( Oliveri del Castillo and Quagliariello, 1969; Casertano et al., 1976; Bonafede, 1991; De Natale et al, 1991; Gaeta et al., 1998) that may played fundamental role in triggering activity.

Mechanical models assume unrest of magmatic chamber and a deep intrusion of magma volume. These models found difficulties when had to satisfy either the measured gravity variation, constrain deriving from observed ground deformation either the hypocentre location of earthquake that accompany the uplift event. Many research considered different rheology, presence of collapse structures modelling as discontinuities stress-strain and dynamic fluid-thermal effects.

Some authors modelled in detail the advent of seismicity and gravity anomalies. Measure evidenced this mini uplifts occurred most of one per decade. Even if the ground is rise every time just for few centimetres, the cumulative effect of these events result in an average rate of uplift of the order of 1 cm/yr.

This rate is enough to compensate almost completely the long term rate of subsidence (Gaeta, 2003). From 1984 there was other minor uplift in June 1989, 1994, 2000 and 2006 (Orsi et al. 1999; Troise et al. 2007). These was accompanied by seismic activity characterized by low magnitude swarm, consisted in about dozen events with hypocentre depth variable from 1 to 3 Km, beneath the Solfatara crater. As the bigger uplifts, the smaller have the same aspect aside the area dimension involved. In fact, the earthquake distribution and the deformation pattern coincide. The aspect of this new phenomenology, are the quick advent of the event and just few years from the end of one

event and the start of the new one, the brief duration of the phenomenon and the complete absence of a permanent residual deformation. After the mini-uplift return to the same rate of subsidence to the value it had before the start of unrest indicates that the thermodynamic state of the system is indistinguishable from that initial (Gaeta, 2003).

An evident anomaly in the area affected to the ground deformation, is an important variation of the temperature rate that increase with the depth. This variation was observed in the Mofete perforations and "San Vito" in which were revealed the existence of a porous solid matrix at that depth, permeated by an aqueous liquid phase. These two sites are inside the area of the caldera. In the Licola's site outside the caldera the temperature increase linearly with the depth. These anomalies cannot be attributed to thermal conductivity. The only possible explanation is the advective heat transport due to the conventions of permeation. The basic model for uplift interpretation involves a change at the base of the aquifer.

De Natale et al.(1991), shows that the uplift and the seismicity are generally linked with either the raising of magma, or intrusion in a shallower magma chamber, either with raising of magmatic body from a deeper camera to a shallower one.

Modelling of pattern and deformation rate before and after the eruption may reveal a lot about the physics of active volcanoes. Many authors proposed that the caldera unrest had to be caused by fluids intrusion or for interaction between hydrothermal system and magmatic intrusion.

In CFC in particular, many similarities of the last bradyseismic crisis with precursors of Monte Nuovo event, seem to bring the idea of increasing of over-pressurization in a shallow magma chamber.

Petrological data suggest a chamber with volume of  $240 \text{ km}^3$  was originally under Campi Flegrei. Diminution of eruption magnitude and progressive migration of activity at the centre of caldera support the idea of reduction and cooling of this reservoir of magma without new alimentation.

Through gravimetric and magnetic measures, it was possible saw the presence of a residual negative anomaly  $10 - mgal$  to 2-3 km of depth linked to a central depress area that have a shape almost circular full of pyroclastics to low density post calderical.

Aeromagnetic measurement shown positive magnetic anomalies due to dense lava bodies linked to a pre-calderic activity.

Absence of magnetic anomalies in coincidence with gravitational anomalies is interpreted as an effect of persistent hydrothermal fluid circulation that may altered magnetic propriety of dense lava. Detailed analysis of movement of three components was done to define the low velocity zone of wave with high ratio  $V_p/V_s$ . observed values are consistent with a layer of not compacted high fractured and saturated of water of low density, less to 3 km of depth .Location of hypocentre indicates a depth minimum of 3.5/4 km in the magmatic chamber and the seismicity principally is located on the border of inflation area. The biggest deformation influences the less dense material feeding the central area and inducing a change in the stress field capable to trigger faulting in the most fragile region norther than there is the concentration of seismic activity. Fumarolic activity is distributed over the entire area either in the sea either on the land. The hottest fumaroles are in the Solfatara crater, but "Fumose" in the Pozzuoli gulf have  $100^\circ C$  of temperature at 15 m of depth. Fluids consist principally in water vapour and carbon dioxide.

High temperature and continuous exchange of heat are consistent with the idea of magmatic source still active at 4-5 km.

Geochemical data are useful because the high mobility of gas may give quickly information on deeper process. Chemical appreciable variation was founding in the hottest fumarole before, during and after the uplift and seismicity associated with episodes of bradysism 1982-1984.

Practically either the history of Campi Flegrei of 10.000 years ago either the geophysics and geochemical evidence of recent crisis indicate that volcanic activity has been progressively restricted to the central part of the caldera and this may be linked to volumetric change of magmatic

chamber submitted to a progressive cooling. Residual magmatic chamber, which top not should be less to 4 km of depth and should submit a central-type basin filled with volcanic deposits of low density.

This area is characterizing by low seismicity velocity, maximum inflation and deflation during recent crisis and major concentration of hydrothermal manifestation of hottest fumarole.

#### 4.1.1 Similarity between 1970–1972 and 1982–1984

Recent episodes of uplift into CFC, shown great similarity as the shape of ground deformation that is practically identical for both of episodes.

Rheology of rocks for applicate stress on periods of long time isn't purely elastic and follow a certain pattern that may be approximated to viscoelastic model. the viscoelastic relaxation time ( $\tau$ ) is the parameter that controls the temporal scale of stress application for which the rheology deviates from the purely elastic model:  $\tau = (3K + \mu)\eta/3K$

Where  $\eta$  is viscosity,  $\mu$  is rigidity, K is bulk modulus. For  $t \ll \tau$  the behaviour is not elastic.

In the continental zone, viscoelastic parameters are on the order of  $10^{-3} - 10^{-4}$  years with viscosity values of  $10^{21}$  Pa/s.

In the caldera, where there are high temperature and fracture in depth, viscosity may reach lower values and so lower relaxation time.

Valuation of shallower rock viscosity at CFC is useful because if the stress is applicate for longer period respect to the relaxation time, the medium flows as a viscous fluid and may deform also with low levels of stress and the consequent deformation remain constant when the stress return to 0 so it's impossible elastic recovery.

Temporal variation of maximum deformation in CFC allows an estimation of lower limit of viscosity.

In fact, while the constant rate of uplift in the period 1982–1984 may be simulated by infinite stress–viscosity combination, the strong subsidence observed from 1984 implicated that a substantial elastic recovery operates actually after 2 years of stress application.

Depth of magma reservoir at CFC may be estimate from vertical profile of temperature done from Agip (1987) that a 2 km north from Pozzuoli have proceeds temperature higher of 420°C at 3Km depth.

Relative depth of seismicity during 1982–1984 is of 3.5 Km. This suggest the lower limit downward and, in the central part of the caldera, rocks don't have a fragile behaviour under stress, probably due to plasticity for high temperature that are close to the fusion point. At shallower depth there are no evidence of body of low rigidity that may be seen from local seismicity or from travel times anomalies or from loss of S waves.

Ferrucci et al. (1990) through seismic activity found evidences of strong phase of converted P-SV, generated by an interface that, according with delay time respect direct P waves, may be locate to 3–4 Km of depth that could be relative to the interface liquid–solid indicating the top of magmatic chamber.

Hydrological data (Agip,1987) shown that CF are supplied of meteoric water either from regional source(Apennines) , either by local source located in the north part of the caldera. The two aquifer resulting are partially linked and partially separated by an impermeable horizon, while the marine water flux is limited of the coast area. Chemical and isotopic characteristics indicate that this thermal water drift from mixage, in variable proportion between three components (meteoric water, marine brine and deep geothermal).

Binary mix of sea water and meteoric, dominate the hot springs west of Cf, along tirrenian cast while the geothermic component seems locate in the central part of the caldera. Chemical and isotopic results indicate that this component may derivate from heated marine ancient water

(>40yr), modified by chemical change with volcanic host rock and diluted by meteoric water during the rising.

#### 4.6 “1982 – 84” Bradyseismic Crisis

In mid 1982 it was recorded in Campi Flegrei an uplift with a maximum displacement of 179 cm and an average rate of 1.44 mm/days and it lasted up 1984. The mechanism of this, like other, bradyseismic event has been debated. The source of this episodes could be magmatic or not magmatic or a combination of both. Casertano et al. (1977) proposed a non magmatic cause suggesting that the pressure source was a shallow aquifer expanding for increasing heat flow from a magma body. Instead many interpretative models which assume a magmatic process as responsible for the unrest episode, were proposed. Berrino et al. (1984), on the basis of vertical ground deformation and gravimetric anomalies data, concluded that this specific crisis was triggered by magma intrusion into a chamber located at 3km depth, but this conflicts with the distribution of earthquakes which are located until 4km depth (Orsi et al., 1999). Ferrucci et al. (1992) identified a body with a strong anomaly propagation of seismic waves velocity at 4 km depth and deep drilling did not found evidence of magma up to 3 km (Agip, 1987). Then Dvorak and Berrino (1991), explain altimetric and EDM data by a pressure source consisting of a planar sheet located about 100 m E of Pozzuoli at 3km depth and this sheet could represent the top of a magmatic body. After 1985 there was a subsidence period where about 30% of 179 cm of uplift has been recovered. The amount of apparent non – reversible strain suggests that a significant part of the ground displacement was due to creep – like phenomena. Orsi et al. (1996) concluded that there is a block resurgence occurred through a simple shearing mechanism which has disjointed the caldera floor in blocks with differential vertical movements. The bay of Pozzuoli is the side of the

resurgent block under compressional stress regime in which no eruption vents have been active. Di Vito et al. (1999) suggest that the zone of high seismicity during the seismic sequence is practically coincident with the “La starza” structure.

Orsi et al. (1999) concluded also that the long-term deformation results from the sum of many short - term deformation events. An interesting characteristic of the bradyseismic events is that the uplift is always accompanied by seismicity that instead is often absent during the subsidence. Through seismicity and ground movement has been demonstrated that the area involved in the deformation has a rectangular shape. Most recently Gottsmann et al. (2006) suggested the existence of multiple causative sources, clustered in two groups, located at different depths. Furthermore, D'Auria et al. (2011) have shown, that the geothermal reservoir consists of at least two parts, located at different depth, evidencing a correlation between long - period seismicity observed during the recent years and fluid transfer episodes from the deep to the shallow part.

DeSiena et al.(2010), together with information from active and passive velocity tomography, shown a possible small melt volume just below the maximum uplift area of the 1983–1985 bradyseismic crisis.

Despite tomography studies did not show clear evidence of extending melting zones, magma intrusions and migration of fluids with an increase in pressure into the hydrothermal reservoir have been considered as a possible source of the ground deformation in the area( Bonafede and Mazzanti, 1998; Gaeta et al., 1998; Gottsman et al., 2006; Battaglia et al., 2006).

#### 4.6.1 Other episods of unrest

Since 1985, the area was interested by general subsidence still in act, with exception of short-duration uplift, in 1989, 1994 and 2000, 2004–2006.

The uplift occurred in July 2–7 and August 22, 2000 was accompanied by 2 swarms at Campi Flegrei with 4 cm of net uplift at Pozzuoli harbour, and by significant increase in the  $H_2O/CO_2$  ratio observed at solfatara fumaroles (Saccorotti 2001). For the first time was observed long period events. Also in this case, the swarms are explained as the interaction of a single-or multi-phase fluid with the surrounding rocks. Fluid-filled cavity is the interpretation for the source process for this swarm. The waveforms of July are interpreted as the resonance of an acoustic wave trapped at the rock-fluid interface of a fluid-filled, buried cavity (Chouet, 1996). Signals of August are typical of brittle shear failure with many similarities with the events recorded during 1982–1984 seismic crisis. Their mechanism are related to a normal fault trending NE–SW, radially oriented with respect the zone of maximum uplift (Saccorotti, 2001).

Orsi et al., (1999) instead interpret the dynamics of CF as a block resurgence along pre-existing NW–SE discontinuities associated with the inward dipping ring fault bordering the inner caldera. Chiodini et al. (2000) show that at the solfatara crater the NW–SE striking faults are overlapped by a system of fractures oriented NE–SW. this pattern is due to fluid overpressure which induce fracturing orthogonal to pre-existing, fluid filled discontinuities.

The August swarm may be interpreted as slow ground uplift that occurred aseismically along the NW–SE discontinuities as a consequence of the high pore pressure of the fluids in the area (Saccorotti, 2001) and the fluid migration plus the heating of the system with stress readjustment (Saccorotti 2001). The movement of fluids may be cause of increase of pore pressure inside the NE–SW fractures, decreasing the normal stress acting the fault surface, triggering the normal slip observed during the swarm.

From 2004 to 2006 a positive ground deformation occurred at CFC accompanied by three swarms in October 2005, October 2006 and December 2006. The location of the events of the first two swarms is beneath the Solfatara volcano with depth from 0.5 to 4 Km while the December 2006

swarms is located 2 km to the north, at depths of 0–2 Km beneath the Astroni crater. The October 2006 swarm was also accompanied by LP events for about 1 week. The level reaching in this episode is of 4 cm by the end of October 2006 (Troise et al., 2007).

Was detected about 300 micro-earthquakes, with spectral features that are indicative of a source process involving brittle shear failure and are classified as volcano-tectonic earthquakes. They were accompanied by several hundred of LP events characterized by lack of clear S-wave arrival and monochromatic low frequency spectra that suggests that these signals are generated by a resonance process. The LP events show also a marked waveform similarity persisting that indicates the involvement of a non-destructive source process (Saccorotti, 2007). Taken together, these observations suggest that their generating process may be the harmonic oscillation of a fluid-filled reservoir repeatedly triggered by time-localized pressure steps (Crosson and Bame, 1985; Chouet, 1988, 1996; Fujita et al. 1995; Jousset et al., 2003, Neuberg et al. 2000).

Saccorotti, 2007 interpreted the 2004–2006 unrest as due to overpressure within a cavity located at a depth of 3–4 km or more and containing fluids of magmatic origin as volatiles and brines accumulating at the top of a degassing magma chamber. The overpressure may be explained as the arrival of a new gas-rich magma from a deep source. This pressurization of the reservoir induces brittle-failure in the overlying rigid layer that is an explanation for the VT earthquake recorded. Lanari et al., (2004) hypothesized a change of source geometry between 1993–1999 subsidence phase and the 2000 uplift.

Gottsmann et al (2006c) suggested the existence of multiple sources for the recent deformation with two clusters of sources, which are located at the centre of the caldera at two different depths.

Manconi et al. (2010) shows a change with time of the position of a single point source in the interval 1992–2008.

In accord with D'Auria et al., (2011), the source of ground deformation have a spatial and temporal complexity. They shown two parts of a geothermal reservoir located at different depth, evidencing

a correlation between long period seismicity, observed during recent years, and episodes characterized by fluid transfer from deep to shallower part.

D'Auria et al. (2012), performing a tomographic inversion of DInSAR data for the 1995–2007 time interval showing that for the period 1995–1999 the main source of subsidence is located below Solfatara area at 2 Km of depth. Results of this inversion could be summarized as:

- 1998 appears a positive strain volume at 3.5 km of depth interpreted as injection of a hot fluid package that in the following period expands, while the eastern part of the volume contracts.
- In 2000 the western volume contracts, maybe due to lateral advection and diffusion process. More, appears a positive model connecting the north-eastern edge of the model, at depth with the center of the caldera at the surface, maybe due to fluid migration related to a LP swarm recorded in July 2000 (Bianco et al., 2004; D'Auria et al., 2011). An increase in CO<sub>2</sub> emissions and an enlargement of the diffuse degassing area was observed around solfatara in the same period (Chiodini et al., 2010, 2011).
- 2006, appearance of an expanding volume in the southern part of the domain, maybe another fluid injection but with a rapid expansion and upward propagation of two cylindrical protusions. This protusion coincide with two volumes identified by seismic tomography as high Vp/Vs low Qp and low Qs bodies (De Lorenzo e tal., 2001; Vanorio et al., 2005; Battaglia et al, 2008; De Siena et al., 2010).

It's possible that happened a change of permeability value under Solfatara with an increasing after 2000 that making easier the rise of the fluid package in 2006.

#### 4.7 Leveling dataset & Analysis

One of the way to monitored the ground deformation are periodic measurements along a leveling network(Fig. 25). Leveling is a set of operating procedures by which is measured the height difference between two points, as for example the difference in height between pairs of points on the Earth's surface. There are numerous methods of leveling; in particular geometric leveling is used to determine the differences in height by means of the difference between two measurements made on a graduated bar. Geometric leveling is classified in:

- Technical
- Precision leveling
- High precision leveling

Data leveling that has been used in this study are measured using the method of leveling precision performed by the Osservatorio Vesuviano.

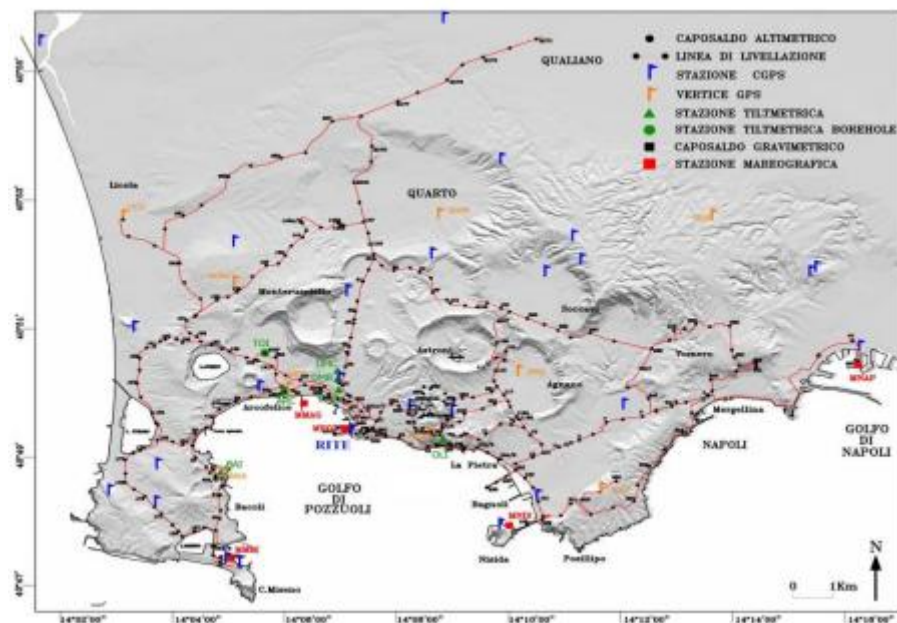


Figure 25 - Geodetic surveillance networks at Campi Flegrei ( C.del Gaudio, Quaderno di Geofisica, 103, 2012).

The Istituto Geografico Militare and Ministero dei Lavori pubblici, before 1975 administrates the reference leveling network; then it was carried out by the Osservatorio Vesuviano which established

a new leveling network, including 30 benchmarks preexisting, and implementing the network until the 370 benchmarks spaced out of 400 m, with a total length of 140 km with 15 loops, at present [Figure 8]. A loop is a configuration that permits to minimize, and check, the errors of measurements. Actually from 2004 the CFc is interesting by an uplift characterized by brief accelerations follow by static of phenomenon (C.del Gaudio, Quaderno di Geofisica, 103, 2012).

The geodetic dataset used in this work consists of about 1100 optical levelling measurement, relative to the period 1982-1985. In this period were performed 13 surveys with variation of the benchmarks ranging from 18 in Aprile 1983 to a maximum of 353 in January 1983 (Fig. 26a).

The ground deformation rate showed three different behaviour with time :

- a marked increase during the first half of 1983. At 25A benchmark was measured an average uplift rate of 10 cm/month.
- started decreasing during the second half of 1984.
- in January 1985 reversing to subsidence.

The deformation shows a radial bell-shaped pattern in the whole period. Comparing the pattern during different intervals, it's possible notice a change in the shape, above all in the earlier phases of the crisis.

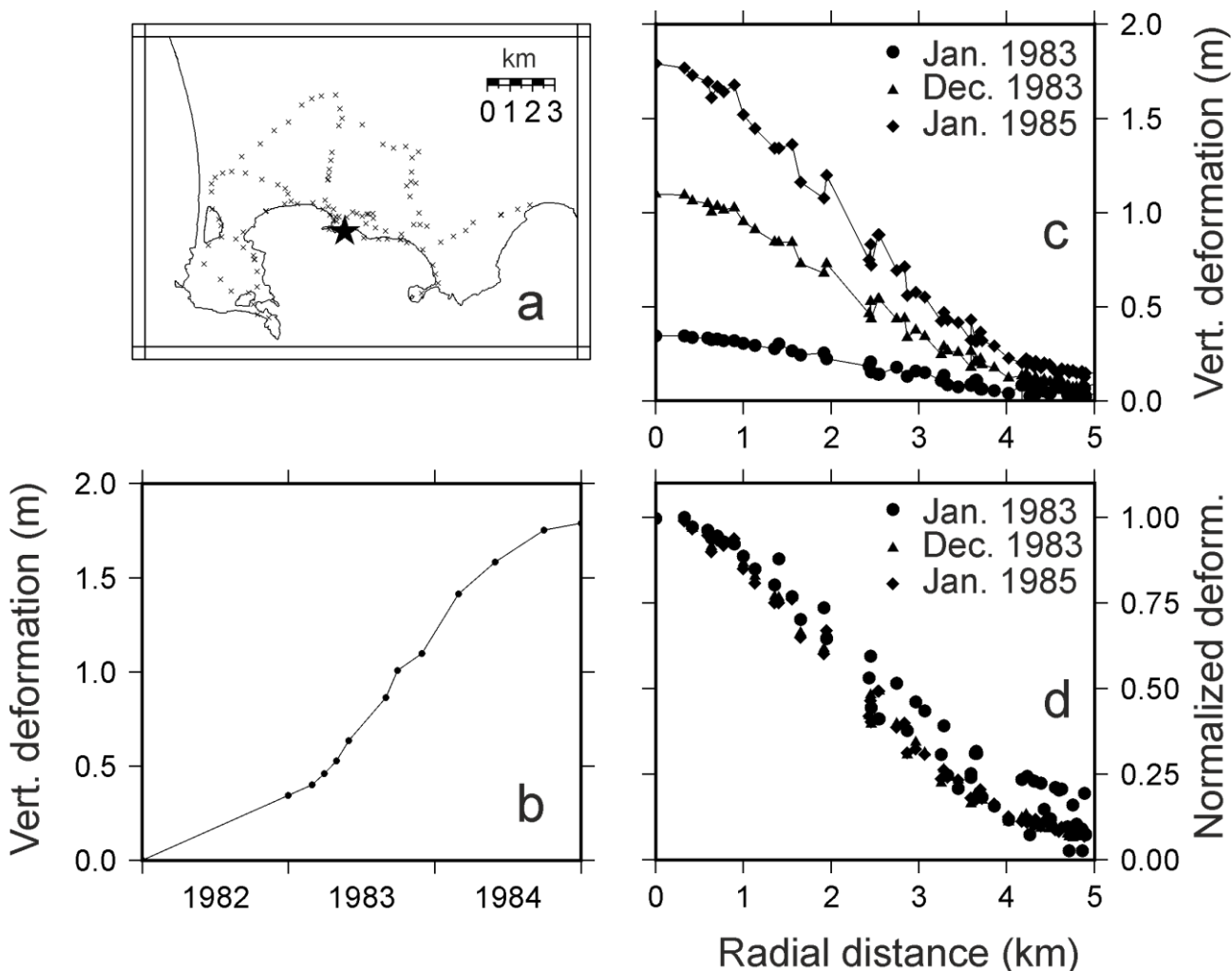


Figure 26 – in 1a is represented the planimetric distribution of benchmarks used between 1982–1985. With the black star is indicated the benchmark 25A. in 2b is represented the vertical deformation measured at benchmark 25A. in 2c is shown the ground deformation pattern as vertical deformation in function of the radial distance from benchmark 25A. different symbols stay for different period in comparison. in 2d there is the same representation of 2c but with vertical deformation normalized to the value of benchmark 25A.

#### 4.4 Inverse Method

Inverse methods define a complex of mathematical method that allow to extract info on a physical system starting from observed data.

Basic elements are: the observations (the data), the system described through parameters and the model that represent our idea about the link between parameters that describe the physical system and the data.

Usually the model is an equation that we expect data and parameters follow. In general, data and model parameters are linked by implicit equation as  $f(d, m) = 0$ .

Inverse theorem aims to solve or invert these equations for model parameters or to search any possible answer in any situation.

The most part of inversion methods includes calculation of direct problem, used to determine synthetic data(theoretical) which comparison with real data give a basis to estimation of parameters through a synthetic model that is created making hypothesis on the parameters.

So, the aim of inverse problems is to define model parameters and evaluation of the effects of measurement errors on parameters estimation.

After the definition of synthetic data, the inverse problem is solved evaluating the residue between observed and theoretical data.

Given a certain number of observations, we want to estimate the value of some parameters of interest, that in the case of ground deformation may be the location of the intrusion, of that deformation, its volume, its shape and / or evaluate the stress change and so on.

### Inverse problem

The simplest inverse problem may be represented with an explicit linear equation

$$Gm = d$$

Many inverse problems involve this equation and the other may be solved using linear approximation. A solution could be use the media that often is better determined than parameters but the media may not have a physic meaning, unless the model parameters not represented a discrete version of a continuous function. The average meaning in some cases is that although data

may not solve model parameter in particular point, they may solve the average of model parameters nearby that points.

Formally, given a vector of observation  $\mathbf{d}$ , we want to estimate an unknown parameter vector  $\mathbf{m}$ , which vector are linked by a mathematical model  $\mathbf{d}=g(\mathbf{m})$ . A forward problem is when given a model  $\mathbf{m}$ , we want predict the data that it will produce, instead a problem is called *inverse* when we want to find the model that produced data that we observed.

Independently from every parametrization, it's possible introduce a space of abstract points, defined as "variety", each point that represent a model possible to describe the system. The Variety is a general notion defined to model space with more dimensions or that may assume various shape. This variety is called *model space* ( $M$ ). individual model are points in the variety and are identified as  $m_1, m_2, \dots$

Define a parametrization means define a set of experimental procedures that allow to measure a set of physic quantities that characterize the system. After the parametrization, for every  $\mathbf{m}$  point of the  $M$  model space, there is a numerical set of values  $(m_1, \dots, m_n)$ . This correspond to the definition of a coordinate system on variety of the mode. To define a good model needs to have a coordinate system and put limitations as to impose a finite dimensional space with a finite number of parameters, because the variety theory with infinite dimension is very complicated. Then need to decide if parameters have continued or discrete values and for simplicity if is possible to use the terminology correspondent to the assumption that chosen every point may be represented by a particular set of values for model parameters

$$M = \{m^\alpha\}$$

Where  $\alpha$  index belong to a set of discrete finite index.

After this introduction we can speak about *model space* and only in this case the sum of two model  $m_1 + m_2$  is the sum of their components. the multiplication of a model from a real number correspond to the multiplication of all the components

$$(m_1 + m_2)^\alpha = m_1^\alpha + (\lambda \cdot m)^\alpha = \lambda \cdot m^\alpha$$

the only object capable to fillet the various formulation of the inverse problem are the probability distribution on the model space that may be define on a finite dimensional variety and independently from every parameterization and choice of coordinate. Anyway define a particular coordinate system is possible describe the distribution of probability using the density of probability. To obtain information on model parameters, needs to take observation from observable parameters. In the same way for the model space, is possible to use another variety of data said *data space* that includes all the results of measures that correspond to a particular point into the variance, and in the same way is possible sustain the data space with structures of a linear variety so that we may talk about linear data space with coordinates

$$d = \{d^i\}$$

That are the component and as always

$$(d_1 + d_2)^i = d_1^i + d_2^i \quad (rd)^i = rd^i$$

With every realization of  $\mathbf{d}$  defined as data vector.

The last variety definable is that variety that represent all the problem parameters. It will have coordinates  $\{x^A\}$  which quantities may be called physical parameters, with variety called *parameters variety*.

Considering just one observation and one parameter linked to the direct problem with  $N(0, \beta^2)$ , a priori distribution for  $\mathbf{m}$  and  $e$  the experimental error. If we repeat the measure of D on the same physical system, the measure will be centered in M, fixed before with a variance due to experimental error only,  $\sigma^2$ . The probability of D, given  $\mathbf{m}$ , is  $f(d|m) = N(m, \sigma^2)$

$f(d|m)$  is the probability for data and models,  $f(m)$  is the probability on model independent from data,

$f(d, m)$  is a priori probability.  $f(d)$  is the definition of marginal probability and depend on a priori variation of  $\mathbf{m}$ .

Direct problem

Solve a direct problem means predict value free from errors of observable parameters  $\mathbf{d}$  that correspond to a given model  $\mathbf{m}$ .

There are some different inverse problems, that may be linear and discrete as  $\mathbf{d} = \mathbf{G}\mathbf{m}$  where  $\mathbf{m}$  is a vector with M unknowns,  $\mathbf{d}$  is a vector with N data and  $\mathbf{G}$  is a matrix MxN where  $\mathbf{m}$  and  $\mathbf{d}$  are finite length vectors and  $\mathbf{G}$  is a function, named direct operator and express our mathematic model of studied physic system.  $\mathbf{d} = \mathbf{G}\mathbf{m}$  is a brief notation for an equation set

$$d^i = g^i(m^1, m^2, \dots) \quad \text{with } (i = 1, 2, \dots).$$

Usually predict values and observations are not equal because uncertainties and imperfections during modelling.

Let  $d = \{d^1, d^2, \dots, d^n\}$  be a set of observable parameters with  $p_D(d)$  the probability density that may represent measurement results. From a priori information is possible extract an information obtained independently from measure results. The probability density relative to measure results is  $p_M(m)$ .

A priori information is independent to observations. We may describe information that we have about model parameter and observables through a joint probability density.

$$P(d, m) = p_D(d)p_M(m)$$

That represent either information obtained on observable parameters, or data, either from a priori information on model parameters.

Considering  $\theta(d, m)$  as the theoretical probability density that represents the information on the physic correlation of  $\mathbf{d}$  and  $\mathbf{m}$ . Information's two state are combined to product information state *a posteriori*:

$$\sigma(d, m) = k \frac{\rho(d, m)\theta(d, m)}{\mu(d, m)}$$

With k normalization constant and  $\mu(d, m)$  homogenous information. The *a posteriori* information defined into the space D&M as marginal probability density

$$\sigma_M(m) = \int_D dd\sigma(d, m)$$

For the model space and

$$\sigma_D(m) = \int_M dm \sigma(d, m)$$

For data space. To extrapolate information from data and model space needs to make two assumptions.

One is the approximation to the use of probability density for  $\mathbf{d}$  given every possible  $\mathbf{m}$  to represent the physic theory

$$\theta(d, m) = \theta(d|m) = \mu_M(m)$$

With  $\mu_M(m)$  the homogenous probability density on the whole model space.

Considering the joint probability, the *a posteriori* information in the model space will be

$$\sigma_M(m) = kp_M(m) \int_D dd \frac{\rho_D(d)\theta(d|m)}{\mu_D(d)}$$

That is the solution of general inverse problem because from this equation is possible extract any information about model parameters.

From  $\sigma_M(m)$  we may obtain a sequence of sample  $m_1, m_2, \dots$  to better understand this informations.

General solution of inverse problem bring to definition of distribution of probability on the whole model space. This is possible when this distribution is very simple. For more general distribution may need to use a bigger exploration of the model space, using, for example, random methods or semi-random for exploration that may resolve many complex problems.

#### 4.4.1 Linear and non-linear problems

If the problem is linear we may write

$$[d_1 : d_N][G_{11} \dots G_{1M} : \ddots : G_{N1} \dots G_{NM}][m_1 : m_M]$$

The solution for an inverse problem is

$$vd - Gmv^2 = \min \rightarrow \hat{m} = G^{-g}d$$

With  $-g$  generalized inverse

From data recorded in nature, we can find a model estimation but, it's almost never the real model because uncertainties and model simplification.

May be that not exist one unique solution also for an infinite number of point, and that the finite number of observation is smaller of model parameters number.

$\hat{m}$  is our problem solution  $\hat{m} = G^{-g}Gm$

Where  $G^{-g}G$  is resolution matrix of the model.

Ideally  $G^{-g}G = I$ , or that model parameters are perfectly resolved

$$[\hat{m}_1 \ \hat{m}_2 : \hat{m}_N] [1 \ 0 \ 0 \ 0 \ 0 \ 1 \ 0 \ 0 \ 0 \ 0 \ 0 \ 1] [m_1 \ m_2 : m_3]$$

Needs to consider errors and if the system is determined, undetermined or overdetermined.

If there are more equations than unknowns ( $N > M$ ), the minimum square solution  $\hat{m}$  must minimize the residual of square

$$\hat{m} = (G^T G)^{-1} G^T d$$

And adds error vectors of measurement

$$d = Gm + e$$

Given the same weight to all errors. To give a different weight instead, needs to estimate  $e^T W e$  where  $W$  is the weight, which estimation is done through mean square solution of errors minimizing the residual norm

$$E(\|\hat{m} - m\|^2)$$

Which solution is

$$W = Q_{dd}^{-1}$$

Where:  $Q_{dd}$  is the covariance matrix of errors on observations.

The best linear impartial estimator will be

$$-\hat{m} = (G^T Q_{dd}^{-1} G)^{-1} G^T Q_{dd}^{-1} d$$

That is minimum square solution that is the point in the parameters space for which the function  $E$  is a minimum. Infact the best estimation for a parameter correspond to the minimum of  $E$  (prediction error). If we determine a variation  $\Delta E$  around a minimum, for the same variation we obtain two possible intervals around the minimum. More we are around the minimum more is minimum the error on the estimated parameter, For errors that follow Gaussian distribution, a good model for optimization useful to data inversion is the dampened minimum square solution. The

damping is applicable to more noisy component, with possibility to improve the signal-noise ratio, in output, through the estimation to damped minimum square.

If  $G_{(x)}$  is our inverse matrix, we use  $G_{(x)}^+$

$$G_{(x)}^+ = G_{(x)}^T (G_{(x)} G_{(x)}^T + \lambda I)^{-1}$$

Where  $\lambda$  is the damping factor of the pseudo inversion operation and is opportunely dimensioned.

Through errors propagation it's possible calculate the variance-covariance matrix.

$$Q_{\hat{m}\hat{m}} = (G^T Q_{dd}^{-1} G)^{-1}$$

That give informations about uncertainty of estimate model parameters and about how estimations of model parameters are related each one with others.

It's possible however, that there isn't an unique solution, also for an infinite number of points, and that a finite number of observations is smaller of number of model parameters.

For non-linear problem it's possible to run a direct model many times, varying model parameters and calculating residual weighed sums of square for each one, with search of model space. Residual weighed sum of square for two model parameters, or misfit function is

$$\varphi(m) = (d - g(m))^T Q_d^{-1} (d - g(m))$$

For more parameters needs to use an algorithm for sampling that may search the model sampling more effectively as for example, Simulated annealing or Markov chain Monte Carlo algorithm.

To solve the inverse problem is possible use many different ways. A classical way , or Bayesian, is one in which are assumed a priori information about the model and is possible to change a posteriori the information state. Algebraically speaking, needs to consider also the matrix problems.

The inverse problem is reduced to matrix on which is possible operate in a simple way. This is possible until is respected some characteristics. If the matrix is square and invertible, the inverse problem is solved with a matrix inversion

$$X = (A^T A)^{-1} A^T B$$

Using different methods as eigenvalues, pivot, analytic expressions. Often the matrix is not invertible so we need other methods. Most common method is the Singular Value Decomposition

(SVD) or, matrix that is decomposed using eigenvalues and eigenvectors, through which is possible extract a pseudo-inverse matrix useful for the solution of the minimum square problem.

#### 4.4.2 Model estimation

Founded the parameters, to explain why that data were recorded, needs to use a good model, that we called  $g$ . the most used model to define a source for volcanic deformation, is the Mogi model(Mogi, 1958). This model take in account a point source of pressure with  $\alpha$  the source ray that is consider when the point source became a spherical source (Fig. 27).

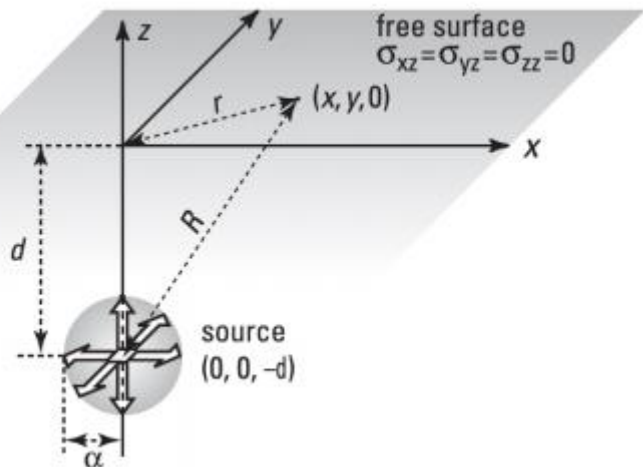


Figure 27 - Schematic Mogi model (Mogi, 1958).

Bigger is the ray source, bigger is the vertical deformation. The displacement surface is radial to the source(Fig.28).

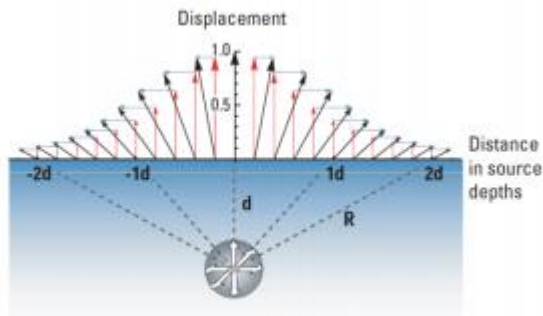


Figure 28 – Schematic view of deformation due to a spherical source.

This model is characterized by four parameters:

$$(u \ v \ w) = a^3 \Delta P \frac{1 - \nu}{G} \left( \frac{x}{R^3} \frac{y}{R^3} \frac{d}{R^3} \right)$$

$\nu$  is Poisson ratio. Mogi model obtained a lot of popularity in volcanic geodesy because has a simple analytic solution for superficial movement and explain very well the observations.

Another model very common is tensile rectangular dislocation (Okada, 1992) (Fig. 29)

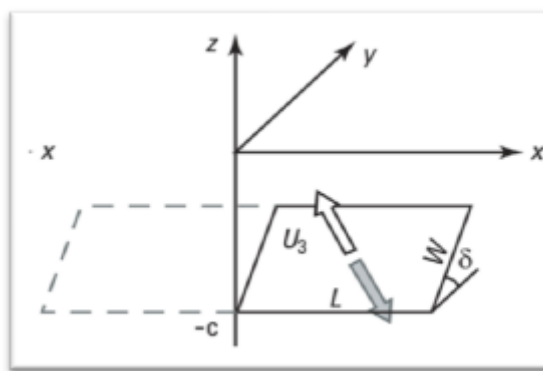


Figure 29 – Okada model (Okada, 1992)

With **L** dike length, **W** dike width,  $\delta$  plane tilt,  $U_3$  opening.

To modelling these sources exist many already done software package in Matlab (Battaglia, 2013)

This model is generally used to dick modelling, which vertical and horizontal movements are linked to its height and its depth(Fig.30).

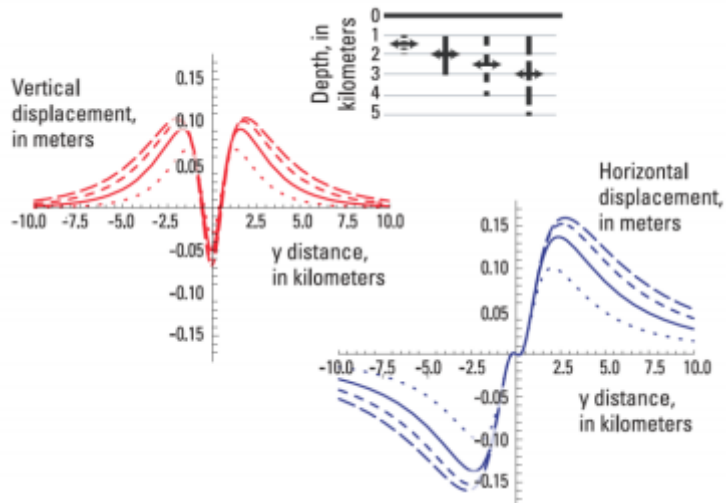


Figure 30 – Value of vertical and horizontal displacement.

with progress of quantity and quality of geodetic measures, as GPS and INSar techniques, it was necessary a more detailed study of morphology and dynamics of deformation sources. In particular, realistic deformation model due to magma injection are very important for volcanic and seismic hazard in area characterized by magmatic activity. So many 2-D models and a better Mogi model are developed. There are also 3D models that may be used. One of this is the sill intrusion model of a penny-shaped horizontal crack in an elastic semi-infinite body (Fig.31).

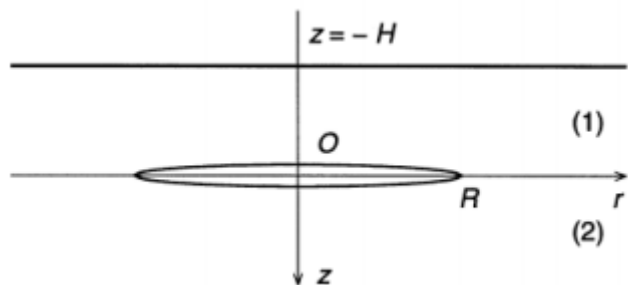


Figure 31 – Penny shaped crack (Fialko et al., 2001)

The horizontal crack has  $R$  ray and  $H$  depth and is in an elastic semi-space. The vertical axis is a symmetry axis with its origin in the centre of the crack, the crack plane divides the semi-space in

two domains. The surface is considered stress-free. Using this model there are founded exact solution for stress and movement(Fialko et al. 2001).

Other complex model are numerical models, or models to finite elements, where practically, start from a simple model, for example a visco-elastic layer, varying the parameters that characterized it, trying which model is the best. For superficial deformation, usually the simplest model is a magmatic intrusion in a magmatic chamber. When there is the intrusion, follow the volcanic building expansion because the pressure increase, and so the stress increase. Through inversion we would to know the stress change in depth using deformation recorded in surface. The fundamental point is to understand the process nature (if linear or exponential, etc.) and we have to impose initial condition and estimate the problem parameters.

#### 4.4.3 Deformation model

Casertano et al.(1976), Berrino et al.(1984), Bianchi et al., (1987) were the first to describe the ground deformation due to magmatic intrusion, and made initial interpretation of measured gravity-height change gradients ( $\Delta g/\Delta h$ )that confirm this hypothesis. Other authors suggest fluid intrusion to explain the caldera deformation and gas emission (De Natale et al., 1991, 2001; Bonafede, 1991; Gaeta et al., 1998; Chiodini et al, 2003) while Bonafede and Mazzanti(1998) and Gottsmann et al.,( 2005) used a single source including both magmatic and hydrothermal components.

Battaglia (2006) using a joint inversion of gravity and deformation data propose a model where, at first there is ground uplift for the bradyseismic crisis of 1983–1984, followed by subsidence in the late stages (1990–1995). The authors find as best fitting source for uplift an horizontal penny

shaped crack located beneath the town of Pozzuoli at a depth between 2.5 and 3.5 km, with a radius of 1.6–2.7 km, a volume increase between 0.021 and 0.027  $km^3$  and a density between 142 and 1115  $kg/m^3$ . Instead, for the deflation period the best fit source is a vertical prolate spheroid 1.9 to 2.2 km deep with aspect ratio from 0.39 to 0.54, volume decrease 0.05 to 0.06  $km^3$  and density between 902 and 1015  $kg/m^3$ . This result indicates a source with location and shape consistent with the shallow geothermal system in the area infect, the depth of the model source overlaps the location of the main aquifer. The difference in source shape between the uplift and the subsidence is explained as a constrain by the difference in the ratio of the horizontal and vertical displacements for the two time periods that is 0.5 between 1980 and 1983 and 0.85 during 1990–1995.

Based on these results, Battaglia et al. (2006) postulate that the whole deformation cycle may be explained in terms of fluid exchange between the deeper and the shallower reservoir that are separated by an impermeable level. That level bring the pressurization and consequently the inflation of the deeper reservoir.

Battaglia et al.(2006) suggests as model of the cause of 1982–1984 crisis the exsolution of hypersaline brine and gas from a crystallizing magma body that accumulates in a horizontal lens above the magma that is separated from the shallow aquifer by an impermeable layer. When occurs a bigger fracture in this zone brine and gases migrated to the aquifer. The subsidence may be caused by faulting of the brittle aquifer increasing the permeability and increasing pressure and temperature (Fournier, 1999).

De Natale(2001) proposed lateral migration of fluids as mechanism of discharge.

Troise et al. (2007) used ground deformation data to demonstrate that the most recent uplift episodes represent the action with a dynamic process similar to that invoke by Battaglia et al. (2006). In this work the inversion of the ground deformation dataset has been performed using a hybrid non-linear technique.

$$z_i^k = s_k a_i$$

Where

- the  $k$ -index is referred to the benchmarks;
- the  $i$ -index to the optical levelling surveys;
- $s_k$  is the vertical deformation at the  $k$ -th benchmark for a given source with normalized amplitude.
- $a_i$  is the source amplitude at the time of the  $i$ -th survey.

Needs to take in account that the relationship between the source amplitudes and the data is linear, but the term  $s_k$  has a highly non-linear dependence from the source. In this work, used a non-linear optimization algorithm was possible to split the problem into a linear inversion.

Through the linear inversion, given a source model  $s_k$  it's possible determine the values  $a_i$ .

To reduce the effect of local biases on the dataset, we consider all the possible differences at the benchmark  $k$  through the relation:

$$d_{ij}^k = z_i^k - z_j^k$$

Substituting in the precedent equation and considering a specific source model, has been obtained a system of linear equation :

$$d = Ga$$

That is possible to solve computing a pseudo-inverse ( $G^+$ ) using a singular value decomposition (Aster et al., 2013)

$$a^{est} = G^+ d$$

After the estimation of the source amplitudes, it's possible compute the residual sum of squares for the considered source model:

$$RSS(s) = \sum_{i,j,k} [(d_{ij}^k)^{obs} - s_k(a_i - a_j)]^2$$

To determinate source model parameters has been optimized the previous function using a genetic algorithm (Sen and Stoffa, 1995) using five different elementary source models as follows(Table 2),

Model	GDOF	DOF	RSS (cm <sup>2</sup> )	AICc
Mogi (1958)	0	15	2.935	-6467.680
McTigue (1987)	1	16	2.731	-6544.621
Fialko et al. (2001)	1	16	0.966	-7684.601
Yang et al. (1988)	4	19	0.865	-7800.115
Okada (1985)	4	19	0.773	-7923.076

Tabel 2 – comparison between models used to estimate the source of ground deformation data.

Where DOF are the number of degrees of freedom associated to the model, GDOF are the DOF related to the geometry of the source.

$$\text{DOF} = 3 + \text{GDOF} + (\text{NS} - 1)$$

Where 3 are the DOF relative to the spatial location of the source and the NS (number of optical levelling surveys)-1 are the DOF associated to the amplitude variations of the source. -1 appears to constrain the amplitude of the source term at the time of the first survey to be null ( $a_1 = 0$ )

These values need to the computation of the Akaike Information riterion (AICc, Burnham and Anderson, 2002) that allows to selection among the candidate models. In detail:

- Mogi source (1958) is the simplest model without GDOF
- McTigue (1987) and Fialko et al.(2001) penny-shaped crack models have 1 GDOF relative to the source radius.
- Yang et al. (1988) that considers a generally oriented ellipsoid and Okada (1985) that considers a simple rectangular crack models have 4 GDOF .

In the modelling shear modulus have 2 GPa and the Poisson's ration is imposed to be 0.25 (D'Auria et al., 2012). As the table 2 shows, the AICc values indicate that the Okada rectangular crack is the best source.

Results of the inversion are shown in the Figure 32)

- In 32a there is the comparison between observed and synthetic data that shows an excellent agreement.
- In 32b is shown the volumetric variation from the crack opening value relative to the Okada source model. The final volumetric variation of the source is about  $0.35 \text{ km}^3$  which is of the same magnitude of small-medium sized eruptions at CFc since 12ky (0.01–0.1  $\text{km}^3$ ) (*Woo and Kilburn, 2010*)
- In 32c is shown the average residual that don't have any systematic trends.
- In 32d the projection of the crack is represented with a red rectangle that has an area of about  $16 \text{ km}^2$  located at 2.56 km in depth. The crack is dipping of  $9^\circ$  toward SW. In the same window, are represented also the average residual of benchmark that show a slight increase in the area E of Pozzuoli maybe relative to the presence of Monte Olibano, whose mechanical properties differs from the surrounding lithologies (*Orsi et al., 1996*)

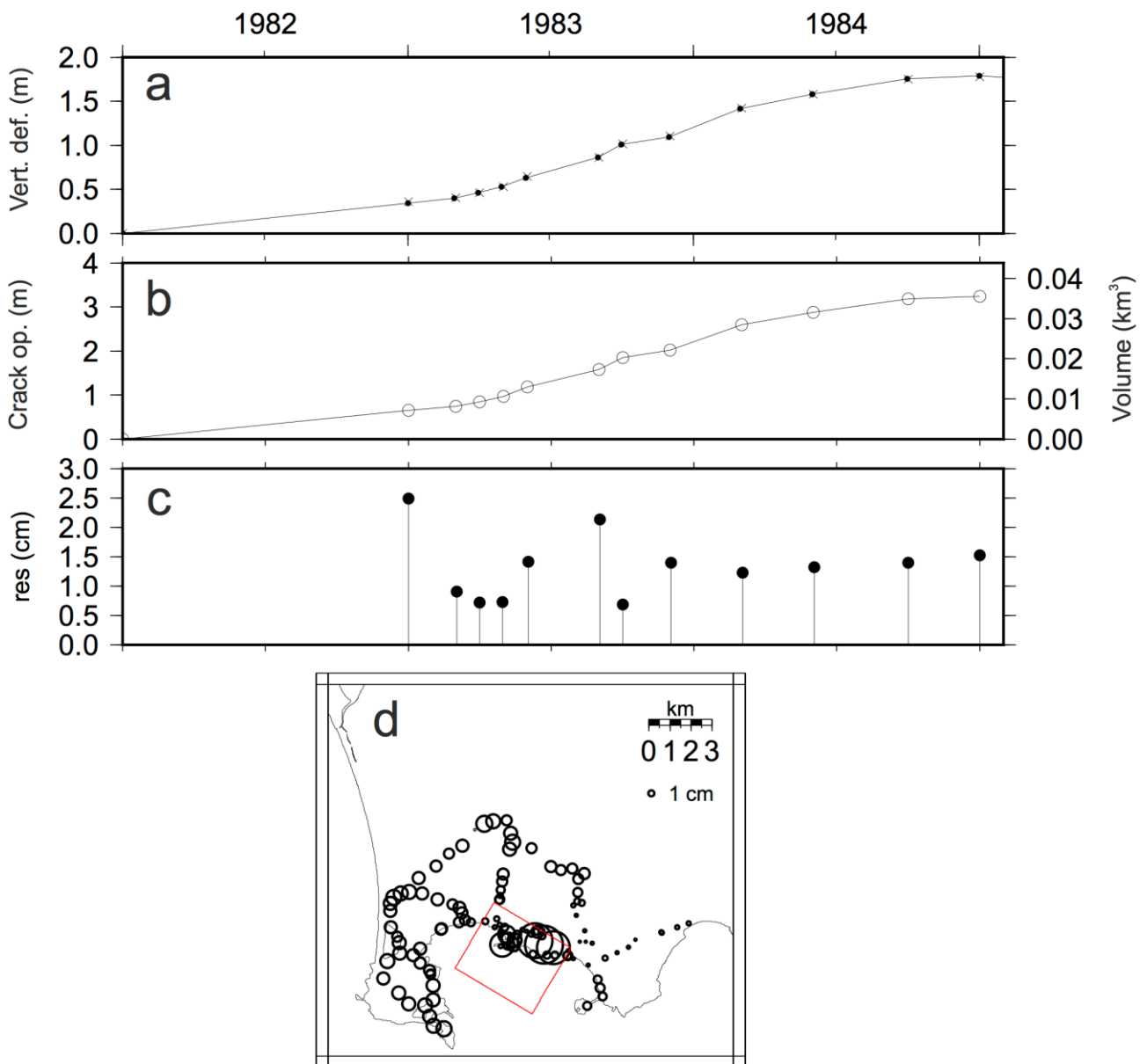


Figure 32 - (D'Auria et al., 2015) Results of the inversion of the geodetic dataset. a) Comparison between the observed (crosses) and the synthetic (black dots) vertical ground deformation at the benchmark 25A. b) Opening of the crack and its volumetric variation (scale on the right). c) Average residuals for each survey. d) Average residuals for each benchmark are indicated with black circles.

## 4.5 Joint Inversion

Inversion is the process for which based on the quality of the input and on the parameters, it's possible obtain a good retrieved model of the subsurface from data acquired on the field. More information we have, better model will be in output. That means that if we don't have a sufficient

amount of information, our model will be necessarily uncertain or erroneous. The information may be both geophysical data and supplementary geological information. To face all the problem related to the non-uniqueness of the solution and those associated to the interpretation of complex data, is the joint analysis of different and integrating dataset. The joint analysis is not so different from a single-objective function inversion. It's possible proceed with a direct modelling or with some automatic inversion procedure. It's important define the misfit of each single considered objective function (Picozzi and Alberello, 2007).

The joint inversion used in this work basically take in account the inversion relative to ground deformation data and the other one relative to focal mechanism dataset. The inversion over the focal mechanism dataset permit to found the stress tensor. Exists numerous way to implement this inversion, one of which is based on the search over the model parameter, using a non-linear optimization technique through a two step algorithm, using the MonteCarlo search and the Mead simplex algorithm.

#### - NELDER & MEAD ALGORITHM

Nelder and mead method (1965) or amoeba method or simplex algorithm is a non-linear optimization technique that allow the search of maximum and minimum of functions with many variables. In a N-dimensions space, is called *simplex* the geometric figure defined from  $N+1$  vertices and from all the line that connect that vertices. The method follows this procedure: Choice of an original simplex identified by  $n+1$  points  $P_0, P_1, \dots, P_N$ , fixed  $P_0$  and choice of the other  $N$  points. So we have

$$P_i = P_0 + \lambda e_i \quad i = 1 \dots N$$

With

$e_i$  unitary vector linearly independent

$\lambda$  constant that may represent the scale constant of the examined problem.

The method is iterative, from every iteration, the method uses what operation make on the original simplex; the method stops when the distance done in one iteration is smaller than a tolerance value prefixed. In 2-D space ( $N=2$ ) a simplex is a triangle ( $N+1=3$ ), in a 3-D space is a tetrahedron and so on.

The choise of the geometrical shape is due to the simplex capability of adapt its shape to the function performance in the space deforming itself and asking for memorizing just  $n+1$  points.

The algorithm keep in memory the  $n+1$  simplex vertices with values correspondent to objective function values and at every iteration try to generate a new simplex substituting the point at which correspond the maximum value of  $f$  with a new point, choice in a timely manner, so the objective function has a smaller value. In particular the  $n+1$  vertices  $\{x_j\}_{j=1}^{n+1}$  are sort by the objective function value

$$f(x_1) \leq \dots \leq f(x_{n+1})$$

The algorithm try to substituting the worst vertices  $x_n + 1$  with a new point in the way

$$x(\mu) = (1 + \mu)x_c - \mu x_{n+1}$$

With

$x_c$  centroid of the remain  $n$  point or

$$x_c = \frac{1}{n} \sum_{j=1}^n x_j$$

The idea is to operate a reflection of  $x_{n+1}$  respect of  $x_c$  where  $\mu > 0$  is a good reflection coefficient.

Typically  $\mu$  value is selected from a value sequence choice as

$$-1 \leq \mu_{ic} < 0 < \mu_{oc} < \mu_r < \mu_c$$

And a typical sequence is

$$\{\mu_r, \mu_c, \mu_{oc}, \mu_{ic}\} = \{1, 2, \frac{1}{2}, \frac{1}{2}\}$$

If the new point satisfy  $f(x(\mu)) \leq f(x_{n+1})$  so in the current simplex  $x_{n+1}$  is replaced by  $x(\mu)$  (Fig.33).

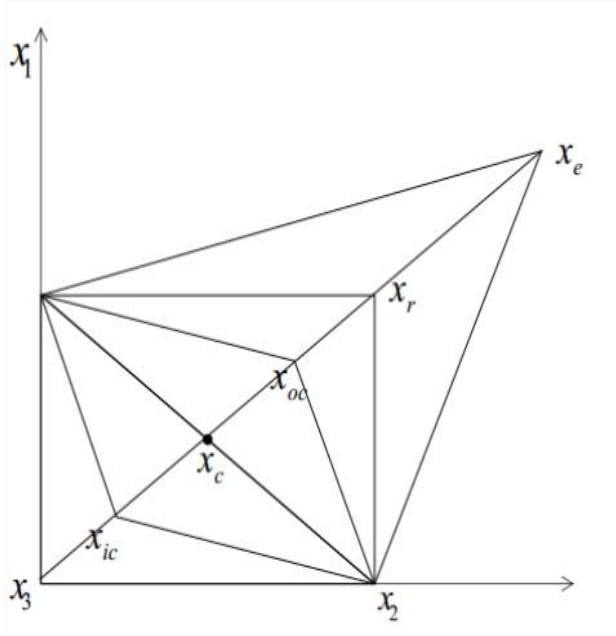


Figure 33 – Nelder and mead method, simplex schematization (Nelder & mead, 1965)

#### - Montecarlo method

Montecarlo method consists in approximation of mathematical problem solution through simulation based on random number. It's a search method random where models are built uniformly and tested in comparison with data. Generally in the Montecarlo inversion every parameter of model may change into a search default range( *a priori* determined). So for every parameter  $m_i$  we define

$$m_i^{\min} \leq m_i \leq m_i^{\max}$$

And a new model vector is build, that may be generated by a random perturbation of a specific number of model parameters in the model vector. Synthetic data will be generating by a new model and compare with observations. This will be accepting (or not) deterministically base on an acceptation criterion that determine how good synthetic data fit with observation.

This process of generation – acceptance/rejection is repeated until a fixed criterion is satisfied. Generally, the “stop” criterion is given by total number of accepted models.

Montecarlo method is often used to evaluate numerically of integral into space with large dimensions. However, evaluate the function systematically on irregular grids is impossible, because it requires too many points. Then Montecarlo sampling this function provides to estimation of result and error. Keilis-Borok and Yanovskaya(1967) and Press (1968,1971) used as first the Montecarlo method for the inverse problems solution. The principal problem on which it is focused is how to use the probability distribution, because, when it is define on all the space with small dimensions, it is directly representable being directly linked with probability density. When the model space has large dimension, representation is impossible but is possible sampling it and the solution seems to be equivalent. Considering a set of samples of probability distribution, they became represented into individual points.

#### 4.5.1 Campi Flegrei caldera joint inversion

In this project the joint inversion is used to find a general model for the stress field acting in a volcanic area during unrest episodes.

Volcanism occurs in areas subject to regional stress that brings deformations that allow rising of magma. Generally, type and orientations of deformations depend on regional stress field but at the same time, a local stress regime exists due to magmatic masses. Deformation relates to the local stress occurs in a medium already deformed under the influence of the regional stress. The evolution of magmatic system brings to volcano-tectonic events such as caldera collapses or resurgence of floor. The deformation generated by these type of events may result in creation or reactivation of faults, generated by regional stress field (Orsi,1999).

Some authors use classical analysis of fault plane solution to evaluate local stress pattern for a given earthquake dataset relative to Campi Flegrei caldera. Gaudiosi and Iannaccone (1984) used focal

solutions of 15 seismic events recorded during 1983 to model the stress pattern of CFC concluding that no regional components seem to dominate during 1983 and that the least compressive stresses are horizontal, whereas the maximum compressive stresses are nearly vertical except in Pozzuoli bay where is horizontal.

Coppa et al. (1985) studying 21 seismic events during 1983–1984 distinguished normal fault solutions on land and reverse faults in the gulf of Pozzuoli.

Aster and Meyer (1988) using 228 microearthquakes recorded during 1983–1984 bradyseismic crisis, reconstructed a three-dimensional velocity structure for CFC, showing a zone of concentrated seismicity in the north of the zone of maximum uplift and suggest a ring-fault structure.

Zuppetta and Sava (1990) used Angelier method to model the local stress field associated with uplift, showing doming coupled with regional extensional to explain the seismic phenomena affecting the area.

Based of the idea that exists a background stress field acting on the volcano before the unrest episode and that the system may have memories about precedent episodes of unrest, a general law may be presented as

$$\sigma(x, t) = \sigma_0(x) + \sigma_M(x)a(t)$$

Where  $a(t)$  is a time-varying function describing the temporal pattern of the ground deformation source, that may be the crack aperture, already known from the inversion of ground deformation data.

$\sigma_M(x)$  is the perturbation stress field in the volcano generated by a determined source that may be computed for a given source model;  $\sigma_0(x)$  is the background stress field acting on the volcano before the unrest episode that needs to be determined from an independent dataset that in our case may be the focal mechanism dataset.

We may express  $\sigma_0(x)$  as the contribute of the regional field of the studied area, with the contribution of a lithostatic load :

$$\sigma_0(x) = \sigma_R + \sigma_L(x) + \sigma_M(x)a_0$$

Where  $a_0$  is a constant which takes into account residual stresses deriving from previous unrest episodes arising from similar ground deformation source.  $a_0$  needs to be determined from an independent dataset, as well.  $\sigma_L(x)$  is the lithostatic load contribution, nearly isostatic that in reality not contributing.

$\sigma_R$  instead is the stationary background regional field.

Substituting

$$\sigma(x, t) = \sigma_M(x)[a(t) + a_0] + \sigma_R.$$

The function  $a(t)$  is already known from the inversion of the ground deformation data,  $\sigma_M(x)$  can be easily computed for a given source model. The unknown regional field and the constant  $a_0$  need to be determined from an independent dataset that may successfully be the focal mechanisms dataset.

It was already mentioned that the inversion of focal mechanisms permits the estimation of the stress tensor.

For accomplish this task we consider for the inversion the approach of Angelier (1990), treated in the Chapter !!! that in brief consist in minimization of the difference between the slip vectors  $s$  on each fault and the direction of the maximum shear stress  $\tau$  acting on it, searching the global minimum of the function

$$E = \sum_k |\delta_k|^2 \quad \delta_k = s_k - [\xi_k - (\xi_k \cdot n_k)n_k]$$

$s_k$  is the slip associated to the k-th focal mechanism of the dataset

$n_k$  is the normal vector to the fault plane

$\xi_k$  is the stress vector acting on the fault surface ( $\xi_k = \sigma n_k$ ).

Than was used a non-linear optimization technique for the search over the model parameter

$$m = [\alpha, \theta, \iota, \psi, \phi_B, a_0]$$

Where  $\alpha$  is the magnitude of  $\sigma_1$ ,  $\theta$  is the trend of  $\sigma_1$ ,  $\iota$  is the plunge of  $\sigma_1$ ,  $\Psi$  the rotation of  $\sigma_3$  around the  $\sigma_1$  axis,  $\phi_B$  is the Bishop's ration and  $a_0$  is the precedent citated constant. The first five parameters are useful to determine the regional stress tensor  $\sigma_R$ . So, it has been used the two-step algorithm with the already mentioned Monte Carlo search and Nelder and Mead (1965) simplex algorithm and the estimation of the uncertainty on each parameters was done with a bootstrap approach (Efron, 1979; Micheal, 1987). Results are shown in the following table (Table 3).

Parameter	Value
$\sigma_1$ magnitude	$0.39 \pm 0.20 \text{ MPa}$
$\sigma_1$ trend	$266^\circ \pm 8.2^\circ$
$\sigma_1$ plunge	$10^\circ \pm 5.9^\circ$
$\sigma_3$ trend	$0^\circ \pm 11.5^\circ$
$\sigma_3$ plunge	$17^\circ \pm 5.3^\circ$
$\phi_B$	$0.42 \pm 0.25$
$a_0$	$0.0003 \pm 0.0250 \text{ m}$

Table 3 - results of joint inversion (D'Auria et al., 2015)

From results is possible deduce that:

- together with the stress field relative to the volcanic process, exists a background regional field that acts on the area, which orientation is compatible with those retrieved by D'Auria et al. (2014) for the Mt. Vesuvius volcano.
- The reduction in the misfit function relative to the regional field is about 4%
- The contribution of this field in the area is negligible. This is possible to understand comparing the modelled stress field and the results.
- The value of  $a_0$  is close to 0. That means that the effect of previous uplift events on the stress field of CFC was completely vanished during the bradyseismic crisis.

To better understand the dynamic behind the modelled stress field retrieved in CFc, it has been analysed its temporal evolution. In fig. 32 (D'Auria et al., 2015) has been computed the theoretical stress field on a regular grid of 8x8x4 km, centred on benchmark 25A, regularly spaced of 250m. In the first column are represented the orientation of  $\sigma_1$  and  $\sigma_3$ , the Okada source retrieved by the inversion of ground deformation data and the magnitude of  $\sigma_1$  as contouring, along a section NNW-SSE reported in the figure in chapter 2(seismic). Through this representation is possible notice that the magnitude of  $\sigma_1$  is concentrated along the edges of the rectangular crack that is usual for the Okada source. That characteristic may explain the two clusters of seismic events retrieved in the location of events recorded during the bradyseismic crisis.

In the other two columns are stereographic projection on which are plotted the principal stress axis attitude. The temporal evolution is limited to 4 period: 1-1-1983; 1-7-1983; 1-1-1984; 1-1-1985;

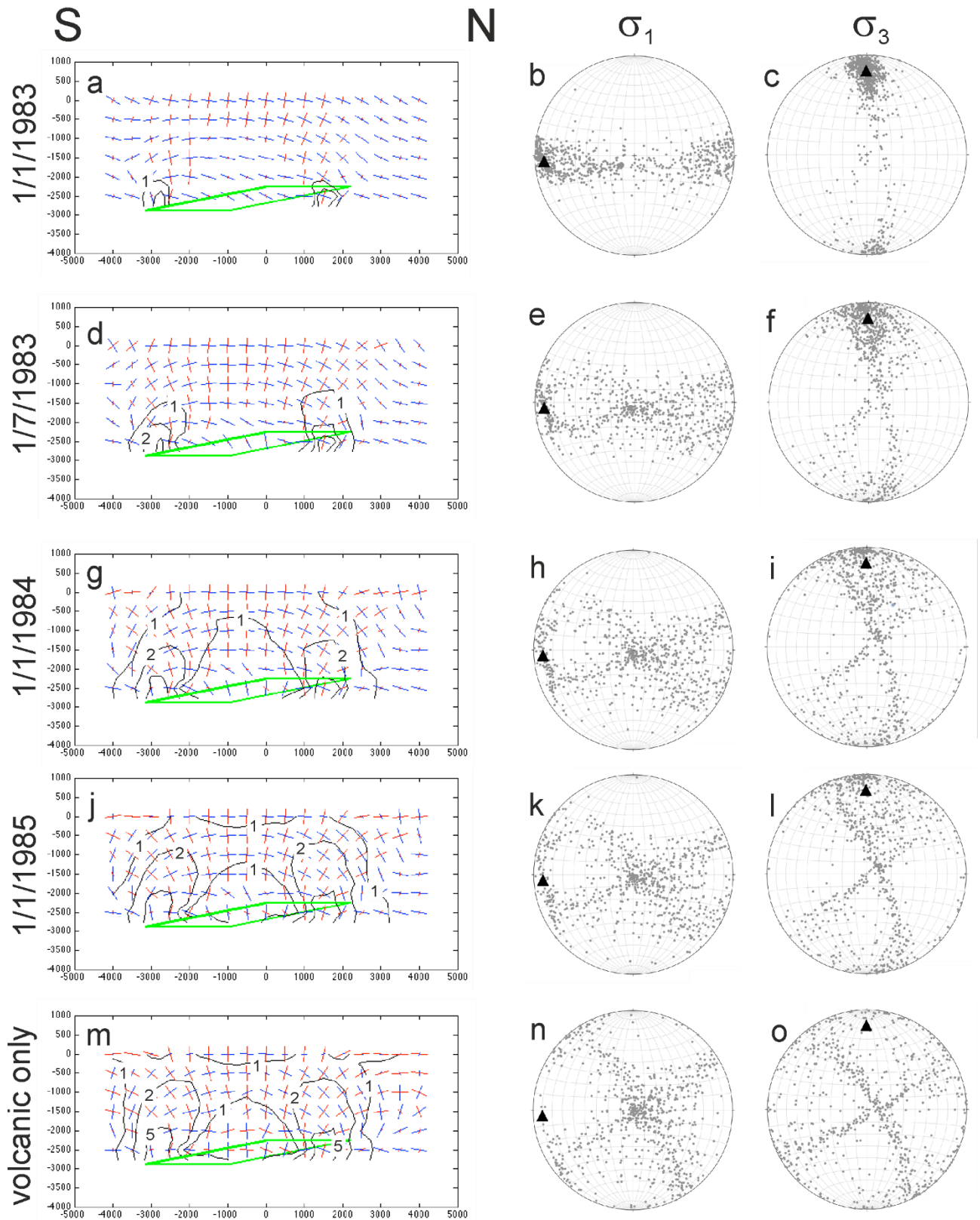


Figure 34 – Results of joint inversion referred to temporal variation.

In the first period, the regional field is still dominant (Fig.34, a,b,c) but already during the first half of 1983. So the volcanic deformation source becomes prevalent on the background regional field. It's possible notice a sub-vertical  $\sigma_1$  and this attitude continue for the entire period. Is also evident the sub-horizontal  $\sigma_3$  that persist until 1985. In Fig.

32 m is shown the stress field generated by the volcanic source alone. Is evident that just the volcanic source is not able to reproduce the distribution of  $\sigma_3$  retrieved in the inversion of focal mechanism dataset, that means that is reasonable include the contribution of a regional field.

In order to analyse seismogenetic process and reologic proprieties of the area, in the last part of this work were deepen studies about the influence of hydrothermal fluids on the behaviour of the system in interest. So, has been analysed the hydrothermal system of Campi Flegrei caldera and has done thermo – fluid dynamic simulations for the assessment of the reliability of the pore fluid pressure values.

## Chapter V – Seismogenesis

### 5.1 Hydrothermal system of Campi flegrei caldera

From 1998 to 2010 measures of gas release at Solfatara crater estimate a diffuse degassing process in the crater and in the surrounding area (about  $1.4 \text{ km}^2$ ) with value between 1000 t/d to 1500 t/d (Chiodini et al., 2010). In recent time (January 2013, Aiuppa et al., 2013), has been performed measure of gas flux from the three main fumaroles at Solfatara founding value of total CO<sub>2</sub> output of up to 600 t/d. The total flux, summing the fumarole fluxes and the diffusive emission, is between

1500 t/d to 2000 t/d and doesn't consider the total hydrothermal CO<sub>2</sub> output, that consists also in numerous smaller fumarolic discharges.

In recent time has been also recorded also a decrease of CH<sub>4</sub> content of the fumaroles. This value is very low in magmatic fluids so it was interpreted as an increase of a proportion of magmatic component

in the Solfatara fumaroles in relation with the increasing of CO<sub>2</sub> and He.

This is explained as resulting from magmatic fluid injections (Chiodini et al. 2012)

Two possible explanation exist for this amount of gas flux and are boiling process of a liquid and the presence of a large zone where there is a gas plume. The last hypothesis is more compatible rather than the first one because it would require unreasonable amounts of boiling water. This value of high diffuse CO<sub>2</sub> fluxes is the same in magnitude of Yellowstone and is generally found hydrothermal areas vapor-dominated.

A geochemical model of campi flegrei caldera exist since 1989 by Cioni et al. and has been refined by many authors (Cioni et al., 1989; Chiodini et al., 1992, 1996, Chiodini and Marini(1989) and Chiodini et al., 2000a; 2001a). Following Caliro et al., 2007 the geochemical model that describe the heat source of the hydrothermal system is a magma chamber locataed about 4 km in depth, that boiling caused gas separation of a gas phase at condition of maximum enthalpy for saturated steam at 236°, 31 bar (Cioni et al., 1984). These gases arise to the surface, mix with boiling meteoric water and create a gas plume that feed fumaroles and diffuse soil degassing at Solfatara crater(Fig. Chiodini et al., 2015). Many physical and numerical simulation support this geochemical interpretation (Chiodini et al., 2003, 2012; Todesco et al., 2003; Todesco, 2009; Rinaldi et al., 2010; Petrillo et al., 2013). All the simulation consisting in the injection at depth beneath the Solfatara crater, at depth varying between (1.5–2.5 km) of a hot CO<sub>2</sub>-water mixture. The flux is constrained by the surface hydrothermal flux measured at Solfatara. In these case the simulation was performed with the TOUGH2 software (Pruess, 1991) under steady-state conditions. Also the results are

concordant with the hypothesis that exists a gas plume under the Solfatara crater that vertically connects the deep injection zone with the surface.

This vertical structure may be an easy way for hydrothermal flow to arise toward the surface.

This vertical connection has been identified also through the S-wave seismic velocity models that delineate a vertical, roughly cylindrical, high-Vs structure that extends from the surface close to Solfatara crater, down to 1.5 km. the presence of the Vs anomalies in the shallower part of the aquifer is related to the presence of gas instead of liquid, suggested by laboratory measurement (Giberti et al., 2006).

At 4 km below the city of Pozzuoli there was identify a low Vp/Vs ratio that may be the deep source of this hydrothermal gas plume and is been interpreted as a high-fluid compressibility rock formation (Vanorio et al., 2005).

The Solfatara aquifer is anomalously high for the water table height and the water temperature up the boiling point (Petrillo et al., 2013). These anomalies are due to large amounts of condensates which are of the order of thousands of tons per day and them recharge and heat the groundwater system (Bruno et al., 2007; Petrillo et al., 2013). The height of the water level indicates that the aquifer may be sustained by a pressurized gas plume. The same hypothesis was verified for the case of vapor-saturated hydrothermal system in Yellowstone (Zohdy et al., 1973) and at Waimangu, New Zealand (Legaz et al., 2009).

The gas phase interests the shallower part of the system named vapour zone, for which gas equilibria in the CO<sub>2</sub>-CO-CH<sub>4</sub>-H<sub>2</sub>O-H<sub>2</sub> system indicate temperature from 200 to 240 °C and  $P_{H_2O}$  from 1 to 20 bar (Chiodini and Marini, 1998; Chiodini et al., 2001a). Isotopes studies support the involvement of magmatic fluids contaminated by metamorphic and meteoric components (Cortecchi et al., 1978; Allard et al., 1991; Panichi and Volpi, 1999; Tedesco and Scarsi, 1999).

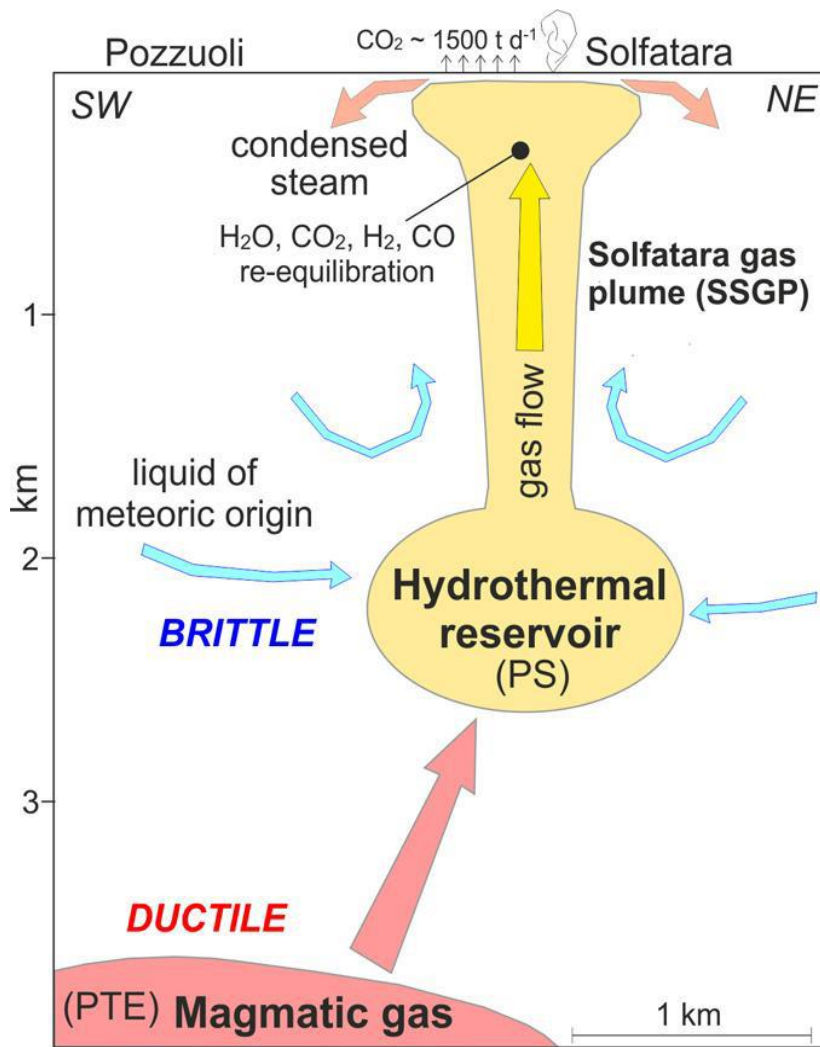


Figure 35 – (Caliro et al., 2007) Schematization of Campi Flegrei deeper structures.

In the figure (35) are synthetically show the main characteristics of the aquifer that consist in

- “magmatic gas” zone . A deep zone of gas accumulation located at 4 km in depth (Vanorio et al., 2005) has been hypothesized (De Siena et al., 2010) the presence of a small batch of magma.
- “hydrothermal reservoir”. A shallower reservoir located at 2 km in depth, where magmatic fluids mix and vaporize liquid of meteoric origin that may forming the Solfatara gas plume.

This line is also supported by recent ground deformation inversion data (Amoruso et al., 2014a, 2014b) that hypothesize the presence of two source, one oriented NW-SE at about 4 km in depth below Pozzuoli that may be geometrically indicated as a pressurized triaxial ellipsoid (PTE – in

the figure 35) and the other one (PS – in the figure 33) that is located at 2 km under the Solfatara crater modelled as a pressurized spheroid.

The simulation has been done simulate a stress-strain changes in the whole caldera volume, due to flow induces in the geothermal system increasing and changing pressure and temperature in the magma chamber.

The set of basic equations describing pressure, temperature and injection rate in a 3D porous medium, at the steady state, as due to a given set of boundary conditions are:

a) mass balance :  $\nabla(\rho\varepsilon\vec{v}) = 0$

where  $\vec{v}$  is the pore velocity,  $\rho = \rho(T)$  is the water density and  $\varepsilon$  is the porosity of the rock.

b) momentum balance

$$\nabla P = -\frac{\eta\varepsilon}{K}\vec{v} - \rho\vec{g}$$

Where K is the permeability,  $\eta$  is the fluid viscosity, P is the pressure and  $\vec{g} = -g_z$  is the gravity acceleration.

Applying the divergence to eq b

$$\nabla^2 P + \nabla(\frac{\eta\varepsilon}{K}\vec{v}) + \nabla(\rho\vec{g}) = 0$$

combining a) and 4 using Businessq approximation

$$\nabla^2 P + \nabla(\rho(T)\vec{g}) = 0$$

c) Energy balance

$$D^*\nabla^2 T = \frac{K}{\eta\varepsilon} \left[ -\frac{\partial P}{\partial x} \frac{\partial T}{\partial x} - \frac{\partial P}{\partial z} \frac{\partial T}{\partial z} - \rho g \frac{\delta T}{\delta z} \right] ???$$

Where D\* is the thermal diffusivity

## 5.2 Pore pressure Analysis

Rock are formed by pore that could be filled by fluids. Gassman(1951) describe pore fluid as a mixture of water and carbon dioxide (20% of carbon dioxide and 80% of water).

Pore fluids have strong control over the frictional strengths of rocks. The fluids inside the pore make pressure around the pore that has to be considered when considering landslides, earthquake generation and strength of lithosphere studies (Fig.36)

Without pore fluids normal stress should be supported by the framework of solid grains.

Variation of pore pressure, influence the state of stress.

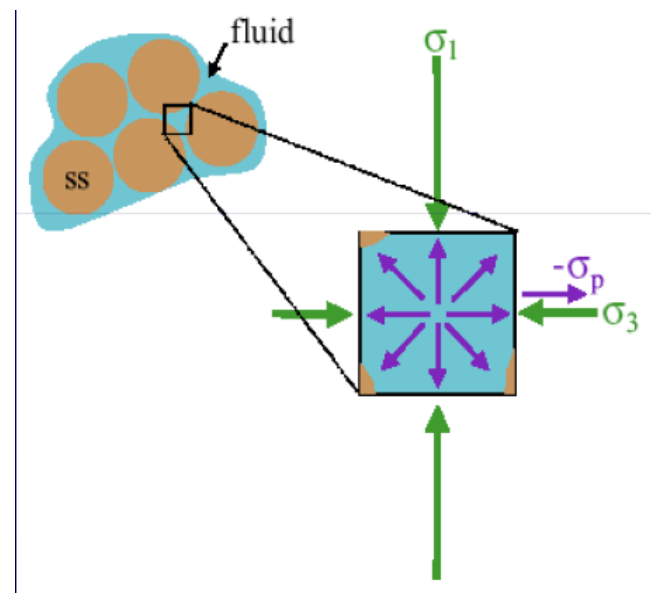


Figure 36 – Pore fluid pressure

Terzaghi(1943), used efficacies stresses concept, developed an argument on how pore pressure could influences the state of stress. For principal stress, efficacies stresses  $\sigma_{V,eff}$ ,  $\sigma_{H,eff}$ ,  $\sigma_{h,eff}$ , are given by

$$\sigma_{V,eff} = \sigma_v - Pp, \quad \sigma_{H,eff} = \sigma_H - Pp, \quad \sigma_{h,eff} = \sigma_h - Pp$$

So the efficace state of stress describes the state of stress considering also pore pressure, that reduces normal stress of a quantity equal to its value.

Assuming that there isn't variation for total stress, high pore pressure, generates low efficacy stress. Pore pressure describes a fluid pressure, and there isn't shear stress transfer from the pore pressure, so pore pressure influence is just for efficacies normal stresses and principals. Spiking about mohr circles, for high pore pressures, they move in the direction of the rupture limit without changing their shapes, so the rock became instable.

McKenzie (1969) showed that if an earthquake occurs on a pre-existing fault, the only constraint focal mechanism provides is that  $\vec{s}_1$  must lie in the dilatational quadrant. Adding the mechanical constraint that a friction law must be satisfied for slip to occur on a plane of weakness, somewhat moderates this result because stress difference or pore pressure must increase as stress misorientation increases(Célèrier,1988; Raileigh et al.,1972; Sibson,1985).

Considering the pore fluid pressure  $p_f$  that lows the frictional strength of the rock and takes a part of the forces that low the normal stress, without effect shear stress. So we could describe this effect with the relation that takes in account the effective stress  $\sigma^e$

$$\sigma^e = \sigma - p_f I$$

The frictional strength reduced by pore pressure is

$$\tau_f = \mu_f (\sigma_n - p_f)$$

so the brittle strength of the Coulomb – Navier criterion became

$$|\tau| = \tau_0 + \mu (\sigma_n - p_f)$$

That is the effective shear stress, while

$$p_c = \sigma_n - \tau / \mu$$

Is the critical pore pressure.

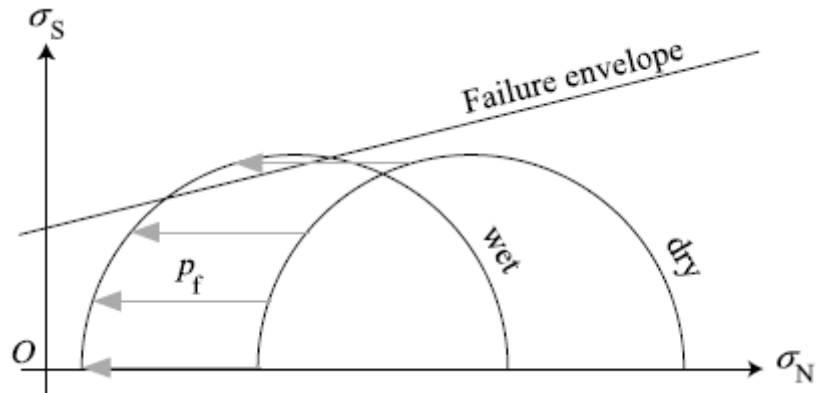


Figure 37 – Coulomb – Navier criterion. Contribution of pore fluid pressure to move the mohr circle of a reference fault to rupture.

In the figure [37] we can compare the mohr circles with and without the contribution of pore pressure. If  $\sigma$  is constant, increased pore fluid pressure shifts the circles to traverse the failure enveloper to activate a shear fracture, reducing the brittle strength of rocks. High pore-fluid pressures zones have several origins like dehydration associated with metamorphism, zones of sedimentary basins and tectonic stress that can control pore-fluid pressure.

An over pressured zone is where the pore-fluid pressure is higher than the hydrostatic pressure of the same depth.

Sleep and Blanpied (1994) showed that both the creation of micocracks during earthquakes in hydraulically clogged fault zones and the followind compactation, might lead to cycles of high pore fluid pressure along faults.

Tezuka 2000 studied the effect of pore pressure in relation with normal and shear stress. The figure shows the effective normal and shear stresses calculated as function of fracture angle  $\theta$  for the case where the maximum principal stress  $\sigma_1$  is twice large as the minimum principle stress  $\sigma_3$ . In the

left part of the figure(a) exists a shaded area which identifies stress conditions that can cause the full opening of fractures. Because the full fracture is completely open, it requires the pore pressure exceed the minimum principal stress, which degree of excess depend on the fracture angle  $\theta$ . In the right part of the figure (b) the shaded area shows condition where the effective shear stress becomes positive and failure occurs. So that denotes that shear slip may occur also for smaller pore pressure increases.

If the effective stress decrease, it's possible produce fracture dilation (Walsh and Grossenbaugh, 1979).

It's possible use the effective normal stress as index for fracture opening because the fracture walls are completely separated when this parameter is equal to zero.

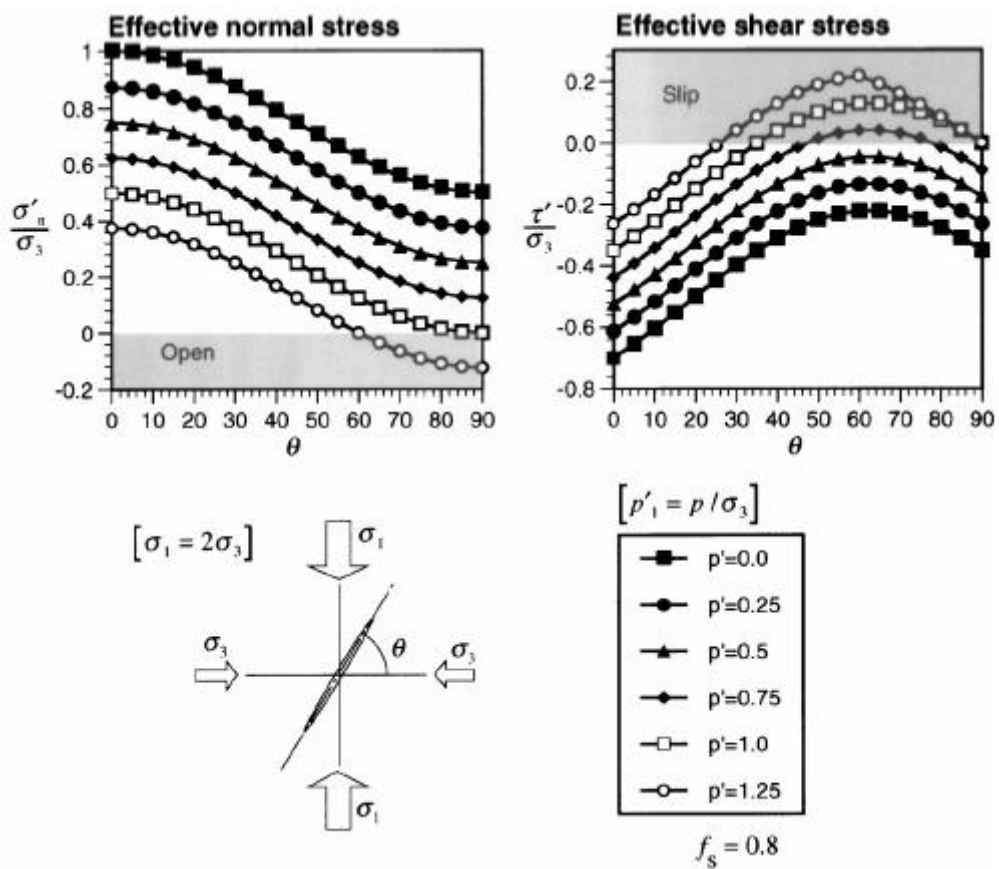


Figure 38 -Plots of effective normal stress (a) and effective shear stress (b) calculated as functions of fracture angle  $\theta$  and normalized by the minimum stress,  $\sigma_3$  (Tezuka, 2000).

Fractures and joints in the rock are assumed have rough surface on contact so the aperture is due to height of asperity which is supported by an elastic matrix (Tezuka 2000). The increase in stress normal to the fracture deforms the asperity and compresses the matrix and decrease the aperture of the fracture (Walsh and Grossenbaugh, 1979).

Using hydraulic injection to evaluate the interaction with stress field with natural fracture system, Tezuka (2000) concluded that the flow paths are created by shear slip along fractures created by elevated pore fluid pressure. These fractures are favourably oriented for shear failure and this orientation and the interaction with the stress field are important characteristics because they control the growth direction of the reservoir.

Many rock physics parameters contribute to changes in seismic velocities of rocks in addition to mineralogy, porosity and in situ stress conditions such as pore fluid properties, which depend on temperature and pressure (Birch, 1960; Spencer and Nur, 1976; O'Connell and Budiansky, 1974; Toksoz et al., 1976; Ito et al., 1979; Christensen, 1985; Wang and Nur, 1989; Sanders et al., 1995; Dvorkin et al., 1999b).

Pore fluid pressure may play a role by inducing a fluid phase transition as well as in keeping pores and cracks open. Dvorkin et al. (1999b) show that crack opening induced by increasing pore pressure leads  $V_p/V_s$  to decrease in gas-bearing rocks.

Vanorio (2005) demonstrate that for a given rock porosity, the increase of pore fluid pressure leads to a decrease in pore fluid compressibility and as a consequence, the  $V_p/V_s$  ratio increases. Assuming that increasing pore fluid pressure leads porosity to increase (for example crack opening).

Velocity anomalies and attenuation are decisive in discriminating volumes permeated by fluids (Nakajima and Hasegawa, 2003). The spatial variation of  $V_p$  may describe the distribution of lithologies and rock properties, and  $V_p/V_s$  ratio maps rock defects, pores and cracks, and their fluid contents. Fluid-filled pores in matrix rocks decrease  $V_p$  and  $V_s$  while variations in  $V_p/V_s$  of a matrix rock including fluids depend on the kind of fluids and on the shape of the pore (Nakajima and

Hasegawa, 2003; Scmeling, 1985; Takei, 2002).

Attenuation of elastic waves depends on many factors through which temperature and presence of fractures that may be permeated by fluids (Eberhart-Phillips et al., 2005)

It's possible quantify alteration using the quality factor  $Q$ , that is the ratio between the energy lost by a wave cycle and the energy of the cycle itself (De Siena, 2010) or through the attenuation coefficient  $\alpha = \pi f r / v Q$  that is a function of distance  $r$  and of frequency  $f$ . The coefficient may vary for the same amount of rock on the basis of chemical composition, temperature and degree of fracturing. In particular, for volcanic areas is essential to know either the  $Q_p$  P-wave quality factor and the  $Q_s$  S-wave quality factor for a complete characterization of the rocks inside the volcano cause the different response of the rocks to longitudinal and shear waves.

Ambiguous interpretation of the cause of velocity anomalies can be removed by a joint interpretation with  $Q_p^{-1}$  and  $Q_s^{-1}$  that may discriminate water filled media and gas reservoirs (Hansen et al., 2004). High attenuation anomalies may indicate presence of melt-filled inclusions, that are always characterized by high  $V_p/V_s$  ratio (Takei, 2002).

Perturbations of the pore pressure of a natural origin like rainfall (Ventura and Vilardo, 1999) may generate seismicity. Possible mechanisms of the induced microseismicity triggering are for example hydraulic fracturing, redistribution of elastic stresses and the pore pressure relaxation.

Shapiro et al. (2003) support the hypothesis that the triggering dominant mechanism is the diffusive process of the pore pressure relaxation in porous or fractured saturated rocks. In some locations in the crust, rocks are close to a critical state of a failure equilibrium so small perturbations of pore pressure modifying the effective normal stress leading to seismic events (Nur and Booker, 1972; Fletcher and Sykes, 1977; Ohtake, 1974; Talwani and Acree, 1985; Zoback and Harjes, 1997). So taking in account this hypothesis, the seismicity triggering in space and time must be controlled by the process of relaxation of the pore pressure perturbation  $p(t, r)$  created at an injection source

The differential equation of diffusion can be applied

$$\frac{\partial p(t, r)}{\partial t} = \partial D \nabla^2 p(t, r)$$

With:

D – hydraulic diffusivity,

t – the time

**r** – the radius vector of the observation point.

This relaxation describes linear relaxation of pore-pressure perturbations in a homogeneous, isotropic, poroelastic, fluid-saturated medium.

For anisotropic and heterogeneous poroelastic media Shapiro et al (1997-2000) and Audigane (2000) used the general form

$$\frac{\partial p}{\partial t} = \frac{\partial}{\partial x_i} [D_{ij} \frac{\partial}{\partial x_j} p]$$

$D_{ij}$  are components of the tensor of the hydraulic diffusivity heterogeneously distributed in the medium and  $x_j$  ( $j=1,2,3$ ) are the components of the radius vector. It's assumed that the probability of the triggering of microseismic events is an increasing function of the power of the pore pressure perturbation (Shapiro, 2003). At  $t_0$  given time it's probable that events will occur at distances which are smaller or equal to the size of the relaxation zone of the pore pressure.

Shapiro (2003) introduce the term "triggering front" that is the spatial surface between the point where occurred an event and the relaxation zone of pore pressure. The triggering front at the time  $t_0$  is the front of the zero phase at the time  $t'$  of a harmonic diffusion wave of pore pressure relaxation radiated with zero phase at the time 0 at the injection source with the frequency  $2\pi/t_0$ .

The radius of the triggering front in a homogeneous and isotropic medium is

$$r = \sqrt{4\pi Dt}$$

With  $t$  is the time of the injection start,  $D$  is a scalar hydraulic diffusivity.

Because seismicity is considerably more probable in the relaxation zone this equation corresponds to the upper bound of the cloud of events in the plot of their spatial-temporal distribution (Shapiro 2003). The shape of the microseismic clouds is more similar to an ellipsoid because location where

rocks are close to a failure equilibrium are randomly distributed in space. After the main event, pore pressure relaxation process as creep process on the rupture will reduce the pore pressure perturbation.

Shapiro(2003) suggests that a big main earthquake (as the Antofagasta earthquake M=8.0) may caused a pore-fluid pressure perturbation in its hypocentre which can be a result of deformations of the saturated porous space of rocks due to the rupture process in the hypocentre. Consequently, the relaxation of the pore-pressure perturbation in the fractured rocks along the subduction plane my triggering mechanism of the Antofagasta aftershocks.

Terakawa(2000) proposed a method based on mapping focal mechanism on 3D mohr diagrams using strike, dip angle and slip angle for a given stress state. Focal mechanisms spatial variation is due to fault strength heterogeneity, due in turn to pore pressure fluid spatial variation (Fig 39).

Fmt method is an analysis technique to estimate fluid pressure in depth from focal mechanism solution given by seismic events. They assumed that fault strength is controlled by coulomb faulting criterion, assumed constant friction coefficient and seismic slip in direction of shear traction acting on pre-existent fault.

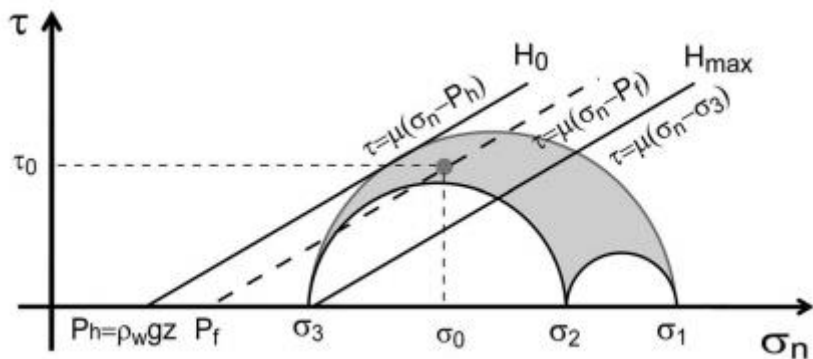


Figure 39 – Theory of FMT in 3D Mohr diagram. The horizontal and vertical axes show normal and shear stresses (Terakawa,2000)

Vertical and horizontal coordinates of each point show normal and shear stress acting on the plane, while relative position of that point show fault orientation in correspondence of the stress pattern.

When movement occurs and the shear stress equals strength fault, fault line intersection goes through this point and horizontal axis shows pore pressure fluid activating the event.

High pore pressure induces seismic slip on unfavourably oriented fault compared to tectonic stress pattern, also in absence of incremental shear stress.

The fault orientation in the stress field is a measure of fluid pore pressure.

The rupture occurs when  $\tau > \mu \cdot \sigma_n - p$ . If assuming that occurs also in the case  $\tau = \mu \cdot \sigma_n - p$

The pore pressure became  $p = \sigma_n - \tau/\mu$

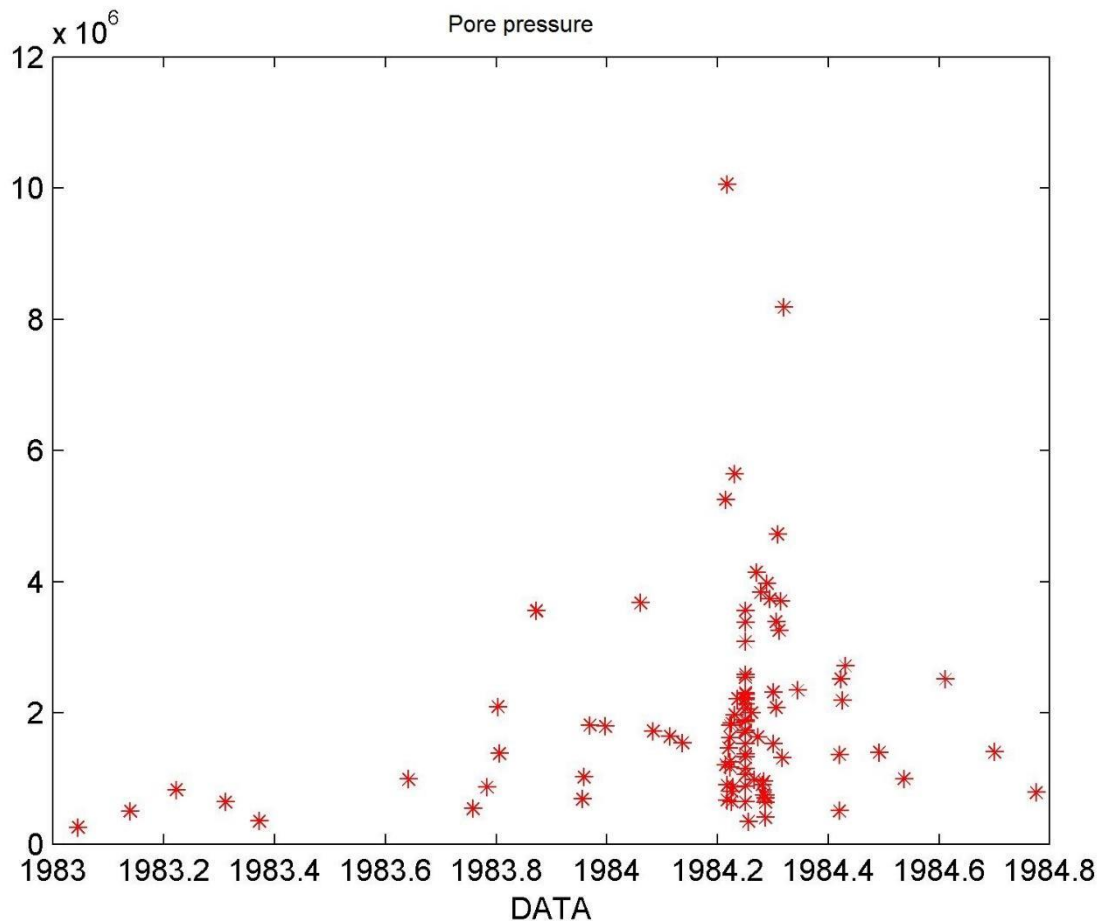
Terakawa(2012) evaluated the misfit between observed slip vector and the calculated shear traction vector, awaited by the stress pattern at hypocentre, for the solutions of two fault planes for each focal mechanism in the original dataset. As real plane they choose the solution with the lowest misfit.

Using a model around the studied area and tricubic splines to represent the fluid pore pressure field in the area.

So, starting from focal mechanisms, is possible estimate pore pressure acting on the fault during the seismic event. Has been implemented an algorithm in Matlab environment, that permits the estimation the pore pressure for each analysed fault. The algorithm starts from the values of Strike, Dip and Rake calculated from focal mechanisms, to deduce some parameters as principal stress and direction and traction vector to calculate Normal and shear stresses using the Angelier method(1982). Finally Normal and total shear stress has been used to extract the pore pressure and the excess of pore pressure following the Coulomb–Navier criterion. It has been imposed  $\mu = 0.6$ .

Results show an excess of fluid pore pressure in the flegorean area, with elevated value in particular in the months of February and April 1984 (Fig 38). The highest values are located between 2.5 and 3 km of depth. From the results it's possible assume that this excess may have strongly influenced the activation of faults, source of seismic events relative to the crisis. In the figures (40,41,42) have been plotted the results of this pore pressure analysis relative to date of occurrence of events

(Fig.40), depth vs data (Fig.41) where the size of the circles indicated the values of the excess of pore pressure, and pore pressure relative only to the depth.



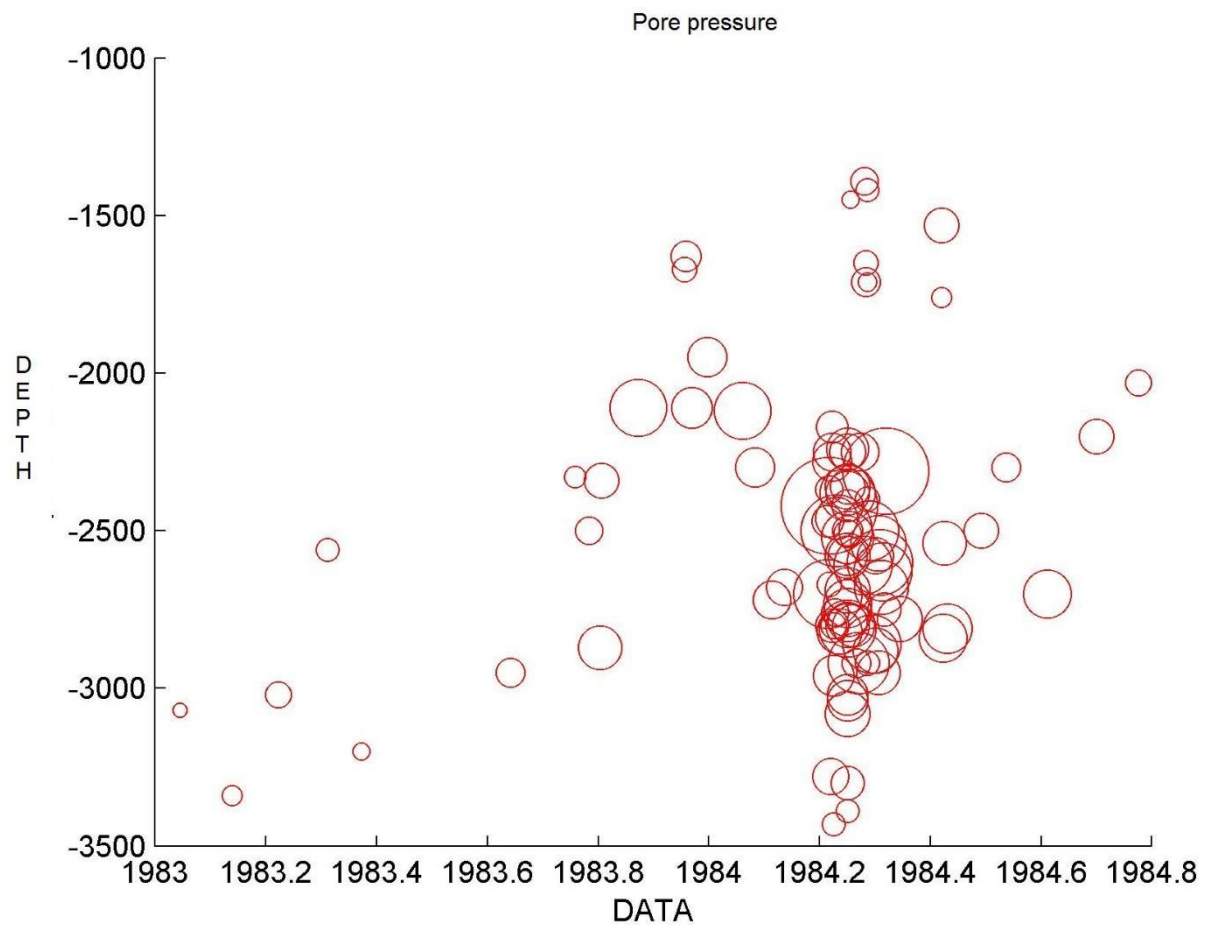


*Figure 41 – Value of excess of pore pressure in the area of Campi Flegrei during the Bradyseismic crisis –1982-84. The values are plotted in reference with depth and data. The size of the circles depend of the value of excess.*

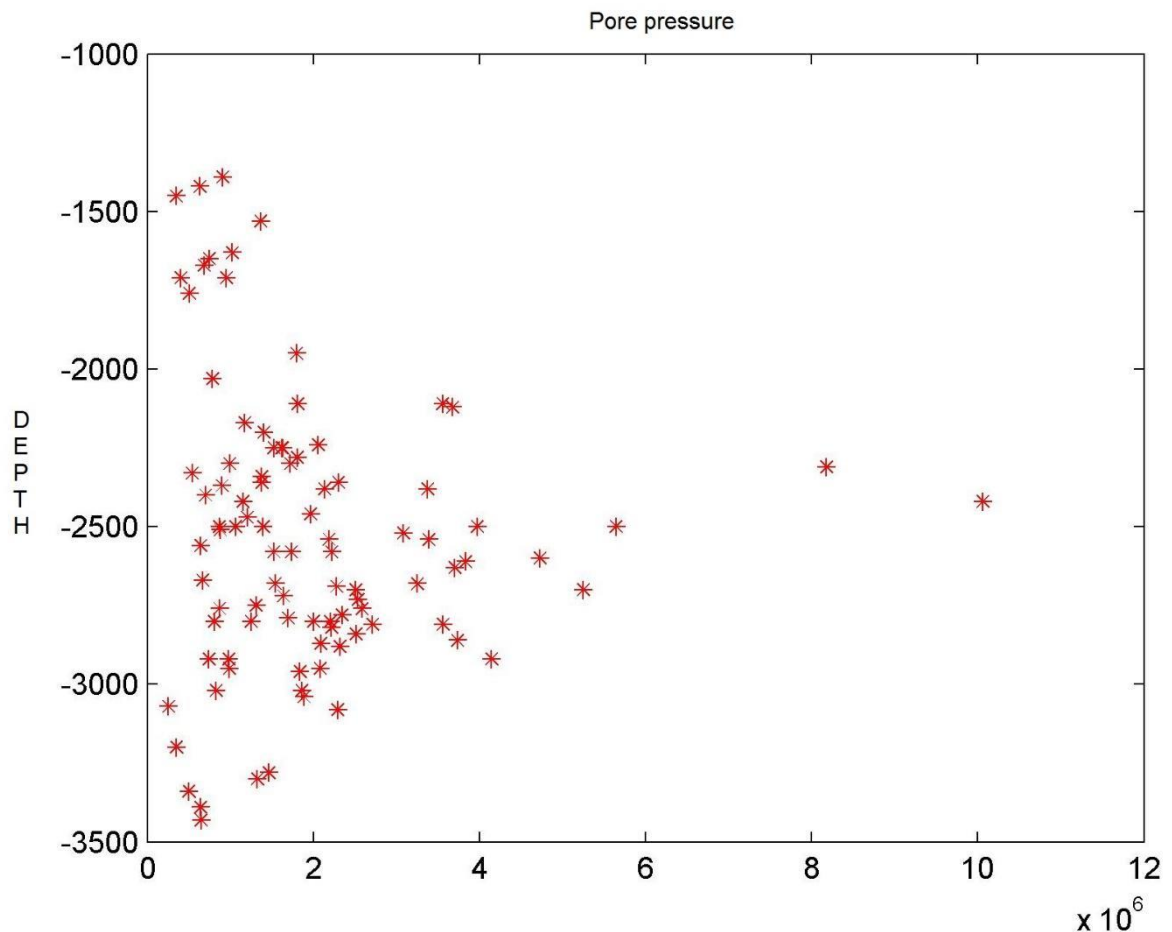


*Figure 42 – Value of excess of pore pressure during the Bradyseismic crisis in Campi flegrei area in reference of depth. It's possible view that the highest value are concentrated between 2.5 and 3 km of depth.*

Plotting the values on the map of flegrean area (fig. 43,44), it's clear that the excess of pore pressure area is comparable with the position of ground deformation calculated through the inversion of ground deformation data of the bradyseismic crisis.

vis

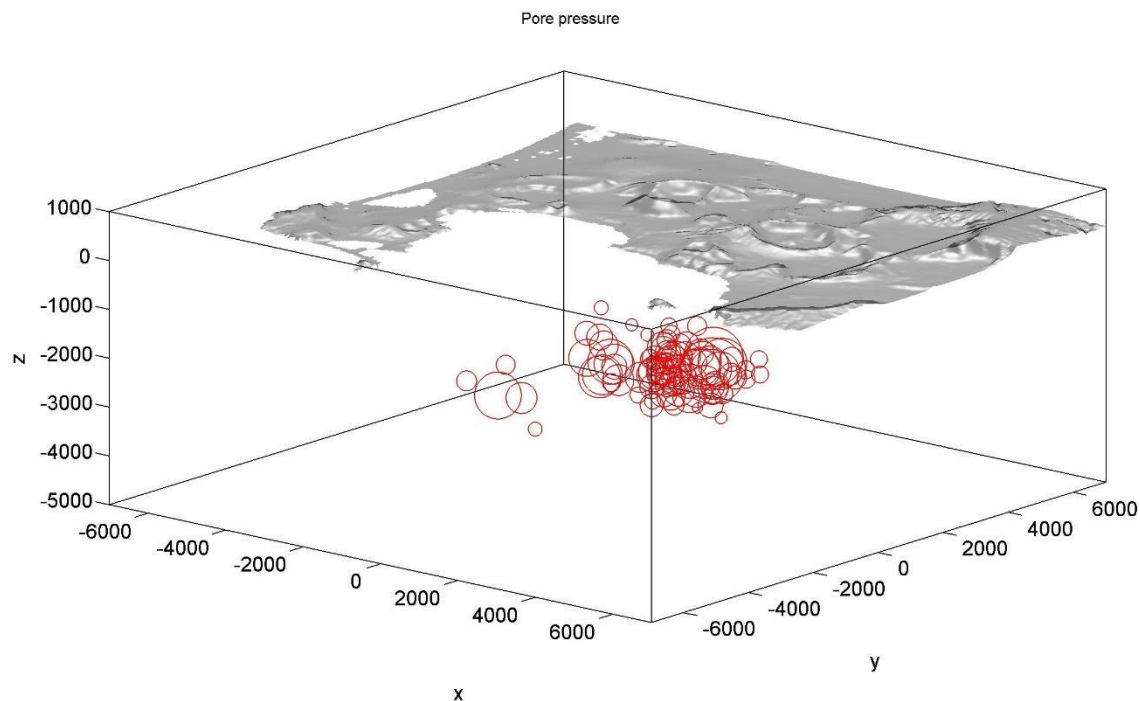


Figure 43 – values of excess of pore pressure plotting using a tomography of Campi Flegrei area. The values are divided in two cluster compatible with the source of ground deformation data.

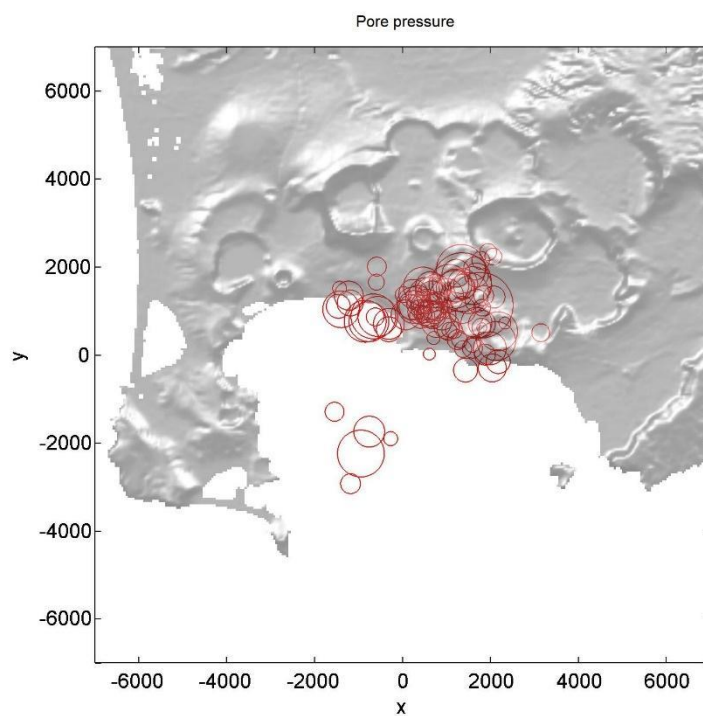


Figure 44 – view from above of the excess of pore pressure plotted on the Campli flegrei map.

### 5.3 Thermo – fluid simulations (MUFITS)

Exists several method that can be used for modelling of hydrothermal activity ( Pruess et al., 1999; Pruess, 2004; Ingebritsen et al., 2010). The most popular is TOUGH2 ( Pruess et al., 1999; Pruess, 2004;) and exist numerous example of its application on Campi Flegrei Caldera ( Todesco, 2009; Petrillo et al., 2013).

MUFITS reservoir simulator is non-commercial software developed for numerical modelling of different scenarios of subsurface exploration. The code is written in Fortran 90 and has a module-based internal structure (Adanasyev, 2013b). can be used to describe reservoirs subjected to faults, layers pinch-out, heterogenous and anisotropic petro-physical data etc. the simulator can also automatically create Cartesian and radial grids for simplified studies. The primary variables are the pressure, the mixture total enthalpy and the composition.

The choice to uses MUFITS (Afanashev, 2013 b) instead of TOUGH2 are the limitation that have that program regarding the impossibility of simulate flux with a temperature higher of the critical value of H<sub>2</sub>O under semi-critical condition. It's not possible uses TOUGH2 to hydrothermal deep flux where pressure and temperature exceed the critical value of H<sub>2</sub>O. So there isn't a way to modelize accurately the deep hydrothermal circulation, in particular in flegrean field where a hot mix flux CO<sub>2</sub>-rich arrive from a deeper magmatic source. The mix arise in superficial area where mixing again with meteoric water and cools and the transition happen through critical condition.

MUFITS simulator (Multiphase Filtration Transport Simulator) is intended for analysis of binary mixture flows in porous media subjected to wide pressure and temperature variations and critical thermodynamic conditions. (Mufits manual)

The primary hydrodynamic variables for simulation, that uses MUFITS are pressure, molar enthalpy and mixture composition.

The flow is described by the equations:

- $\frac{\partial}{\partial t} \left( \frac{1-m}{v_s} \right) = 0$  mass conservation equation for rock material. M is the porosity, v

the molar volume, s-index denotes parameters of rocks.

- $\frac{\partial}{\partial t} (m \sum_{i=1}^3 \frac{M_{(j)}x_{i(j)}}{v_1} s_i) + \operatorname{div} (\sum_{i=1}^3 \frac{M_{(j)}x_{i(j)}}{v_1} w_i + D_{(j)}) = Q_{(j)}$   $j = 1, 2$

mass conservation equation for each component of the binary mixture.

- $\frac{\partial}{\partial t} (m \sum_{i=1}^3 \frac{e_i}{v_i} s_i + (1-m) \frac{e_s}{v_s}) + \operatorname{div} (\sum_{i=1}^3 \frac{h_i}{v_i} w_i + D_e) = A_g + Q_e$  energy

balance equation with M the molar density, x- component molar fraction, s- saturation, w- darcy velocity, e- internal energy, h-enthalpy, D-fluxes caused by diffusion and heat conduction, Q- a given sinks and sources rates, Ag – work done by gravity

- $A_g = \sum_{i=1}^3 \frac{M_i}{v_i} w_i g$  work done by gravity with g the gravity acceleration.

Indexes denote phase parameters

- $w_i = -K \frac{f_i}{\mu_i} (\operatorname{grad} p_i - \frac{M_i}{v_i} g), \quad i = 1 \dots 3$  Darcy correlation with K rock

permeability, f-relative permeability, mu viscosity, p pressure

- $x_{i(1)} + x_{i(2)} = 1, \quad M_i = M_{(1)}x_{i(1)} + M_{(2)}x_{i(2)} \quad x_i \equiv x_{i(1)}$  relations between molar fractions and molar densities are true.

- $\sigma(P, h, x)$  thermodynamic potential of binary mixture where the entropy depending on pressure, enthalpy and mixture composition.
- $\sum_{i=1}^3 \sigma(P, h_i, x_i) V_i \rightarrow \max, \quad \forall t, r$  conditional maximum problem solved for thermodynamic equilibrium of binary mixture determination. T is the time, r is the spatial location, V is phase molar fraction. P pressure, ht total enthalpy, xt composition of the mixture.
- $\sum_{i=1}^3 V_i = 1 \quad \sum_{i=1}^3 h_i V_i = h_t \quad \sum_{i=1}^3 x_i V_i = x_t \quad 0 \leq V_i \leq 1$  relations defined by temperature, volume, internal energies
- $T = \left(\frac{\partial \sigma}{\partial h}\right)^{-1} (P, h_i, x_i), \quad v_i = -\frac{\partial \sigma}{\partial P} \left(\frac{\partial \sigma}{\partial h}\right)^{-1} (P, h_i, x_i) \quad e_i = h_i - Pv_i$  relations defined by temperature, volume, internal energies
- $s_i = \frac{v_i V_i}{\sum_{k=1}^3 v_k V_k} \quad i = 1 \dots 3$  set relations between phase molar fractions and saturation
- $\mu(P, h, x) \quad \mu_i = \mu(P, h_i, x_i)$  a given viscosity function depending on pressure, enthalpy and composition of the mixture

- $f_i = f_i(s_1, s_2, s_3, P, h_t, x_t, r)$ ,  $P_i = P_i(s_1, s_2, s_3, P, h_t, x_t, r)$  relative permeability and phase pressure depending on thermodynamic equilibrium of binary mixture
- $m = m(P, T, r)$ ,  $K = K(P, T, r)$ ,  $e_s = e_s(P, T, r)$  set reservoir rock properties dependence on thermobaric conditions.

So, Mufits is designed for simulation of non-isothermal flows of binary mixtures in a porous media.

The property of the mixture are specified by thermodynamic potential  $\sigma(P, h, x)$  where P is the pressure, h the molar enthalpy, x a mixture molar composition and  $\sigma$  the molar entropy.

The multiphase flows of CO<sub>2</sub>-H<sub>2</sub>O mixture is described using the system of balance equations of mass, energy together with the Darcy equations for modelling multiphase flows of CO<sub>2</sub>-H<sub>2</sub>O mixture:

$$\frac{\partial}{\partial t} \left( \phi \sum_{i=1}^p \rho_i c_{i(j)} s_i \right) + \operatorname{div} \left( \sum_{i=1}^p \rho_i c_{i(j)} w_i \right) = 0 \quad j = 1, 2 \quad (x)$$

$$\frac{\partial}{\partial t} \left( \phi \sum_{i=1}^p \rho_i e_i s_i + (1 - \phi) p_r e_r \right) + \operatorname{div} \left( \sum_{i=1}^p \rho_i h_i w_i - \underline{\lambda} \operatorname{grad} T \right) = 0 \quad (x2)$$

$$w_i = -K \frac{f_i}{\mu_i} (\operatorname{grad} P - \rho_i g) \quad i = 1, \dots, p. \quad x3$$

With

- $\Phi$  porosity
- p number of phases
- i and j subscripts refer to the phase and the component of the fluid mixture
- R subscript refer to the rock.
- $c_{i(j)}$  the j-th component mass fraction in the i-th phase
- $s_i$  the i-th phase saturation

- $\rho_i$  the density
- $w_i$  the darcy velocity
- $e_i$  is the internal energy
- $h_i$  is the specific enthalpy,
- $f_i$  the relative permeability
- $\mu_i$  the viscosity
- $\lambda$  the effective heat conductivity
- $T$  the temperature
- $k$  the absolute permeability of the matrix
- $P$  the pressure.

The three-phases (liquid H<sub>2</sub>O, CO<sub>2</sub>, and gaseous CO<sub>2</sub>) equilibria of CO<sub>2</sub>-H<sub>2</sub>O mixture are possible under relatively low temperature and pressures. Under elevated temperatures, only two-phase equilibria, formed by H<sub>2</sub>O-rich and CO<sub>2</sub>-rich phase are possible. The parameters of host rock are given by

$$\rho_r = \text{const}, e_r = C_r T, \lambda_r = \text{const}$$

With  $C_r$  is the rock heat capacity. The effective heat conduction coefficient is described as

$$\underline{\lambda} = (1 - \phi)\lambda_r.$$

To predict CO<sub>2</sub>-H<sub>2</sub>O mixture properties, has used cubic equation of state (EoS) in a wide range of pressures and temperatures (Afanashev, 2013a). The coefficients of the equation of state for the mixture are determined by a nonlinear regression to a large number of laboratory measurements of the mixture properties, which are provided in the literature (Todcheide and Franck (1963), Takenouchi and Kennedy (1964), Seitz and Blencoe (1999) and Fenghour et al. (1996)).

In fig. xx there are the representation of CO<sub>2</sub>-H<sub>2</sub>O mixture pressure-composition phase diagram for the range of temperatures from 150°C to 350°C. The green curve, calculated using fitted EoS, bounds the two-phase state region. The points are the laboratory measurement of Todcheide and

Franck (1963) and Takenouchi and Kennedy (1964). Only these datasets are used in fitting EoS to two-phase equilibria of CO<sub>2</sub>-H<sub>2</sub>O mixture. The shape of the two-phase state region is very sensitive to temperature: a small variation of temperature result in a significant shift of the two-phase state envelope. At high temperatures, T=257–350°C a maximum pressure for the two-phase equilibria exist (yellow region). C is the critical point for the given temperature. At higher pressures, there is a continuous transition from aqueous phase to CO<sub>2</sub>-rich liquid as CO<sub>2</sub> molar fraction increases. If the temperature increases, approaching the critical temperature, the two-phase state region becomes smaller.

Fig 45 and 46 give the possibility to estimate the accuracy of volumetric properties prediction. The lines represent the EoS results, the points are laboratory data for the density. The lines are passing through the points ensuring a good accuracy of EoS in prediction the mixture density.

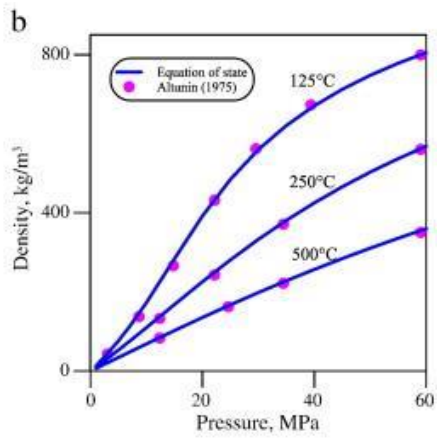
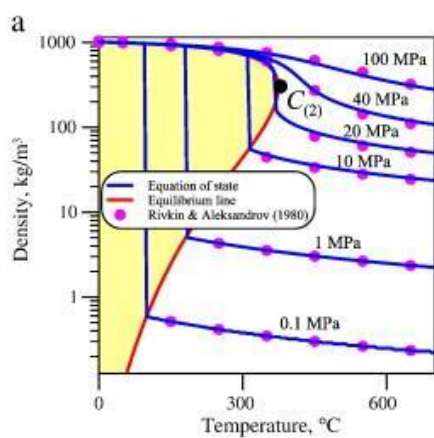
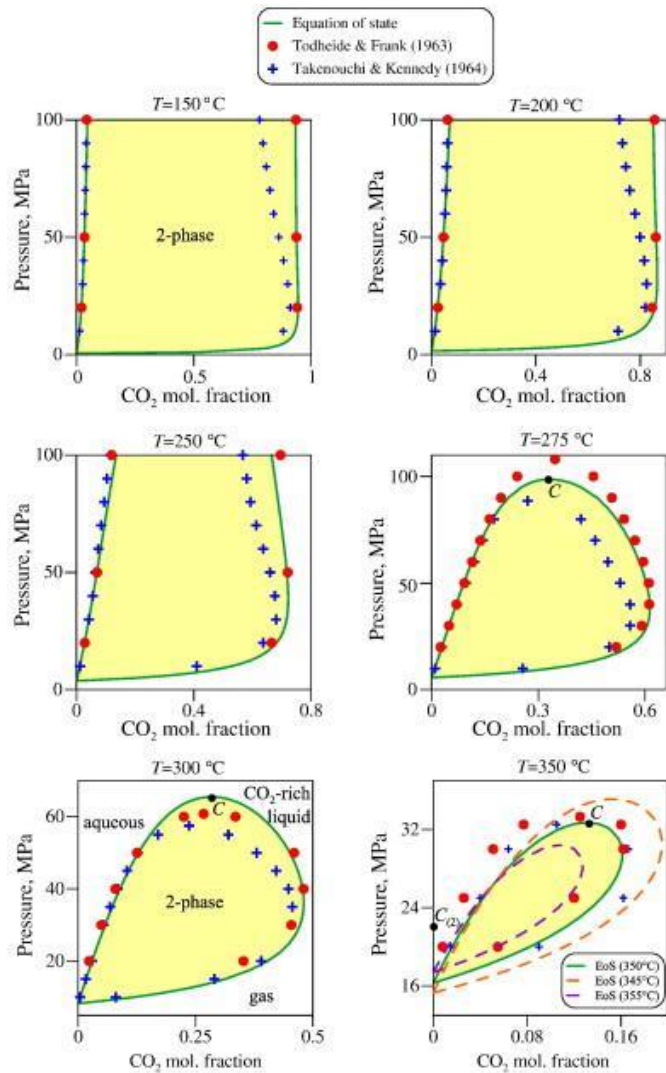


Figure 45- Densities of pure  $H_2O$ (A) and  $CO_2$ (B)

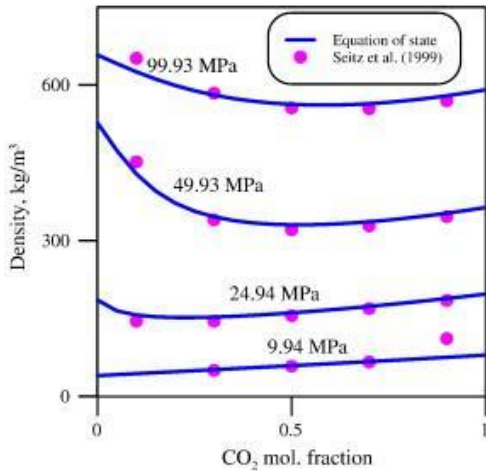


Figura 46 – Density of  $\text{CO}_2\text{-H}_2\text{O}$  mixture at  $T=400^\circ\text{C}$

MUFITS has been firstly applied on Campi Flegrei caldera by Afanasyev, Costa and Chiodini (2015) that consider the hydrothermal convection at Campi Flegrei caldera to demonstrate the flexibility and the robustness of MUFITS considering the parameters of controlling mass and energy flows in Campi Flegrei hydrothermal system. (FIGURE)

## 5.4 The Campi Flegrei caldera Model

The model take in account was which proposed by Chiodini et al. (2015) with a magmatic source degassing at 4 km in depth. In this model, the gas mixes with gases of hydrothermal system creating a plume that arise under the Solfatara crater.

Through TOUGH2 code (Pruess, 1991, 2004) Petrillo et al. (2013) created a 3D innovative model of CF that takes in account different rock physical properties , the bathymetry of the submerged part of the caldera and the aquifer tomography.

In this work has been used the permeability and porosity model derived from density value obtain by tomographic inversion of gravity data. This data have been retrieved applying empirical relations

on published data on samples cored in deep wells or sampled in outcrops at CF caldera (Zamora et al., 1994; Vanorio et al., 2002; Giberti et al., 2006).

The density value ( $\rho$ ) values express in  $g\ cm^3$  were firstly transformed in porosity ( $\phi$ ) following the empirical relation

$$\phi(\%) = -39 \times \rho + 113$$

The estimated error, associated to the porosity is about 7% (has been used a L2 norm because the errors follows the Gaussian distribution). The highest values characterize the shallowest levels and the caldera filling according to the density distribution. This porosity data were used to estimate the permeability values using the approach of Costa(2006) where permeability depend on  $\phi$  expressed as volumetric fraction:

$$k = Cc \times \phi^m / (1 - \phi)$$

Where Cc and m are two parameters depending on the rock types and by Costa (2006), for volcanic products, the best estimation of Cc is  $6.15 \times 10^{-13} m^2$  and 2.89 for m. Petrillo et al (2013) used k- $\phi$  measurement (Vanorio et al., 2002; Giberti et al., 2006) to estimate Cc for CF tuffits which are the most diffuse type of rock caldera filling. So, Cc is  $1.58 \times 10^{-13}$  and m is 2.632, estimating from the last equation considering a non-linear least square approach.

The permeability range vary from  $5 \times 10^{-17}$  to  $7 \times 10^{-14} m^2$  with the highest values in the shallowest levels and in the caldera filling.

Following the line of Petrillo et al. (2013) the computational domain consists of a parallelepiped 3000 m high and 12000 m of length and width, saturated with water and CO<sub>2</sub>, differentiated in 21853 same sized elements. The bottom boundary and vertical side are imposed impermeable to the fluids flow. The bottom and top boundary surfaces are fixed at specific temperature and pressure conditions and the top boundary is open to heat and fluids flow. The temperature was fixed at the top at 10°C as the average value of the area, and the pressure is 0.1 MPa, supposing that the reservoir is connected to the atmosphere saturated by pure gaseous CO<sub>2</sub>, varying with depth, set according to an averaged linear thermal gradient of 0.13 °C/m, while the pressure was assumed at

atmospheric value for top boundary, linearly increasing with depth following the hydrostatic gradient. At the bottom the pressure was fixed at 27 Mpa and the temperature at 400°C. The model is initially saturated by water and low CO<sub>2</sub> contents. The entire domain is set with rock's physical properties that in most cases were derived by density values obtained with tomographic inversion of gravity data recorded by several survey at CF( Imbò et al., 1964; Maino and Tribaldo, 1971)(Fig. 47). The heat capacity and rock heat conductivity were taken from Todesco et al., (2003), the relative permeability was set following Brooks and Corey (1964):

value	Rock properties
2400 kg/m <sup>3</sup>	rock density,
1Kj/kg/K	rock heat capacity,
1.5 W/m/K	rock heat conductivity

*Table 4 – rock properties during the simulation*

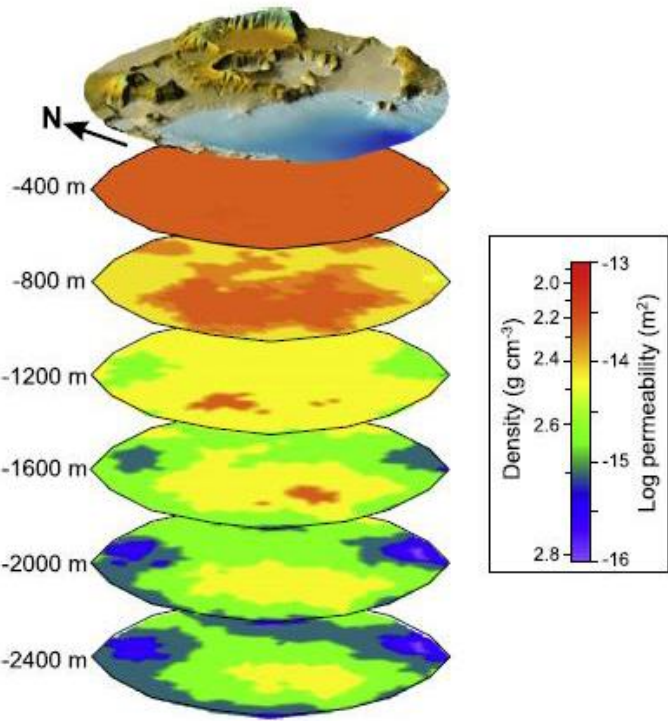


**Table 1**  
Rock properties during the simulations.

Rock type	Grain density ( $\rho$ , kg m $^{-3}$ )	Porosity ( $\phi$ )	Permeability ( $k$ , m $^2$ )	Heat conductivity ( $\lambda$ , W m $^{-1}$ °C $^{-1}$ )	Heat capacity ( $C$ , J kg $^{-1}$ °C $^{-1}$ )
<i>Case a)</i>					
Rock1	2400	0.2	1E-15	1.5	1000
Bottom	2400	0.03	1E-19	1.5	1E+6
Sea	2400	0.1	1E-16	1.5	1000
Top	2400	0.45	3.66E-14	1.5	1000
<i>Case b)</i>					
Rock1	2400	0.2	1E-14	1.5	1000
Bottom	2400	0.03	1E-19	1.5	1E+6
Sea	2400	0.1	1E-16	1.5	1000
Top	2400	0.45	3.66E-14	1.5	1000
<i>Case c) and 3D complete</i>					
Rock1	2340	0.45	3.66E-14	1.5	1000
Rock2	2470	0.39	2.27E-14	1.5	1000
Rock3	2660	0.26	6.28E-15	1.5	1000
Rock4	2760	0.17	1.91E-15	1.5	1000
Rock5	2810	0.12	6.46E-16	1.5	1000
Rock6	2830	0.08	2.12E-16	1.5	1000
Rock7	2860	0.05	7.68E-17	1.5	1000
Bottom	2860	0.03	1E-19	1.5	1E+6
Sea	2400	0.1	1E-16	1.5	1000
Top	2340	0.45	3.66E-14	1.5	1000

*Figure 47– Petrillo et al. Horizontal slices of the Heterogeneous 3D model based on the density tomography of the Campi Flegrei caldera. Table of rock properties during simulations.*

## 5.5 Simulations of the Hydrothermal system

Several tests have been performed by varying the parameters within unrealistic and realistic ranges, to try the capability of the program Mufits and to choose the appropriate parameters for Campi Flegrei.

Simulation consisted in injection of fluid  $CO_2/H_2O$  at 2700 m in depth from a rectangular source of 3x3x1 cells located under the Solfatara crater, comparable with which founded from the inversion of ground deformation data. To better estimate the best model, was done may simulation varying the temperature, pressure and injection rate (Tabel 5).

For test the software, the initial simulations were done by made two injection in variable time for the first one (3000 and 1000 years) and 20 years for the second injection, of a hot mixture of a CO<sub>2</sub>-H<sub>2</sub>O, varying the injection temperature, pressure and rate as the table (5). The rate of the first injection has been fixed to 642.2 ton/day for each cell of the source, following the rate of 67 kg/s used by Petrillo et al(2013). The rate of the second injection was variable of a multiplied rate of ten to fifty times the rate of the first injection.

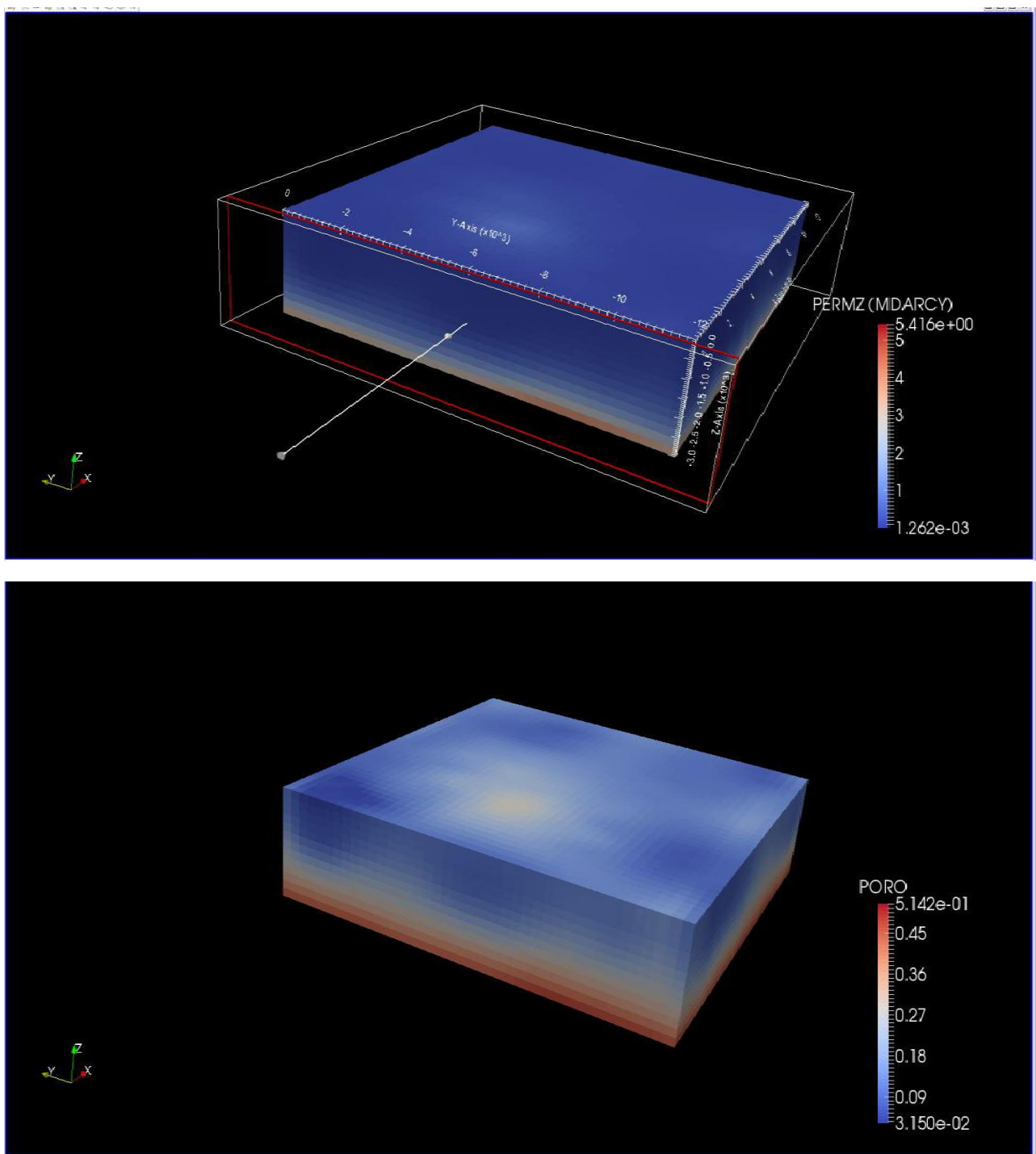


Figure 48,49 – Simulations of Campi Flegrei System. a) is the representation of permeability, b) represent the distribution of porosity in the area.

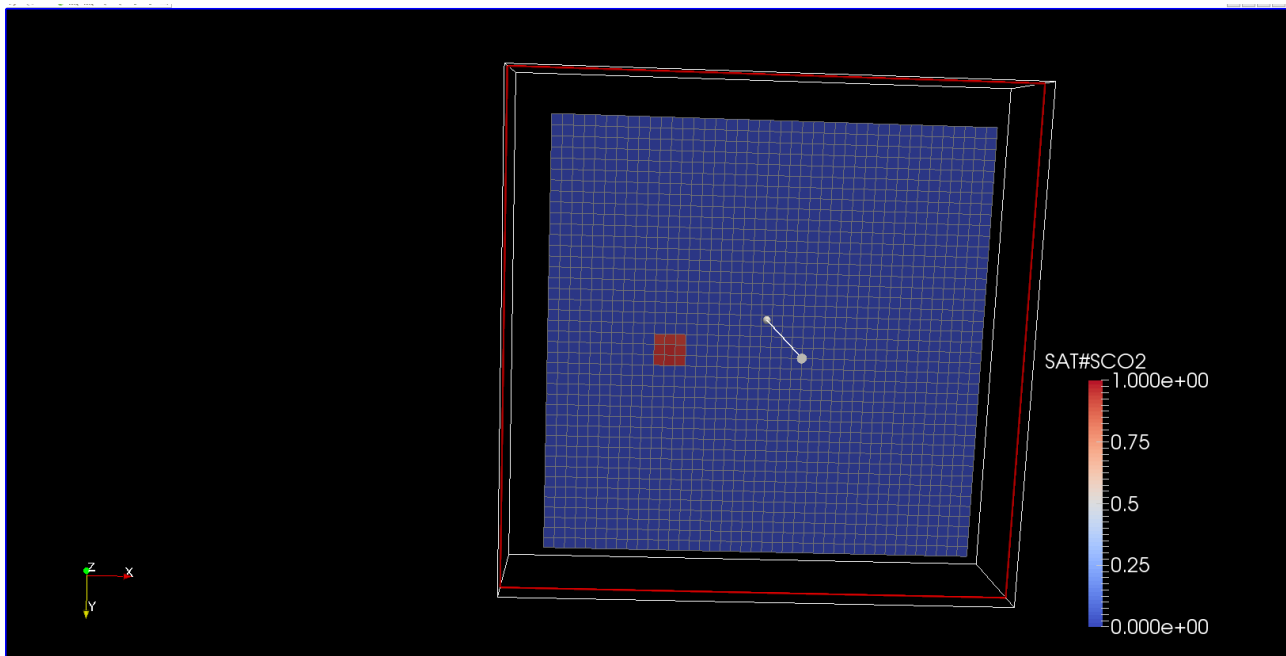


Figure 50 – Source of injection used during the simulation.

Table 6 contains value of tests done with two injections. For the first injection has been tried all the possibility with temperature from 600°C to 900°C, injection pressure of 50 and 100 Mpa. For the second injection instead was noted that increasing the injection rate, high temperature or pressure need to be lower. Otherwise the simulations are unsuccessful.

*Table 6 – Parameters for the first injection*

Injection rate	Injection temperature	Injection pressure	Years of injection
<b>5779.8 (ton/day)</b>	<b>900–600 °C</b>	<b>50,100 Mpa</b>	<b>1000,3000</b>

*Table 6b- Parameters for the second injection*

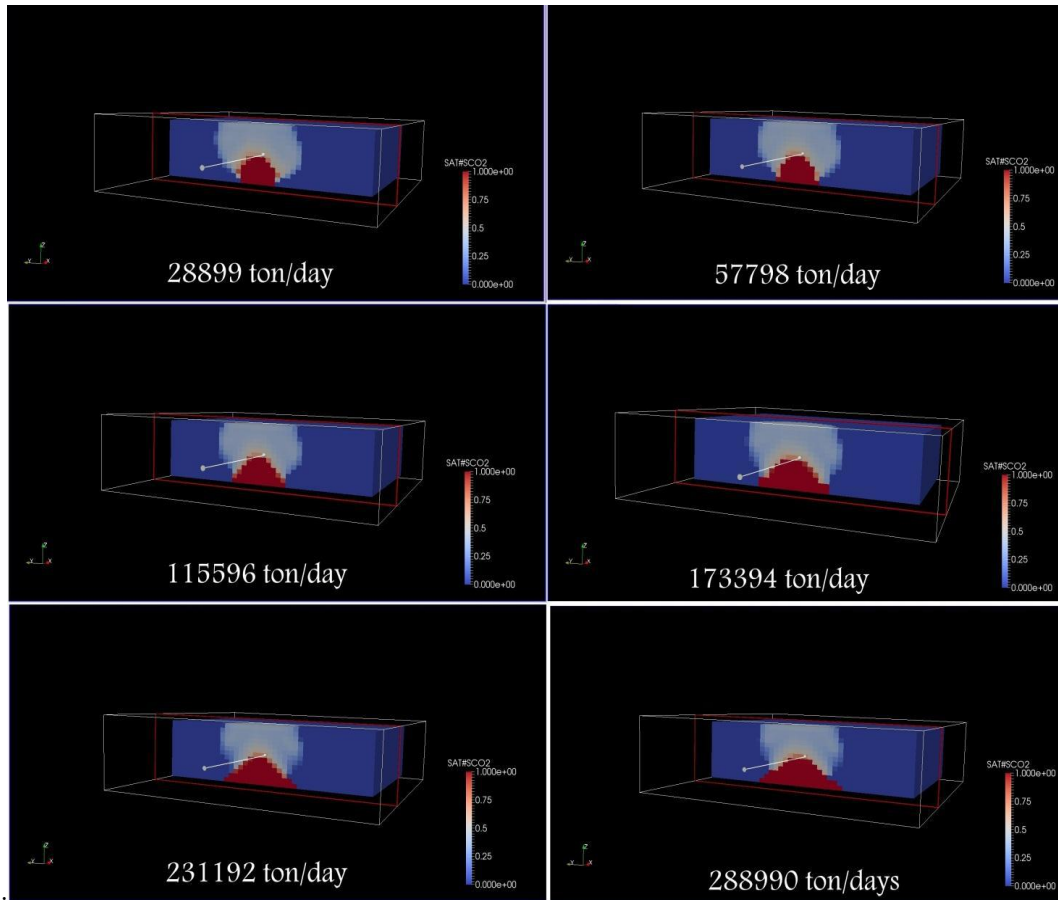
Injection rate	Injection temperature	Injection pressure	Years of injection
<b>28899 (ton/day)</b>	<b>800°</b>	<b>100 Mpa</b>	<b>20</b>
<b>57789 (ton/day)</b>	<b>800°</b>	<b>100 Mpa</b>	<b>20</b>
<b>115596(ton/day)</b>	<b>800°</b>	<b>100 Mpa</b>	<b>20</b>

173394(ton/day)	800°	100 Mpa	20
231192(ton/day)	700°	30 Mpa	20
288990(ton/day)	700°	20 Mpa	20

### 5.5.1 Results

The injection of hot fluids by the source through the medium generates a thermal perturbation propagating toward the surface. Regarding the simulation test done with two injections with variable time, rate, pressure and temperature of injection, in the most cases, the results are similar. For the first hundreds of years the temperature pattern is dominated by a central plume starting from the source and propagates toward the surface as an axisymmetric structure. After about 1000 years of run, the flow laterally spreads from the central plume, reach the surface and expands radially from the central plume. The diameter of the expansion and velocity of reaching the surface depends on the duration and rate of injection. With high value of injection rate and long-time of injection, the expansion is bigger than the other either at the surface than at the bottom. With lower rate the dispersion of the flux at the bottom is limited immediately under the source, for higher value, is visible also a laterally expansion of the perturbation (Figure 49). Other test has been done also considering just one injection instead of two. Differences between the comparison of the results are relative of the bottom expansion. With just one injection just few cells under the source are included in the perturbation. The parameters that better evidenced the difference of these results are saturation (SAT#SCO2) and Temperature (TEMPC). Different time of injection marked a visible change in the shape of perturbation. Testing for just 1020 years, the shape remember a mushroom with the higher values in the immediate vicinity of the source. Testing for 3020 years, the higher value are concentrated around a vertical almost cylindrical area well defined over and under the

source, and the diffusion of saturation on the surface is at least two order of magnitude than the injection tests for 1020 years. The higher value in the longer-time injection almost reach the surface



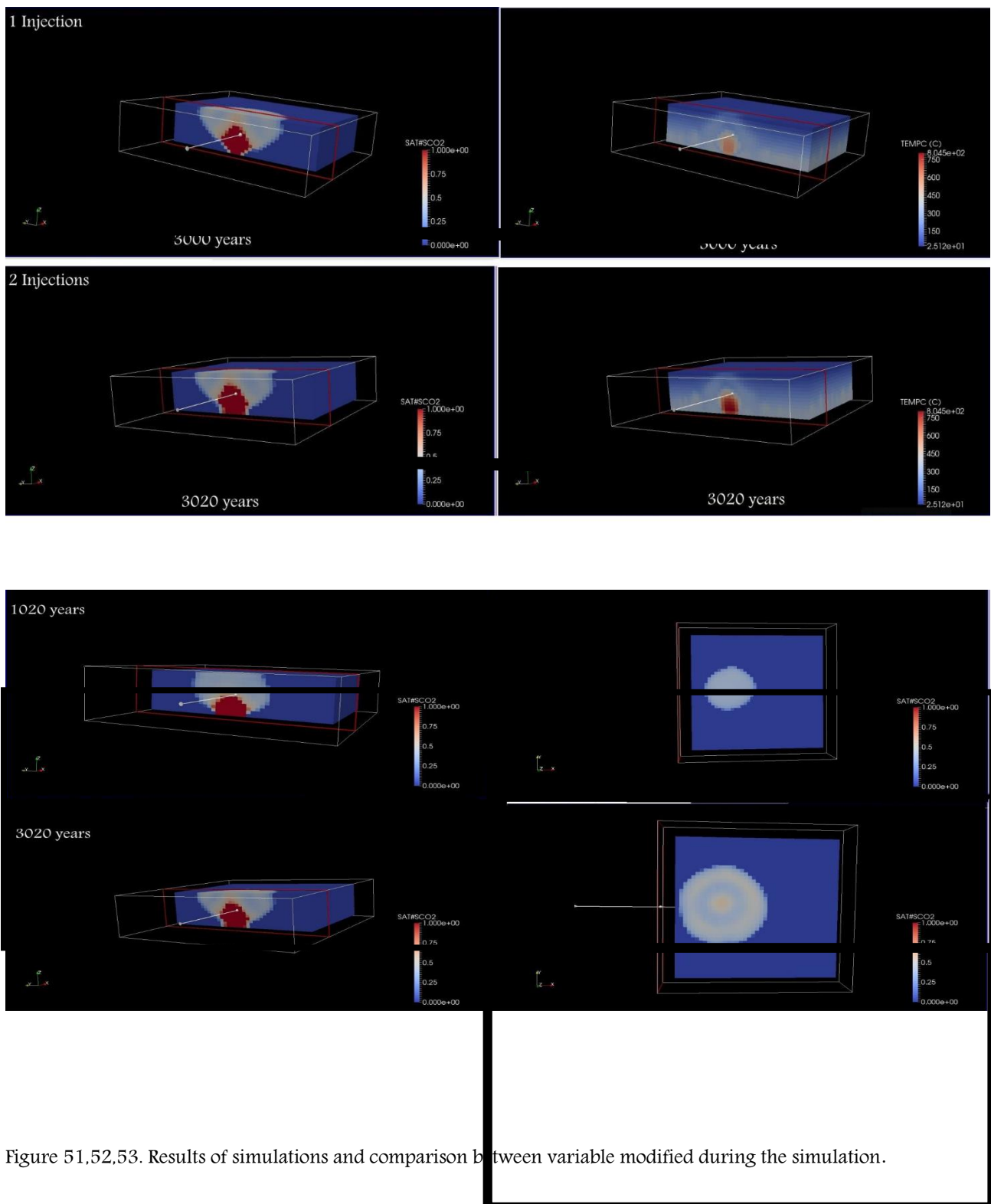


Figure 51,52,53. Results of simulations and comparison between variable modified during the simulation.

## 5.6 Bradyseismic crisis simulations

Than, has been performed a roughly simulation to represent the bradyseismic crisis 1982–1984, consisted in just one injection of 2 years. Also in this time has used a variable rate starting from 642.2 ton/day for each cell of the source to a multiplied rate from ten to fifty times the initial rate, varying the injection temperature and pressure as the table (6), to estimate the best model that may represent the unrest period. So it has been supposed that for the bradyseismic crisis, the source of ground deformation was just one injection hold for two years due to a hot mixture of CO<sub>2</sub>-H<sub>2</sub>O entered in the system with high temperature and pressure. The source was located near the town of Pozzuoli at 2700 m in depth, consisting in 3x3x1 cells (Fig 50) same as the previous simulations. Tabel 7 contains values of parameters test done with program Mufits. For two years of injection all the values tried give in output a good simulation.

*Table 7– Parameters of simulation of bradyseismic crisis 1982–1984*

Injection rate	Injection temperature	Injection pressure	Years of injection
5779.8 (ton/day)	800–600 °C	5– 50,100 MPa	2
11559.6 (ton/day)	800–600 °C	5– 50,100 MPa	2
17339.4 (ton/day)	800–600 °C	5– 50,100 MPa	2
28899 (ton/day)	800–600 °C	5– 50,100 MPa	2

### 5.6.1 Results

Mufits outputs are characterized by a .txt files day by day, with results of interest values for each cells of the grid. In the figure dsb have been plotted two days of 730 simulated that are representative of the results obtained. The results are referred to the injection 1, that is the more

realistic scenario regarding the injection rate, following the simulation done by Petrillo et al., (2013). The temperature choose is the intermedia ( $700^{\circ}$ ) and the pressure of injection in this case is 100 MPa in order to estimate the worst case of the simulation performed.

The magenta stars are referred to the day 109, that has been choose just as a sample of the initial period of the injection. The blue stars are referred to day 730 that is the last day of simulation. As is possible to see, the comparison shows a clear increase of the pressure during the constant injection until the end of the simulation. The value, in the figure 54 are represented in MPa, are confrontable with the results obtained by the pore pressure excess retrieved from the focal mechanism dataset. There is an overpressure that increase with the injection in particular in the area around the source of the injection that is at about 2700 m in depth comparable with the estimated source of the bradyseismic crisis of 1982–84, obtained by the inversion of the ground deformation data.

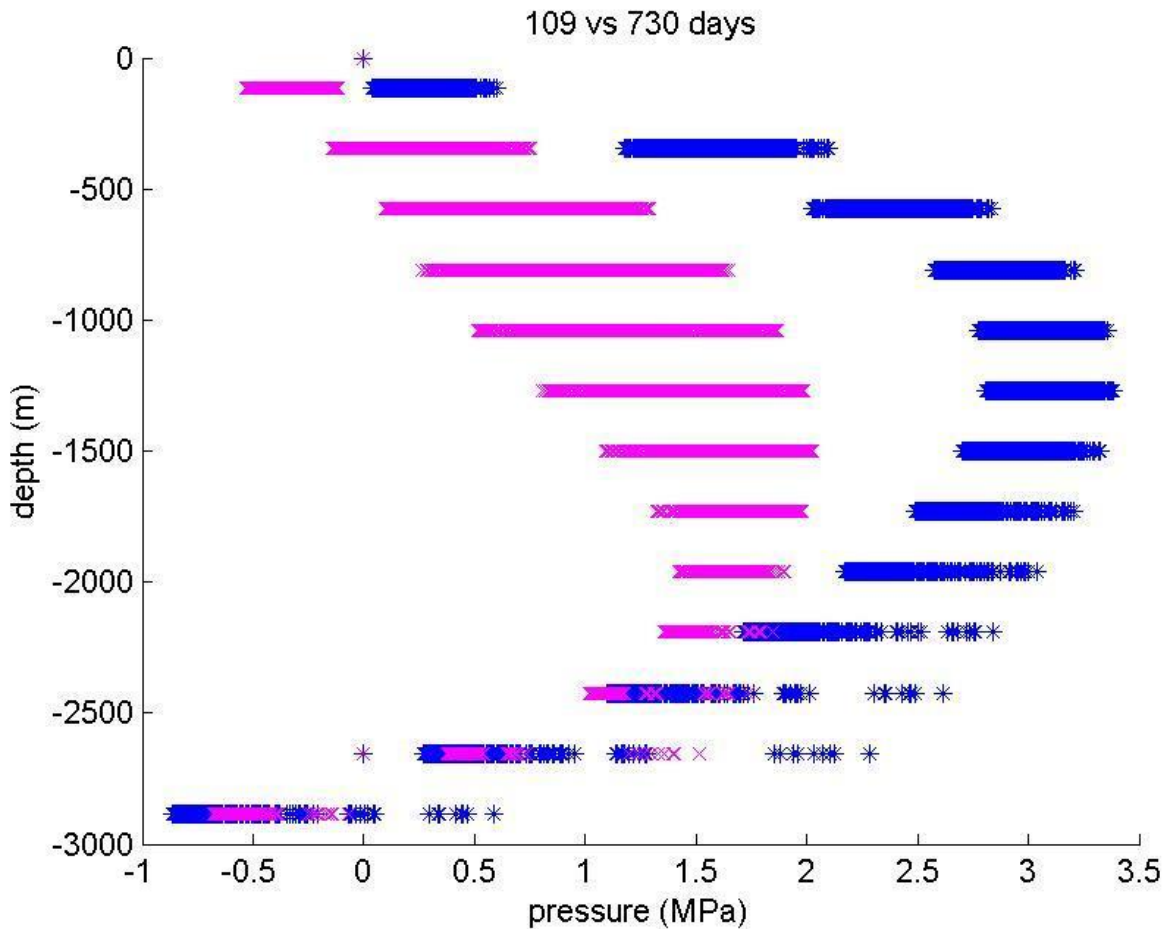


Figure 54 – Comparison between two days of simulation. The magenta one is a day sample choose to represent the initial part of the injection. The blue one represents the last day of the simulation. Is visible an increase of overpressure in particular in the area above the source choose for the injection. the value are comparable with the results relative to the excess of pore pressure obtained from ground deformation data.

## 5.7 Discussions

In this work has been done a complete analysis of Campi Flegrei caldera and its main characteristics to better understand the dynamic of the interest area. Starting from the analysis of cartaceous dataset of the 1970 and 1982–84 unrest crisis, complete seismological analysis has been performed where was possible. All the retrieved recorded events were located and where possible has been extrapolated the focal mechanism. The inversion of focal mechanism dataset has been performed

to estimate the behaviour of the stress field of the area during the bradyseismic crisis that interested Campi Flegrei caldera in 1982–1984 and has been compared with the records done from 1989 to 2012 where other minor unrest events interested the area. In order to complete this analysis, two methods in comparison have been used (MIM and RDM). The overall results show that the stress field acting in the Campi Flegrei Caldera during the 1982 unrest is dominated by a well-defined sub-vertical  $\sigma_1$  and a less defined sub horizontal  $\sigma_3$  with a prevalence of NNE–SSW trends, with visible spatial and temporal variation during the crisis. At the same time has been performed also a non-linear inversion of an optical levelling dataset to determine the source causes of the deformation which, as shown from the best-fit ground deformation analysis, is a simple subhorizontal crack 8x8x4 km at 2.5 km depth. From this analysis the results show that the retrieved sub-vertical  $\sigma_1$  is related to the effect of the ground deformation source, while the obtained pattern of  $\sigma_3$  require an additional background field. In order to determine the general features of this field, was used a novel approach of joint inversion (D'Auria et al., 2015) that results in a weak extensional N–S regional stress field driving the orientation of the  $\sigma_3$  axes. These results indicate that the stress field can be related to volcano dynamics and could be linked to the intrusion of fluids. Following this hypothesis analysis of the excess of pore fluid pressure have performed. Starting from the Coulomb–Navier criterion, using the focal mechanism dataset it has been possible estimate the pore pressure acting on the fault during the seismic events and calculate if there was a reduction of normal stress due to the excess of pore pressure that eventually trigger the fault slip. Results show effectively an excess of pore pressure in the flegrean area with elevated values in particular during 1984, located 2.5–3 km in depth congruently with the retrieved deformation source depth. In the last part of the work, to analyse the hydrothermal system of Campi Flegrei caldera and in order to confirm the reliability of pore pressure fluid results, thermo – fluid dynamic simulations has been performed used MUFITS simulator. This program permits simulation with realistic and almost unrealistic values of temperature, pressure and rate of injection of fluids in the system, one of the

reason for which was preferred to usual TOUGHT2. Results of simulations are comparable with the retrieved excess of pore pressure indicating an overpressure in the area near the source of injection and immediately above, with depth of overpressure comparable with the depth of the source modelled in the inversion of ground deformation data.

## Bibliography

- Aki et al., 1965.* Maximum Likelihood esitmate of b in the Formula  $\log N = a - b M$  and its Confidence Limits. Bulletin of the Earthquake research institute Vol. 43 (1965), pp. 237–239.
- Amoruso et al., 2008.* Simultaneous inversion of deformation and gravity changes in a horizontally layered half-space: Evidences for magma intrusion during the 1982–1984 unrest at Campi Flegrei caldera (Italy). Earth and Planetary Science Letters 272 (2008) 181–188.
- Amoruso et al., 2014.* Paired deformation sources of the Campi Flegrei caldera (Italy) required by recent (1980–2010) deformation history. J. Geophys. Res. Solid Earth, 119, 858–879, doi:10.1002/2013JB010392.
- Anderson, E.M., 1936.* The dynamics of the formation of cone sheets, ring dykes, and cauldron subsidence. Royal Society of Edinburgh Proceedings, v. 56, part 2, p. 128–163.
- Angelier et al., 1979.* Determination of the mean principal directions of stresses for a given fault population. Tectonophysics, 56 (1979) T17–T26.
- Angelier et al., 1982.* Inversion of field data in fault tectonics to obtain the regional stress – I. Single phase fault populations: a new method of computing the stress tensor. Geophys. J. R. astr. Soc. (1982) 69, 607–621.
- Angelier, 1984.* Tectonic analysis of fault slip data sets. JOURNAL OF GEOPHYSICAL RESEARCH VOL. 89, NO. B7, PAGES 5,835–5,848, JULY 10, 1984
- Angelier, 1990.* Inversion of field data in fault tectonics to obtain the regional stress–111. A new rapid direct inversion method by analytical means. Geophys. J. Int. (1990) 103, 363–376.
- Angelier, 2002.* Inversion of earthquake focal mechanisms to obtain the seismotectonic stress IV—a new method free of choice among nodal planes. Geophys. J. Int. (2002) 150, 588–609.

*Angelier and Mechler, 1977.* Sur une methode graphique de recherche des contraintes principales également utilisables en tectonique et en seismologie: la methode des diedres droits. Bulletin de la Société géologique de France, (7), t.XIX, n°6, 1309–1318.

*Angelier, & Manoussis, 1980.* Classification automatique et distinction des phases superposées en tectonique de failles. CR Acad. Sci. Paris, 290, 651–654.

*Aster and Meyer, 1988.* Three-dimensional velocity structure and hypocenter distribution in the Campi Flegrei caldera, Italy. Tectonophysics, 149(3), 195–218.

*Aster et al., 2013.* Parameter estimation and inverse problems (Academic Press).

*Brandsdottir and Einarsson, 1979.* Seismic activity associated with the September 1977 deflation of the Krafla central volcano in northern Iceland. J. Volc. Geotherm. Res., 6, 197–212.

*Barberi et al., 1984.* Phlegraean Fields 1982–1984: brief chronicle of a volcano emergency in a densely populated area. Bull. Volcanol., 47(2): 175–185.

*Baisch et al., 2003.* A model for fluid-injection-induced seismicity at the KTB, Germany. Geophys. J. Int. (2003) 152, 160–170.

*Battaglia et al., 2003.* The mechanics of unrest at Long Valley caldera, California. 1. Modeling the geometry of the source using GPS, leveling and two-color EDM data. Journal of Volcanology and Geothermal Research 127 (2003) 195– 217.

*Battaglia et al., 2003b.* The mechanics of unrest at Long Valley caldera, California. 2. Constraining the nature of the source using geodetic and micro-gravity data. Journal of Volcanology and Geothermal Research 127 (2003) 219^245.

*Battaglia et al., 2004.* The Interpretation of Gravity Changes and Crustal Deformation in Active Volcanic Areas. Pure appl. geophys. 161 (2004) 1453–1467 0033 – 4553/04/071453 – 15 DOI 0.1007/s00024-004-2514-5.

*Battaglia, 2006.* Evidence for fluid migration as the source of deformation at Campi Flegrei caldera (Italy). GEOPHYSICAL RESEARCH LETTERS, VOL. 33, L01307, doi:10.1029/2005GL024904, 2006.

*Battaglia et al., 2008.* Merging active and passive data sets in traveltome tomography: The case study of Campi Flegrei caldera (Southern Italy). Geophysical Prospecting, 2008, 56, 555–573 doi:10.1111/j.1365-2478.2007.00687.x

*Bailey, R.A., 1989.* Geologic map of Long Valley caldera, Mono-Inyo Craters volcanic chain, and vicinity, Mono County, California. U.S. Geological Survey Miscellaneous Investigations Map I-1933, scale 1:62,500

*Beauducel et al., 2004.* 3-D Modelling of Campi Flegrei Ground Deformations: Role of Caldera Boundary Discontinuities. Pure appl. geophys. 161 (2004) 1329–13440033 – 4553/04/071329 – 16 DOI 10.1007/s00024-004-2507-4.

*Benioff, 1951.* EARTHQUAKES AND ROCK CREEP. Bulletin of the Seismological Society of America, January 1951, v. 41, p.31-62.

*Benoit et al., 1996.* Global volcanic earthquake swarm database and preliminary analysis volcanic earthquake swarm duration. ANNALI DI GEOFISICA, VOL XXXIX, N.2, MARCH 1996.

*Berrino et al., 1992.* Gravity-height correlations for unrest at calderas. Journal of Volcanology and Geothermal Research, 53 ( 1992 ) 11-26.

*Berrino et al., 2008.* 3D Gravity Inversion by Growing Bodies and Shaping Layers at Mt. Vesuvius (Southern Italy) Pure appl. geophys. 165 (2008) 1095–1115 0033-4553/08/061095-21 DOI 10.1007/s00024-008-0348-2-.

*Bianco et al., 2004.* The role of hydrothermal fluids in triggering the July–August 2000 seismic swarm at Campi Flegrei, Italy: evidence from seismological and mesostructural data. Journal of Volcanology and Geothermal Research 133 (2004) 229–246.

*Bishop, 1966.* The strength of solids as engineering materials, Geotechnique, 16 , pp. 91–130.

*Blacic et al., 2009.* Converted phases analysis of the Campi Flegrei caldera using active seismic data. Tectonophysics 470 (2009) 243–256.

*Blackwell et al., 1985.* A Transient Model of the Geothermal System of the Long Valley Caldera, California. JOURNAL OF GEOPHYSICAL RESEARCH, VOL. 90, NO. B13, PAGES 11,229–11,241, NOVEMBER 10, 1985.

*Bonafede, 1991.* Hot fluid migration, an efficient source of ground deformation: Application to the 1982–1985 crisis at Campi Flegrei–Italy. J. Volcanol. Geotherm. Res., 48, 187–198.

*Bonafede et al., 1998.* Modelling gravity variations consistent with ground deformation in the Campi Flegrei caldera (Italy). Journal of Volcanology and Geothermal Research 81 1998. 137–157.

*Bott, 1959.* The mechanics of oblique slip faulting, Geol. Mag., 96, 109–117.

*Bruno et al., 2002.* Thewestern undersea section of the Ischia volcanic complex (Italy, Tyrrhenian sea) inferred from marine geophysical data .Geophysical Research Letters, 29 ,57, 1-4

*Bruno et al., 2003.* Structural setting of the Bay of Naples (Italy) seismic reflection data: implications for Campanian volcanism [Tectonophysics 372 (2003) 193–213].

*Bruno et al., 2007.* Geophysical and hydrogeological experiments from a shallow hydrothermal system at Solfatara Volcano, Campi Flegrei, Italy: Response to caldera unrest.JOURNAL OF GEOPHYSICAL RESEARCH, VOL. 112, B06201, doi:10.1029/2006JB004383, 2007.

Burnham and Anderson, 2002. Model selection and multimodel inference: a practical information-theoretic approach. Springer.

*Bucher, 1920.* The mechanical interpretation of joints. Part 1 journal of Geologu 28: 707–730.

*Caliro et al., 2005.* Recent activity of Nisyros volcano (Greece) inferred from structural, geochemical and seismological data. *Bull Volcanol* (2005) 67:358–369 DOI 10.1007/s00445-004-0381-7.

*Caliro et al., 2015.* Tectonic stress and renewed uplift at Campi Flegrei caldera, southern Italy: New insights from caldera drilling. *Earth and Planetary Science Letters* 420(2015)23–29.

Camacho et al., 2011. Simultaneous inversion of surface deformation and gravity changes by means of extended bodies with a free geometry: Application to deforming calderas. *J. Geophys. Res.*, 116, B10401, doi:10.1029/2010JB008165.

Cannavò et al., 2014, A Joint Inversion of Ground Deformation and Focal Mechanisms Data for Magmatic Source Modelling. *Pure and Applied Geophysics*, doi:10.1007/s00024-013-0771-x.

*Cappelletti et al., 2003.* Post-eruptive processes in the Campanian Ignimbrite. *Mineralogy and Petrology* (2003) 79: 79–97 DOI 10.1007/s00710-003-0003-7.

*Chiaraabba et al., 2006.* An insight into the unrest phenomena at the Campi Flegrei caldera from Vp and Vp/Vs tomography. *Terra Nova*, 18, 373–379, 2006.

*Chiodini et al., 2001.* CO<sub>2</sub> degassing and energy release at Solfatara volcano, Campi Flegrei, Italy. *Journal of Geophysical Research: Solid Earth* (1978–2012), 106(B8), 16213–16221.

Chiodini et al., 2003. Magma degassing as a trigger of bradyseismic events: The case of Phleorean Fields (Italy). *Geophys. Res. Lett.*, 30(8), 1434, doi:10.1029/2002GL016790.

*Chiodini et al., 2010.* Long-term variations of the Campi Flegrei, Italy, volcanic system as revealed by The monitoring of hydrothermal activity. *J. Geophys. Res.*, 115, B03205, doi:10.1029/2008JB006258.

*Chiodini et al., 2015.* Evidence of thermal-driven processes triggering the 2005–2014 unrest at Campi Flegrei caldera. *Earth and Planetary Science Letters* 414(2015)58–67.

*Cusano et al., 2008.* Hydrothermal origin for sustained Long-Period (LP) activity at Campi Flegrei Volcanic Complex, Italy. *Journal of Volcanology and Geothermal Research* 177 (2008) 1035–1044.

*D'Auria et al., 2008.* A unified 3D velocity model for the Neapolitan volcanic areas, In Conception, Verification and Application of Innovative Techniques to Study Active Volcanoes (ed. Marzocchi W. and Zollo A.), pp. 375–390, ISBN 978-88-89972-09-0.

*D'Auria et al., 2011.* Repeated fluid-transfer episodes as a mechanism for the recent dynamics of Campi Flegrei caldera (1989–2010). *JOURNAL OF GEOPHYSICAL RESEARCH*, VOL. 116, B04313, doi:10.1029/2010JB007837, 2011.

*D'Auria et al., 2012.* The 4D imaging of the source of ground deformation at Campi Flegrei caldera (southern Italy). *JOURNAL OF GEOPHYSICAL RESEARCH*, VOL. 117, B08209, doi:10.1029/2012JB009181, 2012.

*D'Auria et al., 2014.* The stress field beneath a quiescent stratovolcano: The case of Mount Vesuvius. *J. Geophys. Res. Solid Earth*, 119, doi:10.1002/2013JB010792.

*D'Auria et al. (2015).* Retrieving the stress field within the Campi Flegrei caldera (Southern Italy) through an integrated geodetical and seismological approach. *Pure Appl. Geophys.* DOI 10.1007/s00024-014-1004-7

*Deino et al., 2004.* The age of the Neapolitan Yellow Tu; caldera-forming eruption (Campi Flegrei caldera ^ Italy) assessed by  $^{40}\text{Ar}/^{39}\text{Ar}$  dating method. *Journal of Volcanology and Geothermal Research* 133 (2004) 157^170.

*DelloIacono et al., 2009.* Seismic images and rock properties of the very shallow structure of Campi Flegrei caldera (southern Italy). *Bull Volcanol* (2009) 71:275–284 DOI 10.1007/s00445-008-0222-1.

*De Lorenzo et al., 2001.* Source parameters and three-dimensional attenuation structure from the inversion of microearthquake pulse width data: Qp imaging and inferences on the thermal state of the Campi Flegrei caldera (southern Italy). *Journal of geophysical research*, VOL. 106, NO.B8, PAGES 16,265–16,286.

*De Natale et al., 1986.* STATISTICAL ANALYSIS AND CLUSTERING FEATURES OF THE PHLEGRAEAN FIELDS EARTHQUAKE SEQUENCE (MAY 1983–MAY 1984). *Bulletin of the Seismological Society of America*, Vol. 76, No. 3, pp. 801–814, June 1986.

*De Natale et al., 1991.* Geophysical and geochemical modelling of the 1982–1984 unrest phenomena at Campi Flegrei caldera (southern Italy). *Journal of Volcanology and Geothermal Research*, 48 ( 1991 ) 199–222.

*De Natale et al., 1995.* Accurate fault mechanism determinations for a 1984 earthquake swarm at Campi Flegrei caldera (Italy) during an unrest episode. Implications for volcanological research. *Journal of geophysical research*, VOL. 100, NO. B12, pages 24,167–24,185, December 10, 1995.

*De Natale et al., 2001.* A mechanical fluid-dynamical model for ground movements at Campi Flegrei caldera. *Journal of Geodynamics* 32 (2001) 487–517.

*De Natale et al., 2006.* The Somma-Vesuvius volcano (Southern Italy) : Structure, dynamics and hazard evaluation. *Earth Science Reviews* 74: 73–111

*De Siena et al., 2010.* Seismic attenuation imaging of Campi Flegrei. Evidence of gas reservoirs, hydrothermal basins, and feeding systems. *JOURNAL OF GEOPHYSICAL RESEARCH*, VOL. 115, XXXXXX, doi:10.1029/2009JB006938, 2010.

*De Siena et al., 2014.* Multi-scale reasonable attenuation tomography analysis (MuRAT): An imaging algorithm designed for volcanic regions. *Journal of Volcanology and Geothermal Research* 277 (2014) 22–35.

*Del Gaudio et al., 2010.* Unrest episodes at Campi Flegrei: A reconstruction of vertical ground movements during 1905–2009. *Journal of Volcanology and Geothermal Research*, 195(1), 48–56.

*Dietrich, J. 1994.* A constitutive law for rate of earthquake production and its application to earthquake clustering. *J. geophys. Res.* 99, 2601–2618.

*Di Girolamo et al., 1984.* Vulcanologia e petrologia dei Campi Flegrei. *Boll. Soc. Geol. It.*, 103 ,349–413.

*Di Renzo et al., 2011.* The magmatic feeding system of the Campi Flegrei caldera: Architecture and temporal evolution. *Chemical Geology* 281 (2011) 227–241.

*Di Vito et al., 1999.* Volcanism and deformation since 12,000 years at the Campi Flegrei caldera (Italy). *Journal of Volcanology and Geothermal Research* 91 1999. 221–246.

*Druitt and Sparks, 1984.* On the formation of calderas during ignimbrite eruptions. *Nature* 310, 679–681;

*Dvorak et al., 1991.* Recent Ground Movement and Seismic Activity in Campi Flegrei, Southern Italy Episodic Growth of a Resurgent Dome. *JOURNAL OF GEOPHYSICAL RESEARCH*, VOL. 96, NO. B2, PAGES 2309–2323, FEBRUARY 10, 1991.

*Dvorak et al., 1997.* VOLCANO GEODESY: THE SEARCH FOR MAGMA RESERVOIRS AND THE FORMATION OF ERUPTIVE VENTS. *Reviews of Geophysics*, 35, 3 / August 1997. 8755–1209/97/9 7 RG-00070515.00.

*Durá-Gómez et al.,* Reservoir-induced seismicity associated with the Itoiz Reservoir, Spain: a case study. *Geophys. J. Int.* (2010) 181, 343–356.

*Dzurisin, 2006.* Volcano Deformation: Geodetic Monitoring Techniques. Berlin, Springer, Springer-Praxis Books in Geophysical Sciences, 441 p.

*Efron, 1979.* Bootstrap methods: Another look at the jackknife. *The Annals of Statistics* 7 (1):1–26.

*Farrar et al., 2002.* Forest-killing diffuse CO<sub>2</sub> emission at Mammoth Mountain as a sign of magmatic unrest. *NATURE* VOL 376 24 AUGUST 1995.

*Ferrucci et al., 1989.* Seismic detection of a major Moho upheaval beneath the Campania volcanic area (Naples, Southern Italy). *Geophysical Research Letters* 16: doi: 10.1029/89GL01444. issn: 0094-8276.

*Fialko et al., 2001.* Deformation due to a pressurized horizontal circular crack in an elastic half-space, with applications to volcano geodesy. *Geophysical Journal International*, 146(1), 181–190.

*Finetti & Morelli, (1974).* Esplorazione sismica a riflessione dei Golfi di Napoli e Pozzuoli. *Boll. Geof. Teor. ppl.*, 16, 175–222.

*Folch and Gottsmann,* Faults and ground uplift at active calderas.

*Frohlich, 1992.* Triangle diagrams: Ternary graphs to display similarity and diversity of earthquake focal mechanisms, *Phys. Earth Planet. Inter.*, 75, 193–198.

*Gaeta et al., 1998.* Genesis and evolution of unrest episodes at Campi Flegrei caldera: The role of thermal fluid-dynamical processes in the geothermal system. *JOURNAL OF GEOPHYSICAL RESEARCH*, VOL. 103, NO. B9, PAGES 20,921–20,933, SEPTEMBER 10, 1998.

*Gaeta et al., 2003.* A physical appraisal of a new aspect of bradyseism: The miniuplifts. *JOURNAL OF GEOPHYSICAL RESEARCH*, VOL. 108, NO. B8, 2363, doi:10.1029/2002JB001913, 2003.

*Gaudiosi and Iannaccone, 1984.* A preliminary study of stress pattern at Phlegraean Fields as inferred from focal mechanisms. *Bulletin volcanologique*, 47(2), 225–231.

*Gebauer et al., 2014.* Crystallization and eruption ages of Breccia Museo (Campi Flegrei caldera, Italy) plutonic clasts and their relation to the Campanian ignimbrite. *Contrib Mineral Petrol*, 167:953, doi:10.1007/s00410-013-0953-7.

*Gephart and Forsyth, 1984.* An improved method for determining the regional stress tensor using earthquake focal mechanism data: application to the San Fernando earthquake sequence. *J. Geoph. Res.*, 89, 9305–9320.

*Geyer and Marty, 2014.* A short review of our current understanding of the development of ring faults during collapse caldera formation. *Front. Earth Sci.*, 26 September 2014.

*Gottsmann et al., 2002.* Deflation during caldera unrest: constraints on subsurface processes and hazard prediction from gravity–height data. *Bull Volcanol* (2002) 64:338–348 DOI 10.1007/s00445-002-0212-7.

*Gottsmann et al., 2003.* Hazard assessment during caldera unrest at the Campi Flegrei, Italy: a contribution from gravity^height gradients. *Earth and Planetary Science Letters* 211 (2003) 295–309.

*Gottsmann et al., 2006.* Unrest at Campi Flegrei: A contribution to the magmatic versus hydrothermal debate from inverse and finite element modeling. *JOURNAL OF GEOPHYSICAL RESEARCH, VOL. 111, B07203*, doi:10.1029/2005JB003745, 2006.

*Gottsmann et al., 2006b.* Spatiotemporal variations in vertical gravity gradients at the Campi Flegrei caldera (Italy): a case for source multiplicity during unrest? *Geophys. J. Int.* (2006) 167, 1089–1096 doi: 10.1111/j.1365-246X.2006.03157.x.

*Gottsmann et al., 2006c.* Unrest at the Campi Flegrei caldera (Italy): A critical evaluation of source parameters from geodetic data inversion. *Journal of Volcanology and Geothermal Research* 150 (2006) 132– 145.

*Gottsmann et al., 2007.* Oscillations in hydrothermal systems as a source of periodic unrest at caldera volcanoes: Multiparameter insights from Nisyros, Greece. *GEOPHYSICAL RESEARCH LETTERS, VOL. 34, L07307*, doi:10.1029/2007GL029594, 2007.

*Gottsmann and Martí, 2008.* Caldera volcanism . Analysis, Modelling and Response. Elsevier Science.

*Gudmundsson, 1998.* Formation and development of normal-fault calderas and the initiation of large explosive eruptions. *Bull. Volcanol.*, 60, 160–170.

*Gudmundsson et al., 2008.* Volcanic hazards in Iceland. *Jökull*, 58, 251–268

*Gudmundsson et al., 1997.* Stress fields generating ring faults in volcanoes, *Geophys. Res. Lett.*, 24, 1559–1562

*Guidoboni et al., 2010.* The Campi Flegrei caldera: historical revision and new data on seismic crises, bradyseisms, the Monte Nuovo eruption and ensuing earthquakes (twelfth century 1582 AD). *Bull Volcanol* DOI 10.1007/s00445-010-0430-3.

*Gvirtzman and Nur, 1999.* The formation of Mount Etna as the consequence of slab rollback. *Nature* 401, 782–785 (21 October 1999) | doi:10.1038/44555;

*Hill, et al., 1990.* The 1989 earthquake swarm beneath Mammoth Mountain, California: An initial look at the 4 May through 30 September activity, *Bull. Seismol. Soc. Am.*, 80, 325 – 339, 1990

*Hill et al., 2002.* Response plans for volcanic hazards in the Long Valley caldera and Mono craters area, California, U.S. Geol. Surv. Bull., 2185, 21 – 44, 2002

*Hippolyte et al., 1994.* A major geodynamic change revealed by Quaternary stress patterns in the Southern Apennines (Italy). Tectonophysics 230 (1994) 199–210.

*Hippolyte et al., 2012.* Keys and pitfalls in mesoscale fault analysis and paleostress reconstructions, the use of Angelier's method. Tectonophysics Volume 581, 18 December 2012, Pages 144–162.

*Hough et al., 2000.* The 1998 Earthquake Sequence South of Long Valley Caldera, California: Hints of Magmatic Involvement. Bulletin of the Seismological Society of America, 90, 3, pp. 752–763, June 2000.

*Huang and Angelier, 1989.* Inversion of field data in fault tectonics to obtain the regional stress–11. Using conjugate fault sets within heterogeneous families for computing palaeostress axes. Geophysical Journal (1989) 96, 139–149.

*Hurwitz et al., 2006.* Hydrothermal fluid flow and deformation in large calderas: Inferences from numerical simulations. JOURNAL OF GEOPHYSICAL RESEARCH, VOL. 112, B02206, doi:10.1029/2006JB004689, 2007.

*Hutnak et al., 2008.* Numerical models of caldera deformation: Effects of multiphase and multicomponent hydrothermal fluid flow. JOURNAL OF GEOPHYSICAL RESEARCH, VOL. 114, 04411 ,Doi:10.1029/ 2008JB006151, 2009.

*Iannaccone et al., 2009.* A new Multidisciplinary Marine Monitoring system for the surveillance of Volcanic and seismic areas. Seismological Research Letters Volume 80, Number 2 March/April 2009.

*Iannaccone et al., 2010.* Long-term Seafloor Experiment with the CU MAS Module: Performance, Noise Analysis of Geophysical Signals, and Suggestions about the Design of a Permanent Network. Seismological Research Letters Volume 81, Number 6 November/December 2010.

*Isaia et al., 2009.* Caldera unrest prior to intense volcanism in Campi Flegrei (Italy) at 4.0 ka B.P.: Implications for caldera dynamics and future eruptive scenarios. GEOPHYSICAL RESEARCH LETTERS, VOL. 36, L21303, doi:10.1029/2009GL040513, 2009.

*Judenherc and A. Zollo, 2004.* The Bay of Naples (southern Italy): Constraints on the volcanic structures inferred from a dense seismic survey. JOURNAL OF GEOPHYSICAL RESEARCH, VOL. 109, B10312, doi:10.1029/2003JB002876, 2004.

*Kamb, 1959.* Ice Petrofabric Observations from Blue Glacier, Washington, Relation to Theory and Experiment. JOURNAL OF GEOPHYSICAL RESEARCH VOLUME 54, No. 11 NOVEMBER, 1959.

*King et al., 1994.* Static Stress Changes and the Triggering of Earthquakes. Bulletin of the Seismological Society of America, Vol. 84, No. 3, pp. 935–953, June 1994.

*Langbein, et al., 1998.* The 1997±98 inflation episode of Long Valley caldera and comparison with the 1989±95 episode. EOS: Trans. Am. Geophys. Union 79 (45), F963

*Lee et al., 1981.* Principles and applications of microearthquake networks in: *Advances in Geophysics*, Supplement 2, Academic Press, New York, 293 pp.

*Lirer et al., 1987.* On the Volcanological Evolution of Campi Flegrei. *Eos*, Vol. 68, No. 16, April 21, 1987.

*Lisle, 1987.* ROMSA: A BASIC PROGRAM FOR PALEOSTRESS ANALYSIS USING FAULT-STRIATION DATA. *Computers & Geosciences* Vol. 14. No. 2. pp. 255–259. 1988

*Lisle, 1992.* New method of estimating regional stress orientations: application to focal mechanism data of recent British earthquakes. *Geophys. J. Znt.* (1992) 110,276–282.

*Lisle et al., 2013.* Separation of multiple stress events by fault striation analysis: an example from Variscan and younger structures at Ogmore, South Wales. *Journal of the Geological Society* 1996, v.153; p945–953.

*Lowenstern et al., 2006.* Monitoring super-volcanoes: geophysical and geochemical signals at Yellowstone and other large caldera systems. *Phil. Trans. R. Soc. A* 2006 364, 2055–2072.doi: 10.1098/rsta.2006.181.

*Macdonald, 1972.* Volcanoes. A discussion of volcanoes, volcanic products, and volcanic phenomena, xii+510 pp., 120 figs, 144 pis. 15 tables. Prentice-Hall, International, New Jersey.

*Macedonio et al., 2014.* Sill intrusion as a source mechanism of unrest at volcanic calderas. In press on *Journal of Geophysical Research*.

*Marti et al., 2000.* The Las CanÃadas caldera (Tenerife, Canary Islands): an overlapping collapse caldera generated by magma-chamber migration. *Journal of Volcanology and Geothermal Research* 103 (2000) 161±173.

*McKenzie et al., 1969.* The relation between fault plane solutions for earthquakes and the directions of the principal stresses, *Bull. Seismol. Soc. Am.* 59, 591–601.

*McTigue, 1987.* Elastic stress and deformation near a finite spherical magma body: Resolution of the point source paradox. *Journal of Geophysical Research: Solid Earth* (1978–2012), 92(B12), 12931–12940.

*Michael, 1984* Determination of stress from slip data: faults and folds. *J. Geophys. Res.*, 89, 11517–11526.

*Michael, 1987.* Use of Focal Mechanisms to Determine Stress: A Control Study. *J. Geoph. Res.*, 92, 357–368.

*Mogi, 1958.* Relations between the Eruptions of Various Volcanoes and the Deformations of the Ground surfaces around them. *Bulletin of the earthquake research Institute*. Vol. 36 (1958) pp. 99–134.

*Morhange et al. 2006.* Rapid sea-level movements and noneruptive crustal deformations in the Phleorean Fields caldera, Italy. *Geology* 2006;34:93–96.

*Moriya et al., 2003.* Multiplet-Clustering Analysis Reveals Structural Details within the Seismic Cloud at the Soultz Geothermal Field, France. *Bulletin of the Seismological Society of America*, Vol. 93, No. 4, pp. 1606–1620, August 2003.

*Nelder and Mead, 1965.* A simplex method for function minimization, *Comput. J.*, 7, pp.308–313.

*Newall & Self(1982)*. The volcanic explosivity index (VEI) an estimate of explosive magnitude for historical volcanism.

Journal of Geophysical Research.10.1029/JC087iC02p01231.

*Okada, 1985*. Surface deformation due to shear and tensile faults in a half-space. Bulletin of the seismological society of America, 75(4), 1135–1154.

*Okada, Y. 1992*. Internal deformation due to shear and tensile faults in a half-space. Bulletin of the Seismological Society of America, 82(2), 1018–1040.

*Orsi et al. 1996*. The restless, resurgent Campi Flegrei nested caldera (Italy): constraints on its evolution and configuration. Journal of Volcanology and Geothermal Research, 74(3), 179–214.

*Orsi et al. 1999*. Short-term ground deformations and seismicity in the resurgent Campi Flegrei caldera (Italy): an example of active block-resurgence in a densely populated area. J. Volcanol. Geotherm. Res., Special Issue "Volcanism in the Campi Flegrei" Orsi G., Civetta L., Valentine G.A. (Eds). 91 (2–4): 415–451.

*Orsi et al. 1999b*. Mechanical and thermo-fluid behaviour during unrest at the Campi Flegrei caldera (Italy). Journal of Volcanology and Geothermal Research 91 1999. 453–470.

*Orsi et al. 2004*. Volcanic hazard assessment at the restless Campi Flegrei caldera. Bulletin of Volcanology, 66(6), 514–530.

*Otsubo et al. 2006*. Improved resolution of the multiple inverse method by eliminating erroneous solutions. Computers & Geosciences 32 (2006) 1221–1227

*Otsubo et al. 2008*. Determination of stresses from heterogeneous focal mechanism data: An adaptation of the multiple inverse method. Tectonophysics 457 (2008) 150–160.

*Patanè et al. 2003*. Seismological constraints for the dike emplacement of July– August 2001 lateral eruption at Mt. Etna volcano, Italy. Annals of geophysics, 46(4), 599–608.

*Pedersen and Sigmundsson, 2004*. InSAR based sill model links spatially offset areas of deformation and seismicity for the 1994 unrest episode at Eyjafjallajökull volcano, Iceland. Geophys. Res. Lett., 31(14), doi:10.1029/2004GL020368.

*Peluso et al. 2007*. Experimental determination of permeability of Neapolitan Yellow Tuff. Journal of Volcanology and Geothermal Research 160 (2007) 125–136.

*Petrosino et al. 1964*. Recalibration of the Magnitude Scales at Campi Flegrei, Italy, on the Basis of Measured Path and Site and Transfer Functions. Bulletin of the Seismological Society of America, Vol. 98, No. 4, pp. 1964–1974, August 2008, doi: 10.1785/0120070131.

*Ramsay, Lisle 2000*. Applications of continuum mechanics in structural geology (Techniques of modern structural geology. Vol.3), 701–1061.

*Reasenberg and Oppenheimer, 1985.* FPFIT, FPPILOT and FPPAGE: Fortran computer programs for calculating and displaying earthquake fault-plane solutions, US Geol. Surv., Open-File Rept, 85-739.

*Ricci et al., 2013.* Volcanic risk perception in the Campi Flegrei area. Journal of Volcanology and Geothermal Research 254 (2013) 118–130.

*Rinaldi et al., 2010.* Hydrothermal instability and ground displacement at the Campi Flegrei caldera. Physics of the Earth and Planetary Interiors 178 (2010) 155–161.

*Rinaldi et al., 2011.* Electrical conductivity, ground displacement, gravity changes, and gas flow at Solfatara crater (Campi Flegrei caldera, Italy): Results from numerical modeling. Journal of Volcanology and Geothermal Research Volume 207, Issues 3–4, 15 October 2011, Pages 93–105.

*Rivera and Cisternas, 1990.* Stress tensor and fault plane solutions for a population of earthquakes. Bull. Seismol. Soc. Am., 80(3): 600–614.

*Rubin et al., 1998.* A reinterpretation of seismicity associated with the January 1983 dike intrusion at Kilauea volcano, Hawaii. J. geophys. Res., 103, 10003–10015.

*Saccorotti et al., 2001.* The July–August 2000 seismic swarms at Campi Flegrei volcanic complex, Italy. GEOPHYSICAL RESEARCH LETTERS, VOL. 28, NO. 13, PAGES 2525–2528, JULY 1, 2001.

*Saccorotti et al., 2007.* Seismicity associated with the 2004–2006 renewed ground uplift at Campi Flegrei Caldera, Italy. Physics of the Earth and Planetary Interiors 165 (2007) 14–24.

*Sachpazi et al., 2002.* Seismological and SAR signature of unrest at Nisyros caldera, Greece. Journal of Volcanology and Geothermal Research 116 (2002) 19^33.

*Scandone, P.. 1979.* Origin of the Tyrrhenian sea and Calabrian arc. Boll. Sot. Geol. Ital.. 98: 27–34.

*Scandone et al., 1991.* The structure of the Campanian Plain and the activity of the Neapolitan volcanoes (Italy). Journal of Volcanology and Geothermal Research Volume 48, Issues 1–2, August 1991, Pages 1–31.

*Scandone et al., 2010.* The relevance of the 1198 eruption of Solfatara in the Phlegraean Fields (Campi Flegrei) as revealed by medieval manuscripts and historical sources. Journal of Volcanology and Geothermal Research 189 (2010) 202–206.

*Segall, 2013.* Volcano deformation and eruption forecasting. Geological Society, London, Special Publications, 380, doi:10.1144/SP380.4.

*Segall, 2010.* Earthquake and volcano deformation. Princeton University Press.

*Segall, 2013.* Time-dependent dike propagation from joint inversion of seismicity and deformation data. Journal of Geophysical Research: Solid Earth, 118(11), 5785–5804.

*Sen and Stoffa, 1995.* Global optimization methods in geophysical inversion. Elsevier.

*Shapiro et al., 2003.* Triggering of Seismicity by Pore-pressure Perturbations: Permeability-related Signatures of the Phenomenon. *Pure appl. geophys.* 160 (2003) 1051–1066 0033 – 4553/03/061051–16.

*Sholtz, 1998.* Earthquakes and friction laws. *NATURE* | VOL 391 | 1 JANUARY 1998.

*Tedesco et al., 1988b.* 10 th OF APRIL 1987 SEISMIC SWARM: CORRELATION WITH GEOCHEMICAL PARAMETERS IN CAMPI FLEGREI CALDERA (SOUTHERN ITALY). *GEOPHYSICAL RESEARCH LETTERS*, VOL. 15, NO. 7, PAGES 661–664, JULY 1988.

*Terakawa et al., 2000.* High-pressure fluid at hypocentral depths in the L'Aquila region inferred from earthquake focal mechanisms. *Geology* 2010;38:995–99.

*Terakawa et al., 2012.* High fluid pressure and triggered earthquakes in the enhanced geothermal system in Basel, Switzerland. *JOURNAL OF GEOPHYSICAL RESEARCH*, VOL. 117, B07305, doi:10.1029/2011JB008980, 2012

*Tezuka et al., 2000.* Stress estimated using microseismic clusters and its relationship to the fracture system of the Hijiori hot dry rock reservoir. *Engineering Geology* 56 (2000) 47–62.

*Toda et al., 2002.* Evidence from the ad 2000 Izu islands earthquake swarm that stressing rate governs seismicity. *Nature*, 419, 58–61.

*Todesco, 2008.* Signals from the Campi Flegrei hydrothermal system: Role of a “magmatic” source of fluids. *JOURNAL OF GEOPHYSICAL RESEARCH*, VOL. 114, B05201, doi:10.1029/2008JB006134, 2009.

*Tramelli, 2013.* A New Method for Optimization and Testing of Microseismic Networks: An Application to Campi Flegrei (Southern Italy). *Bulletin of the Seismological Society of America*, 103(3), 1679–1691, doi:10.1785/0120120211.

*Trasatti et al., 2005.* Structural and rheological constraints on source depth and overpressure estimates at the Campi Flegrei caldera, Italy. *Journal of Volcanology and Geothermal Research* 144 (2005) 105–118.

*Troise et al., 1997.* A model for earthquake generation during unrest episodes at Campi Flegrei and Rabaul Calderas. *GEOPHYSICAL RESEARCH LETTERS*, VOL.24, NO.13, PAGES 1575–1578.

Troise et al., 1998. Evidence for static stress interaction among earthquakes in the south-central Apennines (Italy). *Geophys. J. Int.* (1998) 134 (3): 809–817. doi: 10.1046/j.1365–246x.1998.00610.x

*Troise et al., 2003.* Coulomb stress changes at calderas: Modeling the seismicity of Campi Flegrei (southern Italy). *JOURNAL OF GEOPHYSICAL RESEARCH*, VOL. 108, NO. B6, 2292, doi:10.1029/2002JB002006, 2003.

*Troise et al., 2007.* Renewed ground uplift at Campi Flegrei caldera (Italy): New insight on magmatic processes and forecast. GEOPHYSICAL RESEARCH LETTERS, VOL. 34, L03301, doi:10.1029/2006GL028545, 2007.

*Umakoshi et al., 2001.* Volcano-tectonic seismicity at Unzen Volcano, Japan, 1985–1999. Journal of Volcanology and Geothermal Research, 112, 117–131.

*Vanorio et al., 2002.* Ultrasonic velocity measurements in volcanic rocks: correlation with microtexture. Geophys. J. Int. (2002) 149, 22–36.

*Vanorio and J. Virieux, 2005.* Three-dimensional seismic tomography from P wave and S wave microearthquake travel times and rock physics characterization of the Campi Flegrei Caldera. JOURNAL OF GEOPHYSICAL RESEARCH, VOL. 110, B03201, doi:10.1029/2004JB003102, 2005.

*Vitale, 2013.* Fractures and faults in volcanic rocks (Campi Flegrei, southern Italy): insight into volcano-tectonic processes. International Journal of Earth Sciences, 1–19.

*Waldhauser, F., 2001.* HypoDD: A computer program to compute double-difference earthquake locations, U.S. Geol. Surv. open-file report, 01-113, Menlo Park, California, 2001.

*Waldhauser F and W.L. Ellsworth,* A double-difference earthquake location algorithm: Method and application to the northern Hayward fault, Bull. Seism. Soc. Am., 90, 1353–1368, 2000.

*Wallace, 1951.* Geometry of shearing stress and relationship to faulting. J.Geol., 59, 111– 130.

*Wicks et al. 2006.* Uplift, thermal unrest and magma intrusion at Yellowstone caldera. Vol 440 | 2 March 2006 | doi:10.1038/nature04507.

*Williams et al., 2002.* Detecting volcanic eruption precursors: a new method using gravity and deformation measurements. Journal of Volcanology and Geothermal Research 113 (2002) 379^389.

*Woo, 2010.* Intrusion and deformation at Campi Flegrei, southern Italy: sills, dikes, and regional extension. Journal of Geophysical Research: Solid Earth (1978–2012), 115(B12).

*Yamaji, 2000.* The multiple inverse method: a new technique to separate stresses from heterogeneous fault-slip data. Journal of Structural Geology 22 (2000) 441–452.

*Yamaji, 2003.* Are the solution of stress inversion correct? Visualization of their reliability and the separation of stresses from heterogeneous fault-slip data. Journal of Structural Geology 25 (2003) 241–252.

*Yamaji, 2007.* An Introduction to Tectonophysics. Terrapub, Tokyo.

*Yamaji et al, 2012.* A spherical code and stress tensor inversion. Computers & Geosciences 38(2012)164–167.

*Yang et al., 1988.* Deformation from inflation of a dipping finite prolate spheroid in an elastic half-space as a model for volcanic stressing. *Journal of Geophysical Research: Solid Earth* (1978–2012), 93(B5), 4249–4257.

*Zuppetta and Sava, 1991.* Stress pattern at Campi Flegrei from focal mechanisms of the 1982–1984 earthquakes (Southern Italy). *Journal of Volcanology and Geothermal Research*, 48(1), 127–137.

*Zollo et al., 2008.* Seismic reflections reveal a massive melt layer feeding Campi Flegrei *GEOPHYSICAL RESEARCH LETTERS*, VOL. 35, L12306, doi:10.1029/2008GL034242, 2008.